4-2012

Ultrafast intense-field photoionization and photofragmentation of systematic series of substituted organic molecules

Timothy D. Scarborough
University of Nebraska-Lincoln, tim.d.scarborough@gmail.com

ULTRAFAST INTENSE-FIELD PHOTOIONIZATION AND PHOTOFRAGMENTATION OF SYSTEMATIC SERIES OF SUBSTITUTED ORGANIC MOLECULES

by

Timothy Daniel Scarborough

A DISSERTATION

Presented to the Faculty of

The Graduate College at the University of Nebraska

In Partial Fulfillment of Requirements

For the Degree of Doctor of Philosophy

Major: Physics & Astronomy

Under the Supervision of Professor Cornelis Uiterwaal

Lincoln, Nebraska

April, 2012

ULTRAFAST INTENSE-FIELD PHOTOIONIZATION AND PHOTOFRAGMENTATION OF SYSTEMATIC SERIES OF SUBSTITUTED ORGANIC MOLECULES

Timothy Daniel Scarborough, Ph.D.

University of Nebraska, 2012

Adviser: Professor Cornelis Uiterwaal

The abundance and relevance of organic molecules similar to benzene makes their study important. Studying the interactions of such molecules with intense light fields has implications for the generation of short-wavelength radiation, attosecond science, high-harmonic generation, and many other fields. However, the computing power necessary to complete fully *ab initio* calculations describing molecules of this size does not exist; this leaves theoretical studies to rely on assumptions and approximations just to calculate the energies of the ground state. Including any sort of dynamics in these calculations is prohibitively complicated, and this makes experimental observations important.

Since many organic molecules are similar, it is possible to construct systematic series out of groups of molecules which differ from each other by a single structural parameter. Any differences in the intense-field behaviors between two molecules in such a series must then be a result of the structural parameter that is different. This dissertation is dedicated to the study of systematic series of organic molecules similar to benzene (C_6H_6). Our experiments are sensitive to the dynamics of photoionization and photofragmentation processes which result from interacting molecules in the gas phase with ultrafast (50 fs, 800 nm) laser pulses.

Preface

The results of Chapter 6 include works published in *Physical Chemistry Chemical Physics* and *The Journal of Chemical Physics.*

Chapter 8 is based on David Foote's undergraduate honors thesis, and much of this work is found in the *Journal of the International Society for Mass Spectrometry.*

The analysis of the focal volume effect which appears in Chapter 5 has been submitted to *Laser Physics Letters.*

Additional publications which are not represented in this dissertation can be found in *Applied Optics* and *New Journal of Physics.*

Acknowledgements

First and foremost, I would like to thank my family for their endless encouragement and patience. Mom, Dad, Andy: you've surely made me the man I am today, and you make me laugh the way only Scarboroughs can. Having three people whose support is truly unconditional continues to mean the world to me.

My deepest thanks to my advisor and friend Kees Uiterwaal, whose tutelage has crafted me into a worthy scientist. The knowledge I've gained from you over the years has provided me with terrific opportunities for the future, and I will be forever grateful to have worked with you. Thank you also for being one of the most positive, friendly, and easy-going people I've ever known, and for being the best boss I've ever had.

I would like to thank my committee members, Herman Batelaan, Martin Centurion, Tony Starace, Steve DiMagno, and Steve Ducharme for their support throughout my graduate career. Bonus points to Herman for helping me learn what has become a lifelong hobby, sailing the open seas (well, lakes anyway).

I have had more than my share of colleagues that deserve credit. Davy Foote and Collin McAcy have been spectacular undergraduate researchers, and I certainly owe them both a debt of gratitude. Whether it's slogging through data analysis or helping with a diagnosis ("the laser is doing *WHAT*?!?"), I have been very fortunate to have the help of such capable undergrads. Additional thanks to Davy for leading the project which forms the basis for Chapter 8. Thanks to Jimmy Strohaber for teaching me the ropes, and thanks to Roger Bach, Scot McGregor, and Shawn Hilbert for collaborations and commiserations through the grad school experience.

Thanks to the genuinely outstanding support staff in our department: Theresa Sis, Kay Haley, Jenny Becic, Joyce McNeil, and Patty Christen in the main office, Bob Kelty and Brian Farleigh in the computer shop, Les Marquart, Mike Jensen, Pat Pribel and Bob Rhynalds for help with the designing, repairing and machining of experimental equipment.

I would like to thank the Max-Planck-Institut für Quantenoptik, in particular, Dr. Hartmut Schröder, for generously lending us our time-of-flight ion mass spectrometer. Thanks to the National Science Foundation, UCARE, and GAANN for funding our research over the years.

Much like the Beatles, I've only gotten by with a little help from my friends. Brett and Sarah, those first two years I don't know how I would've kept it together without the two of you to lean on. Thanks to Bryan, Floyd and Chelsea, Mike and Michaela, Schmeichel, Dylan, Eli and Bri. Letting me be a part of such a tight group of friends at a time when I needed it meant more to me than most of you probably realize. Thanks to Alaina, Dobby, and Steve for sticking by my side through the years.

A special thanks goes to Evan Hoffmann for the best, most meaningful and fulfilling friendship of my life, and to Diana Hoffmann, whose strength and insight continue to amaze me.

This dissertation is dedicated to the memory of Evan Charles Hoffmann. If you could see me now…

Table of Contents

Chapter 1 – Introduction

1.1 – Motivation for research 1

1.2 – Summary of chapters 5

Chapter 2 – Introduction to intense-field processes

2.1 – Ionization processes 9

2.1.1 – Tunneling ionization 9

2.1.2 – Multiphoton ionization 11

2.1.3 – Resonance-enhanced multiphoton ionization 11

2.2 – Intense-field interactions 12

2.2.1 – The ponderomotive energy 12

2.2.2 – Channel closing 13

2.2.3 – Channel closing in REMPI 14

2.2.4 – Dynamic resonance 15

2.3 – The Keldysh parameter γ 17

Chapter 3 – Resonance-enhanced multiphoton ionization

3.1 – Multiphoton ionization: the I^N power law 22

3.2 – Resonance enhancement 25

3.3 – Rate model simulations 29

3.3.1 – Resonant vs. nonresonant MPI 31

3.3.2 – Distinguishing between similar processes 33

3.3.3 – Rate models in the presence of loss channels 36

Chapter 4 – Molecular processes

4.1 – The molecular Hamiltonian 41

4.2 – Molecular symmetry point groups 43

4.3 – Molecular orbitals 47

4.4 – Hückel's $(4n + 2)$ rule for aromaticity 48

4.5 – Spectroscopic notation in molecules 50

4.6 – Electronic transitions in molecules 51

4.6.1 – Transition rates and Fermi's golden rule 51
4.6.2 – Allowed and forbidden transitions 52
4.6.3 – Intersystem crossing 54
4.7 – Vertical and adiabatic energies 57
Chapter 5 – Experimental design
5.1 – Laser system 62
5.2 – Ionization chamber 65
5.3 – Time-of-flight mass spectrometer 67
5.4 – The focal volume effect 73
5.4.1 – The problem 73
5.4.2 – Three-dimensional spatial resolution 75
5.4.3 – Simulating the focal volume effect 80
5.5 – Experimental errors and their causes 86
5.5.1 – Pressure variations 86
5.5.2 – Excessive count rate 88
5.5.3 – Threshold voltage 93
5.5.4 – Spatial chirp in the laser pulses 98
5.4.1 – Spatial laser mode quality 100
5.7 – LabVIEW control program 101
Chapter 6 – Molecular ionization of systematic series
6.1 – The halobenzenes 107
6.2 – The CNOF isoelectronic series 116
6.3 – Compound functional groups: methyl, hydroxyl, and methoxyl substitutions 121
6.4 – The azabenzenes 123
6.4.1 – Through-bond and through-space interactions 123
6.4.2 – Parent ion yields 126
Chapter 7 – Molecular fragmentation of systematic series
7.1 – The halobenzenes 141
7.2 – The CNOF isoelectronic series 149
7.3 – Compound functional groups: methyl, hydroxyl, and methoxyl substitutions 155
7.4 – Amine vs. nitro substitution 157

7.5 – The azabenzenes 161
7.5.1 – Understanding the perturbation to the ring 161
7.5.2 – Fragmentation 168
Chapter 8 – Metastable molecular fragmentation
8.1 – Kinematics of a metastable molecular ion 174
8.2 – Observation of metastable ions 178
8.2.1 – Metastable fragments of pyridine 179
8.2.2 – Recovering mass information 182
8.2.3 – Recovering lifetime and kinetic energy release information 184
8.2.4 – Tuning diffuse peaks 186
8.2.5 – Determining mass values 192
8.2.6 – Kinetic energy release values 194
8.3 – Conclusions 196
Chapter 9 – Predicting the dynamics of astatine-containing molecules
9.1 – Comparison to the halobenzenes 202
9.2 – Intense-field dynamics 204
9.2.1 – Predicting the dynamics 204
9.2.2 – A possible sub-femtosecond process? 207
9.4 – Plausibility of an experiment 211
9.5 – Conclusions 216
Chapter 10 – Conclusions and future outlook
10.1 – Conclusions 219
10.2 – Future outlook 220
10.2.1 – Biomolecules 220
10.2.2 – Tunable laser source 221
Appendices
Appendix A – Programs and simulations 225
Appendix B – Symmetry point groups and operations 236
Appendix C – Further evidence of REMPI 238

Figures and tables

Chapter 1

Figure 1 – The halobenzenes....3
Figure 2 – The CNOF isoelectronic series....3
Figure 3 – Compound substitutions in anisole....4
Figure 4 – The azabenzenes....5

Chapter 2

Figure 1 – Tunneling ionization....10
Figure 2 – Channel closing due to the ponderomotive potential....14
Figure 3 – Avoided channel closing through REMPI....15
Figure 4 – Dynamic resonance....16
Figure 5 – Tunneling in an oscillating external field....17
Figure 65 – The Keldysh parameter in multiphoton and tunneling ionization....19

Chapter 3

Figure 1 – Resonance enhancement....26
Figure 2 – (3 + 4) REMPI in the ideal case....30
Figure 3 – Log-log slopes of iodobenzene....31
Figure 4 – Resonance enhancement....32
Figure 5 – (3 + 4) REMPI: favoring the four-photon transition....34
Figure 6 – (3 + 4) REMPI: favoring the three-photon transition....35
Figure 7 – Population densities for competing (3 + 4) and (4 + 3) REMPI....36
Figure 8 – Loss from the excited state....37
Figure 9 – Intensity-dependent loss to fragmentation....39

Chapter 4

Figure 1 – Reflection operation in molecular hydrogen....44
Figure 2 – Linear combination of atomic orbitals....46

Figure 3 – Types of molecular orbitals 47
Figure 4 – Bonding and antibonding orbitals 48
Figure 5 – Hückel's ($4n + 2$) rule for aromaticity 49
Figure 6 – Uniform bonds in benzene 49
Figure 7 – Illustration of the Franck-Condon principle 52
Figure 8 – Beyond the Born-Oppenheimer approximation 53
Figure 9 – Intersystem crossing 56
Figure 10 – El Sayed's rules for intersystem crossing 57
Figure 11 – Vertical and adiabatic transitions 58

Chapter 5

Figure 1 – Diagram of the laser system 63
Figure 2 – Schematic of the interior of the Spitfire regenerative amplifier 64
Figure 3 – Acceptance slits 66
Figure 4 – Schematic of the time-of-flight mass spectrometer 68
Figure 5 – Tuning the time-of-flight curve 70
Figure 6 – Focused in time and spatially-resolved TOF. 71
Figure 7 – Focusing and defocusing the TOF curve 72
Figure 8 – Spatial ion distributions of xenon 75
Figure 9 – The effect of eliminating focal averaging 77
Figure 10 – The effects of three-dimensional spatial resolution 79
Figure 11 – Different sizes of detection volumes 81
Figure 12 – Isovolume intensity curves of the detection volumes 83
Figure 13 – Isovolume intensity curves on a logarithmic intensity scale 85
Figure 14 – Normalizing for pressure fluctuations 87
Figure 15 – Multiple detections in a single peak 89
Figure 16 – Undercounting due to high count rate 90
Figure 17 – Different signals from identical processes 91
Figure 18 – Ion yields for identical processes 92
Figure 19 – Electrical ringing in the multichannel plate 94
Figure 20 – Electrical reflections in the multichannel plate 95

Figure 21 – Different voltage signals for different fragments 96
Figure 22 – Missing peaks due to high threshold voltage 97
Figure 23 – Counts as a function of threshold voltage 98
Figure 24 – Spatial chirp seen in the ion peaks 99
Figure 25 – The diffraction catastrophe 100
Figure 26 – Step-by-step control sequence of the automated LabVIEW program. 102

Chapter 6

Figure 1 – Parent ion yields of benzene and the monohalobenzenes 108
Figure 2 – Mathematically-fitted slopes of the halobenzenes 110
Figure 3 – Energy diagrams of observed processes in benzene and the monohalobenzenes 112
Figure 4 – Multiply-charged halobenzenes 115
Figure 5 – Mathematically-fitted slopes of the CNOF series 117
Figure 6 – Multiply-charged CNOF series 120
Figure 7 – Parent ion yield of anisole 122
Figure 8 – Singly- and multiply-charged yields of toluene, phenol, and anisole 123
Figure 9 – Lone pair orbitals in the azabenzenes 124
Figure 10 – The HOMO band of benzene and the azabenzenes 125
Figure 11 – Mathematically-fitted slopes of the azabenzenes 128
Figure 12 – Multiple ionizations of the azabenzenes 131
Table 1 – Fitted slopes and ionization potentials of the halobenzenes 111
Table 2 – Fitted slopes and ionization potentials of the CNOF series 119
Table 3 – Fitted slopes and ionization potentials of the azabenzenes 130

Chapter 7

Figure 1 – Fragmentation of benzene 140
Figure 2 – Ionized halogen atoms from halobenzene parents 142
Figure 3 – Phenyl ions from halobenzene parents 143
Figure 4 – Fluorine ions 145
Figure 5 – Chlorine ions 146

Figure 6 – Bromine ions 147
Figure 7 – Iodine ions 148
Figure 8 – Appearance intensities of halogen charge states 149
Figure 9 – Mass spectra of the CNOF series 150
Figure 10 – All fragment yields of the CNOF series 151
Figure 11 – Fragments with differing numbers of carbons in the CNOF series 152
Figure 12 – Fragments relevant to substituent dissociation in the CNOF series 153
Figure 13 – Hydrogen rearrangement 154
Figure 14 – All fragment yields of the toluene, phenol, and anisole 156
Figure 15 – Donating and withdrawing groups 157
Figure 16 – Mass spectra of nitrobenzene 158
Figure 17 – All fragment yields of aniline and nitrobenzene 159
Figure 18 – Fragments with differing numbers of carbons in aniline and nitrobenzene 160
Figure 19 – Fragments relevant to dissociation of the nitro group in nitrobenzene 161
Figure 20 – Perturbed potentials 163
Figure 21 – Correction coefficients to the lowest-order mode 165
Figure 22 – Correction coefficients for all modes 166
Figure 23 – Lone pair orbitals in pyrimidine 167
Figure 24 – Increased bond orders in the azabenzenes 168
Figure 25 – Mass spectra of the azabenzenes 169
Figure 26 – All fragment yields of the azabenzenes 170

Chapter 8

Figure 1 – Diffuse peak in pyridine 180
Figure 2 – Ionic yield as a function of intensity 181
Figure 3 – Consistency of the metastable feature 182
Figure 4 – Extinction curve for the molecular parent ion 186
Figure 5 – Tuning the metastable peaks 187
Figure 6 – Broad feature evolution 188
Figure 7 – The labeling scheme for the peaks (1), (2), and (3) 189

Figure 8 – All six metastable peaks 190
Figure 9 – Labeling scheme and decreasing voltage progression of (4), (5), and (6) 191
Figure 10 – Extinction curves for all six metastable peaks 195
Figure 11 – Extinction curves to energy distributions 196
Table 1 – Extinction voltages for the six observed metastable peaks 192

Chapter 9

Figure 1 – Calculated energies of the phenyl halides 203
Figure 2 – Intersystem crossing in bromobenzene and iodobenzene 205
Figure 3 – Triplet states 206
Figure 4 – Predicting the intersystem crossing lifetime of astatobenzene 209
Figure 5 – Intersystem crossing in astatobenzene 210
Figure 6 – The decay chain of 211-astatine 212
Table 1 – Astatine-containing molecules and their relevance to medicine 201
Table 2 – Ionization potentials and spin-orbit properties of the halogens and halobenzenes 207

Chapter 10

Figure 1 – DNA and RNA nucleotides 220
Figure 2 – Rigid dynamic resonance in a tunable laser source 222
Figure 3 – Flexible dynamic resonance in a tunable laser source 223

Chapter 1 – Introduction

1.1 – Motivation for research

Our goal is to study the photodynamics of systematic series of analogous molecules. Within each series, molecules differ from each other in a single structural parameter. This approach allows us to study the effects of the substituent on molecular intense-field photodynamics. Many of these have the general structural formula C_6H_5–R, where R is a substituent functional group such as the nitro group –NO_2 or the methyl group –CH_3. Such functional groups often determine the characteristic role of a substituted molecule in an application, which makes them worth investigating. The ongoing interest in intense-field molecular dynamics (and the dynamics of ionization processes, in particular) [1-3] is driven by their relevance in attosecond pulse generation [4,5], generation of short-wavelength radiation [6] and, ultimately, the desire to control chemical reactions [7] and electronic dynamics on ultrafast timescales [8]. Much of our research is dedicated to the study of ionization. The removal of a single electron is perhaps the most fundamental dynamic process which can be undergone by a molecule; more complicated dynamics such as rescattering [1] often require ionization as a first step in the process.

We focus our studies on aromatic hydrocarbon molecules, particularly those with structural similarities to the benzene (C_6H_6) system. The inherent stability of the aromatic ring structure allows for a wide variety of atomic substitutions to the system while maintaining many of the basic properties. This abundance of substituted aromatics allows us to find correlations between molecular properties and their intense-field dynamics.

Such molecules have relevance to interstellar media [9,10], upper-atmosphere pollution [11], and a wide array of biological systems. Perhaps none is more relevant than pyrimidine, which serves as the base structure of the nucleotides of DNA and RNA.

Unfortunately, the intense-field dynamics of molecules is immensely more complicated than that of atoms. Unlike atoms, molecules may vibrate, rotate, and break apart. While atoms all belong to a full rotational symmetry group, there is a wide variety of different molecular symmetries and orbitals. As such, the resources needed for fully *ab initio* computational studies of molecular photodynamics in intense fields are far beyond reach [12]. The Hamiltonian of a molecular system must include the interactions of all of its particles:

$$H = \sum_i \frac{p_i^{\,2}}{2m_i} + \sum_{ij} \frac{q_i q_j}{4\pi\varepsilon_0 \left|\vec{r}_i - \vec{r}_j\right|}. \qquad \textbf{(1.1)}$$

Benzene, for example, has 12 nuclei and 42 electrons, which makes the analysis of such a system prohibitively difficult. Entire careers have been spent studying singly-ionized molecular hydrogen (H_2, with only one electron); the extent of drastic simplifications needed to even approximate a system as complicated as benzene makes experimental verification of the intense-field behaviors of molecules increasingly important.

Each group of molecules which we investigate contains within itself a series of different ways a perturbation to the benzene system is introduced. For instance, the first series of molecules we consider is the monohalobenzenes, which are seen in Fig. 1: a benzene ring with a single halogen replacing a hydrogen atom. While each halobenzene represents a single bond to a carbon, the perturbation is introduced differently in each case by the increasing size of the substituent. As will be discussed in Chapter 4, the

presence of large atoms can lead to significant spin-orbit coupling which, as we will see in the case of the halobenzenes, is the controlling aspect of this perturbation's effects on the molecular dynamics.

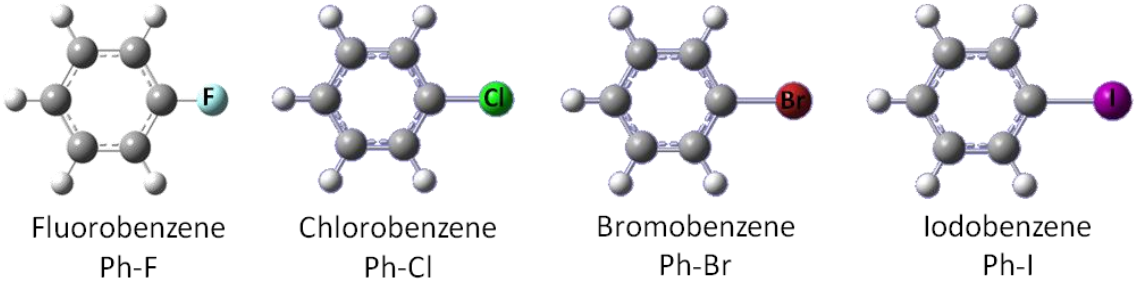

Figure 1 – The halobenzenes. Fluorobenzene, chlorobenzene, bromobenzene, and iodobenzene form a series of molecules in which a halogen atom is substituted onto a benzene ring in place of a hydrogen atom. In this series we can study the effects of progressively heavier substituents.

Next we will examine a similar series of perturbations to the benzene system: the CNOF isoelectronic series (named as such for the largest atom in the substituent group), which is seen in Fig. 2. This series is similar to the halobenzenes in that the perturbation involves the substitution of a hydrogen atom, but instead of increasing the size of the substituent, the character of the perturbation changes while maintaining the same number of electrons.

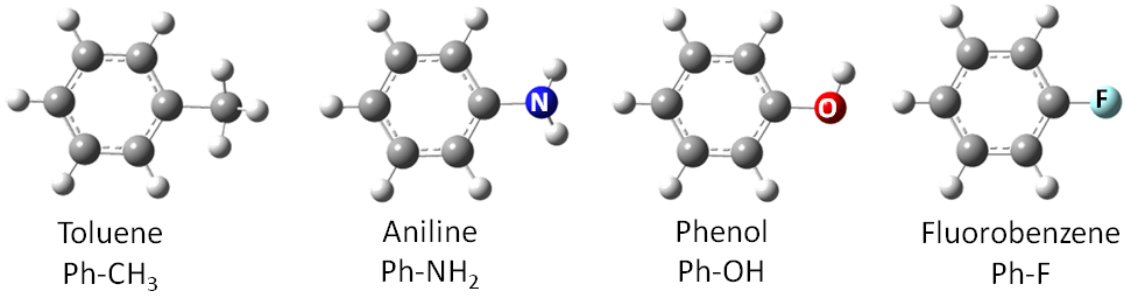

Figure 2 – The CNOF isoelectronic series. Toluene, aniline, phenol, and fluorobenzene form a series of molecules in which a functional side group is substituted onto a benzene ring in place of a hydrogen atom. This represents different perturbations to the system while maintaining similar size and the same number of electrons.

By substituting methyl ($–CH_3$), amine ($–NH_2$), and hydroxyl (–OH) groups, as well as atomic fluorine, we can study how the behavior changes as the primary atom of the substituents moves across instead of down the periodic table (as in the halobenzenes). Additionally, as an aside to the CNOF series, we will also examine a compound substitution. The hydroxyl and methyl groups seen already in phenol and toluene, respectively, can be combined into a single methoxyl group ($–O–CH_3$), as seen in Fig. 3.

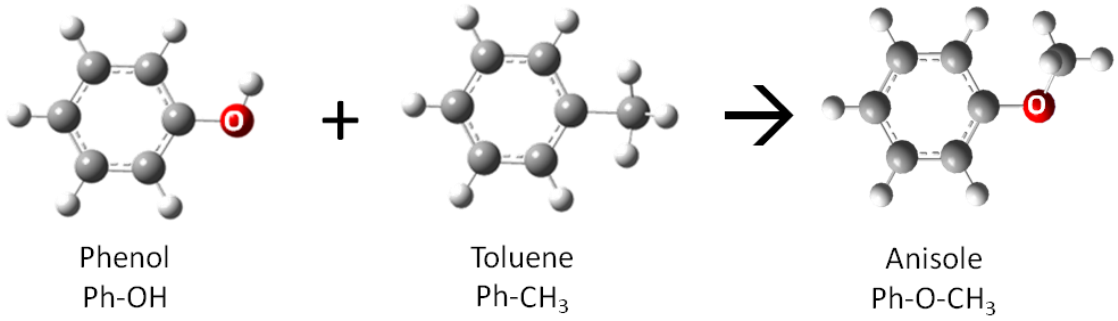

Figure 3 – Compound substitutions in anisole. The methyl and hydroxyl groups in toluene and phenol, respectively, can be combined into a methoxyl group. Anisole represents this compound substitution.

Functional groups can not only substitute for one or more hydrogen atoms; one or more nitrogen atoms may substitute for a carbon atom in the ring, making the molecule heterocyclic. Perhaps the most fundamental of these aromatic heterocycles, pyridine (azabenzene), involves the replacement of a single C–H unit with a nitrogen atom. This alters the system, though it remains isoelectronic with benzene.

If this substitution is made twice, three separate isomers result depending on the relative positions of the two nitrogen atoms in the ring, as shown in Fig. 4: pyridazine (1,2-diazine), pyrimidine (1,3-diazine) and pyrazine (1,4-diazine). Introducing nitrogen atoms into the ring causes a more direct perturbation to the benzene system and distinctly alters the symmetry of the ring for each case.

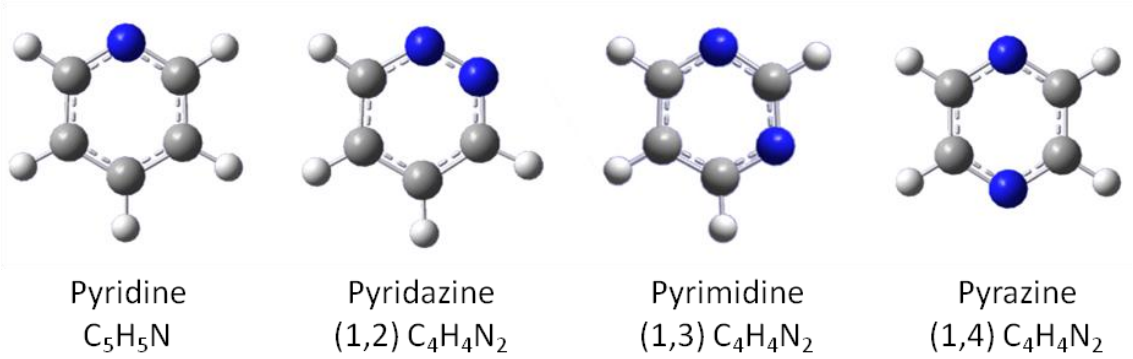

Figure 4 – The azabenzenes. Replacing a C–H unit with a nitrogen atom inside the ring represents a direct perturbation to the structure of the benzene system. Pyridine involves such a substitution, and pyridazine, pyrimidine, and pyrazine represent two nitrogen substitutions in different geometries.

Carrying out our experiments while varying a single structural parameter allows us to make practical generalizations about the effects that parameter has on the molecule. Forming a series of these parameters then allows us to make predictions when applying our observations to larger, more complex systems. Ultimately, our goal is to build a framework of knowledge which will pave the way toward the understanding of the photodynamical interactions of chemically and biologically relevant systems.

1.2 – Summary of chapters

Intense laser fields induce several types of interactions which can be ignored in the presence of weaker fields. Chapter 2 will give an introduction to the most relevant of these interactions to the experimental cases considered. The primary methods of ionization are described, including tunneling, multiphoton, and resonance-enhanced multiphoton ionization. Also among the topics will be the interaction of ultrashort, intense laser pulses with free electrons. The energy associated with this interaction is known as the ponderomotive potential, and this energy contributes to effects known as channel closing and dynamic resonance.

Because it is the dominant ionization process in our experiments, resonance-enhanced multiphoton ionization will be the subject of the entirety of Chapter 3. Rates of ionization are derived and the enhancement over the nonresonant case will be explored and clarified. Additionally, a series of numerical simulations are investigated to determine the nature of how a resonant process reveals itself in experimental cases.

Chapter 4 consists of introductory descriptions of the molecular processes which will prove relevant to our experiments. The theory of molecular orbitals is introduced along with the notation that describes them. Interactions between singlet and triplet molecular states are discussed in detail, and the guidelines that govern transitions between orbitals are discussed along with the causes of enhancement and suppression of certain transitions.

Our experimental methods are discussed in Chapter 5. The laser systems used to create ultrashort light pulses are described in detail, as is the vacuum system. The molecular ion detection scheme is derived along with the kinematics of the time-of-flight ion mass spectrometer. The focal volume effect is described, including theory, simulations, and a description of how our experiment avoids the effect. Chapter 5 concludes with a thorough description of defects in the experiment and how they are identified and avoided. Eliminating these errors is particularly crucial to the integrity of the experimental data.

Chapters 6 and 7 contain the bulk of our experimental results. Intense-field photodynamics of the halobenzenes, the CNOF isoelectronic series, the azabenzenes, compound substitution in anisole, and a comparative study of aniline and nitrobenzene

are studied; photoionization dynamics are presented in Chapter 6, and results of photofragmentation are presented in Chapter 7.

An atypical type of photofragmentation result is presented in Chapter 8. While our time-of-flight setup is tuned to focus ions in time such that ions with a given mass-to-charge ratio arrive at the detector as a narrow peak, some peaks remain unfocused and broad. These peaks are the result of ionic fragments that break apart midway through their flight toward the detector; because portions of their flight occur with different masses, the kinetics of their flight is considerably different than a typical ion. The details of the kinetics of these ions and the properties of their fragmentation are the subject of this chapter.

Chapter 9 was completed in partial fulfillment of the Comprehensive Examination for the UNL Graduate Department. In this chapter, the intense-field dynamics of molecules containing astatine are examined. Astatine is the heaviest known halogen; it was not considered along with the rest of the halobenzene series because no stable isotopes of astatine exist. In fact, the longest-lived isotope of astatine has radioactive half-life of approximately eight hours. This chapter examines the motivation for researching astatine-containing molecules, what we expect to see in an experiment, and the plausibility of carrying out the experiment. The key result of this section is the identification of a possible sub-femtosecond intersystem crossing transition based on the heavy-atom effect.

References

[1] Corkum, P. 1993, "Plasma Perspective on Strong-Field Multiphoton Ionization," *Physical Review Letters,* vol. 71, no. 13, pp. 1994-1997.

[2] Becker, A. & Faisal, F.H.M. 2005, "Intense-field many-body S-matrix theory," *Journal of Physics B-Atomic Molecular and Optical Physics,* vol. 38, no. 3, pp. R1-R56.

[3] Hertel, I.V. & Radloff, W. 2006, "Ultrafast dynamics in isolated molecules and molecular clusters," *Reports on Progress in Physics,* vol. 69, no. 6, pp. 1897-2003.

[4] Chang, Z., *Fundamentals of Attosecond Optics,* CRC Press, 2011.

[5] Sansone, G., Poletto, L. & Nisoli, M. 2011; 2011, "High-energy attosecond light sources," *Nature Photonics,* vol. 5, no. 11, pp. 655-663.

[6] Boutu, W., Haessler, S., Merdji, H., Breger, P., Waters, G., Stankiewicz, M., Frasinski, L.J., Taieb, R., Caillat, J., Maquet, A., Monchicourt, P., Carre, B. & Salieres, P. 2008; 2008, "Coherent control of attosecond emission from aligned molecules," *Nature Physics,* vol. 4, no. 7, pp. 545-549.

[7] Rabitz, H. 2006, "Strong-arming molecular dynamics," *Science,* vol. 314, no. 5797, pp. 264-265.

[8] Sansone, G., Kelkensberg, F., Morales, F., Pérez-Torres, J.F., Martín, F. & Vrakking, M.J.J. 2012, "Attosecond Time-Resolved Electron Dynamics in the Hydrogen Molecule," *IEEE Journal of Selected Topics in Quantum Electronics,* vol. 18, no. 1, pp. 520-530.

[9] Salama, F. & Allamandola, L.J. 1992, "Is a pyrene-like molecular ion the cause of the 4,430-Å diffuse interstellar absorption band?" *Nature,* vol. 358, no. 6381, pp. 42-43.

[10] Rosi, M., Bauschlicher, J., Charles W. & Bakes, E.L.O. 2004, "The Stability of Polycyclic Aromatic Hydrocarbon Dications," *The Astrophysical Journal,* vol. 609, no. 2, pp. 1192-1196.

[11] Ramanathan, V. & Feng, Y. 2009, "Air pollution, greenhouse gases and climate change: Global and regional perspectives," *Atmospheric Environment,* vol. 43, no. 1, pp. 37-50.

[12] Methods are beyond reach, however see http://www.physorg.com/news194276894.html. Though impressive, this research required immense and costly resources on a record supercomputer, with software developed and specifically optimized for its architecture. No resources exist to simulate the intense-field photodynamics of larger molecules.

Chapter 2

Introduction to intense-field processes

Many of the interactions discussed in this dissertation occur only in the presence of intense electric fields (~10^{11} V/m). This chapter will give a brief overview of the intense-field processes which will be relevant to our experiments: ionization processes, high-field interactions in electronic transitions, and using the Keldysh parameter to predict the type of process.

2.1 – Ionization processes

Perhaps the fundamental basic interaction between an intense light field and an atom or molecule is the removal of an electron from the system to create a positive ion. There are many mechanisms which can result in ionization, though some of these (such as above-threshold or rescattering ionization [1]) will not turn out to be relevant to the work in this dissertation. Those with direct relevance are introduced in this section.

2.1.1 – Tunneling ionization

Consider an electron which is bound in a potential barrier. When a uniform, linearly-polarized external electric field is present, there is an additional energy V due to the electric field E which depends linearly on position z:

$$V = -eEz. \tag{2.1}$$

This distorts the bound potential by raising one side of the barrier and lowering the other side (given the definition $z = 0$ at the center of the potential), as seen in Fig. 1.

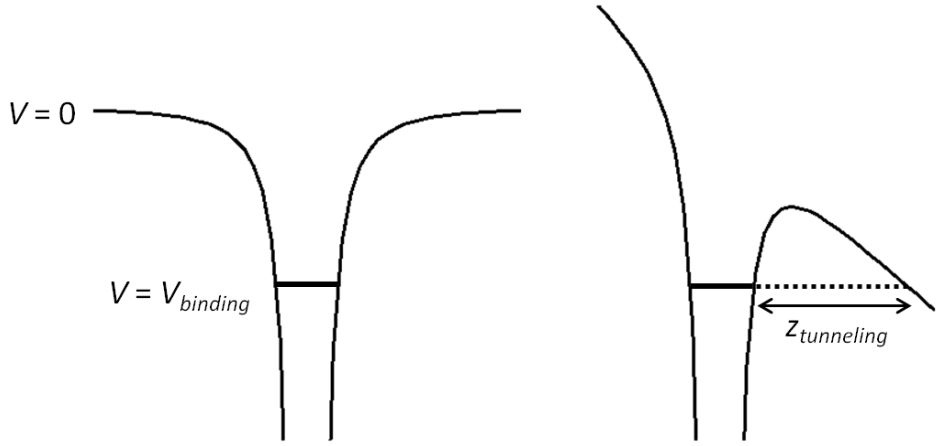

Figure 1 – Tunneling ionization. When a potential well is distorted by an external electric field, one side of the potential is raised in energy, while the other is lowered. On the lowered side, electrons bound by the well can reach the continuum by tunneling through the barrier. The removal of the electron leaves the source of the potential barrier (an atom or molecule) as a positive ion, so this process is known as *tunneling ionization.*

On the side which is lowered, one can define a position $z_{tunneling}$ for which the combined energy of bound potential well and the external electric field is equal to the binding energy. For $z > z_{tunneling}$ the potential is less than the binding energy, and there will be some probability for the electron to tunnel through its barrier and into the new, distorted continuum. Much work has been done to describe rates of tunneling ionization, perhaps most notably with regard to ADK theory [2,3] and S-matrix theory [4]. Tunneling is the dominant ionization process in the presence of static or quasi-static (typically meaning $\hbar\omega$ << ionization potential (IP)) external fields [5]; quickly-oscillating fields (as will be discussed in Section 2.3) can suppress tunneling ionization, leaving other mechanisms to dominate ionization.

2.1.2 – Multiphoton ionization

One example of such a mechanism which can occur in regions of large photon flux is ionization by more than one photon. Even in the absence of an energetic resonance with an electronic transition, a single photon can be absorbed into a short-lived (lifetimes are determined by the time-energy uncertainty relation) virtual state. When the photon densities are large, it is possible for additional photons to be absorbed by the electron before the virtual state decays [5]. To achieve high enough photon flux to induce multiphoton absorption, intense fields are needed; this puts multiphoton absorptions in direct competition with tunneling ionizations, since strong fields affect the potential barriers as described in the previous section.

2.1.3 – Resonance-enhanced multiphoton ionization

Multiphoton processes do not necessarily have to result in an ionic state; multiphoton absorptions can also lead to excitation within the binding potential. If a multiphoton process is split into multiple steps, namely photoexcitation followed by photoionization, this process is enhanced in comparison to the nonresonant multiphoton ionization (MPI) (details of this enhancement will be discussed in Chapter 3). This sort of two-step process is known as resonance-enhanced multiphoton ionization (REMPI). The present description of this process will remain brief, but the entirety of Chapter 3 is dedicated to a full description of REMPI, as it is the primary mechanism of ionization observed in experiments in this dissertation.

2.2 – Intense-field interactions

This section describes electronic processes which occur only in intense light fields. Interactions relevant to this dissertation include the ponderomotive energy of a free electron, channel closing in atomic and molecular systems, and dynamic resonance.

2.2.1 – The Ponderomotive Energy

The ponderomotive energy [1] is often referred to as the "quivering" energy of the electron. When a free electron is in the presence of an oscillating electric field, the electron gains an energy associated with the oscillation. The time-dependent force felt by the electron is

$$F(t) = eE(t) = eE_0 \sin(\omega t) \tag{2.2}$$

where the electric field E (with peak E_0) has carrier frequency ω[†]. This leads to harmonic motion of the particle. Its velocity can be found as

$$v(t) = \int a(t)dt = \frac{eE_0}{m}\int \sin(\omega t)dt = -\frac{eE_0}{m\omega}\cos(\omega t). \tag{2.3}$$

The ponderomotive potential is defined as the time-averaged kinetic energy of this harmonic motion, which is

$$U_P = \left\langle \frac{1}{2}mv^2 \right\rangle = \frac{e^2E_0^2}{2m\omega^2}\left\langle \cos^2(\omega t)\right\rangle = \frac{e^2E_0^2}{4m\omega^2}. \tag{2.4}$$

In a more practical form, this can be arranged in terms of two parameters which are easy to determine in an experimental setting. As a function of laser intensity and laser wavelength, the ponderomotive potential is

---

[†] This analysis makes two assumptions: first, that the laser field is linearly polarized, and second, that the laser's bandwidth can be neglected. Our experiments do indeed use linearly polarized light with a frequency distribution of $\omega = 2.36\times10^{15}$ rad/s $\pm 1.7\%$. While this spread is not necessarily negligible, the analysis as presented remains valid as a suitable approximation since the energy as described is time-averaged; higher- and lower-frequency contributions will average to the carrier frequency.

$$U_P = \left(\frac{e^2}{8\pi^2 m c^3 \varepsilon_0} \right) I\lambda^2 = 9.33 \cdot I(10^{14}\,\mathrm{W/cm^2}) \cdot \lambda^2(\mu\mathrm{m}^2) \qquad \textbf{(2.5)}$$

where the numerical relation gives U_P in electron volts. In experimental terms, this means that for an 800 nm laser, an intensity of 10^{14} W/cm^2 provides 6 eV of ponderomotive energy, which is then directly proportional to *I*. For pulsed lasers, the amount of ponderomotive energy can change within the duration of the pulse (as the pulse intensity itself is not constant in time), which can lead to other effects as discussed below.

2.2.2 Channel Closing

The ponderomotive energy can be important not only to free electrons, but to dynamics of bound electrons as well. A bound electron does not couple to the external field in the same way as a free electron; its binding potential perturbs the harmonic motion supplied by the external field. Further, a bound electron may be partially shielded by the other electrons within the atom or molecule. When an oscillating external field couples energetically to a bound electron, it is known as the AC Stark effect, the details of which can be found in [6,7]. For the purposes of this discussion, it is sufficient to note that bound electrons experience smaller energetic changes due to external electric fields than free electrons.

Consider an ionization process which requires *N* photons in a weak field. When the intensity is raised, any electron that would be promoted to the continuum must be supplied with enough energy to account for the quivering motion. Electrons which are not supplied with enough energy will not reach the continuum; this effectively raises the IP if the bound states are not similarly affected, as seen in Fig. 2. In this case there will eventually be enough intensity such that *N* photons do not supply enough energy to create an ion. In this way, the *N*-photon channel closes and (*N* + 1) photons are required until

higher intensities, when more channels close as a result of the additional ponderomotive energy. This behavior was first observed experimentally by Kruit et al. [8] in above-threshold ionization spectra, and has been well-documented since.

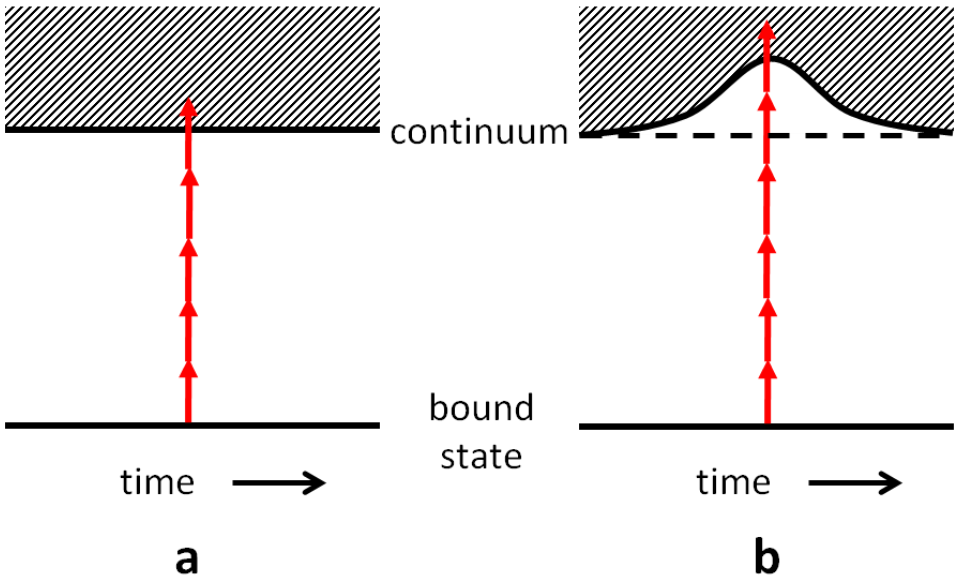

Figure 2 – Channel closing due to the ponderomotive potential. Because an external electric field affects free electrons differently than bound electrons, large external fields can raise the effective ionization potential of an atom or molecule. When this happens, an ionization process which takes *N* photons in the low-field case (**a**) may require (*N* + 1) or more photons in the high-field case (**b**). Because the *N*-photon channel has closed in the presence of a large field, this phenomenon is known as *channel closing*.

2.2.3 – Channel Closing in REMPI

There are also systems in which channel closing can be avoided. In a multi-step ionization process such as REMPI, an electron is first excited and then ionized in separate multiphoton events. The diagram in Fig. 3 shows the low-field (**a**) and high-field (**b**) cases. It is thought that electrons in excited states behave differently in an external field than those in occupied bound states [9]; namely, that they are more susceptible to being shifted similarly to the continuum.

If an electron is excited on the rising edge of the laser pulse, as in Fig. 3 (**b**), the electron follows the energy of the excited state. Because this can more closely mirror the energetic shift in the continuum, the same number of photons may be sufficient to ionize regardless of the intensity, and channel closing is avoided.

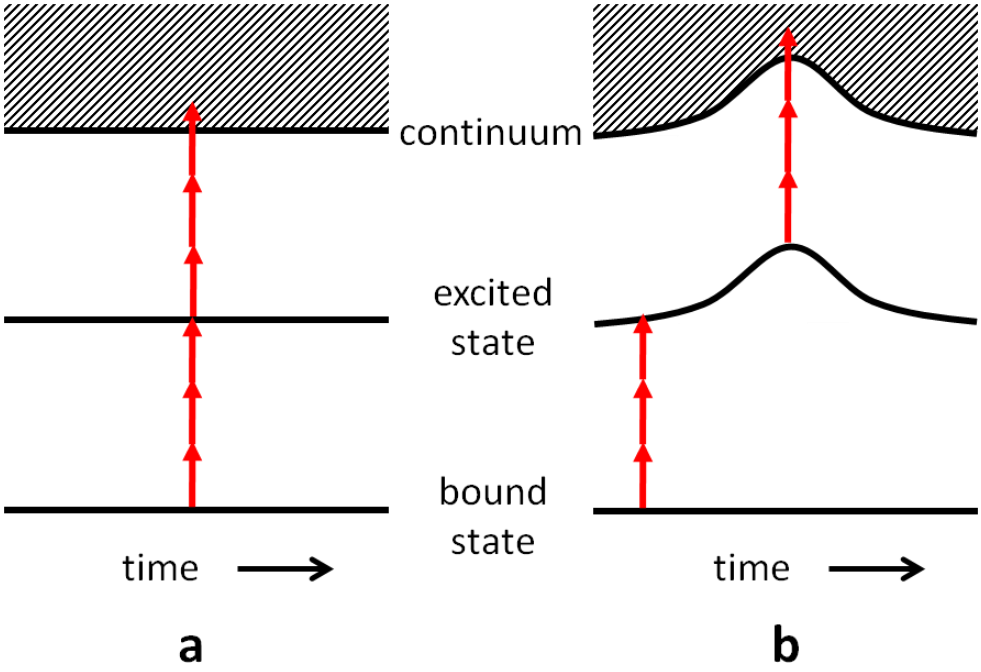

Figure 3 – Avoided channel closing through REMPI. Excited states of an atom or molecule can behave more like the continuum in the presence of ponderomotive effects [9]. As a result, a two-step multiphoton ionization event which involves excitation followed by ionization in the low-field case (**a**) can avoid channel closing in the high-field case (**b**). When an electron is excited early in the laser pulse (when ponderomotive effects are small) its ponderomotive energy shift mirrors that of the continuum, so additional photons are not necessary to create an ion.

2.2.4 – Dynamic Resonance

Yet another consequence of the interaction between external fields and bound states is known as *dynamic resonance* [10]. Consider an electronic transition to an excited state that is not energetically resonant with an integer number of photons; this is depicted in Fig. 4 (**a**). In this case the resonant condition cannot aid the ionization and the process is suppressed in comparison to the resonant case (here the "resonant case" refers to

transitions favored by energy considerations in Fermi's Golden Rule, which is discussed further in Chapter 4).

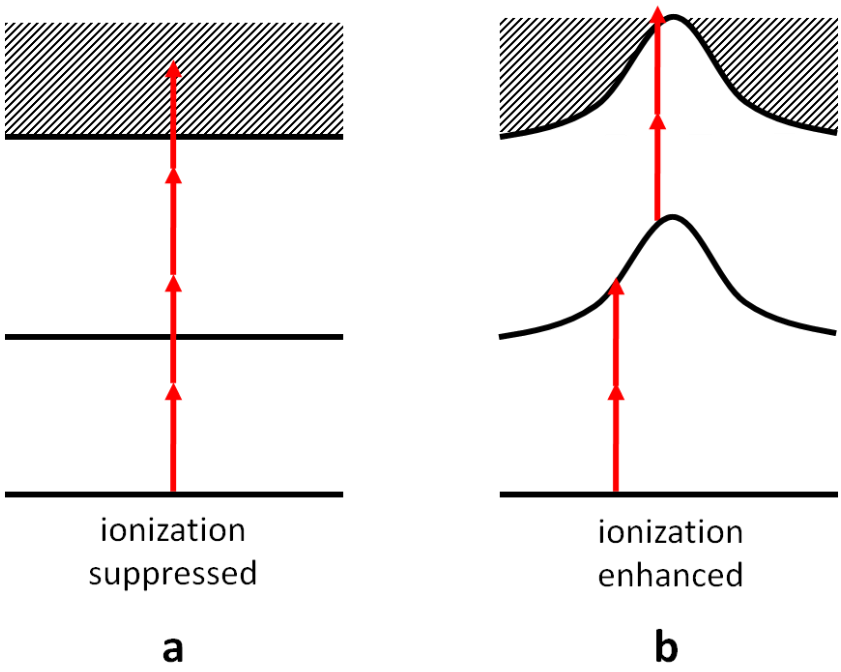

Figure 4 – Dynamic resonance. Electronic excitations which are energetically nonresonant in the unperturbed case (**a**) may be forced onto resonance in the presence of external fields (**b**). When this happens, a nonresonant multiphoton ionization process can become resonant, which enhances the rate of ionization.

However, as was the case in channel closing, both excited and free electrons can be similarly affected by coupling to the field, as is depicted in Fig. 4 (**b**). As the excited state energy is being shifted by the external field, it can at some point find itself on resonance with an integer number of photons, and the transition is now allowed. The resonance is forced onto the system by the dynamic coupling to the field, which is why it is called a dynamic resonance.

2.3 – The Keldysh Parameter γ

The oscillating electric field provided by laser fields often results in a competition between MPI and tunneling ionization. The yields of both processes increase with larger intensities, but depending on the oscillations of the field either process may become dominant. At high frequencies (wavelengths less than ~1 μm, depending on intensity), tunneling ionization is typically suppressed, since an electron's tunneling rate through the barrier is slower than the period of oscillation. This is demonstrated in Fig. 5, where an electron in these barriers would be turned back toward the binding potential as it tries to tunnel out [11].

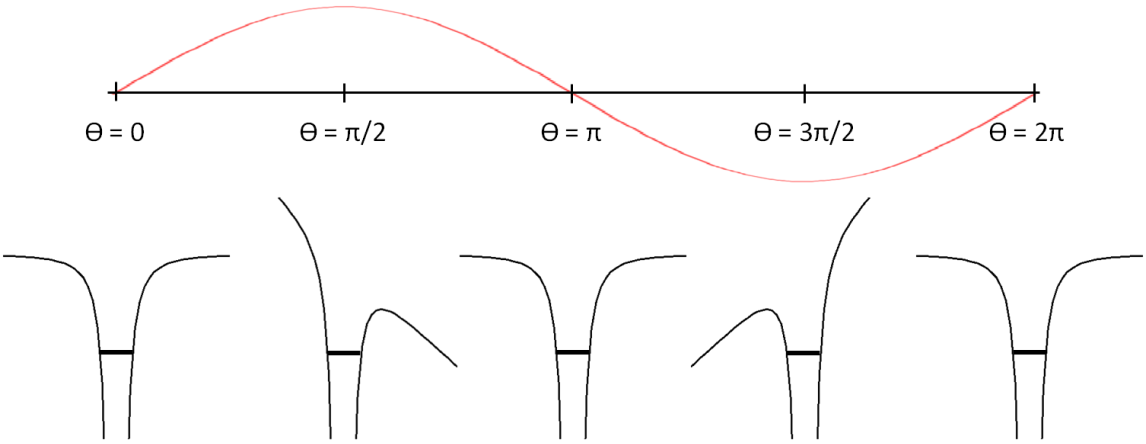

Figure 5 – Tunneling in an oscillating external field. When in the presence of an oscillating external electric field, tunneling ionization becomes more complicated. As the field changes its sign, the direction of tunneling changes with it; fast oscillations suppress tunneling since the bound electron probability density is pushed back toward the potential as the field is reversed. Shown are Coulomb potentials perturbed by an oscillating field with the field's phase ranging from 0 to 2π.

At lower frequencies this effect is reduced and tunneling becomes more likely, while multiphoton processes are now suppressed compared to high laser frequencies. Consider, for example, a 10 eV potential well: to ionize an electron from this potential would take four 400 nm photons, seven 800 nm photons, or ten 1200 nm photons. As the

wavelength increases (and the frequency decreases) more photons are necessary to reach the IP. As the order of the process goes up, its rate decreases as the probability to absorb N photons simultaneously is smaller than the probability to absorb $(N-1)$ photons.

To predict whether a process will be tunneling or MPI it is customary in intense-field studies to use Keldysh's adiabaticity parameter [2], represented by the symbol γ. This parameter effectively compares the tunneling time (inverse of the rate at which tunneling takes place) to the period of the laser, though it can also be calculated by the IP and ponderomotive energy (U_p).

$$\gamma = \sqrt{IP/2U_P} = \frac{\text{tunneling time}}{\text{laser period}} \qquad \textbf{(2.6)}$$

The justification for this comparison is as follows: when the potential resulting from the laser field is added to the IP, this creates a barrier which can be tunneled through. If the tunneling rate is not sufficiently fast to make tunneling likely before the laser field oscillates back in the other direction, tunneling ionization becomes suppressed and MPI will be favored. If, on the other hand, the laser period is long compared to the tunneling time, a bound electron will tunnel out of the well with much greater likelihood.

The customary guideline, illustrated in Fig. 6, states that when $\gamma \ll 1$, tunneling ionization dominates, and that when $\gamma \gg 1$ MPI is the dominant ionization process. While this can be useful as a very loose estimate, in a practical sense it is limited in its validity, with its issues stemming from the applicability of the tunneling theory [12,13]. It assumes, for example, a simple Coulomb potential barrier; attempts have been made to generalize γ for the more complicated physical systems found in molecular cases [14,15], though their applicability remains open to question.

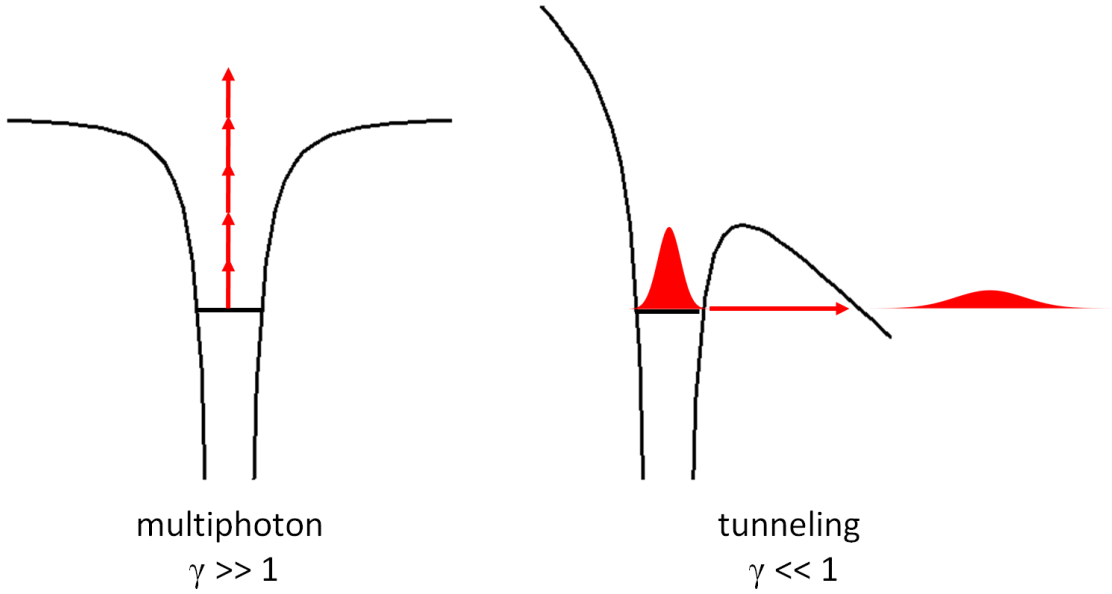

Figure 6 – The Keldysh parameter in multiphoton and tunneling ionization. The Keldysh parameter γ is customarily used as a guideline when predicting whether an ionization process will be multiphoton or tunneling ionization. When γ >> 1, multiphoton ionization is preferred, and when γ << 1, tunneling ionization is preferred. Though this is an oversimplification, it is typically used as a first approximation in predicting the dynamics.

Ref. [1] discusses problems involving misconceptions about tunneling ionization which are applied to the Keldysh analysis. Ultimately, these issues emphasize that, while the Keldysh parameter can be useful as a rough guideline, in practice the description of the dynamics is considerably more complicated. Further, the Keldysh parameter applies only to the case of nonresonant MPI vs. tunneling ionization. In the case of MPI under resonant conditions, the resonant process is enhanced compared to the nonresonant MPI, and so it may be preferred to tunneling ionization even when γ << 1. Our experiments involve such resonances in the multiphoton processes, and so although we often operate under conditions where γ ≈ 1 ($\gamma = \sqrt{IP/2U_P} = \sqrt{10\text{eV}/2(6\text{eV})} \approx 1$ for typical organic molecules at ~10^{14} W/cm^2), multiphoton processes are expected.

References

[1] Yamanouchi, K. (ed), *Lectures on Ultrafast Intense Laser Science 1*, Springer, 2010.

[2] Keldysh, L. 1965, "Ionization in Field of a Strong Electromagnetic Wave," *Soviet Physics JETP-USSR,* vol. 20, no. 5, p. 1307.

[3] Ammosov, M., Delone, N. & Krainov, V. 1986, "Tunnel Ionization of Complex Atoms and Atomic Ions in a Varying Electromagnetic-Field," *Zhurnal Eksperimentalnoi i Teoreticheskoi Fiziki,* vol. 91, no. 6, pp. 2008-2013.

[4] Reiss, H. 1980, "Effect of an Intense Electromagnetic-Field on a Weakly Bound System," *Physical Review A,* vol. 22, no. 5, pp. 1786-1813.

[5] Faisal, F.H.M., *Theory of Multiphoton Processes,* Plenum, New York, 1987.

[6] Shankar, R., *Principles of quantum mechanics,* Plenum Press, New York, 1994.

[7] Liboff, R.L., *Introductory quantum mechanics,* Addison-Wesley, San Francisco, 2003.

[8] Kruit, P., Kimman, J., Muller, H. & Vanderwiel, M. 1983, "Electron-Spectra from Multiphoton Ionization of Xenon at 1064, 532, and 355 nm," *Physical Review A,* vol. 28, no. 1, pp. 248-255.

[9] deBoer, M. & Muller, H. 1992, "Observation of Large Populations in Excited-States After Short-Pulse Multiphoton Ionization," *Physical Review Letters,* vol. 68, no. 18, pp. 2747-2750.

[10] Bordyug, N.V. & Krainov, V.P. 2007, "Dynamic resonances in ultra-short laser pulses," *Laser Physics Letters,* vol. 4, no. 6, pp. 418-420.

[11] Corkum, P. 1993, "Plasma Perspective on Strong-Field Multiphoton Ionization," *Physical Review Letters,* vol. 71, no. 13, pp. 1994-1997.

[12] Reiss, H.R. 2008, "Limits on tunneling theories of strong-field ionization," *Physical Review Letters,* vol. 101, no. 4, pp. 043002.

[13] Reiss, H.R. 2010, "Unsuitability of the Keldysh parameter for laser fields," *Physical Review A,* vol. 82, no. 2, pp. 023418.

[14] DeWitt, M. & Levis, R. 1998, "Calculating the Keldysh adiabaticity parameter for atomic, diatomic, and polyatomic molecules," *Journal of Chemical Physics,* vol. 108, no. 18, pp. 7739-7742.

[15] DeWitt, M. & Levis, R. 1999, "Concerning the ionization of large polyatomic molecules with intense ultrafast lasers," *Journal of Chemical Physics,* vol. 110, no. 23, pp. 11368-11375.

Chapter 3

Resonance-enhanced multiphoton ionization

The leading process of single ionization in our experiments, as will be seen in Chapter 6, is a two-step multiphoton process which involves separate transitions: one from the ground state to an excited neutral state and another from the excited state to an ionic state. This process is known as resonance-enhanced multiphoton ionization (REMPI). The aim of this chapter is to determine the rate of ionization due to REMPI as it depends on laser intensity. As such, we will introduce rates of ideal multiphoton absorption, generalize to the resonant case, and conduct rate model simulations to model the ionic yields as a function of intensity for a variety of experimentally relevant situations.

3.1 – Multiphoton ionization: the I^N power law

Attempting to calculate the rate of a transition in the multiphoton case is prohibitively complicated if done in a rigidly formal sense. Generalizing the analysis of Boyd [1] to the *N*-photon case, one finds the *N*-photon transition rate (*w*) from an initial (*i*) to a final (*f*) to be

$$w_{i\to f}^{(N)} = \left| \sum_{ab\ldots yz} \frac{\mu_{ia}\mu_{ab}\ldots\mu_{yz}\mu_{zf}}{\hbar^N \left(\omega_{af} - (N-1)\omega\right)\left(\omega_{bf} - (N-2)\omega\right)\ldots\left(\omega_{yf} - 2\omega\right)\left(\omega_{zf} - \omega\right)} E^N \right| 2\pi\rho_f \left(\omega_{if} - N\omega\right) \quad \textbf{(3.1)}$$

where matrix elements μ couple intermediate virtual states ($ab...yz$) which have transition energies $\hbar\omega_{ab}$ supplied by an electric field E with carrier frequency ω, and the final transition enters a density of states dependent on the total transition energy $\rho_f\left(\omega_{if} - N\omega\right)$. The matrix elements and final density of states involve complicated calculations.

Instead of this approach, a simpler analysis can be undergone which describes multiphoton transition rates well; this analysis is described in [2]. In determining the rate of absorption of a photon, one must consider two factors: the likelihood of absorption given the presence of a photon, and the likelihood that a photon is present. As such, the rate of absorption (w) will ultimately be proportional to both the absorption cross section (σ) and the number of photons in which pass through some area per unit time, called the photon flux (F)

$$w \propto \sigma F . \tag{3.2}$$

Because the flux of photons defines the energy per unit time through an area, it is useful to represent this relation through the intensity, which allows for a direct equality

$$w = \sigma I . \tag{3.3}$$

In the multiphoton case, further considerations must be made [2]. Let us consider the two-photon case: for a laser field with carrier frequency ω, we have the energy-time uncertainty relation

$$\Delta E \cdot \Delta t = \hbar\omega \cdot \tau \approx \hbar \tag{3.4}$$

for a post-absorption virtual state with lifetime τ. A second photon can be absorbed if the interaction occurs while the system is in the virtual state, and the rate will be the same as

the rate for the first photon, since the single-photon process has not changed. As such, the rate for the combination of processes is

$$w_2 \simeq (\sigma_1 I \tau)\sigma_1 I = \sigma_2 I^2 \tag{3.5}$$

where the subscripts denote the order of the multiphoton absorption. One can then continue to generalize the multi-step absorption to higher orders:

$$w_N \simeq (\sigma_1 I \tau)^{N-1}\sigma_1 I = (\sigma_1^{\,N}\tau^{N-1})I^N = \sigma_N I^N . \tag{3.6}$$

The result $w_N = \sigma_N I^N$ may be referred to as the I^N power law, and the approximate nature of Eq. 3.5 is absorbed into a corrected *N*-photon cross section. These parameters, known as *generalized cross sections*, are measured empirically, and have been observed to approximately follow the so-called "10^{-33N}" power law [3]:

$$w_N \propto 10^{-33N}\,\frac{I^N}{(\hbar\omega)^N} \tag{3.7}$$

where $\hbar\omega$ is the photon energy. Corrected to fit the parameters used in our experiment, this approximates that for intensities less than ~2.5×10^{14} W/cm^2, lower-order processes should have higher transition rates. The REMPI signatures we observe are measured at lower but comparable (10^{13} to 10^{14} W/cm^2) intensities, so while we expect lower-order transitions to have larger rates, this is at best a rough guideline.

The I^N relation is useful in identifying the order of a process through an experiment; calculating the base-10 logarithm of both the rate and intensity gives (neglecting units)

$$\log_{10}(w_N) = \log_{10}(\sigma_N) + N\log_{10}(I) \tag{3.8}$$

and

$$\frac{\partial \log_{10}(w_N)}{\partial \log_{10}(I)} = N\,. \tag{3.9}$$

The latter result means that when the rate of ionization (the dependent quantity in our experiments) is plotted against the intensity (the independent experimental quantity) in a double-logarithmic representation, the linear slope of the data is equal to the integer number of photons which limit the process. This allows determination of the order of a presumed REMPI process.

3.2 – Resonance enhancement

Let us investigate the mathematics behind the enhancement of the ion yield by a resonance. Consider a six-photon nonresonant multiphoton ionization (MPI) process (the *N*-photon process was generalized in Section 2.3). The rate for such a process may be written as

$$w_6 \simeq (\sigma_1 I \tau)^5 \sigma_1 I = \sigma_6 I^6 \tag{3.10}$$

Consider next the rate for a three-photon excitation to a resonant state followed by a three-photon ionization from this excited state (referred to as (3 + 3) REMPI)†. A schematic for both the resonant and nonresonant cases is shown in Fig. 1. In the resonant case, one of the virtual states is replaced by an eigenstate of the system. Fluorescence lifetimes of such states are typically on the order of nanoseconds to microseconds [4], whereas the laser pulses we consider only interact with the system for 50 femtoseconds. Instead of being limited by the virtual state lifetime, the system is limited by the pulse duration of the laser Δt_{pulse}.

† The order of the processes does not necessarily occur as excitation followed by ionization. Formally, the external field induces coherent coupling between states such that, upon wavefunction collapse, there is some probability for the electron to be found in the ionic state. In this formal description there is no concept of an order in which transitions occur. However, for the purposes of general explanation, the viewpoint of "first excite, then ionize" serves as an adequate description.

$$w_{3+3} \simeq \left\{(\sigma_1 I\tau)^2 \sigma_1 I\right\} \Delta t_{pulse} \left\{(\sigma_1 I\tau)^2 \sigma_1 I\right\} \quad \textbf{(3.11)}$$

$$w_{3+3} = w_6 \frac{\Delta t_{pulse}}{\tau} \quad \textbf{(3.12)}$$

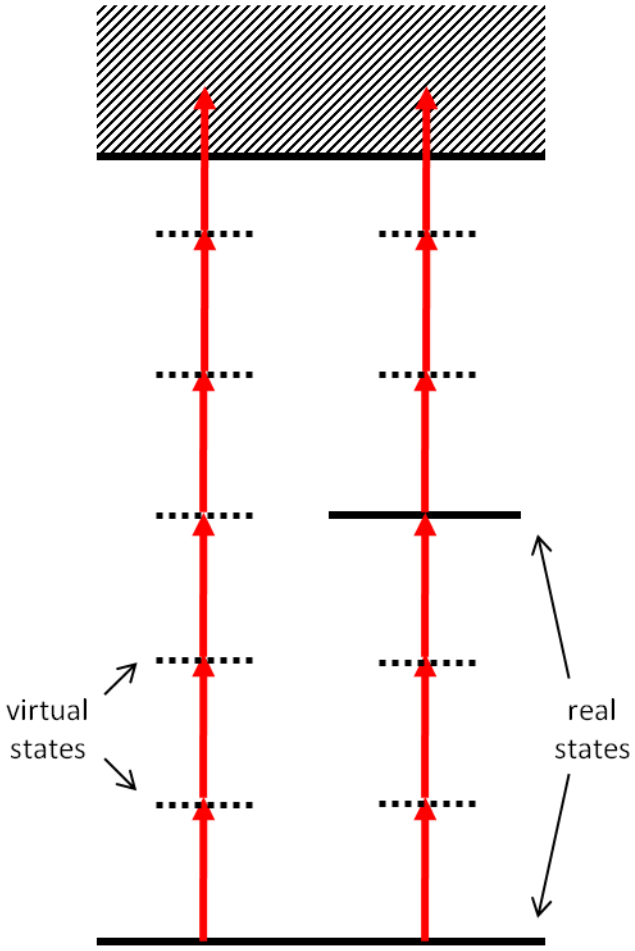

Figure 1 – Resonance enhancement. Nonresonant (left) and resonance-enhanced (right) multiphoton ionization both involve absorption of the same number of photons to create an ion. However, rates of absorption are limited by the lifetimes of the intermediate states; if the system relaxes to its ground state before absorption of the next photon the transition does not occur. Stationary states (that is, eigenstates) of the system have longer lifetimes than virtual states, and so the rate of a multiphoton ionization process which is resonant with a real intermediate state is enhanced in comparison to the nonresonant case.

As discussed in Section 2.3, the virtual state lifetime is determined from the time-energy uncertainty relation:

$$\Delta E \cdot \Delta t = \hbar\omega \cdot \tau \approx \hbar . \quad \textbf{(3.13)}$$

Though it is not exact, this relation gives an approximate sense of the timescale of such a virtual state, since $\tau \approx \omega^{-1}$. For laser pulses with a carrier wavelength of 800 nm, as is the case in our experiments, we find $\tau \approx 425$ as. Again applying our experimental conditions, our pulses have duration Δt_{pulse} = 50 fs. This is where we see the enhancement of REMPI: inserting these values into Eq. 3.12 shows that the rate of ionization for the (3 + 3) REMPI is ~100 times greater than the nonresonant six-photon ionization.

This enhancement, however, cannot be the case at all intensities; at high enough intensity a target will reach an ionization probability of 1, and the yields of resonant and nonresonant process must agree. Consider the MPI probability as described in [2]:

$$P = 1 - \exp\left(-\int_{-\infty}^{\infty} \sigma_N I^N dt\right) \quad \textbf{(3.14)}$$

where the notation has been altered for consistency within this text, and the spatial and temporal intensity distributions have been absorbed into I. The same number of photons is needed for the resonant and nonresonant cases, so the difference between the resonant and nonresonant cases is essentially built into the generalized cross sections from Eq. 3.6, but at high enough intensity both yields reach a probability of one. This probability, however, assumes a single transition between the initial and final states. Generalizing this into two separate transitions for the REMPI case gives

$$\begin{aligned} P &= P_{excitation} \times P_{ionization} \\ &= \left(1 - \exp\left(-\int_{-\infty}^{\infty} \sigma_N I^N dt\right)\right)\left(1 - \exp\left(-\int_{-\infty}^{\infty} \sigma_M I^M dt\right)\right) \\ &= \left(1 - e^{-\sigma_N I_0^N \tau}\right)\left(1 - e^{-\sigma_M I_0^M \tau}\right) \end{aligned} \quad \textbf{(3.15)}$$

for a *N*-photon absorption from the ground state and a *M*-photon ionization from the excited state. If, as appears in the third line, the temporal shape of the laser pulse is absorbed into τ, we are left with the generalized cross sections and peak intensity I_0 largely determining the rates of absorption (neglecting temporal pulse shape and intense-field complications as discussed in Chapter 2). When both single-transition probabilities are small compared to unity, both factors limit the ionization and the resulting log-log slope (see Eq. 3.9) is that of the expected (*M* + *N*) ionization.

However, as the transitions become more likely at high intensity, the exponential terms approach zero at different rates for different multiphoton orders. As an example, consider a (2 + 3) REMPI where two-photon excitation has a considerably larger cross section (and thus the exponential term decreases more quickly). For some range of intensities, the exponential term in the excitation will be negligible while the same term in the ionization is not. When this happens the excited state becomes quickly populated on the rising edge of the laser pulse, and only the second transition limits the ionization probability.

$$P \cong \left(1-e^{-\sigma_M I_0^M \tau}\right)\left(1-e^{-\sigma_N I_0^N \tau}\right) \cong (1)\left(1-e^{-\sigma_N I_0^N \tau}\right) \quad \textbf{(3.16)}$$

As such, there will be some range of intensities for which only one of the transitions limits the ionization probability and instead of a log-log slope of (*M* + *N*), the slope is instead just *N*. The presence of two separate regions of intensity with different integer slopes is a signature of REMPI, and will be used throughout this dissertation as evidence of resonance enhancement.

This analysis describes the ideal case of REMPI beneath the intensity at which both transition probabilities saturate. To investigate the non-ideal case, a series of

numerical simulations was calculated in MATLAB [5] to show the behaviors of REMPI under a variety of experimental conditions. A version of this program is found in Appendix A.1.

3.3 – Rate model simulations

Our measured slopes are integer, as is the case for an idealized REMPI process. To ascertain whether the idealized analysis applies to more complicated conditions, one can consider a rate model to simulate the resonance processes involved‡. Given that the processes are MPI (and thus have transition rates proportional to intensity to the power M or N), a model will show that an (M + N) REMPI photon process will be displayed in a double-log plot of yield vs. intensity as an initial slope (M + N) (as might be expected from lowest-order perturbation approach), giving way to higher-intensity slope of either M or N. The model is based on the three-level population rate equations in Eq. 3.17, with additional variations explored in each section to describe different experimental conditions.

$$\begin{aligned}
\frac{dn_{ground}}{dt} &= -\sigma_M I^M n_{ground} + \sigma_M I^M n_{excited} \\
\frac{dn_{excited}}{dt} &= \sigma_M I^M n_{ground} - \sigma_M I^M n_{excited} - \sigma_N I^N n_{excited} \\
\frac{dn_{ion}}{dt} &= \sigma_N I^N n_{excited}
\end{aligned} \qquad \textbf{(3.17)}$$

Applying this model to, for example, (3 + 4) REMPI such that M = 3 and N = 4 shows that at low intensities both transitions occur independently as their relative probabilities are both small. As such, the total MPI slope is M + N = 7 at low intensity, and the excited

‡ A rate model (unlike a density-matrix formalism) does not include considerations of coherence; as mentioned in the previous footnote, coherent coupling of states more formally describes the underlying dynamics. However, as discussed by Milonni and Eberly [6], a rate model is often used even when coherence is present, as it is for most systems an adequate approximation for describing dynamics. Due to considerations such as molecular rotational alignment and coherence mixing through virtual states in a multiphoton process, the coherence conditions are averaged out in an ion yield and a rate model is justified.

state population is negligible. Seen in Fig. 2 are the log-log slopes as a function of peak intensity (pulse energy) and the population densities of the ground (green dashed), excited (red dotted), and ionized (blue) states. At higher peak intensity the lower-order process (here the excitation) begins to saturate; as a result the excited state becomes populated (to its limit of 50%) almost instantaneously on the rising edge of the pulse. At this point the ionizing transition is all that limits the ionization, and so the yield then rises as I^4, so with slope $N = 4$ in the double-log plot of yield vs. peak intensity.

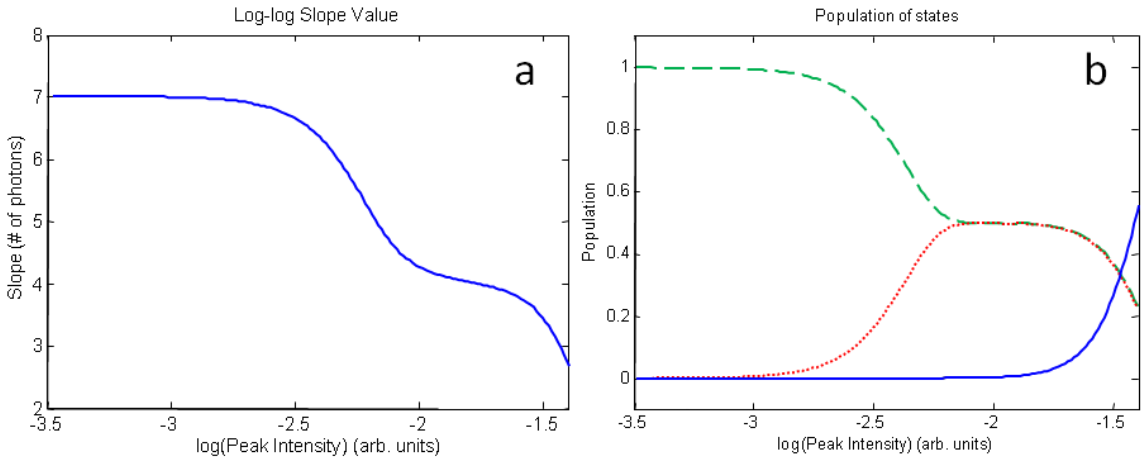

Figure 2 – (3 + 4) REMPI in the ideal case. In the idealized case, both the low-intensity and high-intensity slopes (**a**) of seven and four are identifiable. Populations (**b**) of the ground (green dashed) and excited (red dotted) and ionized (blue) states are show, with the ground and excited states each sharing approximately 50% population upon saturation of this transition.

These results are not merely a product of an idealized simulation; Fig. 3 shows the log-log slopes as a function of intensity for iodobenzene. Full analysis of the ionization rates of iodobenzene will be presented in Chapter 6, but the important feature at present is that its ionic yield represents (3 + 4) REMPI as in the simulation in Fig. 2. Though the slope-seven region in iodobenzene is poorly defined (due to counting statistics for low

ionic yields), the slope-four region is well-defined and serves as an example of the validity of the simulations presented.

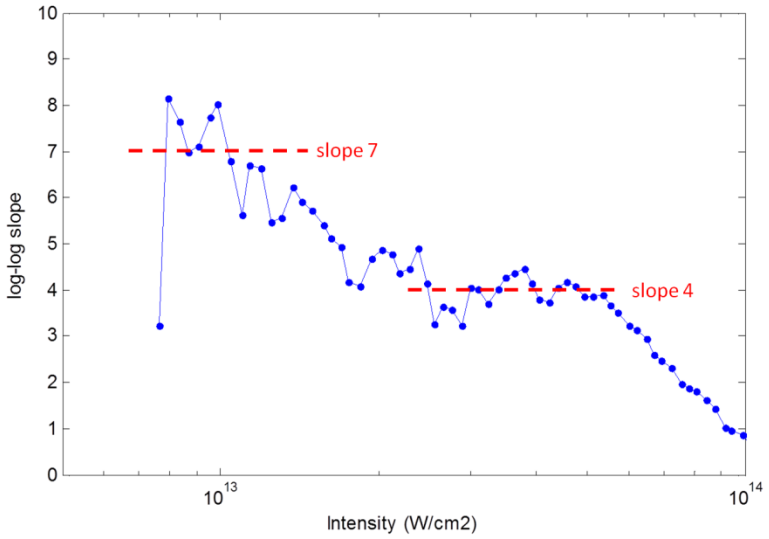

Figure 3 – Log-log slopes of iodobenzene. Like the simulations presented in this chapter, the ionic yield of iodobenzene shows signatures of (3 + 4) REMPI.

3.3.1 – Resonant vs. nonresonant MPI

If all other considerations are equal, a multi-step resonant ionization process is inherently preferred to a nonresonant process, given that the total number of photons in each process is the same. Consider, for example, a competition between (3 + 4) REMPI and direct nonresonant seven-photon ionization. Each process involves the absorption of seven photons, but the "enhancement" in REMPI is evident in Fig. 4. This simulation represents the resonant (blue) and nonresonant (green dashed) cases with the same relative cross sections, and the ion yield in the resonant case is enhanced by greater than a decade throughout entire curve.

The enhancement occurs due to the low order of each process. Three- and four-photon processes become possible at lower intensities than a seven-photon process, and

so even though they both must happen to create an ion, the combination is still preferred over the direct nonresonant ionization.

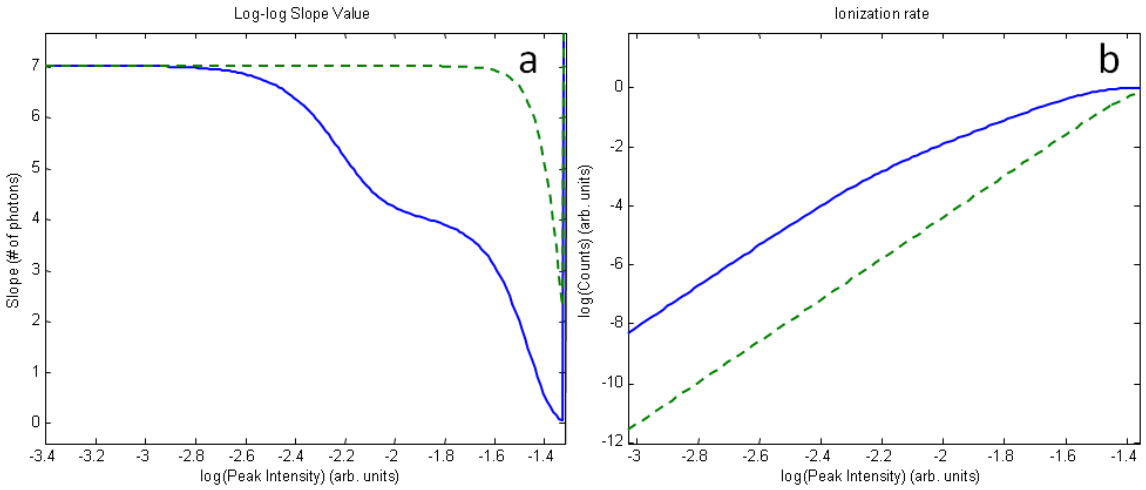

Figure 4 – Resonance enhancement. The nonresonant (green dashed) and resonant (blue) cases are presented in terms of log-log slope values (**a**) and ionic yields (**b**). Both yields have slopes of seven at low intensity, with the resonant process kinking to a slope of four at higher intensity. As seen in the yields, the resonant process is enhanced by orders of magnitude.

Another difference between the resonant and nonresonant cases, also seen in Fig. 4, is that the blue (REMPI) curve has a sort of "kink" where an integer slope (when plotted on a log-log scale) turns into a different integer slope. This is the result of the saturation of probability for one of the transitions, typically the lower-order process. Analyzing the slopes of the linear regions, as derived above, reveals the number of photons involved in the process; the change in slope means that one of the transitions is saturated such that it has effectively become immediately populated on the rising edge of the laser pulse. As a result, the higher-intensity (post-saturation) slope represents the number of photons in the limiting process, which is ultimately what allows us to identify the dynamics of the relevant transitions.

In the example presented, the lower-order process saturates earlier than the higher-order process when both have comparable relative cross sections. This should not come as a surprise; one can think of the exaggerated case of (50 + 2) REMPI, where the two-photon transition will saturate many orders of magnitude of intensity less than the 50-photon transition. It should be noted that with identical relative cross sections, both transitions saturate at the same intensity and the high-intensity slope ceases to be found. Instead, the curve goes from the low-intensity slope to zero slope, as both transitions are effectively instantaneous and the ionization probability is 1. This is avoided by giving the lower-order transition a (~50%) larger relative cross section, which is justified by the earlier discussion of the "10^{-33N}" power law [3].

3.3.2 – Distinguishing between similar processes

In the aromatic systems we study, there may be multiple transitions competing for excitation; in some cases, this is even expected between (3 + 4) and (4 + 3) REMPI processes where both three- and four-photon excitations may be near resonance. But when the orders are close as in the (3 + 4) case, what happens when the transitions are reversed as in our (50 + 2) example? Does a (4 + 3) REMPI appear any differently in an experiment than the (3 + 4)? In order to find a yield with a kink from slope seven to slope three, the relative cross sections must be skewed to unrealistic values.

Fig. 5 shows such a calculation for $(\sigma_4 I^4)^{1/4} = I^{6/4}$ and $(\sigma_3 I^3)^{1/3} = I^{2/3}$; this essentially favors the four-photon transition rate by a factor of 2.25.This significantly overestimates the strength of the four-photon transition in comparison to the three-photon transition, and it is only with this overestimation that we begin to see slopes of seven and three. If, on the other hand, the three-photon transition is favored with values of

$(\sigma_4 I^4)^{1/4} = I^{3/4}$ and $(\sigma_3 I^3)^{1/3} = I^{4/3}$, which favors the three-photon transition rate by a factor of 1.78 (so that the rates are closer than in the previous example), we find the results in Fig. 6.

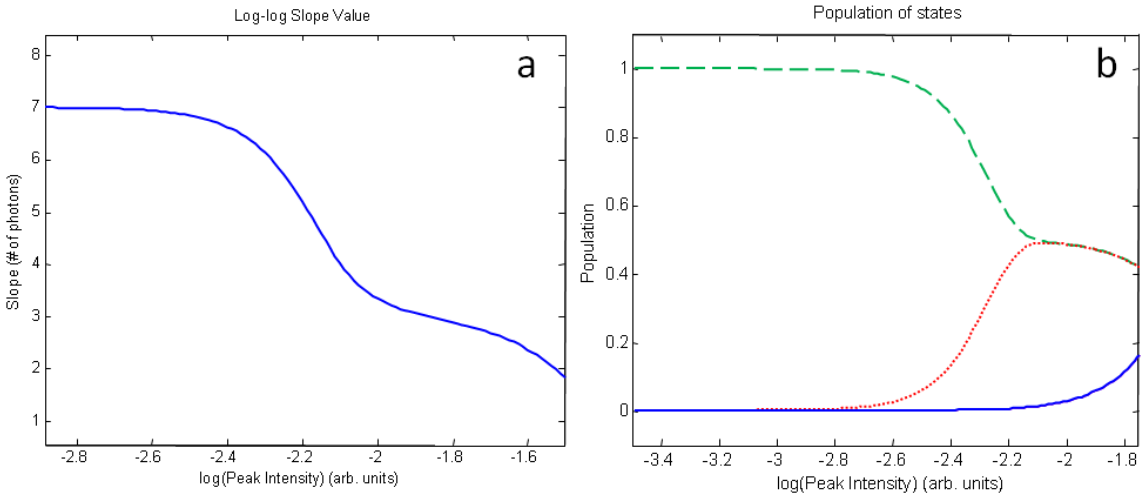

Figure 5 – (3 + 4) REMPI: favoring the four-photon transition. In order to force slopes (**a**) of seven and three, indicative of the four-photon transition saturating before the three-photon transition, the four-photon transition had to be favored by an unrealistic margin. Ground (green dashed), excited (red dotted) and ionic (blue) state populations are shown (**b**).

With less relative preference, we find similar approximate dependencies on quality of the high-intensity slopes. However, the key difference between the two cases is that for the latter the four-photon resonant excited state never gains any significant population. When the excitation finally begins to take place in significant amounts, the three-photon ionization transition is already saturated. As such, even though the four-photon process is the excitation step, it is still this step which limits the ionization, which results in the high-intensity slope of four.

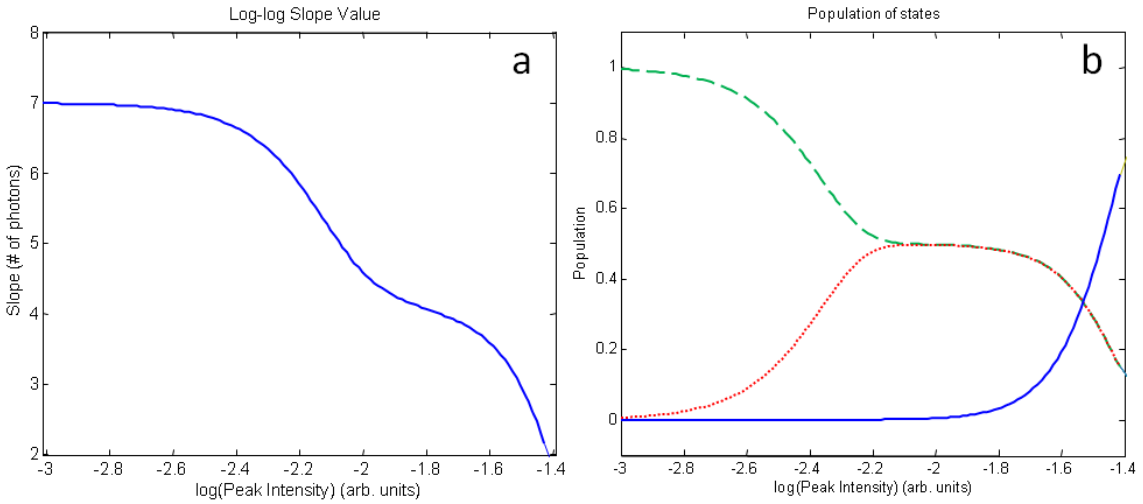

Figure 6 – (3 + 4) REMPI: favoring the three-photon transition. Slopes (**a**) of seven and four, indicative of the three-photon transition saturating before the four-photon transition, can be observed by favoring the three-photon transition only slightly. Ground (green dashed), excited (red dotted) and ionic (blue) state populations are shown (**b**).

One thing of note in the (3 + 4) vs. (4 + 3) rate models is that when the ionization yields' separate ionization paths are treated as separate ionic states (used to denote the total yield from each process), the yields from each process are nearly equal, with the (3 + 4) REMPI (blue curve) only slightly preferred, as seen in Fig. 7. Even though the three-photon excitation is greatly preferred, the ionization step in the (4 + 3) process is fast enough that, even with very little excited-state population, it compensates for the comparatively slow excitation.

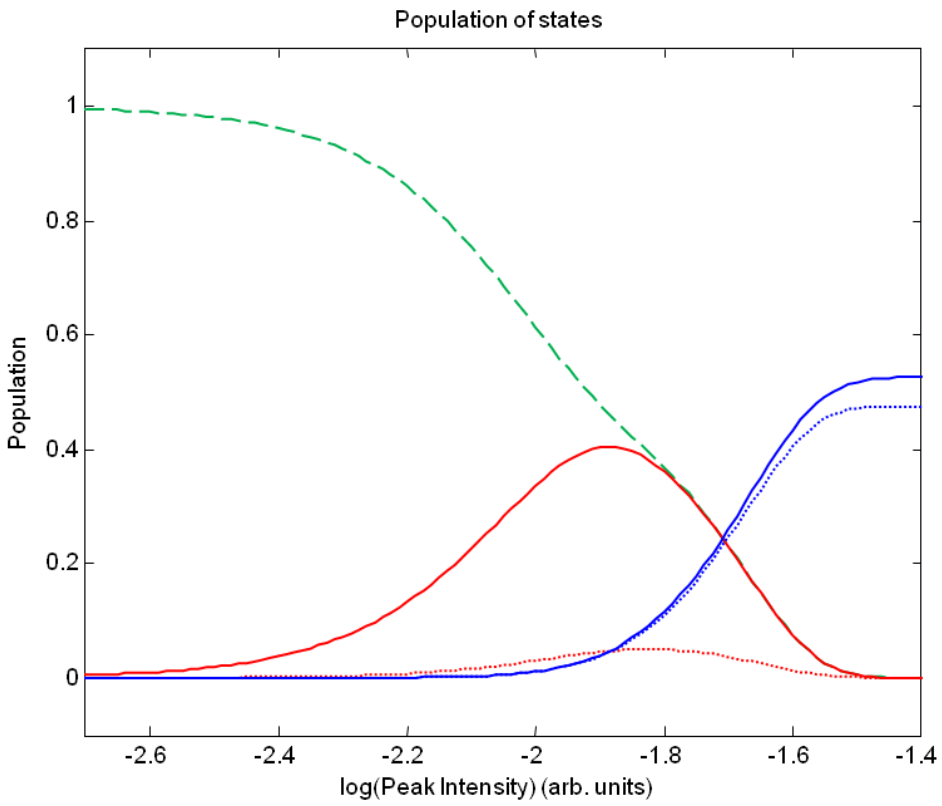

Figure 7 – Population densities for competing (3 + 4) and (4 + 3) REMPI. Comparing the rates of excitation (red) and ionization (blue) from the ground state (green dashed) through competing channels of (3 + 4) (solid curves) and (4 + 3) (dotted curves) REMPI shows that the excited state population unsurprisingly favors the lower-order transitions. However, while three-photon absorption dominates the excitation, the three-photon ionization in the (4 + 3) process nearly compensates for the excited state population. Ultimately, the rate of ionization through each process is similar, with the (3 + 4) REMPI slightly preferred.

3.3.3 – Rate models in the presence of loss channels

There are some molecular systems, as will be seen in Chapter 7, for which molecular ionization is in direct competition with other processes which detract from the ionic yield of the molecular parent. When this happens, there is a possibility that these loss channels may distort the yield of observed parent ions and deviate a multiphoton yield away from the I^N power law. Loss channels fall into two main categories: loss from the resonant excited state, and loss from the ionic parent.

Loss from the resonant excited state will be considered first. Such a loss channel often stems from a radiationless transition [7,8] such as internal conversion or intersystem crossing (both processes are described in Chapter 4), and can be strong enough to create significant loss in the parent molecules. As an example we will revisit in Chapter 6, the $^{1}\pi\pi^{*}$ state in iodobenzene converts into the $^{3}n\sigma^{*}$ state (this notation will be discussed in Chapter 4), which leads to fragmentation. This loss channel occurs so quickly that nanosecond and picosecond experiments using excitation to these states were unable to detect any of the intact parent [9]. Seen below in Fig. 8 are the state populations of the ground (green dashed), excited (red dotted), ionic (blue), and the loss channel (black dot-dashed) states under simulation of (3 + 4) REMPI.

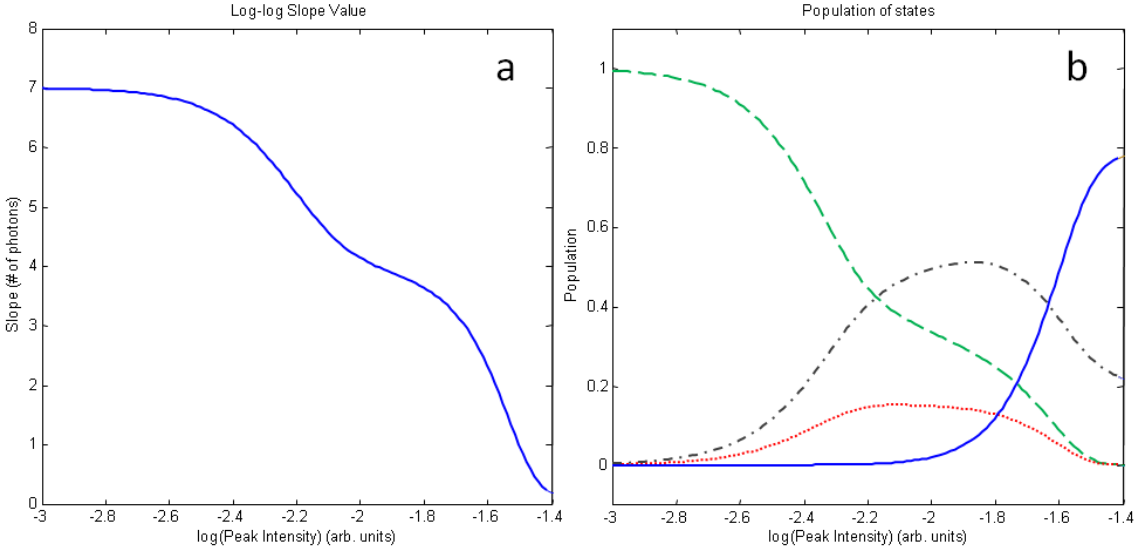

Figure 8 – Loss from the excited state. Some molecular processes such as intersystem crossing and internal conversion can cause loss channels from excited states. Because such loss could prevent accurate measurements of the slopes, the effects must be investigated. However, even when excited state loss dominates excited state population, the slopes (**a**) remain identifiable. Populations of the ground (green dashed) and excited (red dotted) states are shown (**b**) along with the loss from the excited state (black dot-dashed) and ionized parent (blue).

Under the conditions of this simulation, the loss channel dominates the excited state throughout the range of intensities such that the excited state never sees its population reach over 20% of the available electron density. Seen in Fig. 8 is the calculation of the slopes from the same simulation. In spite of the dominance of the loss channel over the excited state, the log-log slopes of the parent ion yield are unaffected, continuing to yield slopes of seven and four as expected for (3 + 4) REMPI. In fact, because the process effectively remains the same even when the excited state's population is reduced, this loss channel is unlikely to significantly affect the parent ion yield unless the loss channel removes nearly the entire probability density from the excited state.

While loss from the excited state does not appear to be a serious threat to the slopes in the parent ion yield, we must also examine losses from the ionic parent itself. In some cases the ionic state is unstable against fragmentation, particularly in the intense fields of a laser. When the simulation was written to account for this loss channel, it was found that the parent yield was suppressed but the slopes remained undisturbed even when the parent ions peaked at a population density of $\sim 10^{-11}$. This is not surprising, since loss which is independent of intensity merely removes a constant fraction of the yield while preserving its features. However, when the loss rate is proportional to the instantaneous intensity, then the slopes are affected.

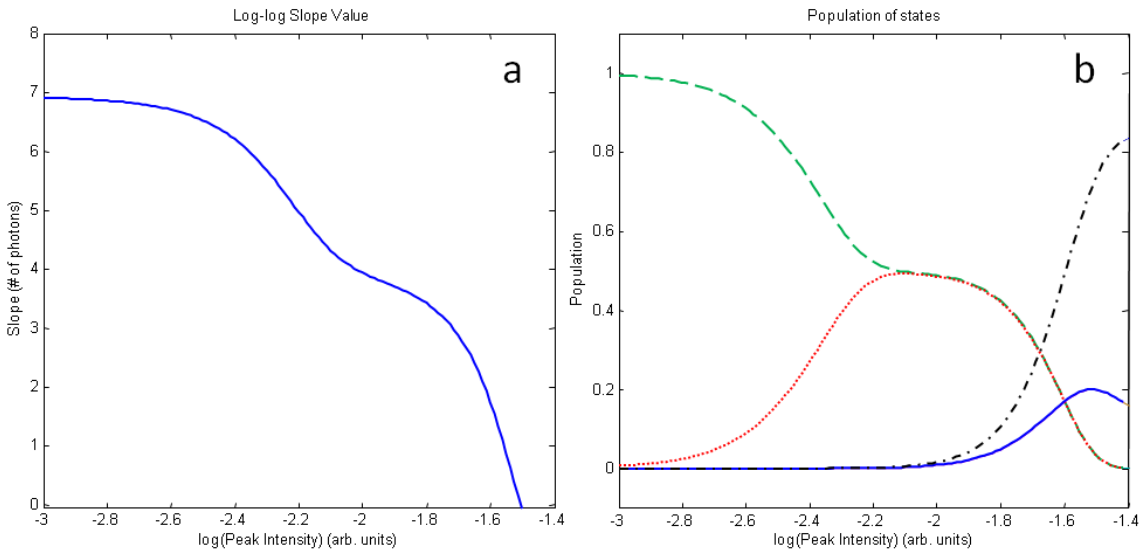

Figure 9 – Intensity-dependent loss to fragmentation. When the rate of loss in the ionic parent molecule depends on intensity, the distortion to the curve is not uniform, and could prevent accurate measurements of the slopes. However, even when fragmentation dominates and changes with intensity the slopes are largely unaffected. Both the low-intensity and high-intensity slopes (**a**) of seven and four are lower than the ideal case, but both remain identifiable. Populations of the ground (green dashed) and excited (red dotted) states are shown (**b**) along with the loss to fragments (black dot-dashed) and ionized parent (blue).

Fig. 9 shows the populations of these states under an intensity-dependent loss channel, with the ionized parent (blue) dominated by the parent loss channel (black dot-dashed). Seen below are the calculated slopes for the same simulation. Here we see that the slopes continue to remain largely unaffected, though the slope-seven region is slightly below seven, and the slope-four region is less defined than the unperturbed case. Higher rates of loss and/or higher powers of dependence on intensity push these trends further, but it is not until the parent ion yield effectively vanishes that the slopes cannot be identified correctly. Even in the cases where fragmentation dominates over parent ionization, the slopes found in an experiment should remain valid.

References

[1] Boyd, R.W., *Nonlinear optics* Academic Press, 2003.

[2] Chin, S. & Lambropoulos, P., *Multiphoton ionization of atoms,* Academic Press, 1984.

[3] Yamanouchi, K. (ed), *Lectures on Ultrafast Intense Laser Science 1*, Springer, 2010.

[4] Geddes, C.D., *Reviews in Fluorescence,* Springer, 2009.

[5] MATLAB 6.1, The MathWorks Inc., Natick, MA, 2000.

[6] Milonni, P. W. & Eberly, J. H., *Laser Physics*, Wiley, 2010.

[7] Klessinger, M. & Michl, J., *Excited States and Photochemistry of Organic Molecules* Wiley-VCH, 1995.

[8] Petr Klán & Wirz, J., *Photochemistry of organic compounds from concepts to practice*, Wiley, 2009.

[9] Dietz, T. G., Duncan, M. A., Liverman, M. G., and Smalley R. E. 1980, "Resonance enhanced two-photon ionization studies in a supersonic molecular beam: Bromobenzene and iodobenzene," *Journal of Chemical Physics*, vol. 73, pp. 4618.

Chapter 4

Molecular processes

There are a number of considerations which separate molecular systems from atomic systems. The aim of this chapter is to introduce the topics that will be necessary to understand the molecular dynamics in later chapters, as well as to introduce the methods and applicability of the approximations necessary to understand the systems.

4.1 – The molecular Hamiltonian

The presence of multiple nuclei along with potentially many electrons increases the number of degrees of freedom beyond the capabilities of precise *ab initio* calculation. Consider a general molecular Hamiltonian that accounts for kinetic energies of all nuclei and electrons (Eq. 4.1, first and second terms, respectively), Coulomb interactions between nuclei (third term), Coulomb interactions between electrons (fourth term), Coulomb interactions between electrons and nuclei (fifth term), and additional terms involving angular momentum, magnetism, and relativistic effects which are typically perturbatively small.

$$H = \sum_i \frac{\hat{p}_i^{\,2}}{2M_i} + \sum_i \frac{\hat{p}_i^{\,2}}{2m_e} + \sum_i \sum_{j>i} \frac{Z_i Z_j e^2}{4\pi\varepsilon_0 \left|\vec{R}_i - \vec{R}_j\right|} + \sum_i \sum_{j>i} \frac{e^2}{4\pi\varepsilon_0 \left|\vec{r}_i - \vec{r}_j\right|} - \sum_i \sum_j \frac{Z_i e^2}{4\pi\varepsilon_0 \left|\vec{R}_i - \vec{r}_j\right|} + \text{magnetic, spin, relativistic, etc.} \quad \textbf{(4.1)}$$

In order to simplify the solutions of the molecular time-independent Schrödinger equation for this Hamiltonian, assumptions must be made. First, terms resulting from relativistic, magnetic, and angular momentum considerations can be ignored for most

systems unless a specific feature of the molecule requires their inclusion (as will be the case in Section 4.6.3). Next, the nuclei are approximated as fixed, since their kinetic energy is small compared to that of the electrons; this eliminates the first term in Eq. 4.1 and makes the third term easy to calculate. The assumption of fixed nuclei is known as the *Born-Oppenheimer approximation* [1]. The electron-electron interactions are often ignored [2], which is called the *independent electron approximation*. While this solution can only be an approximation (though corrections can be applied to compensate for the loss in accuracy), it allows the Hamiltonian to be separated into a sum of independent single-electron Hamiltonians

$$H = H_{e1} + H_{e2} + H_{e3} \cdots, \tag{4.2}$$

with the Hamiltonian of electron *i* defined as

$$H_{e,i} = \sum_i \left(\frac{\hat{p}_i^{\,2}}{2m_e} - \sum_j \frac{Z_j e^2}{4\pi\varepsilon_0 \left| \vec{r}_i - \vec{R}_j \right|} \right) \tag{4.3}$$

This separation allows a straightforward construction of the molecular stationary states Φ and eigenenergies E_n from the stationary states and eigenenergies of the H_e, which we write as

$$H_e \varphi_n = E_n \varphi_n . \tag{4.4}$$

From this, we have for the complete molecule

$$\Phi = \varphi_{n_1} \varphi_{n_2} \varphi_{n_3} \cdots \tag{4.5}$$

and

$$E = E_{n_1} + E_{n_2} + E_{n_3} + \ldots \tag{4.6}$$

Each of these single-electron wavefunctions represents a molecular orbital (MO). Many methods (Hartree-Fock, density functional theory, configuration interaction, etc.) to calculate the orbitals and their energies exist, along with quantum chemistry calculation software (Gaussian, GAMESS, etc.), but many of the properties of a MO can be determined without full calculations. The properties of the orbitals, as discussed in the next section, are restricted by the overall framework of the molecule.

4.2 – Molecular symmetry point groups

Molecules may be classified according to the symmetry of their nuclear framework (if this framework is symmetric to begin with). Such classifications are based on the symmetry operations (reflections, rotations, etc.) which commute with the Hamiltonian of the system. For example, the hydrogen molecule can undergo a reflection about a plane dividing the two atoms such that their positions are exchanged. The Hamiltonian of the reflected system is identical to the original case, so this is an operation $\hat{R}$ which commutes with the Hamiltonian.

$$\hat{R}\hat{H} - \hat{H}\hat{R} = 0 \tag{4.7}$$

Hence, eigenfunctions of the Hamiltonian must also be eigenfunctions of the reflection operator,

$$\hat{H}\left(\hat{R}|\psi\rangle\right) = E\left(\hat{R}|\psi\rangle\right). \tag{4.8}$$

This means that $\hat{R}|\psi\rangle$ is also an eigenfunction of the Hamiltonian. Given that $|\psi\rangle$ must be normalized, the new function $\hat{R}|\psi\rangle$ must also be normalized; as such, the reflection can only have eigenvalues of

$$\hat{R}|\psi\rangle = \pm 1|\psi\rangle. \tag{4.9}$$

This means that the system must be either symmetric or antisymmetric upon a given reflection (or rotation, inversion, etc.)[†]. Take for example a hydrogen molecule under a reflection through its center, as pictured in Fig. 1. A reflection through the center of the molecule interchanges the atoms but does not change the energy of the system; this operation commutes with the Hamiltonian and the MOs within the system will have eigenvalues of +1 or -1 under this operation.

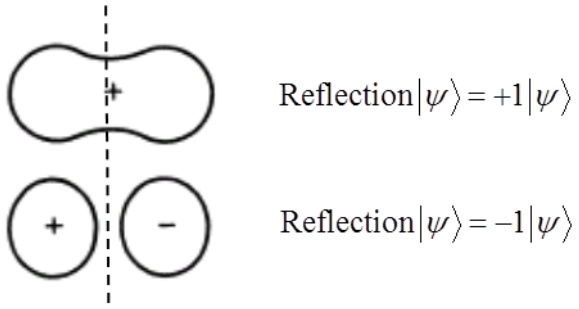

Figure 1 – Reflection operation in molecular hydrogen. A reflection operation, when performed on a hydrogen molecule through its center axis, can have eigenvalues of +1 or -1. Labels on the orbitals (+ and –) refer to the phase of the orbital.

By defining the symmetry operations which meet certain restrictions [3], one can assign a molecule to a *molecular point group*. Each of these point groups has irreducible representations, which may for this purpose be considered an abstract kind of simultaneous eigenfunctions of the group's symmetry operators. These irreducible representations are uniquely labeled by a set of simultaneous eigenvalues (known as characters); one for each operator in the point group. For instance, the C_{2v} point group (that of the water molecule) contains four operators. One of its irreducible representations is specified by the list of characters {+1,–1,–1,+1}. Because this is a clumsy notation, the

[†] This is not strictly true; some operations can have imaginary eigenvalues which represent a global phase shift in the molecule, and degenerate orbitals (of *E* character) can have eigenvalues with magnitudes other than 1. However, of the molecules we study, all symmetry eigenvalues are 1 or -1 with the exception of the degenerate orbitals of benzene, which can also have eigenvalues of 2 or 0. Symmetry character tables for the molecules we study can be found in Appendix B.

more elegant so-called Mulliken symbols are in widespread use. For instance, the list just mentioned is referred to by the Mulliken symbol B_1. Because the one-electron MOs must be a simultaneous eigenfunction of all operators in the point group, they are often labeled by Mulliken symbols [4]. The water molecule, for instance, has MOs of B_1 symmetry character. Thus, the spatial symmetries of the molecule's nuclear framework allows only specific symmetries for its MOs. Revisiting the hydrogen molecule example: if one hydrogen atom in the example in Fig. 1 is substituted with a fluorine atom, reflection in a plane perpendicular to the internuclear axis is no longer a symmetry operator which has an eigenvalue. Consequently, orbitals with the symmetry of those pictured do not exist in HF. For the molecules considered in this dissertation, the relevant symmetry character tables can be found in Appendix B.

The relevance of MO symmetry in ionization has been well-documented. Given the same intensity, the ionization probability of O_2 is smaller ("suppressed ionization") than that of Xe [5,6], in spite of their similar ionization potentials (IP). However, no such difference was observed for N_2 and Ar, who also have similar IPs. The S-matrix theory [7] explains suppressed ionization as constructive or destructive interference between the sub-waves of the ionizing electron coming from the various atomic centers in the molecule that "can significantly influence the total ionization yields of the molecule". Photoelectron spectra are also affected: Ref. [8] observed symmetry-induced interference effects in the above-threshold ionization spectra of O_2 and N_2. In particular, the different behaviors of O_2 and N_2 were ascribed to the different symmetries of their highest occupied molecular orbits (HOMOs), which is π_g for O_2, but σ_g for N_2. Differences in the symmetry characters of the HOMOs are relevant, as it is often assumed that the HOMO is

the "active molecular orbital of interest" [7]. Still, [9] discuss lower-lying MOs, and consider the HOMO and the next-lower MO, the "HOMO – 1".

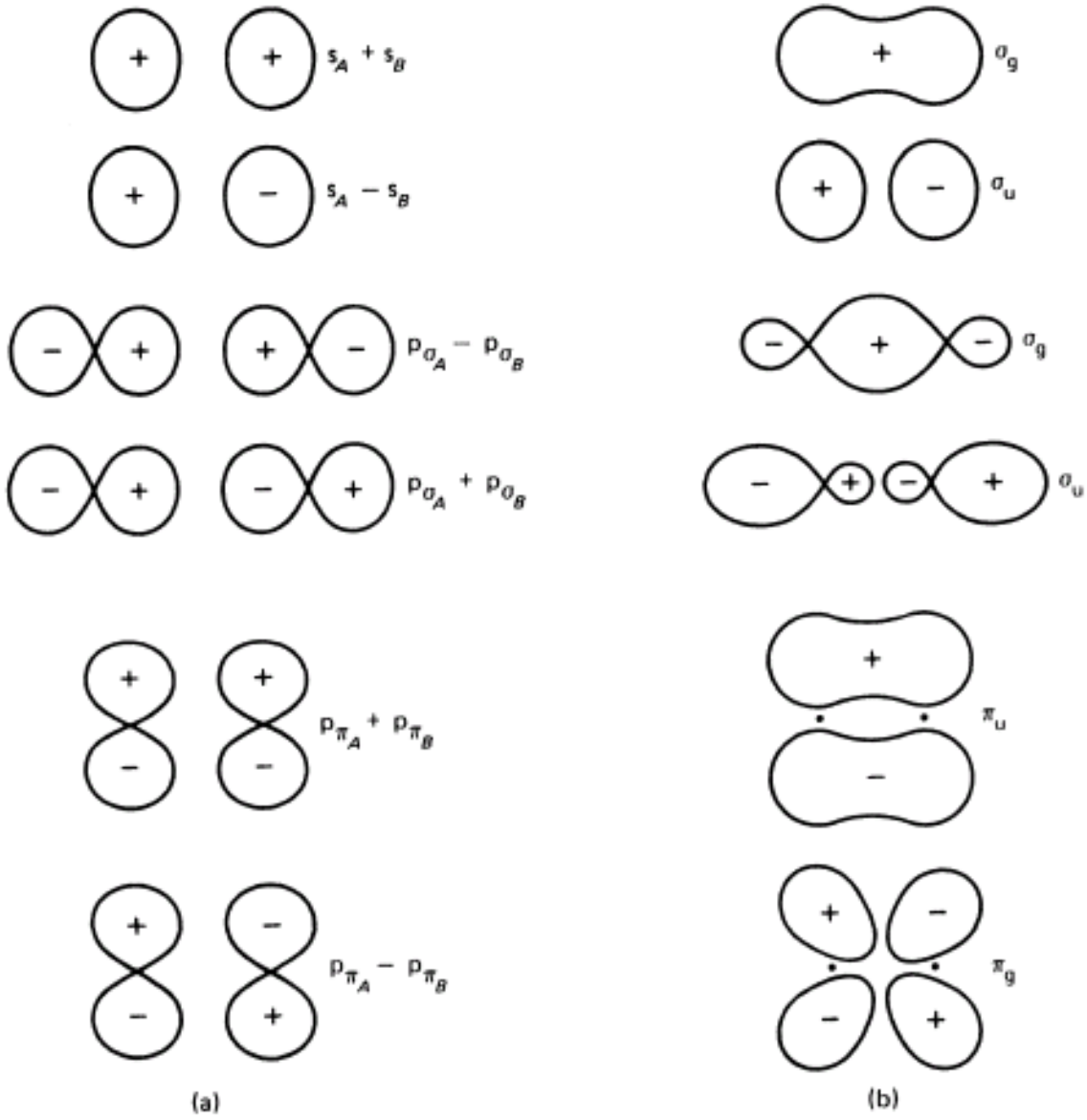

Figure 2 – Linear combination of atomic orbitals. A first approximate toward visualizing molecular orbitals is to form linear superpositions of atomic orbitals. Shown are superpositions of atomic *s* and *p* orbitals (**a**) and their resulting σ and π molecular orbitals (**b**). Indices *A* and *B* denote atomic nuclei, and *g* and *u* denote *gerade* and *ungerade* orbitals (symmetric and antisymmetric under spatial inversion $\vec{r} \rightarrow -\vec{r}$, respectively). Image from [2].

4.3 – Molecular orbitals

As discussed in Section 4.1, a MO can be extensively complicated to calculate. Perhaps the simplest way to visualize them, though not necessarily the most accurate, is by the linear combination of atomic orbitals (LCAO) method. In this method, the atomic orbitals are added or subtracted from each other in a superposition to make a combined orbital for the molecule. For the simplest example of the LCAO method, we take the H_2 molecule, as seen in Fig. 2.

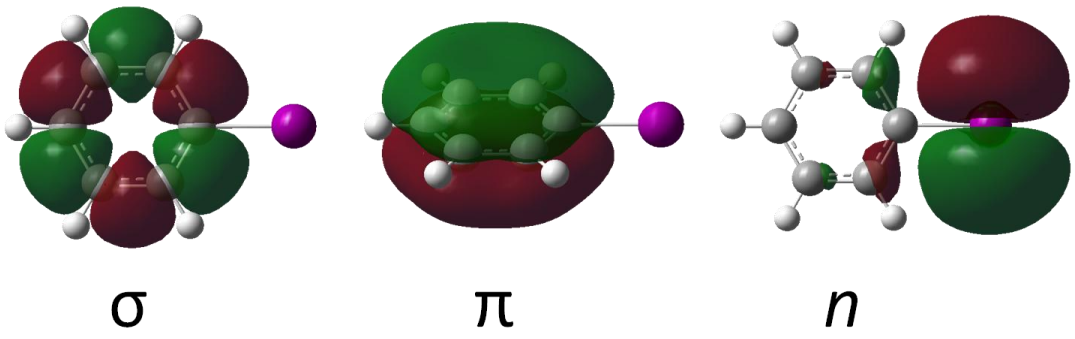

Figure 3 – Types of molecular orbitals. Molecular orbitals which are relevant to the present work include σ, π, and *n* orbitals, examples of which are shown here for the planar molecule iodobenzene (C_6H_5I). Orbitals with electron density connecting atoms primarily in the plane of the molecule are σ orbitals, which provide the framework for the molecule. π orbitals have electron density out of the plane of the molecule. Finally, *n* orbitals are primarily atomic in nature.

Combining these orbitals allows us to define a framework for the MOs. For the purposes of this dissertation, there are three relevant types of MOs which will be discussed: σ, π, and *n* orbitals. σ orbitals are formed with electron density between two atoms while remaining in the plane of the atoms. Organic molecules are typically thought of as constructed by a skeleton of carbon σ bonds which tie the nuclei together, with other orbitals added over this structure [10]. The π bonds are created from the out-of-plane (typically denoted carbon p_z) orbitals, and typically form weaker bonds than σ bonds. Finally, *n* orbitals denote those orbitals which are primarily atomic in nature, as

their superposition with other orbitals is weak. Examples of these σ, π, and *n* orbitals are seen in Fig. 3 for the example of iodobenzene.

As shown in Fig. 4, symmetric orbitals are typically more stable (bound by greater energy) than antisymmetric orbitals [11], since the antisymmetry condition requires at least one node in the distribution. Nodes in the electron density give a natural breaking point in the bond, making dissociation more likely. As such, the antisymmetric superposition of orbitals it usually denoted as "antibonding", and marked by an asterisk.

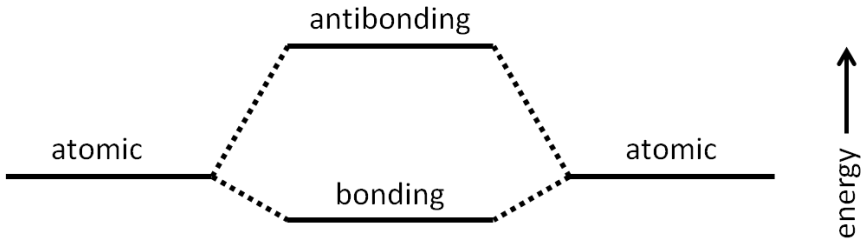

Figure 4 – Bonding and antibonding orbitals. When two atomic orbitals combine to form a molecular orbital, their superpositions typically have different energies. One (usually the symmetric superposition in the simplified case) becomes more deeply bound, while the other (antisymmetric superposition) becomes more weakly bound.

4.4 – Hückel's (4*n* + 2) rule for aromaticity

The molecules we investigate in this dissertation are all aromatic, meaning that the structure of their π orbitals enhances the stability of the molecule more than is expected from the individual bond strengths. Hückel MO theory deals only with the π electrons and constructs secular determinants to solve the eigenvalue equation $\hat{H}_{MO}\psi = E\psi$, which is worked out in detail in [12]. For planar molecules the guideline for aromaticity is to satisfy the so-called (4*n* + 2) rule, which refers to the number of π electrons to make an aromatic system. Take the example of benzene, whose π energies are shown qualitatively in Fig. 5. Six individual atomic p_z orbitals superimpose to create

six MOs, three of which are bonding and three of which are antibonding. The maximum enhancement in stability of the system occurs when all bonding orbitals are filled with spin-paired electrons and all antibonding orbitals remain empty. To meet this condition, six electrons are needed, which satisfies $(4n + 2) = 6$ for $n = 1$.

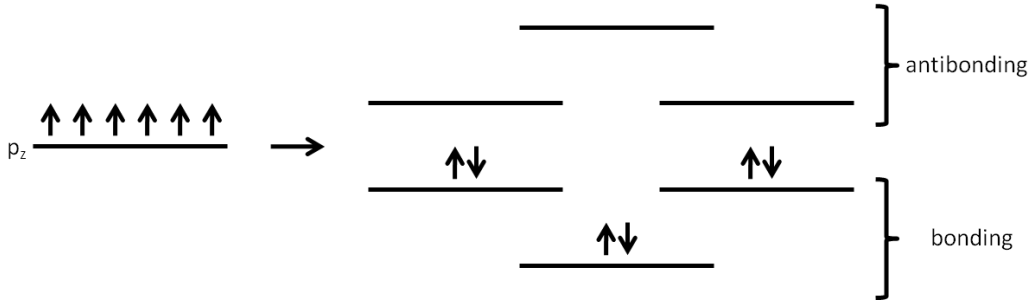

Figure 5 – Hückel's (4*n* + 2) rule for aromaticity. Increased molecular stability is found when all bonding orbitals (and no antibonding orbitals) are occupied in a π system, which increases the average strength of the bonds. According to Hückel's rule for aromaticity, this occurs when $(4n + 2)$ π electrons are present. Shown is the case for $n = 1$, where six electrons create enhanced aromatic stability.

Each carbon atom of benzene shares one valence electron with a hydrogen atom as well as one with each neighboring carbon to fill a σ bond. It is then left with one valence electron to contribute to a π orbital. One π electron from each carbon satisfies Hückel's $(4n + 2)$ rule for aromaticity, but with six π electrons, only three bonds can be formed.

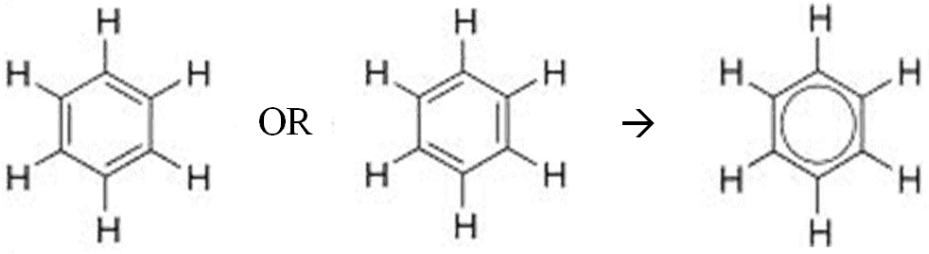

Figure 6 – Uniform bonds in benzene. Instead of alternating single and double bonds in a conjugated system, the aromatic π system in benzene spreads electron density uniformly around the system. This uniformity increases the overall stability of the molecule.

Instead of forming a conjugated system which alternates between single and double bonds in the π system, the electrons form an aromatic system in which all six bonds have equal strength, as shown in Fig. 6. This uniformity lowers the energy and enhances the stability of the ring, which is why aromatic compounds are prevalent throughout organic chemistry.

4.5 – Spectroscopic notation in molecules

The electronic configuration of atoms refers to how many electrons occupy each spatial orbital. The nitrogen atom in its electronic ground state, for example, is represented as $N(1s^2 2s^2 2p^3)$. Often the core electrons are implied and the notation simplified to include only the valence electrons, since these are often the orbitals relevant to bonding: $N(\ldots 2p^3)$. Molecular electron configurations are specified in a similar way: often, only the outer orbitals are specified. Because the present work focuses on (primarily single-electron) excitation of the highest-energy bound states, we use a conventional notation in which only the unpaired electrons are specified. Consider a molecule with a bound π state and a π* excited bound state (with the asterisk denoting an antibonding orbital): an excitation transition could be represented as $\pi^2\pi^{*0} \rightarrow \pi^1\pi^{*1}$. Such a transition is denoted as a ππ* transition, and the excited state as a ππ* state denoting two unpaired electrons: one in a π orbital and another in a π* orbital. Further, the spin multiplicity of the state is typically included as a superscript prefix. Thus, we refer to a transition to an excited singlet state as a $^1\pi\pi^*$ transition. This will be the notation used throughout the remainder of the text when referring to molecular states and transitions.

4.6 – Electronic transitions in molecules

4.6.1 – Transition rates and Fermi's golden rule

While rates of multiphoton transitions were discussed in Chapters 2 and 3, rates of other types of transitions between electronic states can be generalized through first-order perturbation theory by a formula known as Fermi's golden rule [12,13]:

$$w_{i\to f} = \frac{2\pi}{\hbar}\left|\left\langle f\left|\hat{H}\right|i\right\rangle\right|^2 \rho_E \qquad \textbf{(4.10)}$$

which describes the rate $w_{i\to f}$ of a transition from initial state $|i\rangle$ to final state $|f\rangle$ due to the perturbing Hamiltonian $\hat{H}$, where the final density of states is ρ_E. The perturbation matrix element $\left\langle f\left|\hat{H}\right|i\right\rangle$ contains the bulk of the relevant information about the transition. The coupling between initial and final states ultimately determines the rate of the transition, but several criteria must be considered. As will be discussed in Section 4.6.3, overlap between spin wavefunctions can be important, particularly in radiationless transitions. Overlap between vibrational energy levels, as seen in Fig. 7, contributes as well. The so-called Franck-Condon principle [14-16] states that the perturbing matrix element scales linearly with the overlap of vibrational wavefunctions χ_v^i and $\chi_{v'}^f$, which are separable from the rest of the wavefunction:

$$\left|\left\langle f_{v'}\left|\hat{H}\right|i_v\right\rangle\right|^2 = \left(\left|\left\langle f\left|\hat{H}\right|i\right\rangle\right|^2\right)\left(\left|\left\langle \chi_{v'}^f\middle|\chi_v^i\right\rangle\right|^2\right). \qquad \textbf{(4.11)}$$

These vibrational factors are known as Franck-Condon overlap integrals.

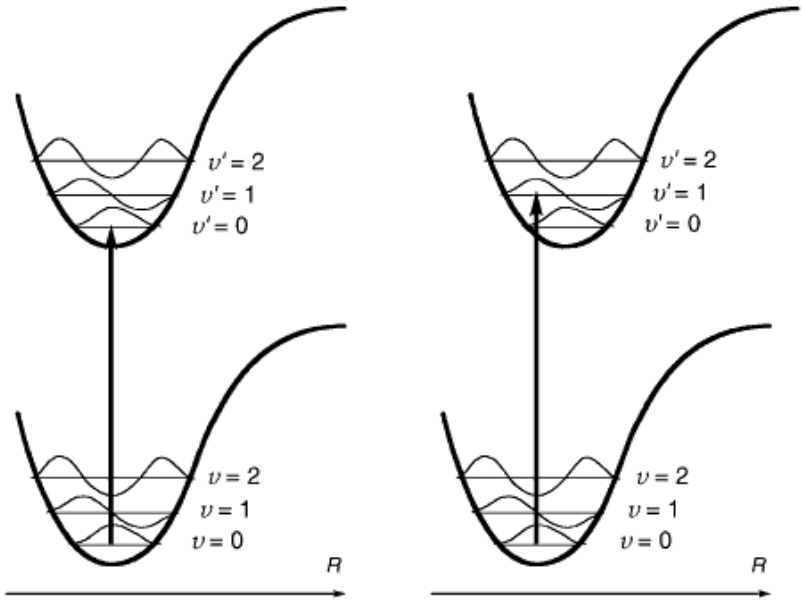

Figure 7 – Illustration of the Franck-Condon principle. Transition rates between initial and final states with overlapping vibrational wavefunctions (*v* and *v*') are preferred. Plotted are electronic binding potentials as a function of the nuclear coordinate of vibration *R* for the cases where the vibrational ground states overlap (left) and when they do not (right). Image from [12].

4.6.2 – Allowed and Forbidden Transitions

In atomic and molecular systems, electronic transitions are often classified as "allowed" or "forbidden" based on arguments such as conservation laws. However, there are some properties of a system that can loosen the restrictions on whether a transition can or cannot occur. The symmetry arguments from which conservation laws are derived often determine which transitions are allowed and forbidden. However, while the Born-Oppenheimer approximation assumes fixed nuclei, this is not truly the case. Although they are effectively fixed through the duration of an ultrashort laser pulse, vibrations in the molecule distort the symmetry and perturb the MOs so that the laser pulse sees a perturbed molecule. Consider a vibration in benzene in which the molecule is squeezed along one of its primary axes, as appears in Fig. 8.

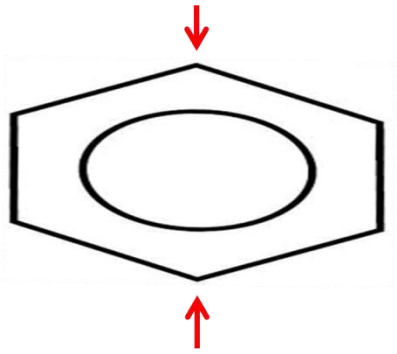

Figure 8 – Beyond the Born-Oppenheimer approximation. When vibrations are present in a molecule, distortions to the symmetry occur. Shown is an exaggerated case for benzene, where the molecule is squeezed along the direction of the red arrows. In this case, the six-fold rotational symmetry of the molecule is removed.

While Fig. 8 shows an exaggerated example, any such distortion removes the six-fold rotational symmetry of the molecule, which means that the molecule no longer strictly fits into the D_{6h} point group. Perturbative corrections would be necessary to calculate the MOs, and transitions forbidden by symmetry considerations would not be strictly forbidden by the perturbed symmetry.

Another example comes from the dynamics of multiphoton absorption. Transitions which are forbidden by symmetry in the single-photon case can be allowed in the multiphoton case. Because the intermediate virtual state in a multiphoton process is not an eigenstate of the system (and is restricted only by uncertainty relations) multiphoton transition matrix elements (as seen in Chapter 3) can be nonzero even when the single-photon transition is symmetry forbidden, particularly when the energetic resonance is strong. This is seen in detail in Ref. [17].

4.6.3 – Intersystem crossing

Another interaction, this one "forbidden" by spin, which will prove relevant to some of the molecules we consider is the coupling of singlet and triplet states. When considering the total wavefunction of a bound electron, it is customary to assume that the spatial wavefunction $|\phi\rangle$ and spin wavefunction $|\chi\rangle$ are separable:

$$|\Psi\rangle = |\phi\rangle_{\text{spatial}} |\chi\rangle_{\text{spin}}. \tag{4.12}$$

This assumption is useful when generalizing to multi-electron systems since the total wavefunction can be treated as the products of two separable wavefunctions.

$$|\Psi_{2\text{ electrons}}\rangle = |\Psi_{e1}\rangle \otimes |\Psi_{e2}\rangle = (|\phi_{e1}\rangle \otimes |\phi_{e2}\rangle) \otimes (|\chi_{e1}\rangle \otimes |\chi_{e2}\rangle) \tag{4.13}$$

Superpositions of the two spin wavefunctions can form a total spin wavefunction consisting of either singlet or triplet states, and it is straightforward to show [18,19] that singlet and triplet states are orthogonal. Thus, if these spin states are pure in their multiplicity and the Hamiltonian is independent of spin (as was assumed in Section 4.1), the matrix element mixing singlet and triplet states vanishes and a transition between the two states is forbidden.

$$\begin{aligned} \langle \chi_{\text{singlet}} | \chi_{\text{triplet}} \rangle &= \langle \chi_{\text{triplet}} | \chi_{\text{singlet}} \rangle = 0 \\ \langle \chi_{\text{singlet}} | H_0 | \chi_{\text{triplet}} \rangle &= \langle \chi_{\text{triplet}} | H_0 | \chi_{\text{singlet}} \rangle = 0 \end{aligned} \tag{4.14}$$

However, this orthogonality holds only approximately. The interaction of the electron's orbital velocity with the magnetic field generated by the spin of a nucleus (known as *spin-orbit coupling* (SOC)) gives rise to a perturbative term in the Hamiltonian of the system, which appears as

$$H_{SOC} = \frac{e^2}{2m_e c^2} \sum_j \sum_\mu \frac{Z_\mu}{\left| r_\mu^j \right|^3} \hat{\boldsymbol{l}}_j^\mu \cdot \hat{\boldsymbol{s}}_j \tag{4.15}$$

with $\boldsymbol{l}$ the orbital angular momentum operator of the j^{th} electron, and r the radial vector from nucleus μ to electron j, consistent with the notation in Ref. [13]. Because this term involves a scalar product between an angular momentum operator that acts only on the spatial part of the wavefunction and a spin operator that acts only on the spin wavefunction, the total wavefunction is no longer purely separable into its spatial and spin wavefunctions.

The SOC term in the Hamiltonian represents only a small perturbation to the overall system, so the eigenfunctions still consist of one primary multiplicity. However, they are no longer pure in their multiplicity, as the impure singlets have a small amount of triplet contribution and vice versa. With the separability of spatial and spin wavefunctions now removed, the orthogonality of the perturbed singlet and triplet states holds only approximately. Ultimately, the SOC relaxes the spin-forbidden selection rule; transition matrix elements are not explicitly forbidden.

Though the matrix elements are typically negligible, there are systems for which they can become significant [20]. Consider Eq. 4.15 for the hydrogen-like case; one finds the expectation value of the radial vector as

$$\left\langle \frac{1}{\left| r_\mu^j \right|^3} \right\rangle \propto \frac{2Z^3}{a^3 n^3 l(l+1)(2l+1)} \tag{4.16}$$

with a the Bohr radius and Z the nuclear charge. The relevant thing to take from this result is the relation to Z; substituting this back into Eq. 4.15 reveals that the SOC

perturbation scales as Z^4. The effect of larger SOC with increasing nuclear size it is often referred to as the *heavy atom effect*.

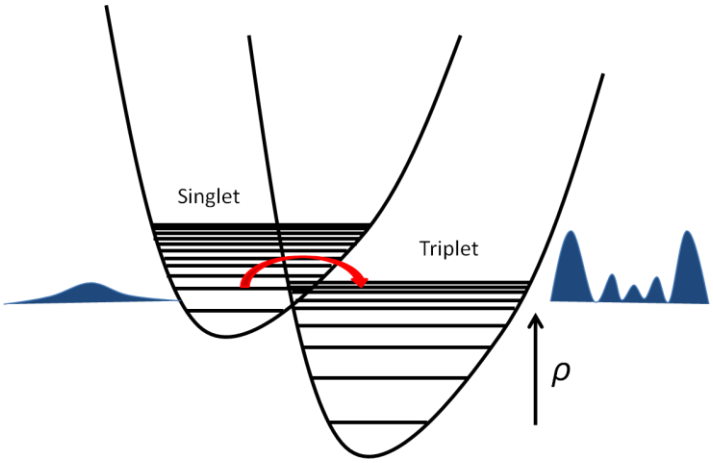

Figure 9 – Intersystem crossing. In the case shown there is a radiationless intersystem crossing between singlet and triplet states. The transition matrix element suffers from poor overlap of vibrational wave functions (blue) as the triplet state is highly vibrationally excited immediately after the transition. However, substantial energetic overlap increases the rate, and the high density of final states (ρ) increases the transition.

An electronic transition between singlet and triplet systems is known as an *intersystem crossing* (ISC), a diagram of which is shown in Fig. 9. When the SOC term is large, the transition may become likely, but other factors also contribute to the transition rate. Transitions between orbitals with similar spatial distributions are suppressed. This is due to the nature of SOC; angular momentum is not conserved in the spin or the spatial wavefunctions, only in the combination. Because ISC involves exchange of angular momentum between spin and spatial wavefunctions, the transition is more likely if the orbitals are spatially rearranged [21]. This forms a set of qualitative rules, known as *El Sayed's rules for ISC*, and some examples are shown in Fig. 10. Energetic and vibrational overlaps between initial and final states are, as with any electronic transition, keys to

enhancing the rate. As mentioned in Section 4.6.1, the details of these conditions are described by the Franck-Condon overlap integrals.

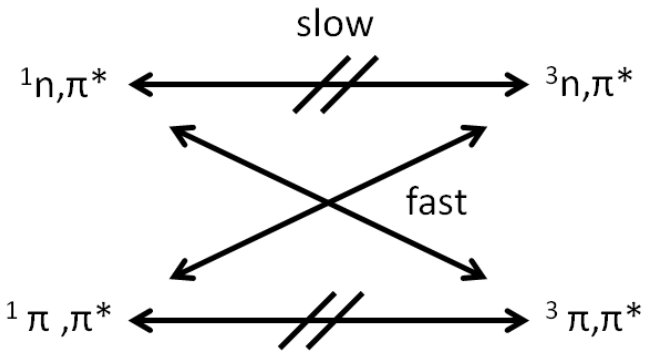

Figure 10 – El Sayed's rules for intersystem crossing. Rates of nonradiative transitions between singlet and triplet states, called intersystem crossings, are governed by qualitative guidelines called El Sayed's rules. Intersystem crossing rates are enhanced by ~10^3 when the initial and final states have different spatial orbital characteristics. Because angular momentum is not conserved in the spin wavefunction in such a transition, neither is it conserved in the spatial wavefunction. For this reason, spatial changes in electron density distribution enhance the process, and these changes are more likely between orbitals of different spatial character.

4.7 – Vertical and adiabatic energies

In optically-induced molecular electronic transitions, two different types of energies are often quoted: vertical energy and adiabatic energy. Vertical energy refers to the energy needed to complete a transition while the nuclear bond coordinate remains fixed; this is taken to be the case in the Born-Oppenheimer approximation, which maintains that the electronic motions are much faster than the nuclear motions, such that the nuclei are assumed to be stationary. Adiabatic energy refers to the energy difference between the initial and final states after the system has relaxed to a vibrational minimum. A schematic of vertical and adiabatic transitions is presented in Fig. 11 [11].

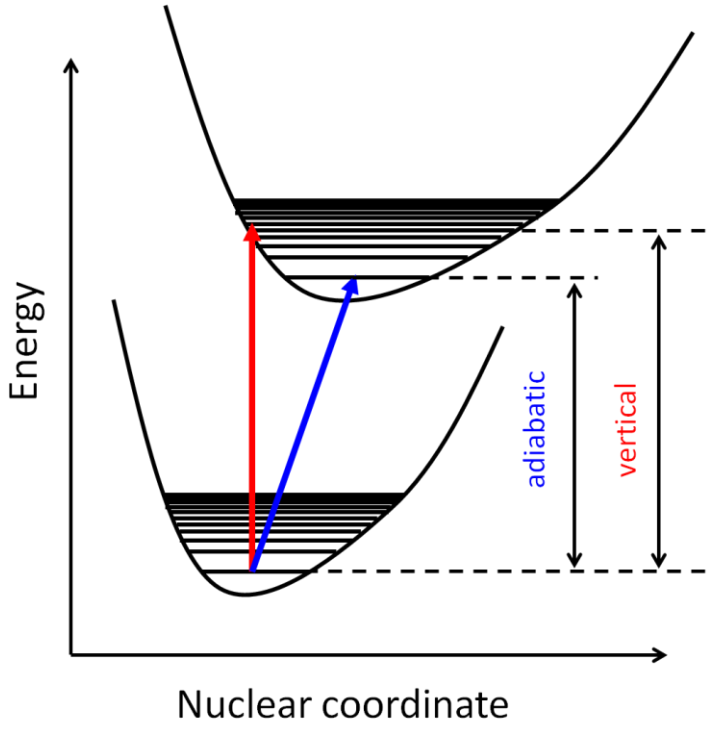

Figure 11 – Vertical and adiabatic transitions. When the nuclear coordinates are assumed to be stationary, the transition energy is referred to as a vertical energy (red). On the other hand, when the nuclear coordinates are allowed to relax to a vibrational minimum, the difference in vibrational ground state energies of the two states is called the adiabatic energy.

Single-photon optical transitions are typically determined by vertical energies [22]. However, when examined empirically, our experiments seem to be restricted by adiabatic energies. Take benzene as an example: the $^1\pi\pi^*$ transition which we claim is responsible for excitation has a well-documented vertical energy of 4.9 eV [23]. Our laser, as detailed in Chapter 5, outputs a carrier wavelength of 800 nm, which means that each photon carries approximately 1.55 eV ± 0.025 eV, with the uncertainty resulting from the bandwidth of the laser pulses (≈26 nm in FWHM). A three-photon transition carries 4.65 ± 0.04 eV of energy, for which the vertical energy of the transition is far out of range; however, we do observe signatures of this transition. This is only one example, as several other molecules which we study exhibit ionization patterns which could only

occur if our experiment is restricted by the adiabatic, and not the vertical, transition energies. The reason for this may be the ponderomotive effects as discussed in Chapter 2. While the reason is highly speculative, the empirical evidence points to our experimental multiphoton absorption energies being dictated by the adiabatic energy.

References

[1] Born, M. & Oppenheimer, R. 1927, "Zur Quantentheorie der Molekeln," *Annalen der Physik,* vol. 389, no. 20, pp. 457-484.

[2] Lowe, J.W. & Peterson, K., *Quantum chemistry*, Elsevier Academic Press, 2006.

[3] Cotton, F. A., *Chemical Applications of Group Theory, 3rd Edition*, Wiley, 1990.

[4] Harris, D. C & Bertolucci, M. D., *Symmetry and spectroscopy: an introduction to vibrational and electronic spectroscopy,* Dover, 1989.

[5] Guo, C., Li, M., Nibarger, J. & Gibson, G. 1998, "Single and double ionization of diatomic molecules in strong laser fields," *Physical Review A,* vol. 58, no. 6, pp. R4271-R4274.

[6] Talebpour, A., Yang, J. & Chin, S.L. 1999, "Semi-empirical model for the rate of tunnel ionization of N2 and O2 molecule in an intense Ti:sapphire laser pulse," *Optics Communications,* vol. 163, no. 1-3, pp. 29-32.

[7] Becker, A. & Faisal, F.H.M. 2005, "Intense-field many-body S-matrix theory," *Journal of Physics B-Atomic Molecular and Optical Physics,* vol. 38, no. 3, pp. R1-R56.

[8] Grasbon, F., Paulus, G., Chin, S., Walther, H., Muth-Böhm, J., Becker, A. & Faisal, F. 2001, "Signatures of symmetry-induced quantum-interference effects observed in above-threshold-ionization spectra of molecules," *Physical Review A,* vol. 63, no. 4.

[9] Kjeldsen, T. & Madsen, L. 2005, "Strong-field ionization of diatomic molecules and companion atoms: Strong-field approximation and tunneling theory including nuclear motion," *Physical Review A,* vol. 71, no. 2.

[10] Hoffmann, R. 1971, "Interaction of orbitals through space and through bonds," *Accounts of Chemical Research,* vol. 4, no. 1, pp. 1-9.

[11] Streitwieser, A., *Molecular orbital theory for organic chemists*, Wiley, 1961.

[12] Petr Klán & Wirz, J. *Photochemistry of organic compounds from concepts to practice*, Wiley, 2009.

[13] Klessinger, M. & Michl, J., *Excited States and Photochemistry of Organic Molecules*, Wiley-VCH, 1995.

[14] Franck, J. & Dymond, E.G. 1926, "Elementary processes of photochemical reactions," *Transactions of the Faraday Society,* vol. 21, no. February, pp. 536.

[15] Condon, E. 1926, "A Theory of Intensity Distribution in Band Systems," *Physical Review,* vol. 28, no. 6, pp. 1182-1201.

[16] Condon, E. 1928, "Nuclear Motions Associated with Electron Transitions in Diatomic Molecules," *Physical Review,* vol. 32, no. 6, pp. 858-872.

[17] Boyd, R.W., *Nonlinear optics,* Academic Press, 2003.

[18] Shankar, R., *Principles of quantum mechanics,* Plenum Press, 1994.

[19] Liboff, R.L., *Introductory quantum mechanics,* Addison-Wesley, 2003.

[20] Zeng, T., Fedorov, D.G. & Klobukowski, M. 2010, "Multireference study of spin-orbit coupling in the hydrides of the 6p-block elements using the model core potential method," *Journal of Chemical Physics,* vol. 132, no. 7, pp. 074102.

[21] El-Sayed, M.A. 1963, "Spin-Orbit Coupling and the Radiationless Processes in Nitrogen Heterocyclics," *Journal of Chemical Physics,* vol. 38, no. 12, pp. 2834.

[22] Eland, J.H.D., *Photoelectron spectroscopy: an introduction to ultraviolet photoelectron spectroscopy in the gas phases,* Butterworths, 1984.

[23] Palmer, M. & Walker, I. 1991, "The Electronic States of the Azines .5. Pyridazine, Studied by Vuv Absorption, Near Threshold Electron Energy-Loss Spectroscopy and *ab initio* Multireference Configuration-Interaction Calculations," *Chemical Physics,* vol. 157, no. 1-2, pp. 187-200.

Chapter 5

Experimental design

Many considerations must be taken into account when designing an experiment, and this chapter is dedicated to describing these considerations. Topics include a description of the laser systems, the vacuum chamber, the ion mass spectrometer, the avoidance of the focal volume effect, examples of experimental faults that can cause defects in the data, and a description of the fully-automated LabVIEW program which controls the experiment.

5.1 – Laser system

The laser system used in our experiments consists of four separate units that ultimately produce ultrashort, high-intensity pulses. A schematic of the system is presented in Fig. 1. The first stage of the system is a pump laser (Spectra-Physics Millennia Vs J) that emits continuous-wave laser radiation at a wavelength of 532 nm, produced by frequency doubling 1064 nm radiation produced from a diode-pumped Nd:YVO_4 crystal.

The second unit in the setup, pumped by the output of the Millennia, is a Spectra-Physics Tsunami mode-locked Ti:sapphire oscillator, which is capable of producing sub-100 fs pulses at a wavelength of 800 nm and a repetition rate of 80 MHz. Each pulse contains ~9 nJ of total energy. This output of the oscillator is used to create amplified pulses using chirped pulse amplification (CPA) [1].

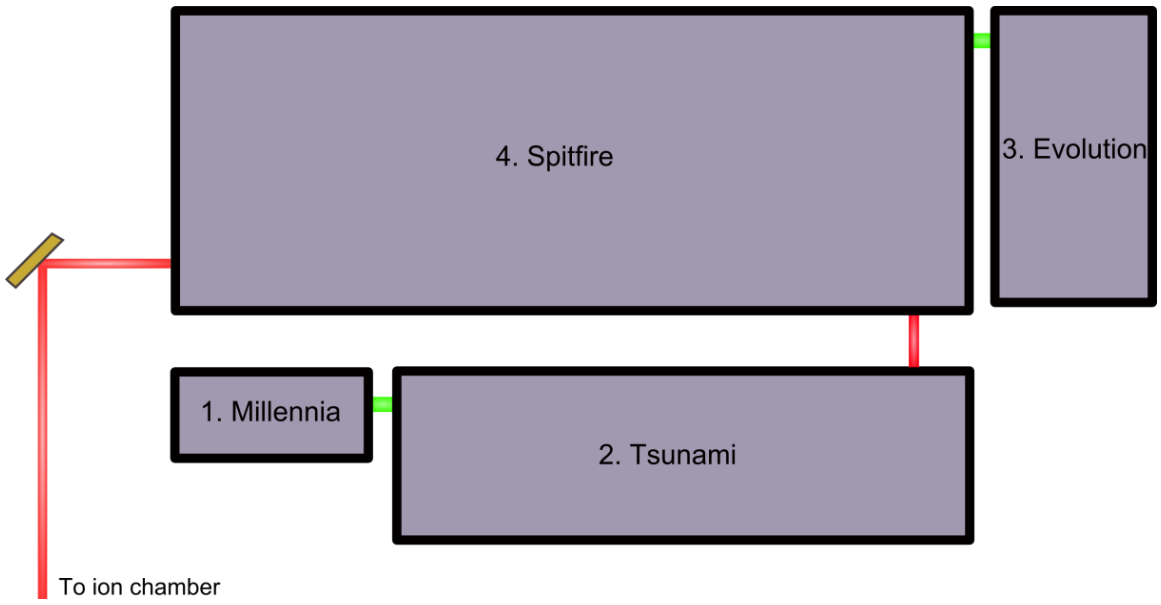

Figure 1 – Diagram of the laser system. The outputs of the Evolution and Tsunami combine in the Spitfire to produce amplified 50 fs, 800 nm pulses at 1 kHz.

The amplifier (a Spectra-Physics Spitfire Ti:sapphire amplifier, unit 4 of the laser system), also requires the input of a pump laser to create population inversion in its two Ti:sapphire crystals. The pump laser for the Spitfire, the third unit in the setup, is a Spectra-Physics Evolution-30: a diode-pumped Nd:YAG laser that emits 527 nm, 200 ps pulses at 1 kHz. The typical output power of the Evolution is 17 W.

One important problem to circumvent in the amplification of ultrashort pulses is the damage that such amplified pulses can do to the sensitive optical devices required for amplification. The solution to this problem is the driving force behind CPA [2], wherein the system stretches the pulses in time before amplification. Fig. 2 shows a diagram of the Spitfire system. The upper-left region is the stretcher, where the pulses are chirped in time. This chirping involves temporally dispersing the spectrum of the pulses by allowing different wavelengths to travel different optical path lengths. This is done in the Spitfire through the use of a grating (1200 lines/mm, top center of Fig. 2). The stretched pulse is

then directed into the regenerative amplifier (bottom of Fig. 2). At a rate of 1 kHz, pulses are selected by a Pockels cell to oscillate through the regenerative cavity, gaining energy on each pass through stimulated emission in a Ti:sapphire crystal (red box, bottom center of Fig. 2) pumped by the Evolution-30. When the pulse energy is at a maximum, a second Pockels cell picks the pulse out of the regenerative cavity and sends it into the double-pass amplification stage in the second Ti:sapphire crystal (upper red box). This amplification stage typically increases pulse energy to ≈3 mJ (compared to 9 nJ from the input beam).

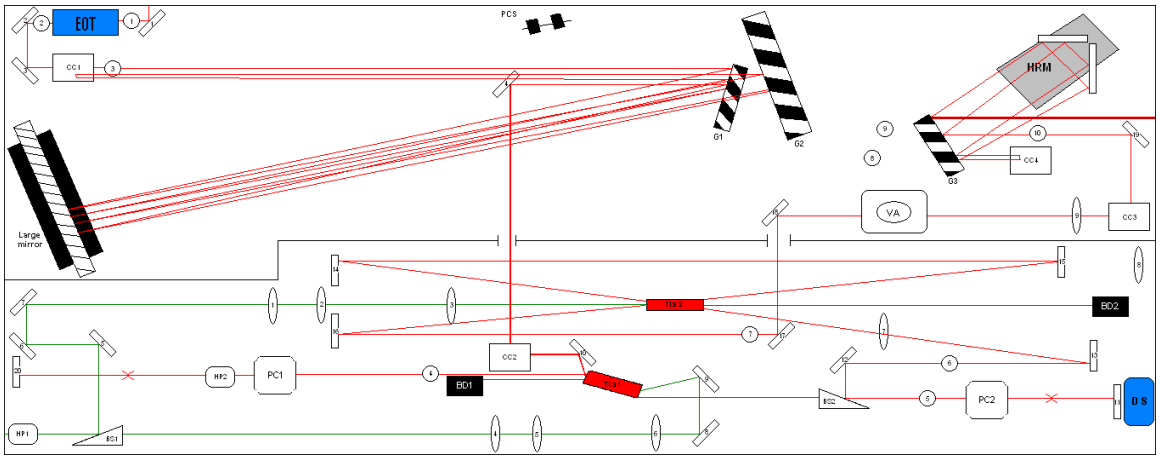

Figure 2 – Schematic of the interior of the Spitfire regenerative amplifier. The stretcher (upper left) increases the temporal width of the pulses. The laser is then fed into the amplifier (bottom half) which amplifies the pulses and selects one every millisecond. This output is then introduced to the compressor (upper right) which recompresses the beam to ~50 fs. Credit to David Foote for preparing the schematic.

The final stage is a recompression of the pulses to ~50 fs, which occurs in the upper-right region of Fig. 2. The pulses are compressed in time at the expense of some of the pulse energy gained in the amplification stage. The final pulses are typically 800 nm in wavelength, 50 fs in duration, with pulse energy of up to 2.4 mJ per pulse. A half-wave plate (labeled "VA" in the compressor in Fig. 2) inserted just before the compressor allows variable attenuation of the final output by a factor of approximately 30.

5.2 – Ionization Chamber

The final output of the laser system is directed into an evacuated stainless steel ionization chamber. This ion chamber is connected via a small opening to another evacuated chamber, the time-of-flight (TOF) tube. The acceptance slit joining the two chambers (15×500 μm) is the only open connection between the two. Both chambers are kept at a low pressure (background pressures for both are less than 10^{-8} mbar) through the use of two turbomolecular pumps which are backed by a rotary pump. Immediately prior to entering the ionization chamber, a focusing lens (UV fused silica, plano-convex with a nominal focal length of 22.7 cm for 800 nm radiation) is placed in front of the beam so that the focus lies directly in front of the small acceptance slit connecting the ionization chamber and the TOF tube. The beam waist at the focus is estimated to be approximately 38 μm. The distance from the laser focus to the acceptance slit is typically about 2 mm, while the acceptance slit and the repeller plate potential (described in Section 5.3) are separated by 3 mm.

The acceptance slit was made by a laser-etching process identical to that described in [3] but with only one movable axis controlled by a stepper motor on a translation stage. Titanium plates (1×2.5 cm, thickness 50 μm) were chosen to avoid magnetic fields and to fit the slit assembly. One such plate was treated as a test target to determine the ideal parameters, namely stepper motor speed and laser power. The plate onto which test patterns were etched can be seen in Fig. 3 (**a**). The resulting slits were photographed under a microscope (magnified between 5 and 50 times) and calibrated to pictures of a test resolution target (Thorlabs R3L3S1P). To optimize the smoothness of the slit while maintaining widths on the order of a few μm, it was found that

approximately one second of delay between 2.5 μm steps with laser pulse energies of ~15 μJ produced the best slits. These parameters were then applied to blank plates, and a single slit was burned into several of these blanks. The slit chosen for use in the experiment, seen in Fig. 3 (**b**), was found through image analysis (also similar to the analysis in [3]) to have width 13.0 ± 1 μm and length 500 μm. Due to the uncertainty in width and deviation from a straight line along the length, we claim no better than 15×500 μm resolution from the slit, which gives us adequate intensity resolution, as will be discussed in Section 5.4.

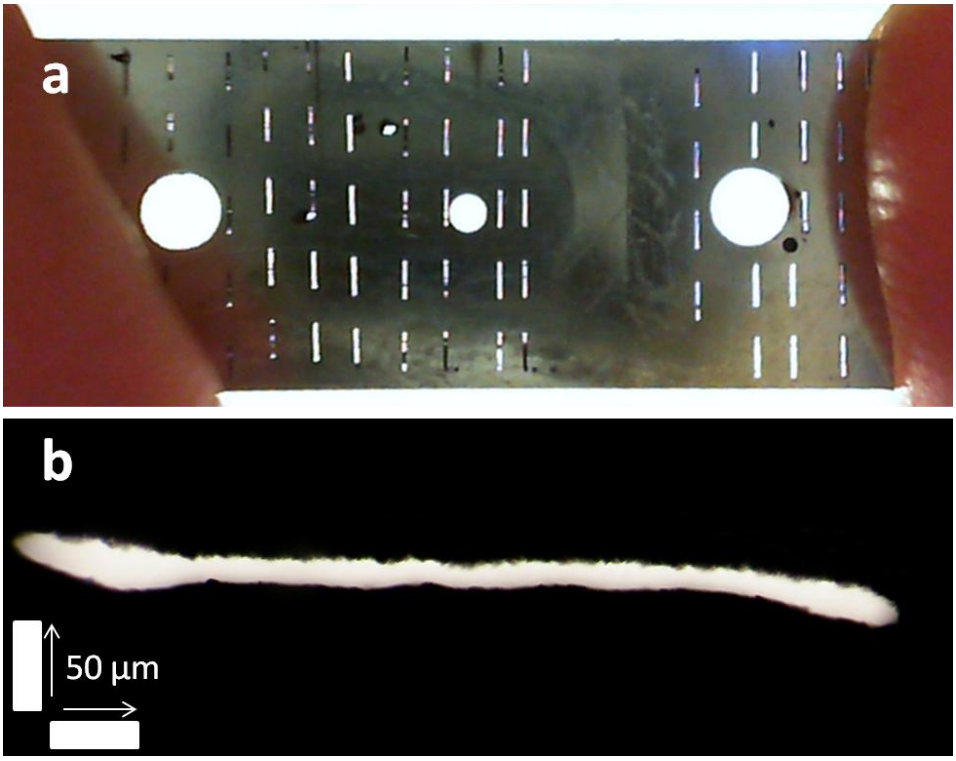

Figure 3 – Acceptance slits. Parameters for laser-etching the acceptance slit were determined empirically by burning a series of slits into a blank titanium plate (**a**). Optimal parameters were then used to burn a single slit into blank plates, one of which (**b**) was chosen as the acceptance slit for the experiment.

A leak valve attached to the side of the ionization chamber is used to introduce molecular vapors into the ionization chamber. The chamber's vapor pressure is typically

adjusted via the leak valve to ~10^{-7} mbar for experiments, which is an optimal pressure to maximize count rates while minimizing pressure-related effects in the TOF data (discussed further in Section 5.5).

5.3 – Time-of-flight ion mass spectrometer

Ions are sent from the chamber into a reflectron-type TOF ion mass spectrometer, which is divided into several distinct regions that govern the trajectories of the ions toward a double multichannel plate (MCP) detector. In order to determine an equation for the total TOF of a single ion, we must consider the forces acting on the ion in each region. The first region to be considered is the acceleration region, which is in between the repeller (at $V_r = 1530\ V$) and the acceptance slit (grounded), separated by distance d_r All these distances and potentials are labeled in Fig. 4. Due to the varying potential in this region, ions experience acceleration equal to $a_r = \left(\frac{qV_r}{d_r}\right)\frac{1}{m}$, where q is the charge of the ion and m is its mass. Using basic kinematics one can find the time that the particle spends in the acceleration region, assuming the initial velocity to be zero[†]:

$$t_a = \sqrt{2d_0 a_r} = \sqrt{\frac{2md_0 d_r}{V_r q}} \quad \textbf{(5.1)}$$

where d_0 is the distance from the acceptance slit that the ion was created. From this, the velocity at the slit is

$$v_a = a_r t_a = \sqrt{\frac{2V_r q d_0}{d_r m}}. \quad \textbf{(5.2)}$$

[†]Initial thermal velocities in the focus are not strictly zero, but are negligible (~100 m/s) in comparison to the velocity after acceleration (~10^5 m/s). Thermal velocities result in a small spread in the detection times (< 1 ns), but do not significantly affect the trajectory.

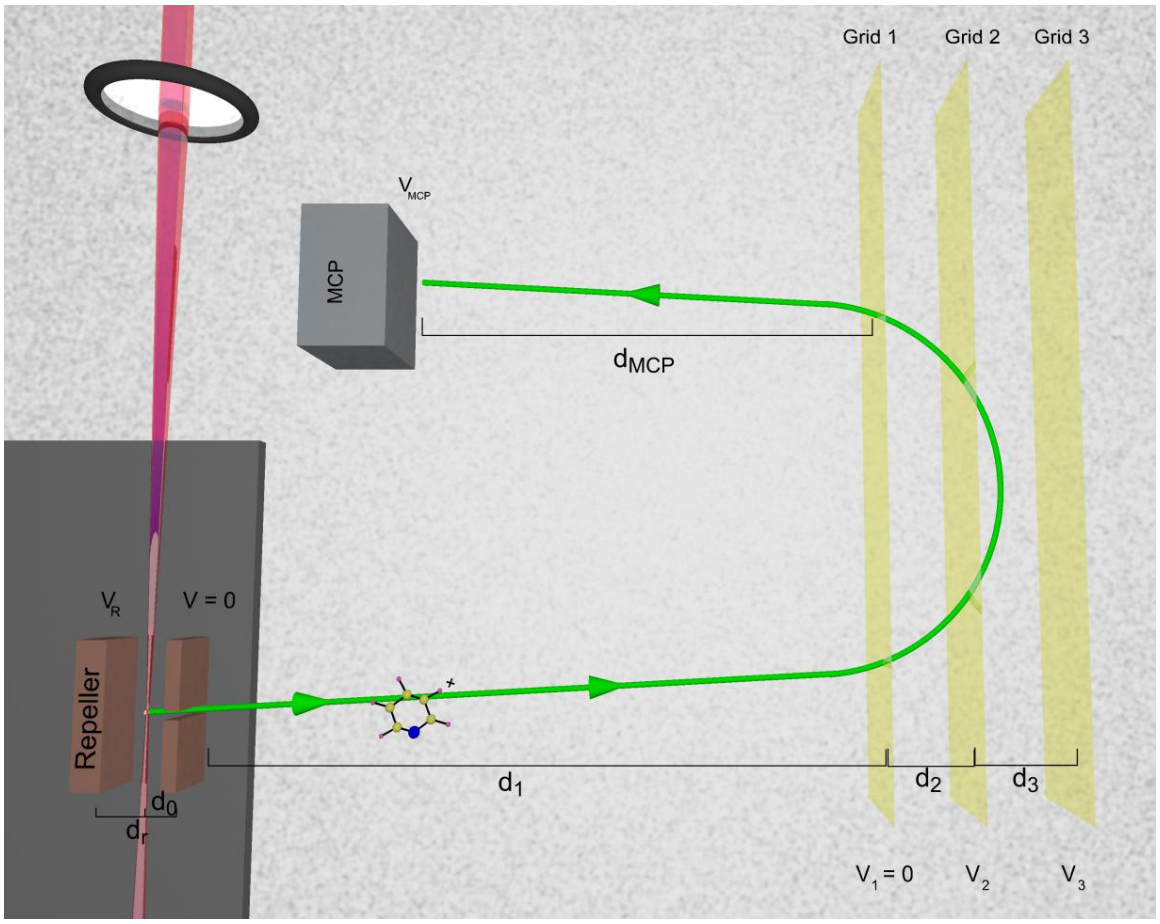

Figure 4 – Schematic of the time-of-flight mass spectrometer. Distances and potentials labeled here will be used throughout the remainder of the work. Ions are accelerated by the repeller into the spectrometer, where mesh grids held at specified voltages guide the ions toward a multichannel plate detector.

After leaving the acceleration region, the ion enters a region with no electric field, called the field-free drift region (of length d_1 as notated in Fig. 2). Because there is no applied force, the velocity remains unchanged, and the total time spent in this region is

$$t_1 = \frac{d_1}{v_a}. \tag{5.3}$$

After this, the ion crosses a mesh grid that is held at ground potential. It now enters the first deceleration region, so called because the potential difference between grid 1 and grid 2, held at $V_2 > 0$, creates a force resisting the forward motion of the ion. For this region, of length d_2, the total time is given by the equation

$$d_2 = v_a t_2 + \frac{1}{2} a_2 t_2^2 \Rightarrow t_2 = \frac{v_a - \sqrt{v_a^2 - 2d_2|a_2|}}{|a_2|}. \quad \textbf{(5.4)}$$

We can substitute $a_2 = \frac{F}{m} = \frac{(V_1 - V_2)q}{d_2 m}$ into the above equation to find the time in the first deceleration region in terms of known voltages and distances. The velocity at the second grid is given by

$$v_2 = v_a + a_2 t_2 = v_a - v_a + \sqrt{v_a^2 - 2d_2|a_2|} = \sqrt{v_a^2 - 2d_2|a_2|}. \quad \textbf{(5.5)}$$

This velocity will be smaller in magnitude than v_a, since the ion is decelerating. After it reaches the second grid with this velocity, the ion enters the second deceleration region. In this region the ion reaches its turning point. The time spent in this region before the ion's velocity reaches zero is

$$t_3 = \frac{v_2}{|a_3|} = \frac{m d_3}{(V_3 - V_2)q} v_2. \quad \textbf{(5.6)}$$

After the ion comes to a halt in the second deceleration region, the electric field that had retarded its motion now accelerates the ion in the opposite direction. It travels back through the deceleration regions, taking an additional time $t_2 + t_3$ to do so. Next it enters a second field-free drift region of length d_{MCP} with velocity v_a (by symmetry), and so the time it spends in this region is

$$t_4 = \frac{d_{MCP}}{v_a} \quad \textbf{(5.7)}$$

After this drift region, it encounters a MCP which counts and records the ions. In summary, the total TOF is the sum of the individual times (remembering to count t_2 and t_3 twice, since the ion travels through them as it decelerates, and again as it is accelerated towards the detector):

$$TOF = t_a + t_1 + 2t_2 + 2t_3 + t_4 \quad \textbf{(5.8)}$$

$$TOF = \frac{v_a}{a_r} + \frac{d_1 + d_{MCP}}{v_a} + \frac{2md_2}{qV_2}\left(v_a - \sqrt{v_a^2 - \frac{2qV_2}{m}}\right) + \left(\frac{2m}{q}\right)\left(\frac{d_3}{V_3 - V_2}\right)\sqrt{v_a^2 - \frac{2qV_2}{m}}. \quad \textbf{(5.9)}$$

Substituting for terms that exclusively involve experimental parameters gives

$$TOF = \sqrt{\frac{m}{q}}\{f(V_r, V_2, V_3, d_r, d_0, d_1, d_2)\} \quad \textbf{(5.10)}$$

for which the mass and charge of the ion are a prefactor, and the shape of the curve depends exclusively on experimental parameters with the exception of the initial distance from the slit d_0. A MATLAB [4] program which calculates the TOF curve for a variety of conditions (including those presented in Chapter 8) can be found in Appendix A.2.

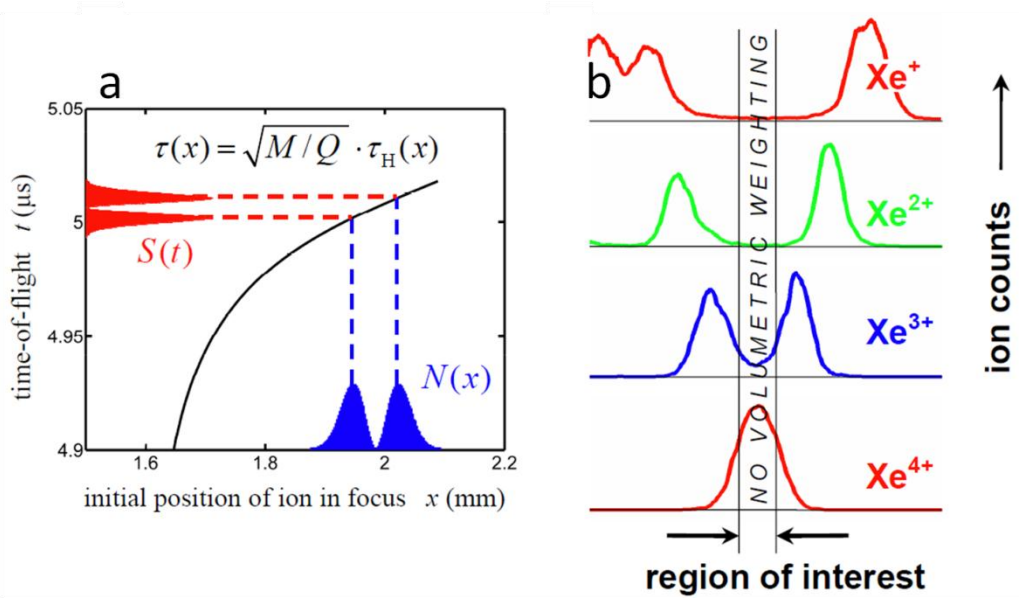

Figure 5 – Tuning the time-of-flight curve. Our mass spectrometer can be tuned (by adjusting the voltages of the reflecting grids) to create a region of the laser focus for which there is an approximately linear dependence of the time of flight on the ion's original distance from the acceptance slit. This results in a direct mapping of the distribution of the ions' position in the focus ((**a**), blue) onto the time of detection ((**a**), red). As a result, we can avoid counting ions which are born at different regions of space (**b**), and therefore different intensities, to give our experiment enhanced intensity resolution. It is this resolution which allows our experiment to have unique precision.

Tuning V_2 and V_3 relative to V_r allows the manipulation of the TOF curve as we see fit. When desired, we can tune the curve so that all ions with the same mass-to-charge

ratio arrive at the detector at the same time (within ~20 ns) referred from here on as *focused in time*. Alternately, we can tune the voltages so that each mass-to-charge ratio forms a distinct peak, but with a direct mapping of the initial distance from the acceptance slit mapped onto the TOF.

Fig. 5 (**a**) shows this mapping of the ion's initial position onto the TOF spectrum. The key is to tune the grid voltages to create a region on the TOF curve for which the slope is approximately linear; if the curve deviates from linear, the spatial distribution will be distorted and information about the initial position of the ion may be lost. To estimate the linearity of the TOF curve, the TOF was calculated as a function of distance d_0 from the acceptance slit. Results are seen in Fig. 6 for the TOF curve when focused in time (**a**) and spatially resolved (**b**).

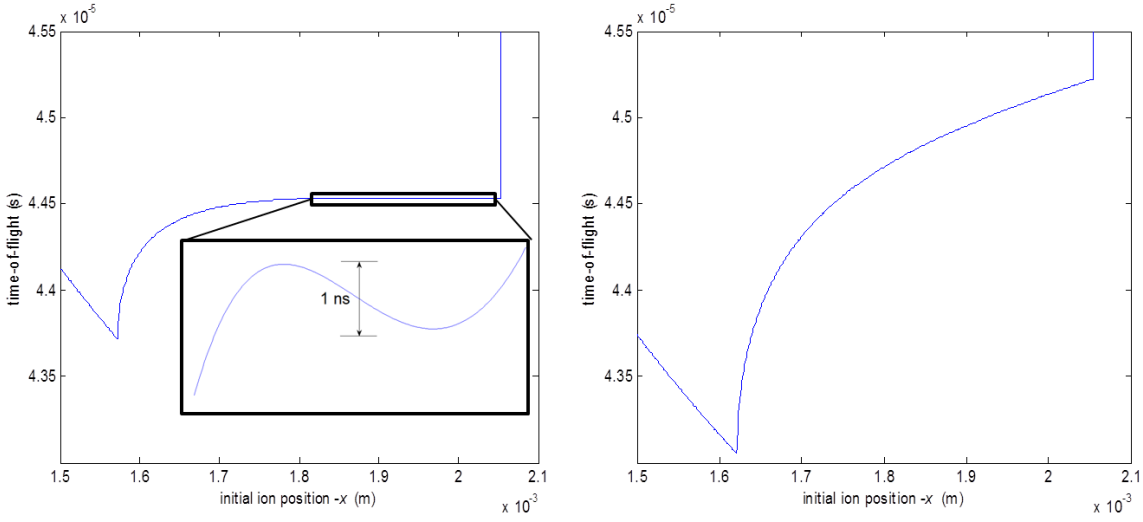

Figure 6 – Focused in time and spatially-resolved TOF. Depending on the voltage settings, our spectrometer can be tuned such that ions from all over the focus land at the same time of flight (left panel), which is known as *focused in time*. Alternately, the curve can be tuned to a linear dependence (right panel) which maps the shape of the spatial ion distribution in the focus onto the time axis.

The region of each curve relevant to fitting is between 1.95 and 2.05 mm away from the slit; this is where the laser is focused in the experiment, which is determined by moving the focus away from the slit until the peaks are no longer reflected toward the detector (as their kinetic energy is greater than the potential V_3. We operate just inside this distance, as this is the region of the TOF curve which most accurately correlates initial position with detection time.

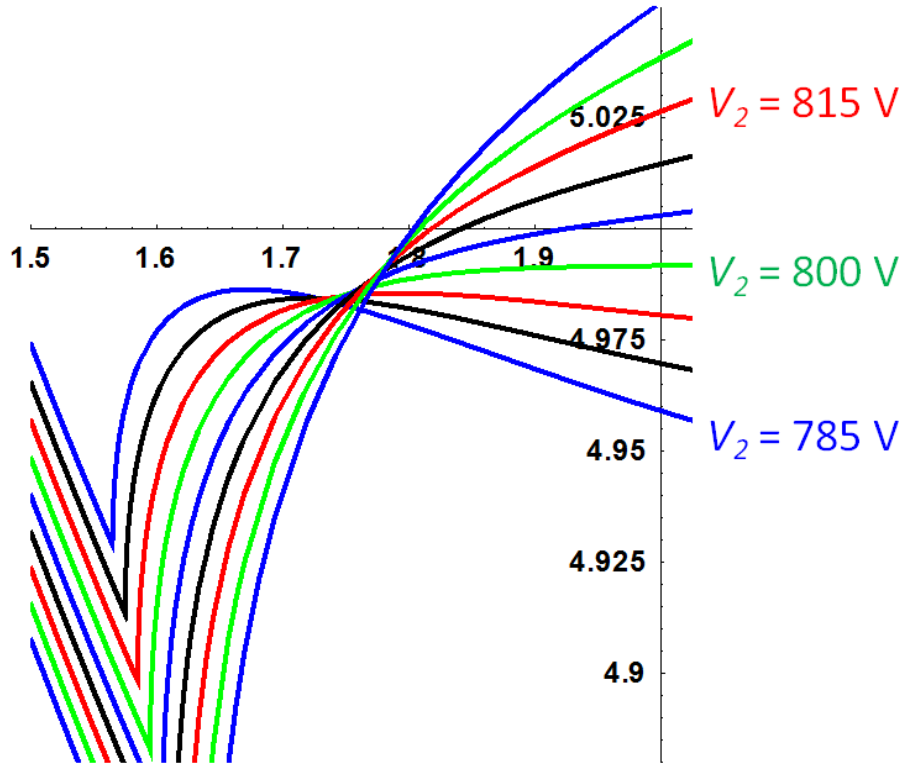

Figure 7 – Focusing and defocusing the TOF curve. The voltage $\boldsymbol{V_2}$ can be tuned so that the TOF as a function of initial ion position has a negative, negligible, or positive slope. When ions are created in a region of the focus where the TOF curve is linear, the spatial distribution of ions in the focus is mapped onto the TOF.

Because we rely on this correlation, it is important to quantify the linearity of the TOF curve. Fig. 6 shows that the focused-in-time curve has what appears to be a small cubic contribution on the "flat" region; if this is magnified in a spatially-resolved TOF

curve it could distort our results. The slope is tuned by changing V_2; an example of this tuning is shown for a hydrogen ion in Fig. 7. Simulations show that even for heavy ions (not only the TOF but also the width of each peak scales as $\sqrt{\frac{m}{q}}$, so the deviation from the linear is greatest for large masses), the deviation is no more than ~1 ns in TOF. As such, the slope is effectively linear within the sensitivity of the experiment.

If the space-to-time mapping is good, what value of V_2 should be used? While the deviation from a linear slope can be minimized for some value of V_2, in practice we set the voltage such that the highest-mass ion peak (which has the greatest peak width) is nearly overlapping its neighboring peak. This spreads the peaks over a large range in time, which enhances our spatial resolution while minimizing counting errors (discussed in detail in Section 5.5). Typical settings for V_2 are 25-30 V greater than the focused-in-time setting ($V_2 = 802$ V).

5.4 – The focal volume effect

Intense-field studies which require a laser to be focused to reach their necessary peak intensities commonly suffer from the *focal volume effect*. This effect and its solutions are discussed in this section.

5.4.1 – The problem

To study the strong-field dynamics of atoms or molecules, intensities exceeding ~10^{12} W/cm^2 are typically needed [5]. To achieve such high intensities, a laser beam of ultrashort (fs) pulses is focused to an area of a few hundreds of μm^2 in cross section. However, near the focus there is a gradient in the intensity. If ions are collected from a large region comparable to the size of the focus, as is common practice [6-8], an experiment will have a poorly-defined intensity; this is known as the *focal volume effect*

[9]. This can be particularly troubling in identifying the underlying mechanisms of ionization. As detailed in Section 2.3, yields of multiphoton processes in the ideal case increase with intensity as $Y \propto I^N$ with N the number of photons in the process [10], but rates of tunneling ionization have a different intensity dependence, as does a resonance-enhanced process, or sequential and nonsequential processes. As an experiment collects ions created in a distribution of intensities, it is collecting ions from volumes containing different physical processes. As such, a target's photodynamics often remains hidden.

As the beam power is increased to generate intensities high enough to saturate the ion yield, the yield increases as $Y \propto I^{3/2}$ without regard for the ionization process at work [11] for a Gaussian beam focus. This relation occurs solely due to the growing size of the interaction volume where the fields are strong enough to ionize the target. A variety of methods [12-22] have been developed to eliminate the focal volume effect, though methods such as intensity-selective scanning and intensity-difference spectra involve deconvolution of the data. Such deconvolution introduces uncertainties based on both the method and assumptions of experimental conditions; this emphasizes the need for experiments to obtain resolution without manipulating the data. Fortunately, some of these experiments have been quite successful: they count ions originating from a well-defined detection volume only, and without the need for deconvolution [20,22]. The aim of this section is to quantify the level of intensity resolution present in such a measurement. Further, we will explore the benefits and drawbacks of setting the detection volume outside the center of the focus.

5.4.2 – Three-dimensional spatial resolution

Mass spectrometers are often tuned such that ions from all positions d_0 in the focus are detected at the same TOF (the focused-in-time case) to give optimal resolution between peaks of different mass. Our system, as mentioned above, is deliberately tuned to create a linear dependence of the TOF on the initial position of the ions in the focus. As a result, the spatial distribution in the focus is mapped directly onto the TOF spectrum. A full description of this approach is found in Ref. [20], and a sample analysis program which is used to select the detection volume can be found in Appendix A.3.

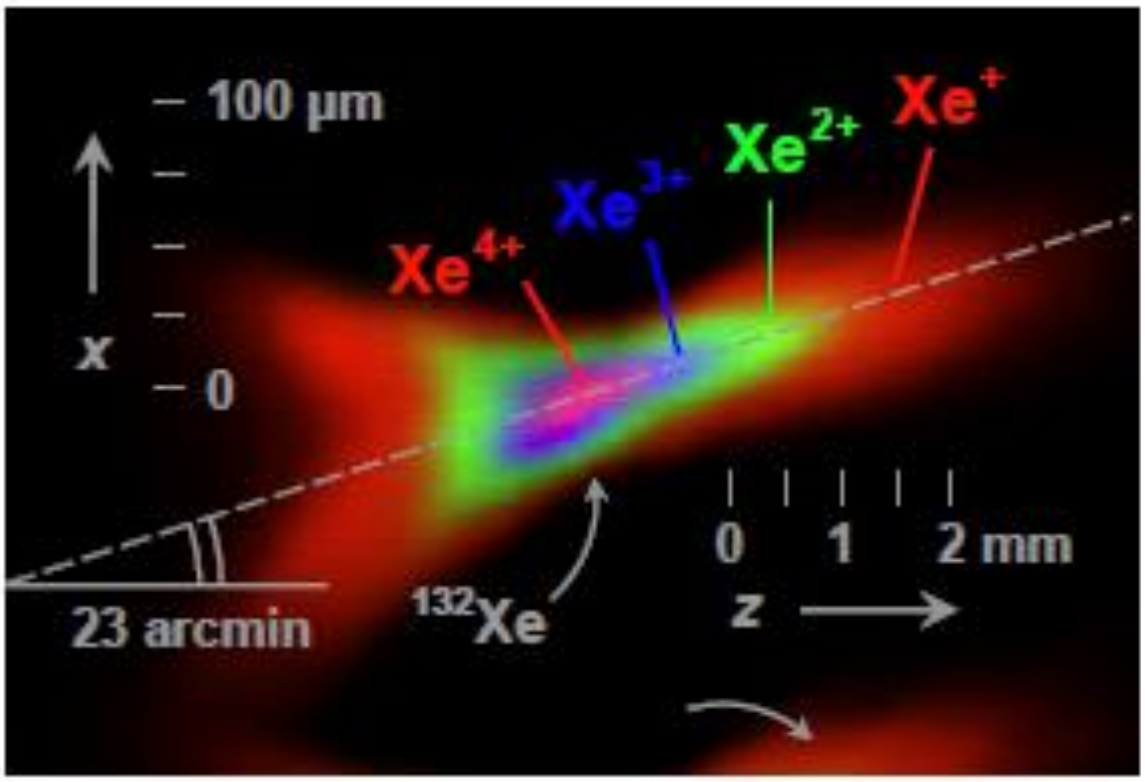

Figure 8 – Spatial ion distributions of xenon. These ionic yields, taken from Ref. [20], show the three-dimensional spatial resolution of the ion yields. Mimicking the shape of the laser's intensity distribution as it focuses and defocuses (propagating from left to right), regions of higher intensity in the center produce ions of higher charge.

The spatial resolution achieved with this technique can be seen in the yields of multiple charge states of xenon in Fig. 8. As an example of the importance of three-

dimensional resolution of the ion yield, Fig. 9 shows an ion yield of benzene as a function of intensity (red squares) as well as another group's result [8] taken without the 3D resolution. The structures we observe (straight lines, kinks, and drops) would have escaped observation when, following common practice, ions had been recorded from the entire focal region, known as the full view (FV) approach. For the purpose of direct comparison, our data is multiplied by a constant factor of ½ in intensity to compensate for differences in intensity calibrations between different groups' data. Such a shift does not distort the results other than to displace the saturation intensity, and is warranted, as it is difficult to determine absolute intensity within a factor of ~2; one must make assumptions about spatial pulse shape, temporal pulse shape, focal conditions, etc., when assigning a peak intensity value to each data point.

Based on our benzene data we have convoluted our data (blue curve) to simulate the yields we would have found if we had used the FV approach; this simulation agrees with the experimental FV data, even overlapping their theoretical curve (dashed curve). The data of Ref. [8], like any using a FV approach, increases without bound at high intensity, though it deviates from the $Y \propto I^{3/2}$ dependence; this deviation likely means their experiment was not truly FV in all three dimensions, though lacking spatial resolution in any one direction (reducing the resolution to 2D) causes a loss of intensity resolution. At the highest intensities, FV data is about three orders of magnitude different from our resolved data, a dramatic discrepancy arising from the different acceptance volume sizes. The single property the FV curves inherit from the resolved curves is their slope for lowest intensities.

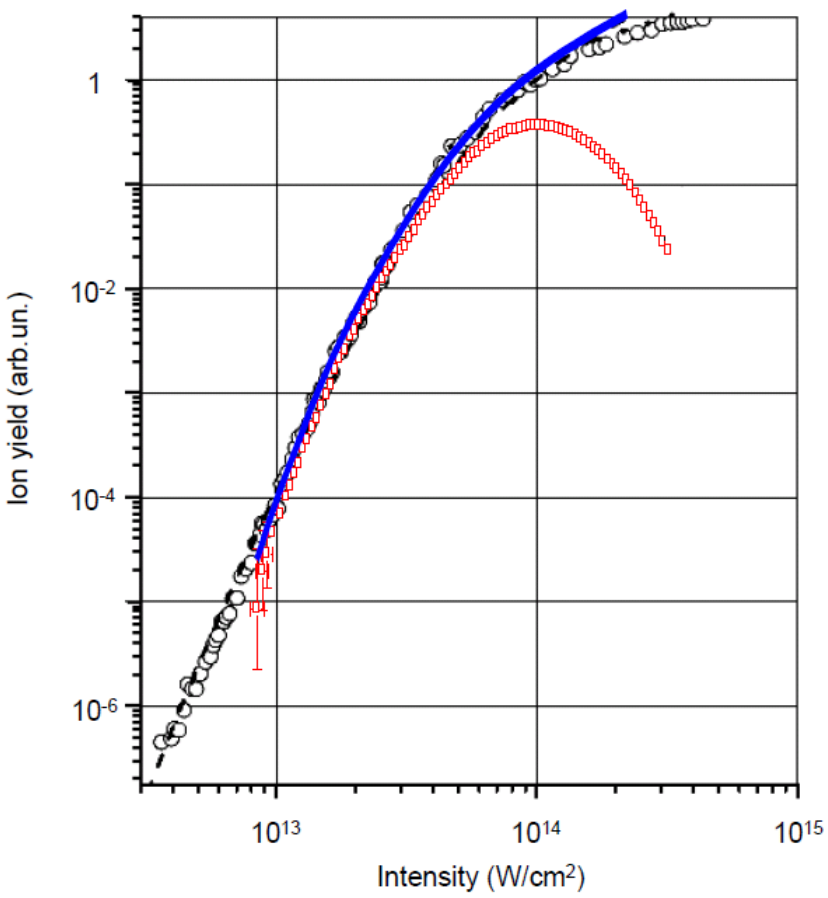

Figure 9 – The effect of eliminating focal averaging. Red open squares: our $C_6H_6^+$ yield as a function of pulse intensity. For comparison we show the results of Ref. [8], where ions were collected from a large region of the focus (full-view, FV): experimental yield (black open circles) and theoretical prediction (black dashed line). The structures in our measured ion yields at ~2×10^{13} W/cm^2 are washed out in Ref. [8] due to integration over the focal volume. Additionally, for intensities beyond ~10^{14} W/cm^2 our ion yield decreases due to competing processes, such as multiple ionization and fragmentation. By contrast, the FV $C_6H_6^+$ yield keeps increasing with a slope of ~3/2, an artifact due to the growing size of the focus. We simulated (blue curve) the FV data by convoluting our own data into a much larger (100×100×2000 μm) acceptance volume. This focal integration washes out our structures.

Because the FV approach has prevented previous works from identifying multiple regions of different integer slopes (a signature of a resonant process as discussed in Chapter 3), we emphasize the importance of excluding the possibility that the kinks in our experimental yields (which, as detailed in Chapter 3, are signatures of a resonant

multiphoton process) are not an artifact of our approach. To do so, Strohaber [23] also investigated the ionization of atomic xenon, in which no such resonant features were expected. The Xe^+ yield does not feature a kink; it rises in agreement with FV results of other groups [24,25]. We conclude our kinks are genuine.

While Fig. 9 represents the differences in the data for the spatially-resolved and FV cases, it is also instructive to simulate numerically the effects of not only the resolved and unresolved cases, but different volumes with resolution so that we can quantify the capabilities of our experiment. We used a MATLAB [4] code to calculate the intensity distribution of a Gaussian beam focus on a cubic grid; this code can be found in Appendix A.4. To mimic our typical experimental setup, a beam waist (1/e full width in intensity) of 50 μm was chosen. With 800 nm pulses, the resulting Rayleigh length [26] is approximately 4.9 mm. Although it does not share the cylindrical symmetry of the beam, we chose a cubic grid (1 μm spacing in all directions) to ensure that each point represented a constant discreet volume with a fixed intensity, and to mimic the conditions of our experimental design. The program sampled intensities from the desired focal region, measuring values from 0 to 1, representative of the fraction of the maximum intensity of the focus $\frac{I}{I_{max}}$. In this way, a histogram was built representing the number of samples (and thus the amount of volume) with a specified intensity according to $V(I_n < I_{n+1}) = \int_{I_n}^{I_{n+1}} \frac{dV}{dI} dI$. These histograms were analyzed to determine the percentage of the total volume $\frac{\Delta V}{V}$ for each intensity interval ΔI.

To emphasize the importance of the three-dimensional spatial resolution, the histograms were compared for the two- and three-dimensionally resolved cases [18]. A detection volume of 15×15×500 μm (15×15 in the transverse directions and 500 in the longitudinal direction) was chosen for the three-dimensionally resolved case to mimic the detection volume used in our typical experimental setup [27]. The two-dimensionally resolved case was simulated for a 15×100×500 μm region so that the unresolved dimension contains nearly all of the focus (approximately 95% of the integrated intensity).

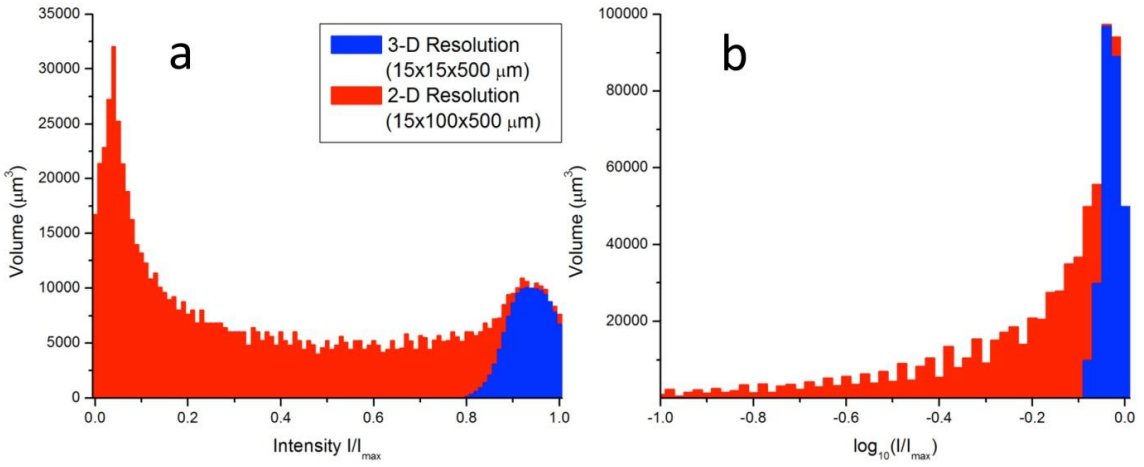

Figure 10 – The effects of three-dimensional spatial resolution. Here we see the amounts of volume containing a given intensity for the two- (red histograms) and three-dimensionally (blue histograms) spatially-resolved detection volumes for linear (**a**) and logarithmic (**b**) intensity axis histograms. The histograms agree from ~90-100% of the maximum intensity, since both regions contain the central focal volume; however, the 2D region also contains lower intensities which are absent in the 3D detection volume.

These histograms can be seen in Fig. 10; the left panel (**a**) plots the volume as a function of intensity, while the right panel, (**b**), plots the volume as a function of the logarithm of the intensity, with the histogram's intensity widths constant on a logarithmic scale. The blue histogram represents the fully three-dimensionally resolved case, and the

red histogram represents the two-dimensionally resolved case. The logarithmic representation is useful because ion yields versus intensity are often plotted in a log-log representation. Near I_{max}, there is a strong correlation between the two; this is because both volumes include the center of the focus. While the 3D volume contains only this center, the 2D case continues to sample other regions, all of which have lower intensity than the center. The volume in the 2D case is stretched out to twice the 1/e full-width along the waist, so nearly the entire width of the beam is sampled. This causes lower intensities to dominate the detection volume. This emphasizes the importance of full 3D spatial resolution of the ion yield: in the 3D case, the entire sampled volume is close to the intensity value claimed in an experimental data point (intensity variation is less than 10% of a decade), whereas the 2D case samples intensities in within a range of at least 25% of a decade. The 3D resolution indeed creates a well-defined intensity such that every ion from the detection volume is more likely to have been created by the same physical process, and this process can be studied without signal contributions from lower-intensity processes [9].

5.4.3 – Simulating the focal volume effect

The aim of these simulations is to quantify the change in intensity resolution which occurs when the detection volume is distorted. The sizes of the chosen detection volumes relative to the focal width of an ideal Gaussian focus are shown in Fig. 11. The boxes representing the regions discussed above are the red (15×100×500 μm (2D)) and white (15×15×500 μm (3D)) boxes. Having established the importance of three-dimensional spatial resolution, we can now explore the results with different sizes of fully 3D resolved regions. One can stretch the region (compared to the white box) along the

direction of propagation (grey box, 15×15×3000 μm), perpendicular to the direction of propagation (yellow box, 50×50×500 μm), or both (pink box, 50×50×3000 μm).

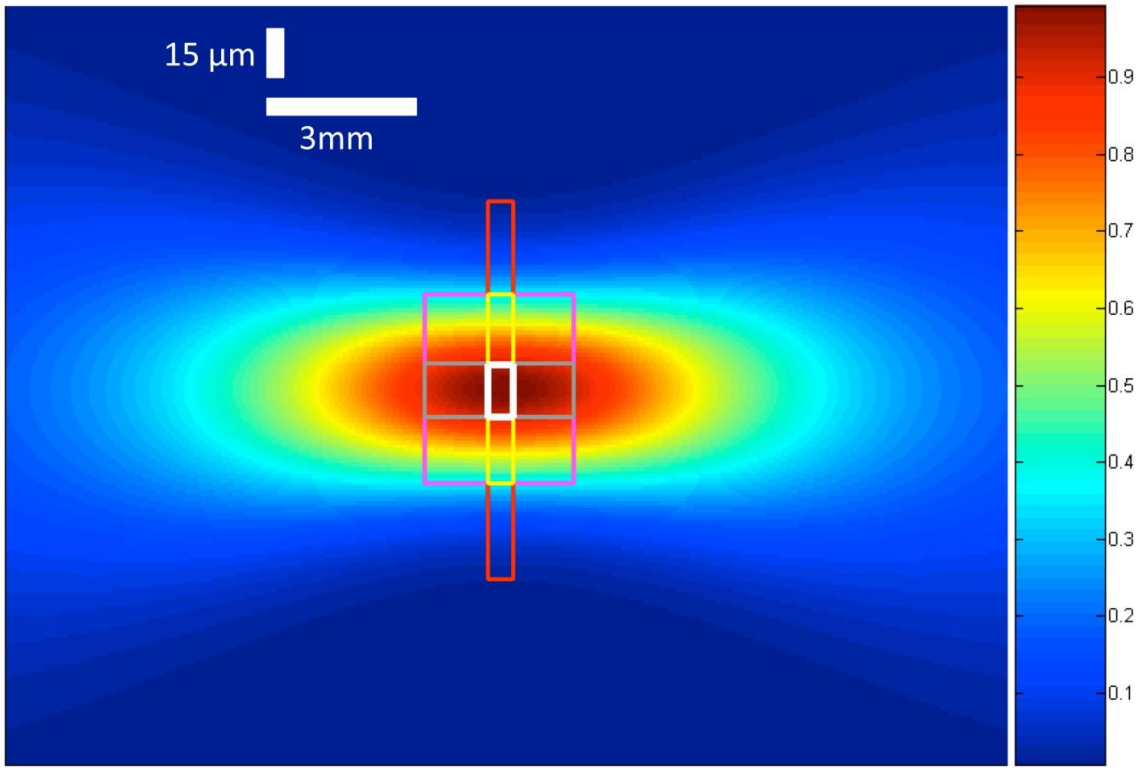

Figure 11 – Different sizes of detection volumes. In the present work we study the intensity distributions contained within detection volumes of 15×15×500 μm (white box), 15×100×500 μm (red), 15×15×3000 μm (grey), 50×50×500 μm (yellow), and 50×50×3000 μm (pink). The magnitude of intensity relative to maximum intensity is represented by the colorscale.

The simulations for each of these differently-sized detection volumes are found in Fig. 12. The four panels indicate the intensity distribution in a detection volume as a function of the longitudinal distance between the center of the volume and the center of the focus. Moving a few millimeters away from the focus can help to stay away from complicating intensity variations. These variations could be caused by possible aberrations (spherical, chromatic), and also from the effect from intrinsic beam

imperfections (e.g. a beam does not have to be Gaussian, the shape of the focus may not be transform-limited, and phasefront imperfections may be present) [26,28,29].

The data represents the volume per unit intensity, $\frac{\Delta V}{\Delta I}$, which can be smoothed to represent $\frac{dV}{dI}$. In Fig. 12 we have plotted the intensities I_α for which $V(I < I_\alpha) = \int_0^{I_\alpha} \frac{dV}{dI} dI = \alpha V_{\text{tot}}$. In other words, the fraction αV_{tot} of the total volume has intensity less than I_α. Consider the two pink curves on each graph: in 45% of the total volume the intensity is less than that given by the lower pink curve (i.e. $V(I < I_{45\%}) = \int_0^{I_{45\%}} \frac{dV}{dI} dI = 0.45 V_{\text{tot}}$), and in 55% of the volume the intensity is less than that of the upper pink curve $V(I < I_{55\%}) = \int_0^{I_{55\%}} \frac{dV}{dI} dI = 0.55 V_{\text{tot}}$. They are shown in the same color to indicate that the two pink curves, as a pair, contain between them the central 10% of the total interaction volume $V(I_{45\%} < I < I_{55\%}) = \int_{I_{45\%}}^{I_{55\%}} \frac{dV}{dI} dI = 0.10 V_{\text{tot}}$: the median ± 5%. The curves represent, from the bottom up, the intensities below which there is 5% of the volume (black), 10% of the volume (red), 25% (green), 40% (blue), 45% (pink), 55% (pink), 60% (blue), 75% (green), 90% (red) and 95% of the volume (black). As a result, the volume between the matching colored pairs is 10 (pink), 20 (blue), 50% (green), 80% (red) and 90% of the total interaction volume (black).

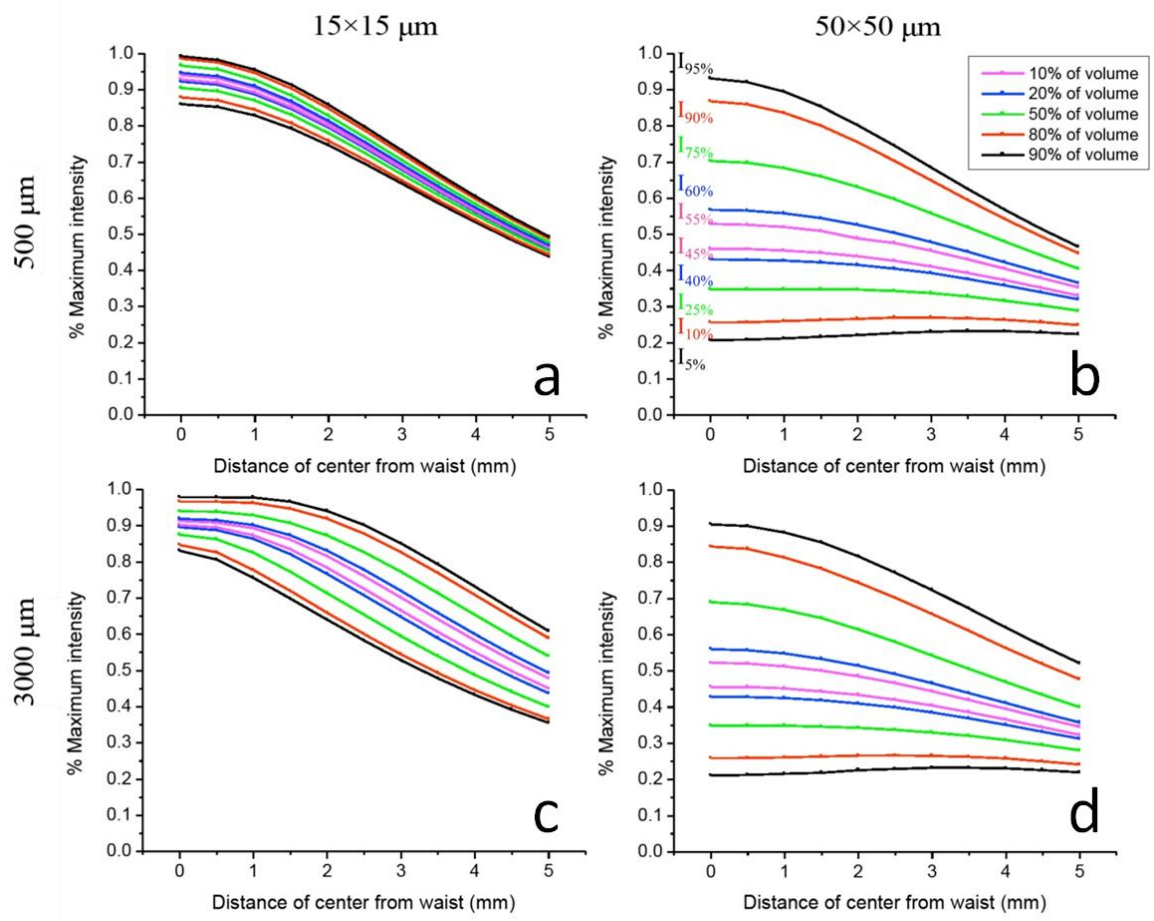

Figure 12 – Isovolume intensity curves of the detection volumes. The data are presented such that the same-colored pairs of curves contain a constant percentage of the total volume, centered on the median. The pairs contain 10 (pink), 20 (blue), 50 (green), 80 (red), and 90 (black) percent of the total volume within the intensities displayed. Smaller volumes contain a narrower range of intensities, and moving the detection region away from the center of the focus along the direction of laser propagation narrows the ranges, though at the expense of peak intensity.

When these cases are analyzed, the effects of the different sizes of detection volumes become evident, and these results are seen in Fig. 12. As each volume is moved far enough away from the focus, the spread in the intensities sampled decreases, but this comes at the cost of peak intensity. The smallest volume, here the 15×15×500 μm region (Fig. 12a), has the narrowest spread in intensities throughout the region, even when sampling the very center of the focus. Stretching the region along the direction of

propagation (as in the 15×15×3000 μm case, Fig. 12c) does not cause much increase in the spreading of intensities, since the 3000 μm length is still smaller than the Rayleigh length. However, stretching the volume perpendicular to the direction propagation (as in the 50×50×500 μm case, Fig. 12b) causes a large distribution of intensities; 90% of the volume ranges between 20.8 and 93.2% of I_{max} with the volume centered at the center of the focus. The spreading decreases considerably as the region is moved away from the center of the focus, since the beam width away from the center increases relative to the detection volume. When the detection volume is stretched in both directions (as in the 50×50×3000 μm case, Fig. 12d), both effects are compounded, though the increase perpendicular to the direction of propagation is seen to be the dominant effect, since the gradients in intensity are much larger in this direction.

While the representation in Fig. 12 helps to visualize intensity distributions for various sizes of detection volumes, it does not necessarily give the best representation of how these varying intensities affect an experiment. Ion counting experiments often present data on logarithmic scales [7,8,14,19,27], as this reveals dynamical information about multiphoton ionization processes [27]. With this in mind, we show in Fig. 13 the same data as in Fig. 12, but this time with a logarithmic intensity axis.

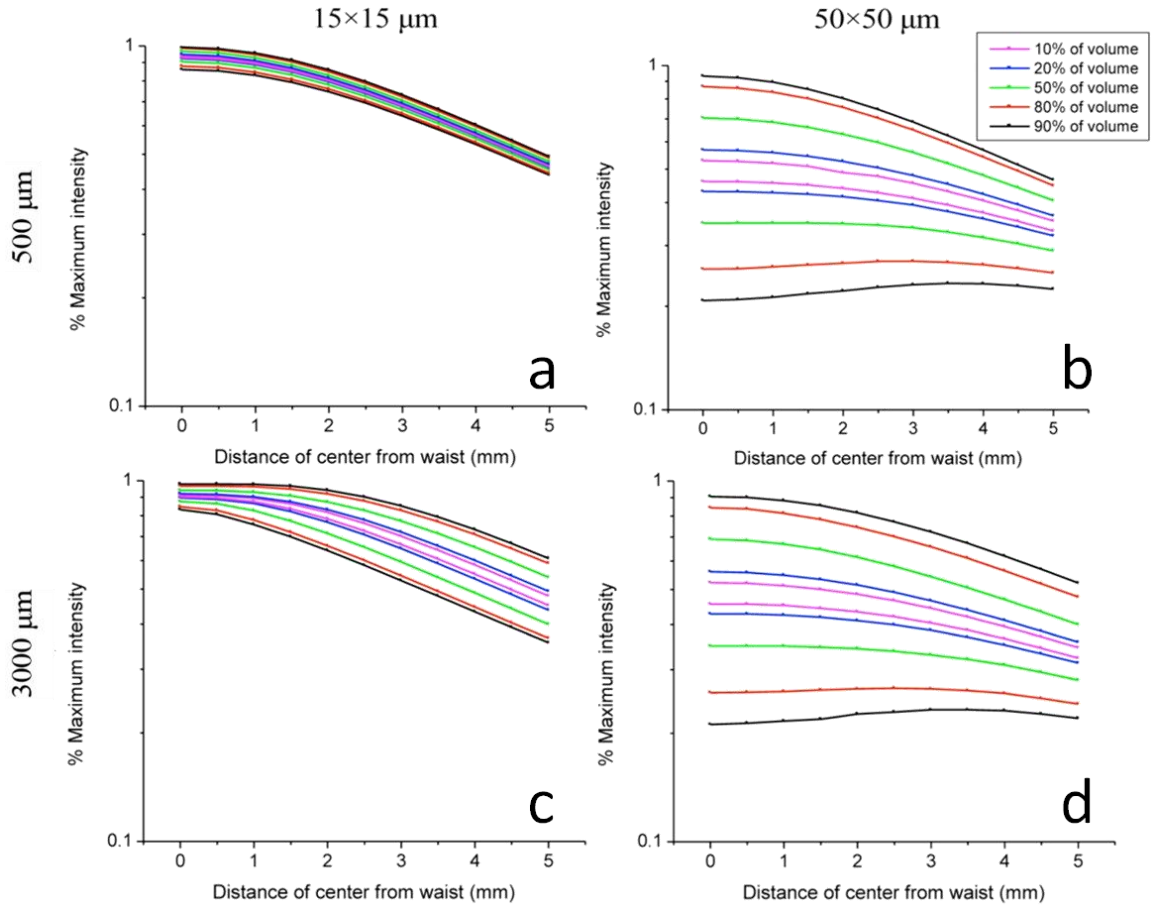

Figure 9 – Isovolume intensity curves of the detection volumes on a logarithmic intensity scale. The same data from Fig. 12 is presented on a logarithmic intensity scale, as this is typically how experimental ion yields are represented. The 15×15×500 µm volume holds an advantage over the others: it maintains its intensity resolution when moved away from the center of the focus. This property makes this small volume superior to the other three volumes we consider here.

This better reflects the effect of the different detection volumes on an experiment. The 15×15×500 µm (Fig. 13a) region is superior to the other volumes in its intensity resolution. Both the 50×50×500 µm (Fig. 13b) and 50×50×3000 µm (Fig. 13d) regions span nearly a full decade along the intensity axis. This represents a formidable issue when ion yields are recorded as a function of what is assumed to be a fixed intensity. The 15×15×3000 µm (Fig. 13c) region has a narrow intensity distribution, but begins to lose

its uniformity beyond ~1 mm outside the focus, spanning ~$1/6^{th}$ of a decade of intensity at 2 mm, and ~$1/4^{th}$ of a decade at a full Rayleigh length. This spoils the advantages of operating a few millimeters away from the focus to avoid focal aberrations (which themselves skew the intensity distribution away from the assumed Gaussian distribution). The 15×15×500 μm region, when plotted on a logarithmic intensity axis, maintains consistent intensity distributions out to a full Rayleigh length (4.9 mm), spanning only $1/15^{th}$ of a decade of intensity throughout the full Rayleigh length while maintaining higher average intensities than the larger detection volumes.

5.5 – Experimental errors and their causes

There are many experimental issues that can cause artifacts in the data which are unrelated to the molecular photodynamics. Discussed in this section are a selection of such issues and their respective effects on our measurements. For the purposes of this section, effects which are typically subtle will be shown in exaggerated cases for the sake of increased clarity.

5.5.1 – Pressure variations

To ensure accuracy in the ion yields, the number of neutral molecular targets should remain constant. However, many of the aromatic molecules we study are measured to have vapor pressures which vary throughout the course of a measurement (as much as a factor of two over a few hours). While the cause of this variability is not fully understood at present, it is not an aberration; measurements of count rate and pressure for constant laser intensity show direct correlation. As such, it is vital to track the pressure while measuring ion yields, as the yield depends directly on the number of neutral targets. Further, at pressures greater than ~10^{-6} mbar so many ions may be created that damage to

the counting card (or less likely, the MCP) becomes a serious risk (the counting card has no internal protection against large voltage signals), so the pressure must be monitored.

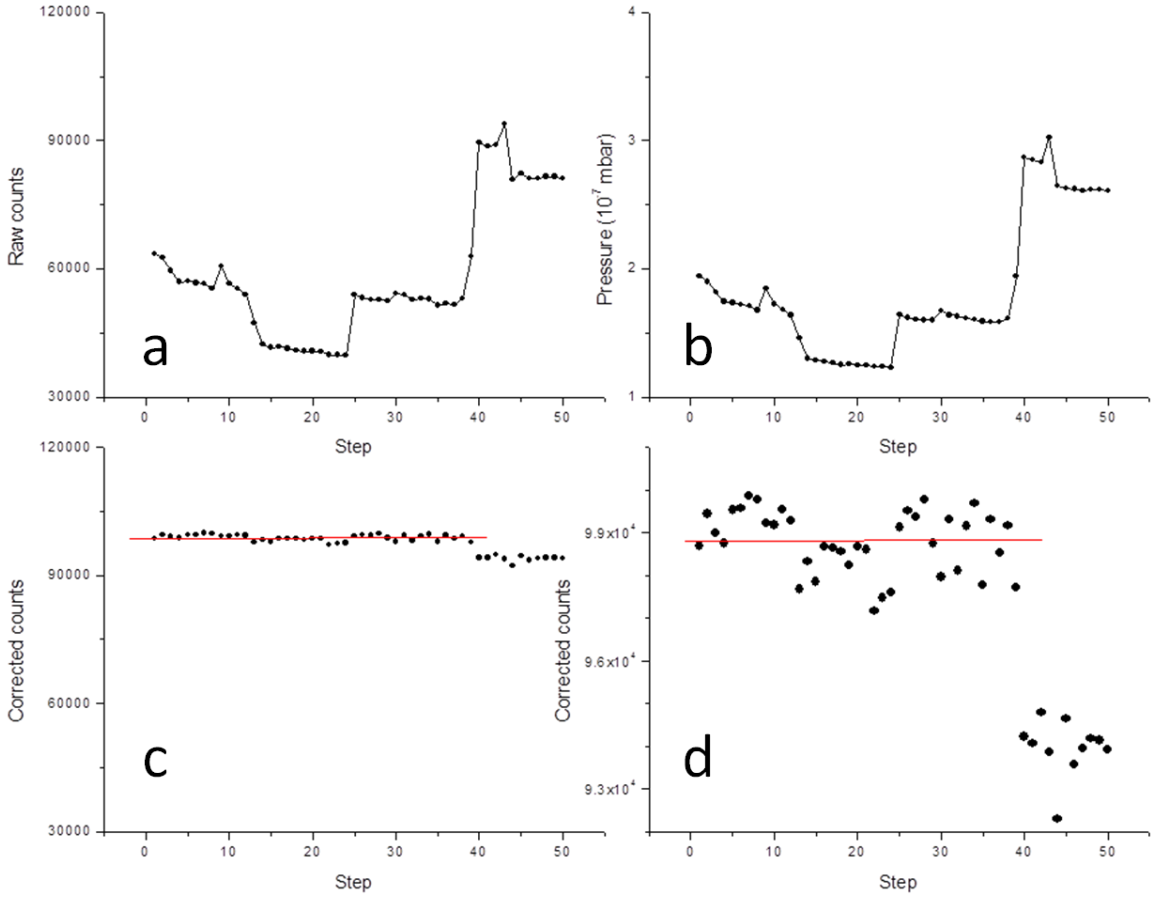

Figure 10 – Normalizing for pressure fluctuations. Changes in the count rate (**a**) are the direct result of changes in molecular vapor pressure (**b**) as long as variations are small. The normalized count rate is shown on the same scale (**c**) and zoomed in (**d**) for clarity.

To correct for an unstable pressure during a measurement, the pressure is averaged over the runtime and saved for each measurement. During analysis, these measurements can then be used to normalize the yield so that each measurement appears as if it had been carried out at constant pressure. To determine how well the normalization works, a dataset was recorded for fluorobenzene with constant intensity

while the pressure was deliberately altered several times throughout the run. Results are seen in Fig. 14.

As one expects, the raw count rate and pressure vary together, and agree quantitatively. When the pressure is then taken into account, in this case normalizing the raw count rate by taking (raw counts)×(maximum pressure of all measurements)/(pressure for each measurement). This normalizes the raw count rate up to the number of counts that would have been observed had each measurement been taken at the highest recorded pressure. As the "corrected counts" panels show, this keeps the fluctuations in corrected count rate to less than one percent in standard deviation until the abrupt rise in pressure around step 40. This suggests that while this method of pressure compensation is effective at correcting for slowly varying pressures, when the pressure changes too quickly the calibration fails somewhat. Fortunately, this sort of abrupt change (the pressure increases by 80% between steps 38-40, approximately three minutes in real time) occurs rarely, if ever, under normal experimental conditions.

5.5.2 – Excessive count rate

The data presented in Fig. 14 represents the heavy isotope of the parent molecular ion (a few percent of parent molecules are one atomic mass unit (amu) heavier due to the natural abundances of ^{13}C, ^{15}N, etc.) henceforth referred to as the *heavy parent*. In this particular case, the parent itself presents another experimental problem: the number of ions measured by the MCP is too high. In this case, "too high" means that instead of individual molecules hitting the MCP at different times and being recorded as different electrical pulses, molecules are hitting the MCP quickly in succession. The resulting voltage signals build on each other and are sent out of the MCP as a single, larger voltage

signal. The counting card recognizes an ion count by the falling slope of a voltage across a specified threshold value; when ion signals begin to overlap, the threshold may be crossed only once for a signal of several ions. This is shown in an oscilloscope trace in Fig. 15, where two individual signals combine to form one signal which, depending on the threshold setting, may not be representative of the actual physical process.

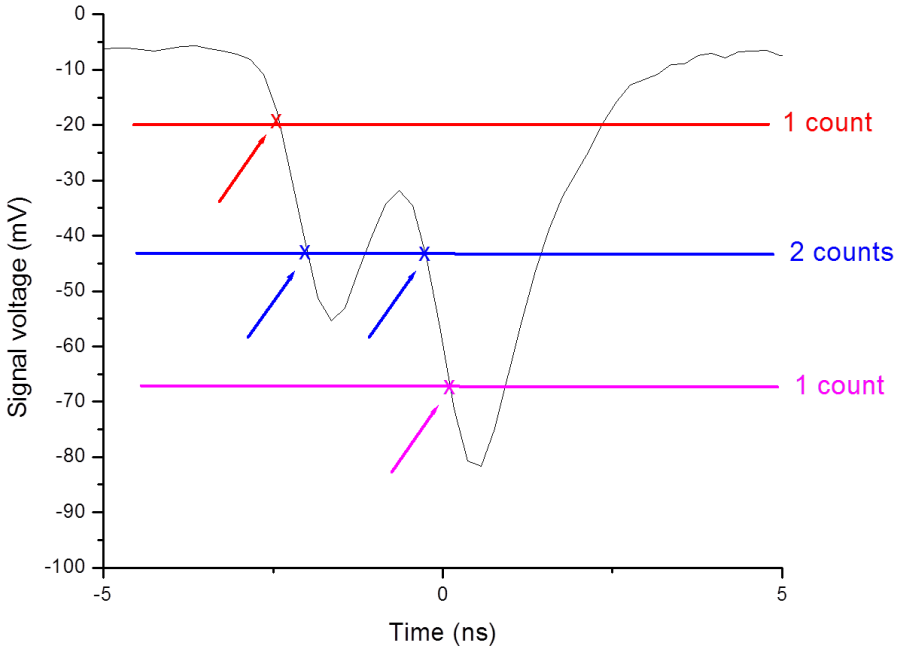

Figure 11 – Multiple detections in a single peak. When a second ion arrives before the voltage signal from the first ion has dissipated, distorted peaks are observed. Depending on the threshold voltage, this can be detected as either one or two counts.

The counting card then sees a single spike when in reality there were two molecules measured, and the ion yield is undercounted. Seen in Fig. 16 are the raw count rate and pressure for the parent ion.

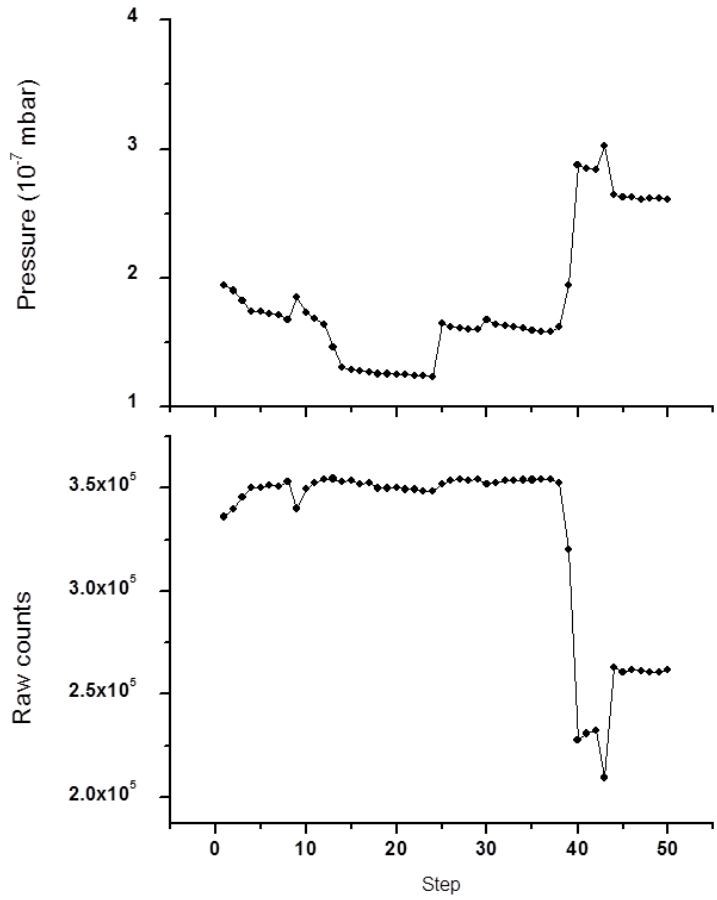

Figure 12 – Undercounting due to high count rate. When dealing with high count rates, the detector cannot always distinguish between incident ions, and some are not interpreted as counts. As a result, the measured count rate (lower panel) does not reflect the target's vapor pressure (upper panel) which determines the true count rate.

Note that for the parent ion, whose ionic yield should differ from its heavy isotope only due to relative abundance, the pressure and the yield do not even qualitatively match. Due to the undercounting as described above, as the pressure increases beyond a certain value, the count rate hits a plateau. At still higher pressures the undercounting becomes strong enough that increasing the pressure actually decreases the ion yield. Seen in Fig. 17 are the raw TOF spectra taken on either side of this threshold.

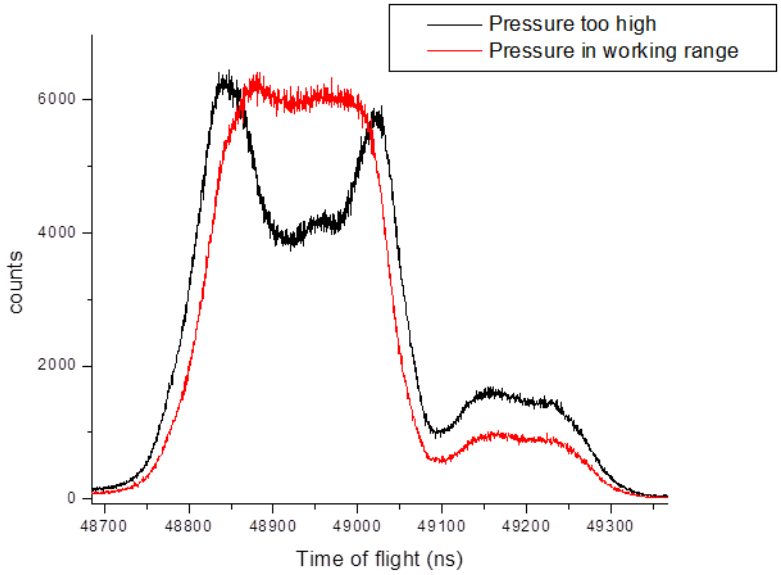

Figure 13 – Different signals from identical processes. Both peaks represent ion counts from the molecular parent, with the small peak on the right being the parent's heavy isotope. Because they are electronically identical, the counts should be directly proportional. However, in high pressures (high count rates, black curve) the peaks do not match; at lower pressures (lower count rates, red curve) the peaks do match, signifying that the count rate is in a workable range.

The red curve (1.3×10^{-7} mbar) falls into a functional counting range while the black curve (2.8×10^{-7} mbar) is undercounted. As can be seen in the heavy isotope (smaller, on the right), the only differences in the peaks are the number of counts due to higher pressure for the black curve. Because the isotopes are electronically identical with the exception of a single neutron, any inconsistencies between the parent and its heavy isotope will be due to experimental artifacts (this will be often be used as a test to rule out experimental problems).

In this case, we can also get quantitative information about what "too high" means in terms of count rates. These curves were measured over 60 seconds runtime equaling 60,000 laser pulses; it appears that the undercounting begins to be a problem at approximately 6,000 counts per bin, or $1/10^{th}$ of a count per bin per laser pulse. Each bin

represents 0.5 ns on the counting card, so the detector saturation occurs when there is, on average, more than one ion reaching the detector every 5 ns. This is plausible given that the typical electrical pulse width coming from the MCP is a few ns wide; this is a reasonable time resolution given that the MCP voltage must drop below the threshold before another pulse can be measured on its rising slope.

One final representation of the high count rate problem is seen during a full intensity-dependent measurement. Seen in Fig. 18 are ion yields taken in aniline for which the count rates were too high, with the fluorobenzene parent ions in black and the heavy parent (with ^{13}C or, less likely, ^{15}N). The heavy parent has been scaled to the parent according to isotopic abundance.

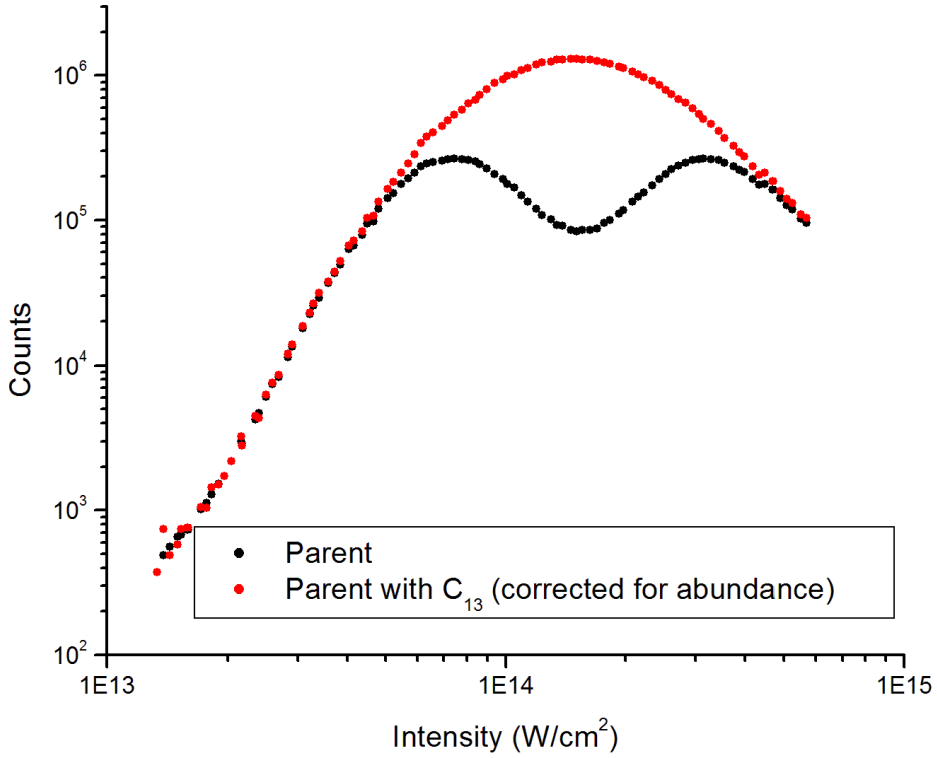

Figure 14 – Ion yields for identical processes. As in Fig. 17, the parent molecular ion (black) is compared to its heavy isotope (red). When corrected for isotopic abundance, the yields should be identical; instead they differ by an order of magnitude due to undercounting when the count rate for the parent is out of the workable range.

In this case, the undercounting of ions becomes clear at high count rate for the parent, as there are simply too many ions being recorded in too short a time. This is not a problem for the heavy parent, however, whose yield is smaller by a constant factor of 14.8 (but is scaled up on the graph to clarify the difference, as mentioned above). As the count rate peaks in the heavy parent, the amount of undercounting in the parent increases. This is typically an easy problem to fix, however. If the peaks in the TOF spectra are not already overlapping at high intensity, the slope of the TOF curve, as described in Fig. 7, can be increased by increasing the voltage V_2 on the second grid. This spreads the distribution of ions in time as they arrive at the MCP and decreases the likelihood of multiple ions arriving at the same time without lowering the total count rate. Once the peaks start overlapping, the pressure can then be reduced to produce an acceptable count rate.

5.5.3 – Threshold voltage

Another (often related) problem in the data is the electrical "ringing" of the MCP output voltage. This is seen in two cases: either the count rate is too high (as described above), or the acceptance threshold voltage of the counting card is too low. Fig. 19 shows an MCP output pulse recorded by an oscilloscope. As the voltage returns to its zero value (~5 mV), it rings down as expected for an underdamped oscillation. The signal in Fig. 19 was measured with 50 Ω impedances on both the output of the MCP and the input of the oscilloscope. For the threshold value shown in red, the underdamped pulse would be interpreted by the experiment as two separate ion counts. A high count rate results in larger and larger voltage signals on the MCP, which in turn increases the ringing. When

the threshold is too low, a normal voltage pulse can be counted twice: once for the actual pulse, and a second time several nanoseconds later as the voltage rings down.

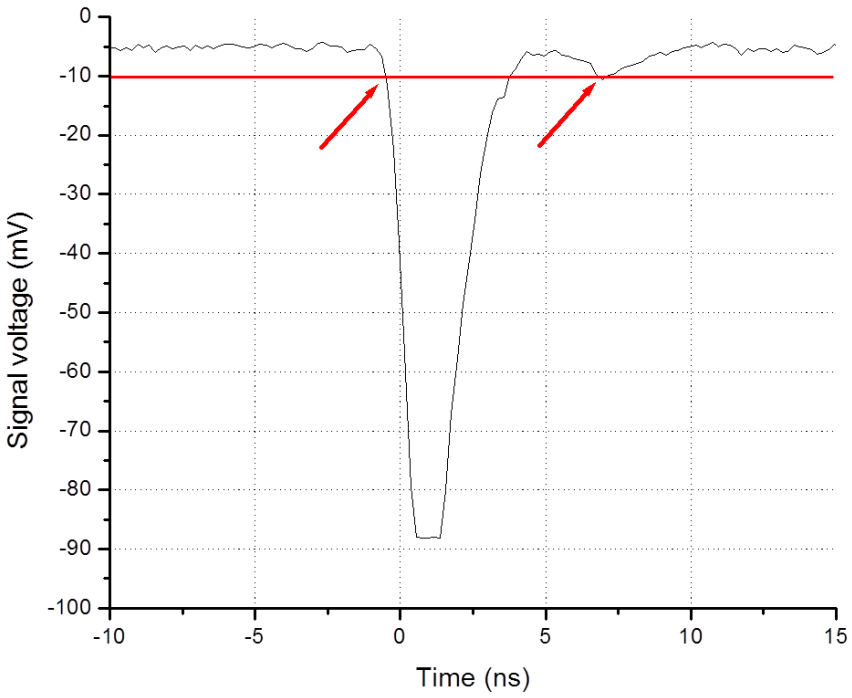

Figure 15 – Electrical ringing in the multichannel plate. When an ion is detected in the multichannel plate, the outgoing voltage does not immediately settle to ground at the end of the pulse. Instead there is a ringing effect which results in a small satellite pulse which, for low voltage thresholds, can be falsely counted as a separate ion signal.

Another problem involving the threshold level can occur when a portion of the voltage reaches the counting card and is reflected back within the BNC cable toward the MCP. Once it reaches the MCP, a portion of the signal is again reflected and reaches the detector a second time. Electrical signals in BNC cables travel at a significant fraction of the speed of light (~1/2), [30] so for a cable a few meters long, a signal's reflection can be measured up to tens of nanoseconds after the original signal. This manifests itself in the ion data as peaks with a satellite peak after the initial signal, as seen in Fig. 20.

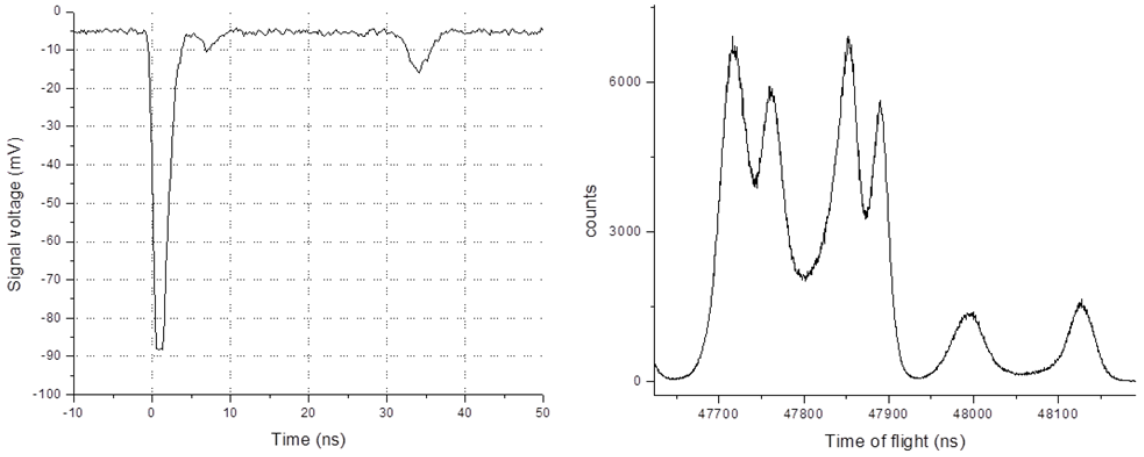

Figure 20 – Electrical reflections in the multichannel plate. When the voltage signal from the multichannel plate reaches the counting card, a portion of the signal can be reflected inside the connecting cable and measured tens of nanoseconds later (left). When the reflection returns to the counting card, it can be falsely registered as an ion count. These extra counts are detected as additional humps in the ion peaks ~40 ns after the main peaks (right).

The right panel shows the resulting peaks growing with satellite peaks appearing several nanoseconds later than the real, uncompromised data. Proper setting of the threshold voltage on the counting card is vital to the fidelity of the experimental results, and unfortunately changes based on factors such as pressure, grid voltage settings and choice of molecular target (which prevents us from defining a universal "correct" setting). If the threshold is set too low, effects such as those above can skew results; however, if it is set too high, legitimate ion signals go unobserved.

It is often the case that different molecules (or different fragments from the same molecule) have different signatures on the voltage output by the MCP. It is also common for the ionic fragments of molecular parent to have different signals; as seen in Fig. 21, different settings of the threshold voltage can completely eliminate the detection of many of the smaller-mass fragments.

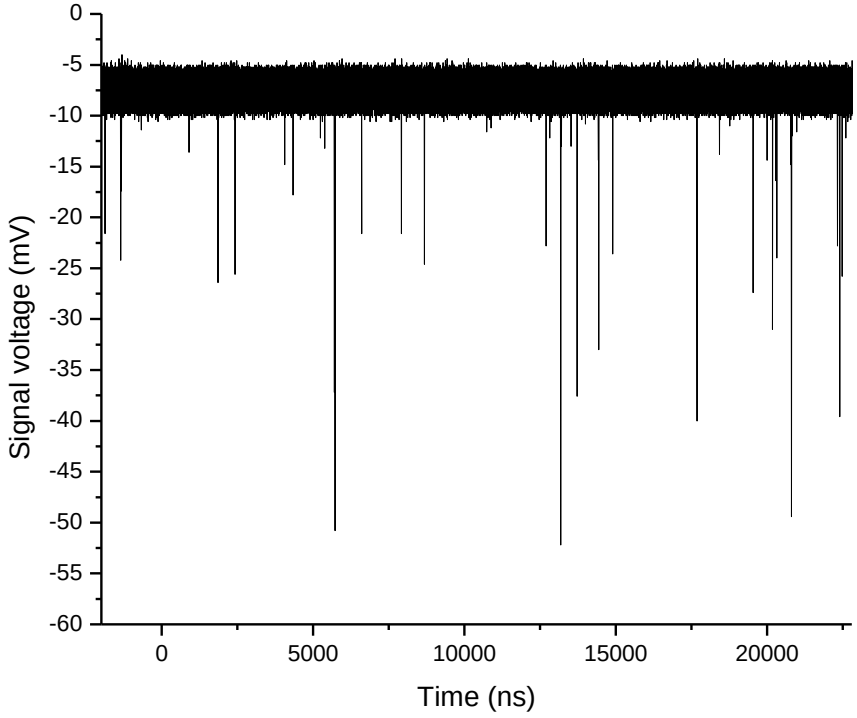

Figure 21 – Different voltage signals for different fragments. Some fragments result in a different voltage signature in the multichannel plate than others. If the threshold voltage is not chosen carefully, entire physical processes may be ignored by the experiment.

As seen in Fig. 22, the threshold voltage increases from the black curve (proper settings) to the red curve (too high) to the green curve (much too high). Once can see the larger fragment peaks at ~24 μs and ~34 μs decrease consistently with higher threshold, but much more notable is the complete disappearance of the smaller peaks. When the threshold voltage is too high, it isn't simply that some counts in the data are missed; *entire physical processes are overlooked*. This could potentially lead to fundamental misconceptions and misunderstandings of the behaviors of the molecules in the intense fields, where the investigation of the molecular photodynamics is the entire point of the experiment.

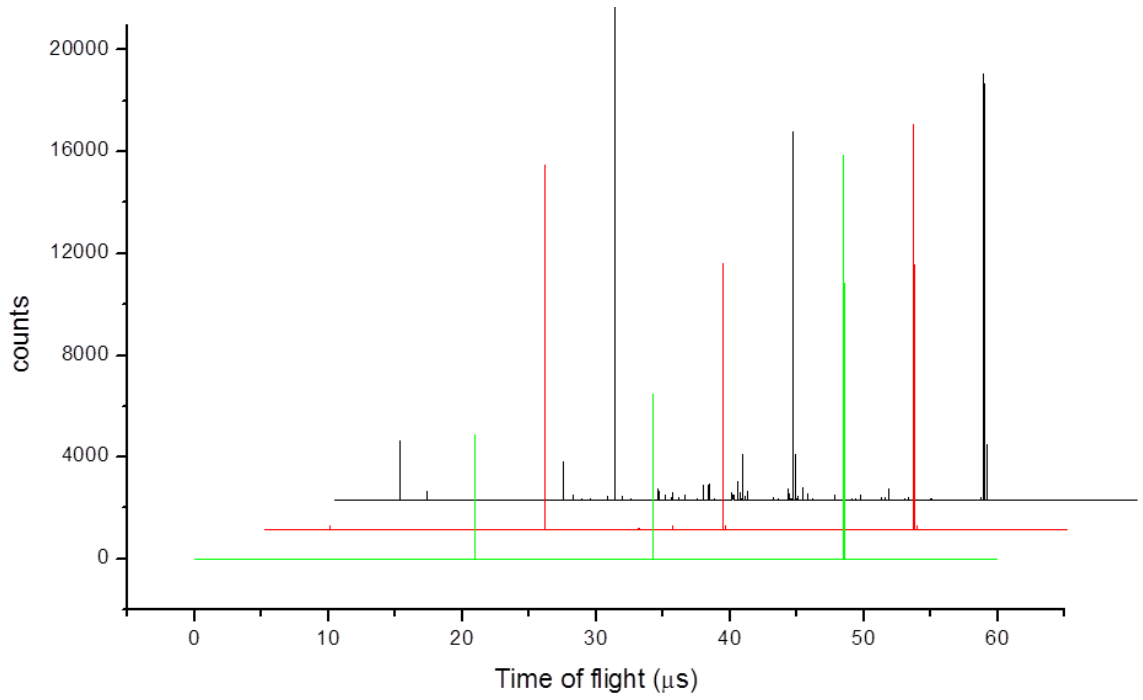

Figure 22 – Missing peaks due to high threshold voltage. When the voltage threshold, which determines whether or not a signal is interpreted as an ion count, is too large, peaks with small voltages are not counted, and entire physical processes are overlooked.

Because it can depend simultaneously on a variety of experimental parameters, proper choice of the threshold voltage is not absolute. Fig. 23 shows the count rates for parent ions, fragments, and all ions combined for a variety of threshold voltages. As the magnitude of the threshold is decreased, more ions are detected. This begins to level off (in the case displayed) at a threshold of around 5-10 mV; a larger voltage fails to include ions (typically smaller fragments, which often have a smaller voltage signature on the MCP), while smaller thresholds begin to sample electrical reflections, electrical ringing, and background noise.

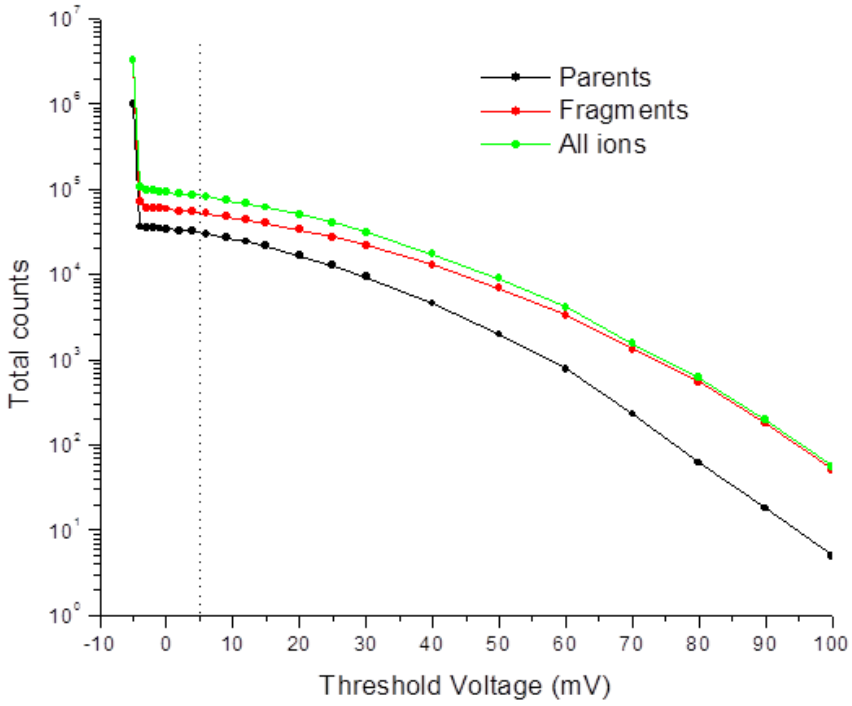

Figure 23 – Counts as a function of threshold voltage. To ensure all ion signals are counted, a small negative threshold should be chosen; however, if the threshold is too small, inconsistencies arise as background noise in the voltage signal is interpreted as a signal.

5.5.4 – Spatial chirp in the laser pulses

There are, unsurprisingly, experimental artifacts in the ion yield data that can result from issues involving the quality of the laser focus. Spatially-dependent frequency distributions (known as spatial chirp) in the focus lead to asymmetric ion peaks in TOF, where the splitting through the middle into two separate lobes may not occur in the actual center. When there is no spatial chirp, the splitting should occur in the direct center with each lobe having approximately the same size and shape. Examples of ion peaks from chirped and unchirped pulses are seen in Fig. 24.

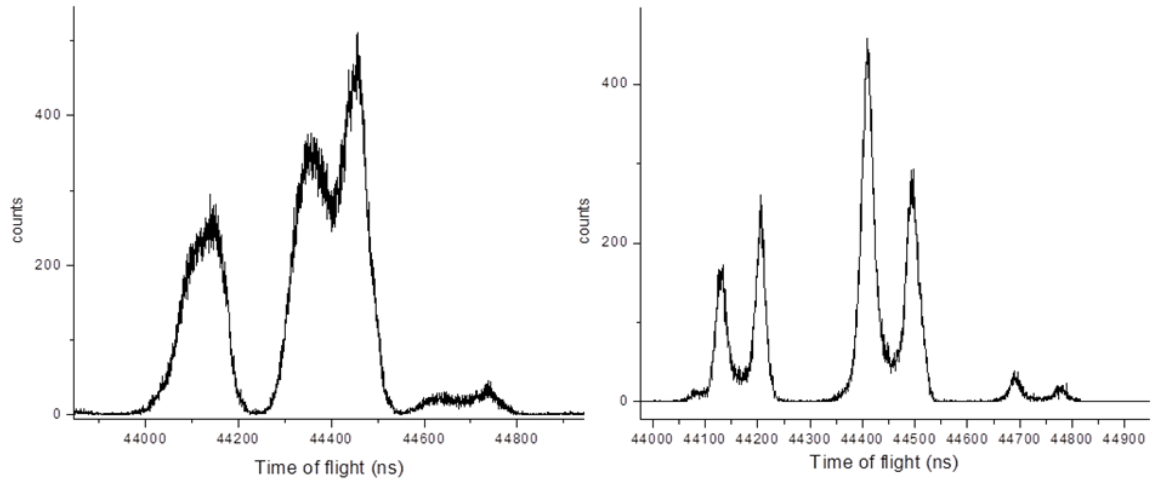

Figure 24 – Spatial chirp seen in the ion peaks. When the laser focus has a spatially-dependent frequency spectrum, asymmetries in the ion peaks are seen (left panel). In the absence of spatial chirp in the laser's focus symmetric peaks (right panel) are observed.

When the beam is chirped, the shapes of peaks in the TOF spectrum can be different depending on the molecular target being observed. As the central wavelength changes for different spatial positions, resonant conditions may depend on position, which can lead to enhancements in ionization for different spatial regions of the focus.

Fortunately, such observations in the TOF spectra can be used to diagnose alignment issues in the laser itself. For instance, if the spatial chirp in the focus changes as a function of changing the temporal chirp in the laser (which involves moving the delay stage of the retroreflector in the Spitfire's compressor), this means that the horizontal alignment of the retroreflector is not fully optimized. When the retroreflector is properly aligned, any spatial chirp in the beam should remain constant as temporal chirp is changed.

5.4.5 – Spatial laser mode quality

In addition to spatial chirp, one must consider a number of other possible problems with the mode quality of the beam. One typically assumes a beam to have a Gaussian cross section, and that as it focuses and defocuses, the profile remains consistent and symmetric [26]. Even when a beam does indeed have an ideal cross section in intensity, the focusing qualities rarely follow the perfect case. The spatially-resolved ion yield in Fig. 8 demonstrate this: as the beam is focused, less intensity is found in the center of the beam, and as it defocuses the pattern becomes more uniform.

This behavior is commonly referred [19,29,31] to as the diffraction catastrophe or, alternately, a caustic focal aberration. In the far field [26], the wavefront propagates in such a way that the minimum focal width and the most intense point do not necessarily coincide, as seen in Fig. 25. The minimum width is called the "disk of least confusion" [32], but it is a poor estimate of the "center" of the focus as it is not the position of greatest intensity.

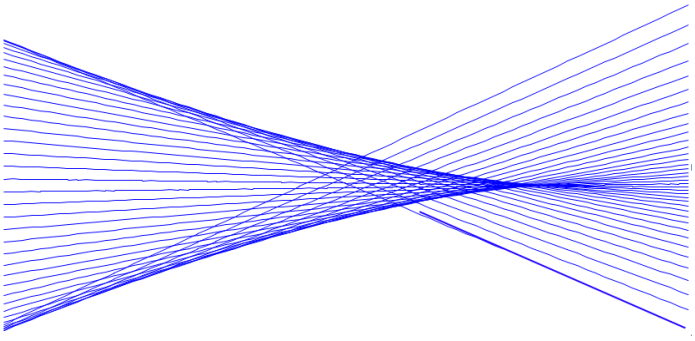

Figure 25 – The diffraction catastrophe. As a laser beam is focused, it can be subjected to a caustic focal aberration known as the diffraction catastrophe. The position where the focal waist is at its minimum is not the position of the highest intensity, and the intensity distribution has a "fish tail" shape on the focusing side, as was seen in the spatially-resolved ion yields in Fig. 8.

The inconsistencies in intensity and the deviation from the assumed Gaussian focus occur on the focusing side for positive spherical aberration [31], which is the case in our experiment as was seen in Fig. 8. The defocusing side, however, has a more uniform intensity which better matches the assumption of an ideal Gaussian focal distribution. To avoid the effects of a caustic focus in our ionic yield experiments, the focus is offset from the acceptance slit by at least 1 mm on the defocusing side, where we observe more uniformity.

5.6 – LabVIEW control program

Measurements are controlled by a LabVIEW program, and a schematic of the basic structure is seen in Fig. 26. The program operates a sequence as follows: first, variables are created and the relevant quantities are calculated based on the input parameters on the program's control panel. Laser power outputs to be measured are calculated such that they are equally spaced on a logarithmic scale between the minimum and maximum powers, which are specified by the user. The acceptable range of the current data point's power is determined ($P \pm \Delta P$). The measurement cycle for each data point begins with a beam block in the path of the laser, and a power measurement is taken to determine the zero reading; this is done before and after each step to compensate for heating effects in the pyroelectric power meter. The block is removed and the program signals a stepper motor control box, which rotates a half-wave plate inside the laser's compressor, attenuating the beam power. The power is measured and adjusted until the reading falls within the range $P - \Delta P < \text{power} < P + \Delta P$.

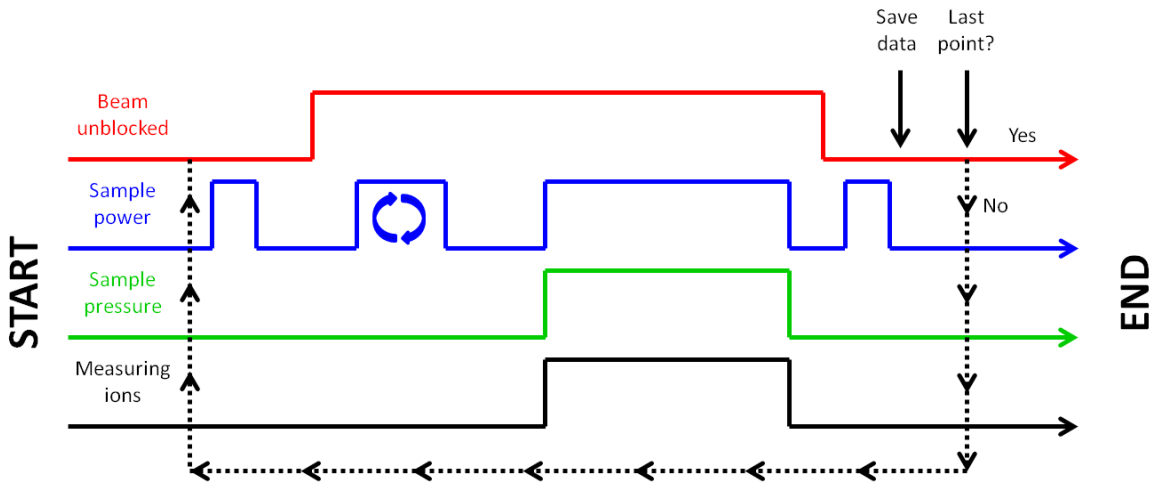

Figure 166 – Step-by-step control sequence of the automated LabVIEW program.

Once the desired beam power is found, the LabVIEW program accesses the p778 counting card software, and a measurement begins as the card counts ions. During this measurement, the beam power and molecular vapor pressure are sampled for calibration. When the counting card software reaches the desired number of triggered pulses, statistics are analyzed on the power and pressure readings to determine the mean and standard deviation. Once again, the beam is blocked and the zero power reading is taken; the "before" and "after" zero measurements are averaged, and this value is subtracted from the mean power reading to give a fully-calibrated power value. The power, pressure, counting card TOF spectrum, and conditions of the counting card program (runtime, number of triggered pulses, and total ion counts) are all saved. Finally, all variables are cleared and the program moves on to the next step, at which point the cycle starts over for the next desired power.

The entire experiment as described above is fully automated. At present, once the experiment is set up and the relevant variables are specified, the experiment is capable of running autonomously without any input, with the lone exception being the changing of

scales on the power meter (which is done to ensure accuracy, as the analog voltage output of the meter is more precise on lower scales). When this is necessary, the LabVIEW program sends the user a prompt specifying the necessary change. To protect oversaturation of the counting card, the program is also designed to prompt the user if the pressure exceeds a user-specified limit.

Typical measurements involve integration over 30 seconds to five minutes per data point; less time reduces counting statistics, while integration over more than five minutes can lead to increased uncertainty in the power readings due to the heating effects mentioned above. Total collection time for a full curve of ion yields as a function of intensity takes between three and eight hours, depending on specifications; our laser system and power supplies are stable over this duration, and are monitored by oscilloscopes and voltage readouts throughout the collection time. As the data are analyzed, all ion yields are normalized to one minute (60,000 laser pulses) of integration time and 1.0×10^{-7} mbar of pressure.

Preparation of the molecular samples involves multiple stages of cleaning the glass sample holder in a sonic bath and thorough baking of both the sample holder and the vacuum system. Viton O-rings are used to connect the sample holder to the leak valve to avoid O-ring absorption of the chemical, and these O-rings are replaced every time a sample is replaced. This ensures that the next molecular vapor will not be contaminated by the previous chemical, and we indeed find that our samples are free from impurities from both previous chemicals and cleaning agents.

References

[1] Maine, P., Strickland, D., Bado, P., Pessot, M. & Mourou, G. 1988, "Generation of Ultrahigh Peak Power Pulses by Chirped Pulse Amplification," *IEEE Journal of Quantum Electronics,* vol. 24, no. 2, pp. 398-403.

[2] Perry, M. & Mourou, G. 1994, "Terawatt to Petawatt Subpicosecond Lasers," *Science,* vol. 264, no. 5161, pp. 917-924.

[3] Strohaber, J., Scarborough, T.D. & Uiterwaal, C.J.G.J. 2007, "Ultrashort intense-field optical vortices produced with laser-etched mirrors," *Applied Optics,* vol. 46, no. 36, pp. 8583-8590.

[4] MATLAB 6.1, The MathWorks Inc., Natick, MA, 2000.

[5] Brabec, T., *Strong field laser physics* Springer, 2008.

[6] Hertel, I.V. & Claus-Peter Schulz, *Atome, Moleküle und optische Physik 1: Atomphysik und Grundlagen der Spektroskopie,*Springer, 2008.

[7] Hankin, S.M., Villeneuve, D.M., Corkum, P.B. & Rayner, D.M. 2000, "Nonlinear ionization of organic molecules in high intensity laser fields," *Physical Review Letters,* vol. 84, no. 22, pp. 5082-5085.

[8] Talebpour, A., Bandrauk, A.D., Vijayalakshmi, K. & Chin, S.L. 2000, "Dissociative ionization of benzene in intense ultra-fast laser pulses," *Journal of Physics B: Atomic, Molecular and Optical Physics,* vol. 33, no. 21, pp. 4615-4626.

[9] Posthumus, J.H. 2004; 2004, "The dynamics of small molecules in intense laser fields," *Reports on Progress in Physics,* vol. 67, no. 5, pp. 623-665.

[10] Yamanouchi, K. (ed), *Lectures on Ultrafast Intense Laser Science 1*, Springer, 2010.

[11] Speiser, S. & Jortner, J. 1976, "3/2 Power Law for High-Order Multiphoton Processes," *Chemical Physics Letters,* vol. 44, no. 3, pp. 399-403.

[12] Wagner, M. & Schroder, H. 1993, "A Novel 4 Grid Ion Reflector for Saturation of Laser Multiphoton Ionization Yields in a Time-Of-Flight Mass-Spectrometer," *International Journal of Mass Spectrometry and Ion Processes,* vol. 128, no. 1-2, pp. 31-45.

[13] Walker, M., Hansch, P. & Van Woerkom, L. 1998, "Intensity-resolved multiphoton ionization: Circumventing spatial averaging," *Physical Review A,* vol. 57, no. 2, pp. R701-R704.

[14] Alnaser, A., Tong, X., Osipov, T., Voss, S., Maharjan, C., Shan, B., Chang, Z. & Cocke, C. 2004, "Laser-peak-intensity calibration using recoil-ion momentum imaging," *Physical Review A,* vol. 70, no. 2, pp. 023413.

[15] Bredy, R., Camp, H., Nguyen, H., Awata, T., Shan, B., Chang, Z. & DePaola, B. 2004, "Three-dimensional spatial imaging in multiphoton ionization rate measurements," *Journal of the Optical Society of America B-Optical Physics,* vol. 21, no. 12, pp. 2221-2226.

[16] Goodworth, T.R.J., Bryan, W.A., Williams, I.D. & Newell, W.R. 2005, "Reconstruction of atomic ionization probabilities in intense laser fields," *Journal of Physics B: Atomic, Molecular and Optical Physics,* vol. 38, no. 17, pp. 3083-3089.

[17] Robson, L., Ledingham, K., McKenna, P., McCanny, T., Shimizu, S., Yang, J., Wahlstrom, C., Lopez-Martens, R., Varju, K., Johnsson, P. & Mauritsson, J. 2005, "Volumetric intensity dependence on the formation of molecular and atomic ions within a high intensity laser focus," *Journal of the American Society for Mass Spectrometry,* vol. 16, no. 1, pp. 82-89.

[18] Wang, P., Sayler, A., Carnes, K., Esry, B. & Ben-Itzhak, I. 2005, "Disentangling the volume effect through intensity-difference spectra: application to laser-induced dissociation of $H_2(+)$," *Optics Letters,* vol. 30, no. 6, pp. 664-666.

[19] Bryan, W., Stebbings, S., English, E., Goodworth, T., Newell, W., McKenna, J., Suresh, M., Srigengan, B., Williams, I., Turcu, I., Smith, J., Divall, E., Hooker, C. & Langley, A. 2006, "Geometry- and diffraction-independent ionization probabilities in intense laser fields: Probing atomic ionization mechanisms with effective intensity matching," *Physical Review A,* vol. 73, no. 1, pp. 013407.

[20] Strohaber, J. & Uiterwaal, C.J.G.J. 2008, "*In situ* measurement of three-dimensional ion densities in focused femtosecond pulses," *Physical Review Letters,* vol. 100, no. 2, pp. 023002.

[21] Strohaber, J., Kolomenskii, A.A. & Schuessler, H.A. 2010, "Reconstruction of ionization probabilities from spatially averaged data in N dimensions," *Physical Review A,* vol. 82, no. 1, pp. 013403.

[22] Schultze, M., Bergues, B., Schroeder, H., Krausz, F. & Kompa, K.L. 2011, "Spatially resolved measurement of ionization yields in the focus of an intense laser pulse," *New Journal of Physics,* vol. 13, pp. 033001.

[23] Strohaber, J., *Intense-field ionization of atoms and molecules: Spatially resolved ion detection and ultrashort optical vortices*, Ph.D. Dissertation, Department of Physics and Astronomy, University of Nebraska – Lincoln, 2008.

[24] Becker, A. & Faisal, F. 1999, "Production of high-charge states of Xe in a femtosecond laser pulse," *Physical Review A,* vol. 59, no. 5, pp. R3182-R3185.

[25] Wiehle, R. & Witzel, B. 2002, "Correlation between Double and Nonresonant Single Ionization," *Physical Review Letters,* vol. 89, no. 22.

[26] Siegman, A.E., *Lasers,* University Science Books, 1986.

[27] Scarborough, T.D., Strohaber, J., Foote, D.B., McAcy, C.J. & Uiterwaal, C.J.G.J. 2011, "Ultrafast REMPI in benzene and the monohalobenzenes without the focal volume effect," *Physical Chemistry Chemical Physics,* vol. 13, no. 30, pp. 13783-13790.

[28] Hecht, E., *Optics* Addison-Wesley, 2002.

[29] Osipov, V.Y. & Buznikov, A.A. 2008, "Calculating the three-dimensional structure of the near-focus diffraction field in the caustic zone of a convergent aberrational laser beam," *Journal of Optical Technology,* vol. 75, no. 8, pp. 495-499.

[30] *The ARRL Handbook For Radio Communications, 88th edition*, National Association for Amateur Radio, 2011.

[31] Nye, J. 2005, "The relation between the spherical aberration of a lens and the spun cusp diffraction catastrophe," *Journal of Optics A-Pure and Applied Optics,* vol. 7, no. 3, pp. 95-102.

[32] Castro-Ramos J., de Prieto O.I. & Silva-Ortigoza G. 2004, "Computation of the disk of least confusion for conic mirrors," *Applied Optics,* vol. 43, no. 33, pp. 6080-6089.

Chapter 6

Molecular ionization of systematic series

The ongoing interest in intense-field molecular dynamics (and the dynamics of ionization processes, in particular) [1-3] is driven by their relevance in attosecond pulse generation [4,5], generation of short-wavelength radiation [6] and, ultimately, the desire to control chemical reactions [7,8]. Unfortunately, although computational work can simulate quite accurately the electronic structures of these molecules, fully *ab initio* simulations of intense-field molecular photodynamics are far beyond reach even for the most advanced supercomputers [9]. This makes experimental investigations all the more crucial. This chapter discusses experimental ionization dynamics of the halobenzenes, the CNOF isoelectronic series, a compound substitution in anisole, and the azabenzenes.

6.1 – The halobenzenes

In the halobenzenes, we find that each target molecule has two regions of intensities with constant integer slope, a signature of resonance-enhanced multiphoton ionization (REMPI). In this process a resonant transition to an excited molecular state becomes saturated such that a smaller number of photons is capable of ionizing from this immediately-populated excited state. This excited state is a $^1\pi\pi^*$ (E_{2u} in benzene) state which has been well-documented in the halobenzenes through nanosecond UV (1 + 1)

REMPI experiments around 266 nm [10-12]. The halobenzenes all follow (M + N) REMPI patterns. At the highest intensities used, the parent ion yields of all five species rapidly decrease as other processes become dominant, such as multiple ionization and fragmentation. These features are seen in the data in Fig. 1; mathematically fitted slopes are seen in Fig. 2 and are summarized in Table 1.

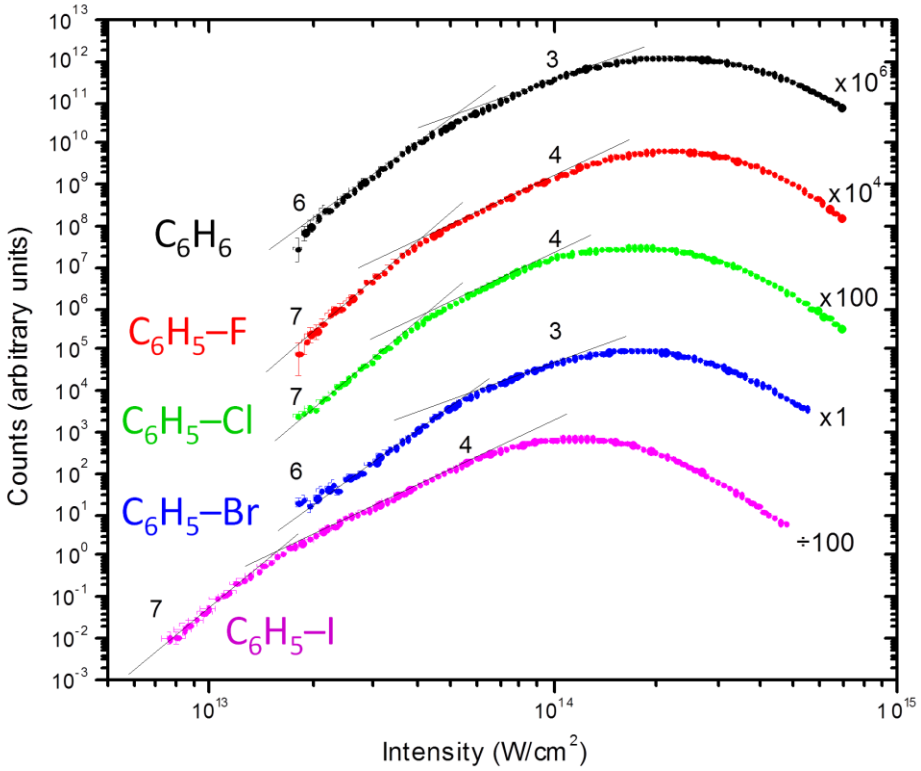

Figure 1 - Parent ion yields of benzene and the monohalobenzenes. Molecular parent ion yields of benzene (black), fluorobenzene (red), chlorobenzene (green), bromobenzene (blue), and iodobenzene (pink) as a function of intensity. Data has been normalized for consistency in pressure and collection time, and has been shifted vertically by two orders of magnitude per dataset to allow viewing on the same graph. Errors in the count rate are based on counting statistics, while errors in intensity are estimated from experimental uncertainties in power measurement and laser stability. Thin black lines, marked with the log-log slope (and thus the number of photons in the process) are meant to guide the eye, and represent our determination of the most accurate integer slope. Mathematically fitted slope values can be found in Table 1.

The curve for benzene most closely indicates a slope-six to slope-three kink, representative of a (3 + 3) REMPI process. However, both slopes rise slightly more quickly than this (see Table 1). Because the six-photon range of our 804 nm photons is 9.25 eV ± 0.06 eV (with the uncertainty due to the bandwidth of the femtosecond pulses), six photons are not always enough to exceed the ionization potential (IP), 9.24 eV, and so we expect some mixing of six- and seven-photon processes. Similarly, the transition from the excited to ionic state in benzene is barely within range of three, resulting in some mixing between three- and four-photon processes. The six-photon result matches previous results carried out at 800 nm [13].

In fluorobenzene and chlorobenzene we observe a shift from seven-photon to four-photon absorption, indicative of (3 + 4) REMPI. This seems counterintuitive, as the IP of both molecules (9.20 eV and 9.07 eV for fluorobenzene and chlorobenzene, respectively) are within the energy of six photons. Channel closing was investigated as a possible explanation, but was determined to be unsuitable, as discussed further below. However, it has been put forward that in substituted benzenes the highest occupied molecular orbital (HOMO) and the HOMO–1 may contribute significantly to ionization [14]. For fluorobenzene and chlorobenzene, there is a difference in energy of the HOMO and HOMO–1 of approximately 0.6 eV [15], which is enough to account for (3 + 4) REMPI if the HOMO–1 transition is more strongly on resonance with an excited state, which seems to be the case here.

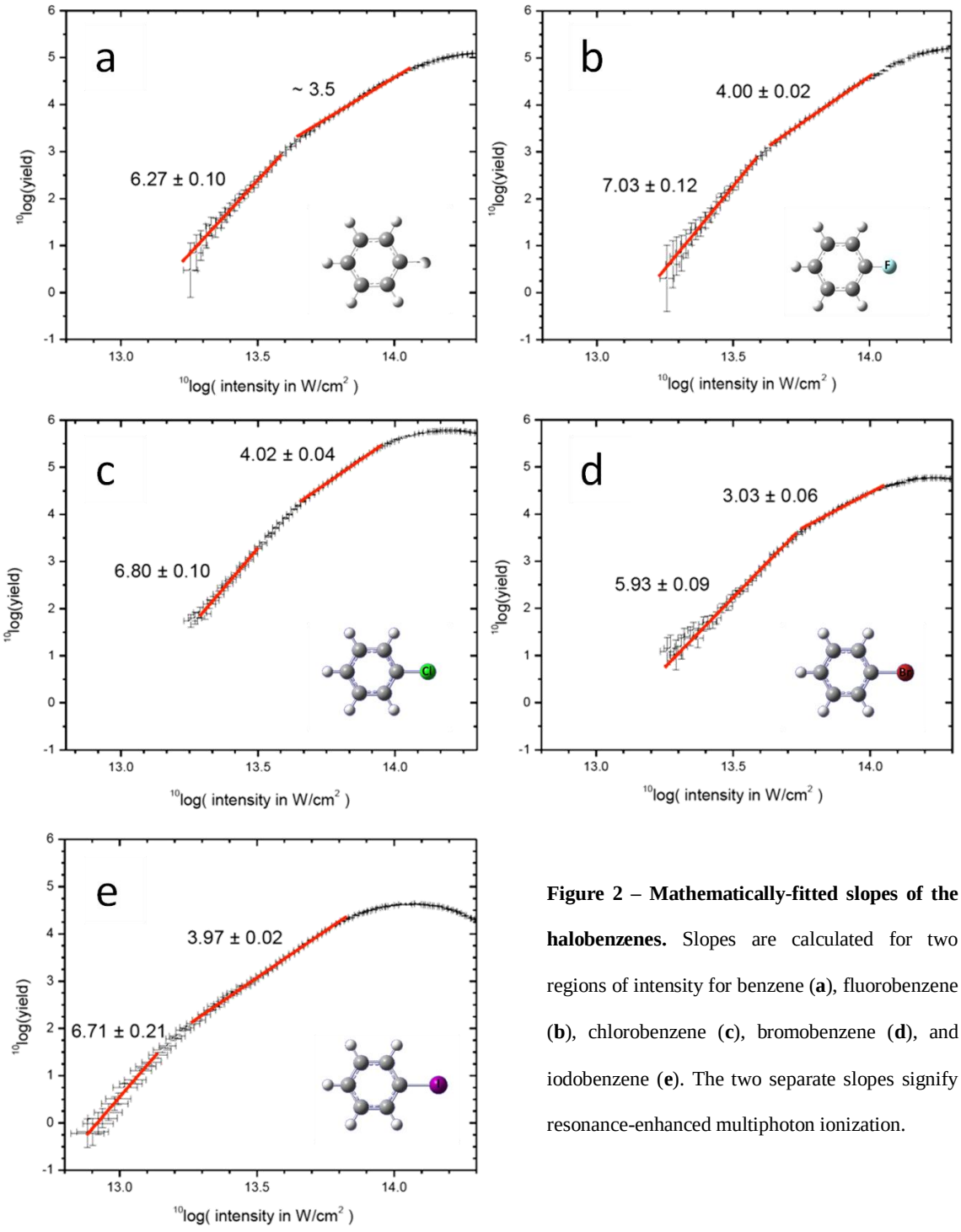

Figure 2 – Mathematically-fitted slopes of the halobenzenes. Slopes are calculated for two regions of intensity for benzene (**a**), fluorobenzene (**b**), chlorobenzene (**c**), bromobenzene (**d**), and iodobenzene (**e**). The two separate slopes signify resonance-enhanced multiphoton ionization.

It is notable that the HOMO–1 plays a role in the halobenzenes but not in benzene; in the higher symmetry of benzene (point group D_{6h}), the two highest occupied MOs are degenerate (E_{1g} character), and their contributions to ionization cannot be

considered independently. The addition of a halogen substituent lowers the molecular symmetry in the halobenzenes to point group C_{2v}. This lifts the degeneracy of the HOMO and HOMO–1; in PhCl ("Ph" denotes a phenyl group, C_6H_5), for instance, these MOs have character B_1 and A_2, respectively [16]. A degeneracy in the $^1\pi\pi^*$ excited state is similarly lifted, resulting in another possible excitation pathway. A qualitative schematic of the relevant transitions is presented in Fig. 3.

Bromobenzene has an even lower IP (9.00 eV), which allows for a six-photon process to dominate the ionization. As the resonant three-photon transition (ground state to $^1\pi\pi^*$) saturates, three-photon ionization takes over. Here ionization from the HOMO–1, which would require seven photons, seems to be insignificant. The heavier halogen substituents induce a larger splitting between the energies of the HOMO and HOMO–1, which seems to push the HOMO–1 farther from a resonant transition.

Species	IP (eV)	Low intensity slope	High intensity slope
Benzene	9.24	6.27 ± 0.10	~3.5 ± 0.1
Fluorobenzene	9.20	7.03 ± 0.12	4.00 ± 0.02
Chlorobenzene	9.07	6.80 ± 0.10	4.02 ± 0.04
Bromobenzene	9.00	5.93 ± 0.09	3.03 ± 0.06
Iodobenzene	8.85	6.71 ± 0.21	3.97 ± 0.02

Table 1 – Fitted slopes and ionization potentials of the halobenzenes.

Of particular interest is iodobenzene, where we observe a seven- to four-photon kink. It is generally accepted that 266 nm (within the same energy spread of three 804 nm photons) excitation of PhI excites the HOMO into a bound $^1\pi\pi^*$ state [17-22], so we expect this transition to be strongly resonant. This singlet state rapidly predissociates to a repulsive $^3n\sigma^*$ triplet state, which leads to bond cleavage in the neutral molecule: PhI* → Ph + I.

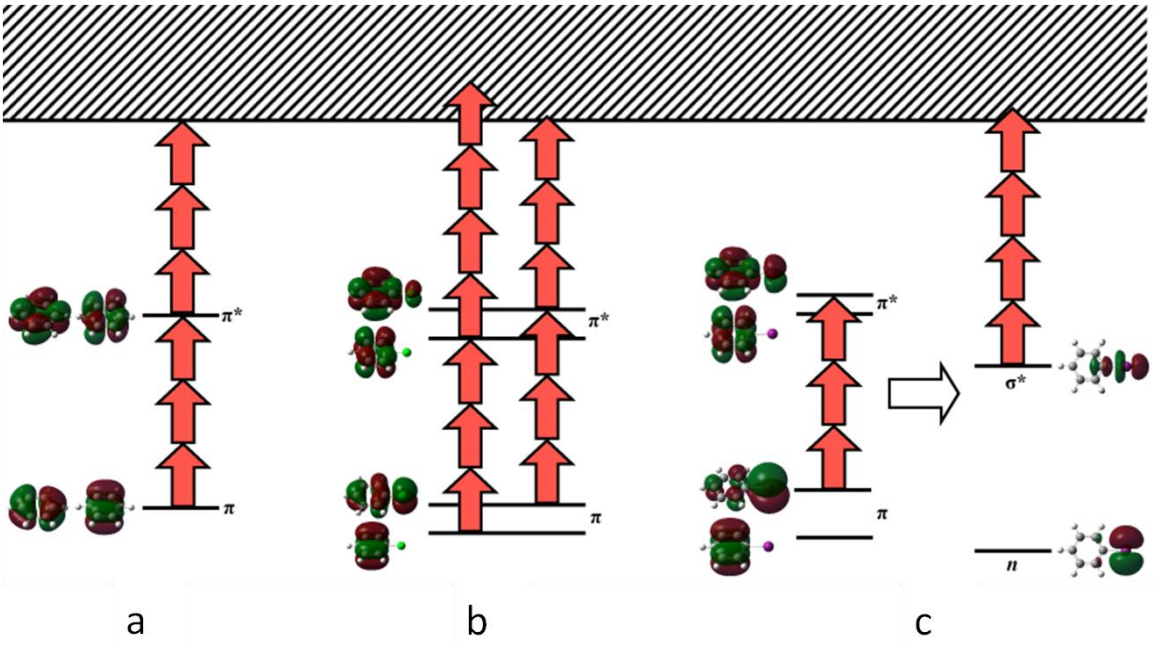

Figure 3 - Energy diagrams of observed processes in benzene and the monohalobenzenes. (**a**) Sketch of (3 + 3) REMPI observed in benzene. Photons are shown as red arrows, the ionization continuum is shown as a checkered area, and the relevant molecular orbitals are shown next to the energy levels. (**b**) Sketch of REMPI processes involving the HOMO and HOMO–1. In the monohalobenzenes the degenerate benzene π (E_{1g}) and π* (E_{1g}) levels are split. In this panel B, the left column of arrows shows (3 + 4) REMPI as seen in fluorobenzene and chlorobenzene dominated by the HOMO–1, and the right column shows (3 + 3) REMPI as seen in bromobenzene where the HOMO–1 does not contribute. (**c**) Sketch of 3-photon excitation from the HOMO, ultrafast intersystem crossing to a dissociative triplet state, and 4-photon ionization as seen in iodobenzene. The intersystem crossing involves an electronic orbital rearrangement, which ends with the HOMO filled and unpaired electrons in both the *n* and σ* states.

Unlike the other halobenzenes, which have $^1\pi\pi^*$ lifetimes ranging from hundreds of picoseconds to several nanoseconds, the unperturbed lifetime of the PhI* $^1\pi\pi^*$ state is between 20 fs and 700 fs [18,23-26]. This ultrafast intersystem crossing in iodobenzene is due to the strong spin-orbit coupling induced by the iodine atom (these effects are described in Chapter 4). For the lighter halogen substituents this coupling is smaller (internal heavy atom effect) [26] and intersystem crossing is unlikely. In our mass spectra for iodobenzene we observe not only an abundance of Ph^+ and I^+, but also ionic states of the iodine atom through I^{8+} (detailed in Chapter 7), which indicates that an absorption, a

predissociative intersystem crossing, and a nascent dissociation occur quickly enough to leave time to ionize the now-independent atom up to eight times (PhI → PhI*($^1\pi\pi^*$) →PhI*($^3n\sigma^*$) → $Ph^+ + I^{N+}$) before the end of the 50-fs laser pulse. As expected for ultrafast intersystem crossing in PhI we observe fragments in its mass spectrum even for the lowest intensities, while fragments of the other halobenzenes are absent (or appear in trace amounts). Further, the energy difference of the HOMO and HOMO–1 in iodobenzene is ≈0.73 eV (nearly half the energy of a photon) [15], so given that the HOMO is strongly resonant, the HOMO–1 is unlikely to contribute to resonant excitation. We thus disregard the role of the HOMO–1 here. This makes the observed slope of four intriguing. Ionizing from the $^1\pi\pi^*$ state would not yield a four-photon process; it is well within the range of three photons. However, ionization from the $^3n\sigma^*$ state during the dissociation explains the four-photon process. Thus, we determine that the slope of four is representative of a three-photon excitation to the singlet $^1\pi\pi^*$ state followed by a nearly immediate intersystem crossing to the dissociative triplet $^3n\sigma^*$ state, which then requires four photons to ionize before it can completely dissociate [10,22], as shown in Fig. 3c. As a result, we find a four-photon process limiting the ionization rate for more than half a decade in intensity.

Each of the halobenzenes is also observed as a multiply-charged parent ion, as seen in Fig. 4. With the exception of benzene, the yields of the multiply-charged halobenzenes behave oppositely to the singly-charged parents: the yields increase with increasing halogen mass. This pattern is strong enough that, for intensities greater than 10^{14} W/cm^2, the doubly-charged iodobenzene parent overtakes the yield of the singly-charged parent. Further, enough doubly-charged iodobenzene is present that a triply-

charged parent is observed. But why is it that, while the singly-charged parents become less stable with increasing halogen mass, the multiply-charged parents become more stable? The parent molecule is destabilized largely through the spin-orbit coupling which leads to a dissociative triplet state. After an electron has been removed, there is only one unpaired bound electron; a triplet state cannot be formed. Strictly speaking, there could be other excited states which have an odd number of unpaired electrons, leading to doublets, quartets, etc. But the singlet-triplet interaction which weakened the parent molecule no longer exists, so the yield of doubly-charged parent molecules is enhanced.

It is also noteworthy that, in the doubly-charged chlorobenzene and iodobenzene, kinks in the yields can be seen similar to those of the parents. While the dynamics of the second ionization are too complex to be determined by the experiment, this suggests one of two possibilities. First, the second ionization may be explicitly dependent on the first ionization such that when the excitation in the neutral parent is saturated, both yields observe the kink. This may be the case in chlorobenzene, as the kinks of both yields occur at approximately the same intensity. The second possibility is that a resonant process becomes saturated in the second ionization; in iodobenzene, the yield of the second ionization does not kink at the same intensity as the first. This separation could indicate independent saturation of two different resonant transitions.

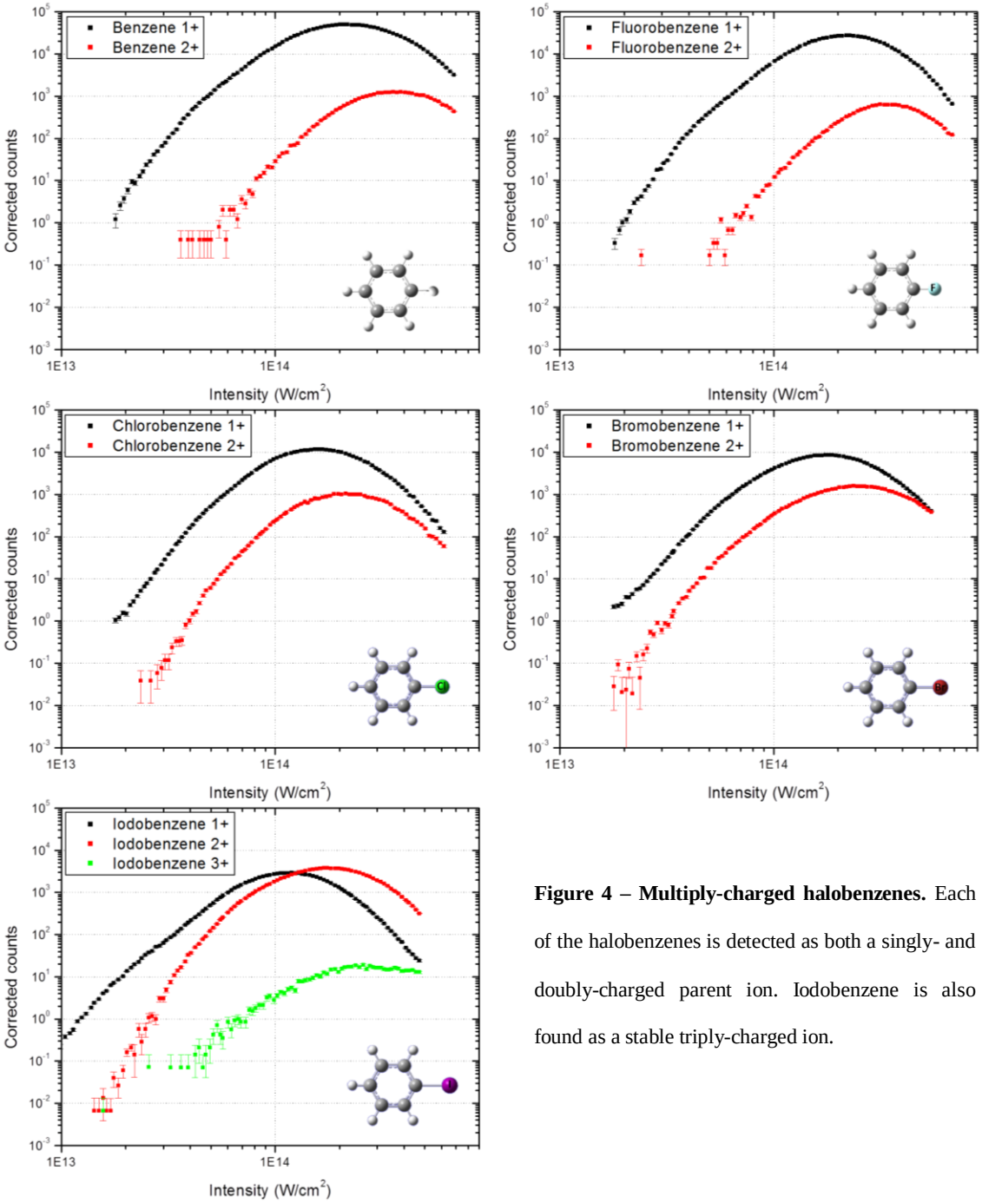

Figure 4 – Multiply-charged halobenzenes. Each of the halobenzenes is detected as both a singly- and doubly-charged parent ion. Iodobenzene is also found as a stable triply-charged ion.

The conclusion to be drawn from the halobenzene series is that the heavy atom effect plays a large role in determining the dynamics. The larger halogens induce greater energetic splitting between the HOMO and HOMO–1, as well as the lowest unoccupied molecular orbital (LUMO) and LUMO+1 [15], and result in a reduced excited state

lifetime due to spin-orbit coupling. Iodobenzene is commonly used in molecular alignment studies [27] with 800 nm pulses, so its strong three-photon absorption and short predissociation lifetime must be consider when planning such an experiment.

6.2 – The CNOF isoelectronic series

The CNOF series is electronically very similar to the halobenzene series; the energetic degeneracies in benzene are lifted, while the same π structures continue to be involved in the ionization dynamics. While the dynamics are similar, it should be noted that at the time of this writing, experimental work is still underway, as the precise slopes involved in this series have shown some inconsistencies. Though we will nevertheless attempt to draw quantitative conclusions, the trustworthiness of the results is not beyond question. It should be noted that the yields of fluorobenzene are different in the CNOF series and the halobenzenes; data on the two series was recorded months apart, so fluorobenzene was measured separately with each series to ensure experimental consistency within each series. No significant differences arise between the two fluorobenzene datasets other than differing ranges of intensity. Results are presented in Fig. 5.

The curve for toluene appears as a slope six followed by a slope of three for higher intensity; this signifies a (3 + 3) REMPI. The slope of six is consistent with the known IP of 8.83 eV, suggesting that the ionization begins in the HOMO, and the slope of three is consistent with saturation of a singlet $^1\pi\pi^*$ state. The methyl group acts as only a weak perturbation on the phenyl ring; the nearest carbon atom sees merely another carbon bond nearby, and thus the nearby structure (namely the energy and stability of the $^1\pi\pi^*$ state) is largely unaffected compared to benzene.

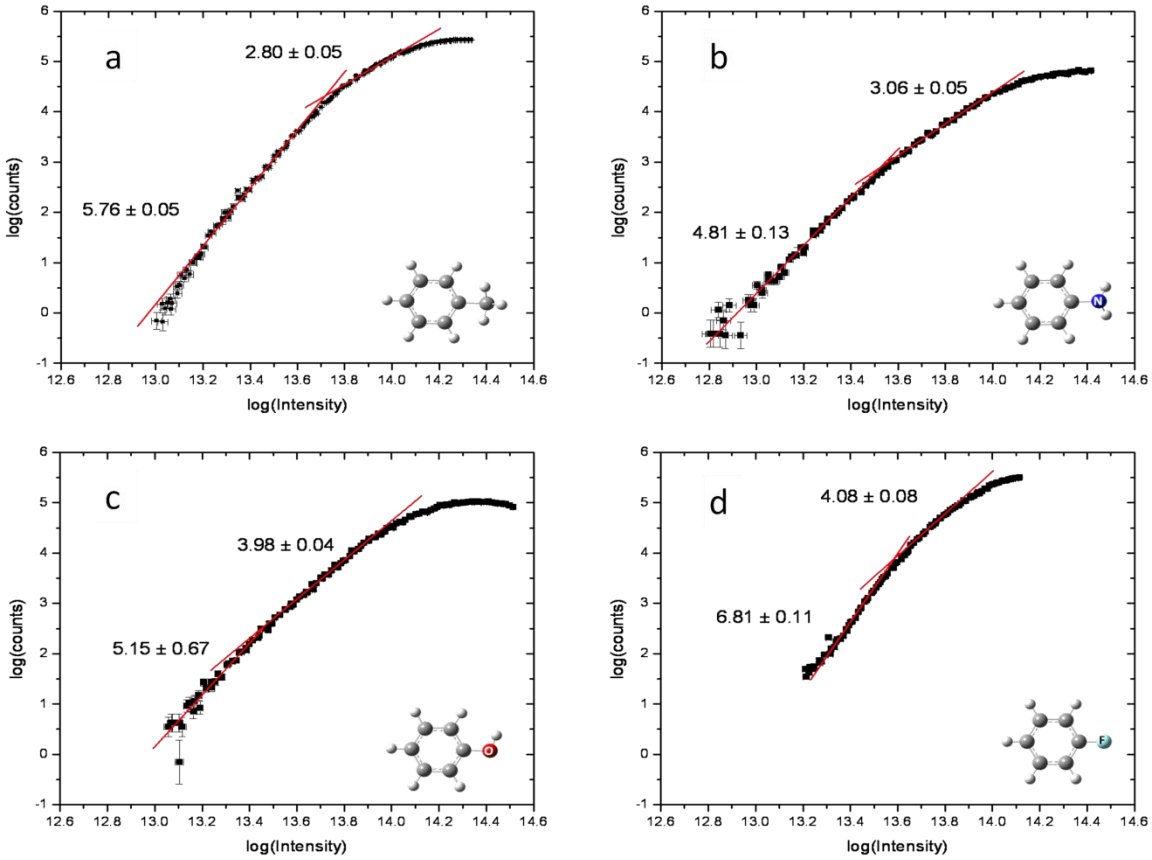

Figure 5 – Mathematically-fitted slopes of the CNOF series. Signatures of REMPI are observed on the fitted curves for toluene (**a**), aniline (**b**), phenol (**c**), and fluorobenzene (**d**).

Aniline, however, rises as a slope five followed by a slope three, consistent with either a (2 + 3) or (3 + 2) REMPI. To achieve ionization from the ground state takes 7.72 eV, almost exactly the limit of five 800 nm photons; this ionization must originate from the HOMO. A two-photon excitation from the ground state makes little sense given the known excitation energies seen in previous experiments [15,28], so a (2 + 3) REMPI seems unlikely. Aniline does, however, have known excitations which are near (within ~tens of meV) resonance with a three-photon excitation at 800nm (4.65 eV). Thus, a three-photon excitation from the HOMO is expected, and so (3 + 2) REMPI makes sense.

It is worth noting that there are three possible candidates for the intermediate state in aniline, as none is directly on resonance with three 800 nm photons. The unperturbed benzene ring has a degenerate HOMO consisting of two orbitals, both with $^1\pi\pi^*$ character. The addition of the sidegroups considered here lowers the symmetry of the molecule (from D_{6h} to C_{2v}) and lifts this degeneracy. While the methyl group in toluene acts as a comparatively small perturbation to the energies of these states, the amine group acts as a much larger perturbation and induces a larger splitting between the $^1\pi\pi^*$ states. These states in aniline have vertical excitation energies of 4.20 eV and 5.34 eV [29]; neither of these is easily accessible with three 800nm photons unless large AC Stark shifts are taking place; we rule out contributions from the 5.34 eV channel, as it is very unlikely to be energetically accessible. However, largely as a result of the lone pair in the nitrogen atom, there is a separate state, absent in benzene and toluene of $^1\pi\sigma^*$ character (largely resulting from a $^1\pi$(3s) Rydberg state) which lies 4.53 eV from the ground state. Although this state is dissociative along an N-H bond [29], this dissociation is thought to occur on longer timescales than our 50 fs laser pulses. While the $^1\pi\sigma^*$ state is closer in energy than the $^1\pi\pi^*$ state to the energy of three photons, [29] states that "There is no strong evidence for the $^1\pi\sigma^*$ … transition in the absorption spectrum, consistent with *ab initio* studies…and our [time-dependent density functional theory] calculations which suggest that the absorption cross section to the $1^1\pi\pi^*$ state is an order of magnitude greater than that to the $1\ ^1\pi\sigma^*$ [potential energy surface]." This suggests that the absorption to the $^1\pi\sigma^*$ state should be comparatively suppressed, though this was done through ultraviolet (1 + 1) REMPI. We thus conclude that the excitation is analogous to benzene and toluene through the $^1\pi\pi^*$ state which occurs through dynamic resonance. To

achieve the proper energy while maintaining the ability to reach the continuum with two additional photons, the excitation may be to a highly vibrationally excited state, though this remains somewhat speculative.

Unlike previous cases [30] in which the resonant excitation is thought to saturate at high intensities, here the two-photon ionization probability seems to saturate before the excitation, effectively short-circuiting the $^1\pi\pi^*$ state to the ionization continuum. Since it takes less intensity to saturate a two-photon transition than a 3-photon transition, this result is not entirely unexpected, and rate model calculations for (3 + 2) REMPI show that the higher-intensity slope indeed appears as a slope of three.

Species	IP (eV)	Low intensity slope	High intensity slope
Toluene	8.83	5.76 ± 0.05	2.80 ± 0.05
Aniline	7.72	4.81 ± 0.13	3.06 ± 0.05
Phenol	8.51	5.15 ± 0.67	3.98 ± 0.04
Fluorobenzene	9.20	6.81 ± 0.11	4.08 ± 0.08

Table 2 – Fitted slopes and ionization potentials of the CNOF series.

In the case of phenol, we see a slope of six followed by a slope four, with the slope of four dominating for over half a decade of intensity. However, the slope of six remains unconfirmed due to the low count rate in this range. In this case there is a competition between two different resonant $^1\pi\pi^*$ excitations: one resonant with three photons, and another approximately resonant with four [31]. Since a two-photon transition will saturate at lower intensity than a three- or four-photon transition, an effective four-photon process is left in competition with the still-unsaturated (3 + 3) process. This is further supported by the fact that the kinks in the curves for aniline and phenol (both the results of the saturation of a two-photon process) occur at 1.75×10^{14}

W/cm^2, while the kinks in the curves for toluene and fluorobenzene (both the results of the saturation of three-photon processes) occur at 4.1×10^{14} W/cm^2.

Finally, data from fluorobenzene exhibit a slope of seven followed by a slope of four. As seen in the previous section, these slopes are attributed to a (3 + 4) REMPI originating from the HOMO–1. Because the HOMO and HOMO–1 are close in energy [15], as are the LUMO and LUMO+1, the preferred excitation pathway seems to originate in the HOMO–1 and excite to the LUMO, which is bound deeply enough to require four photons for ionization. A summary of slopes and relevant quantities are shown in Table 2.

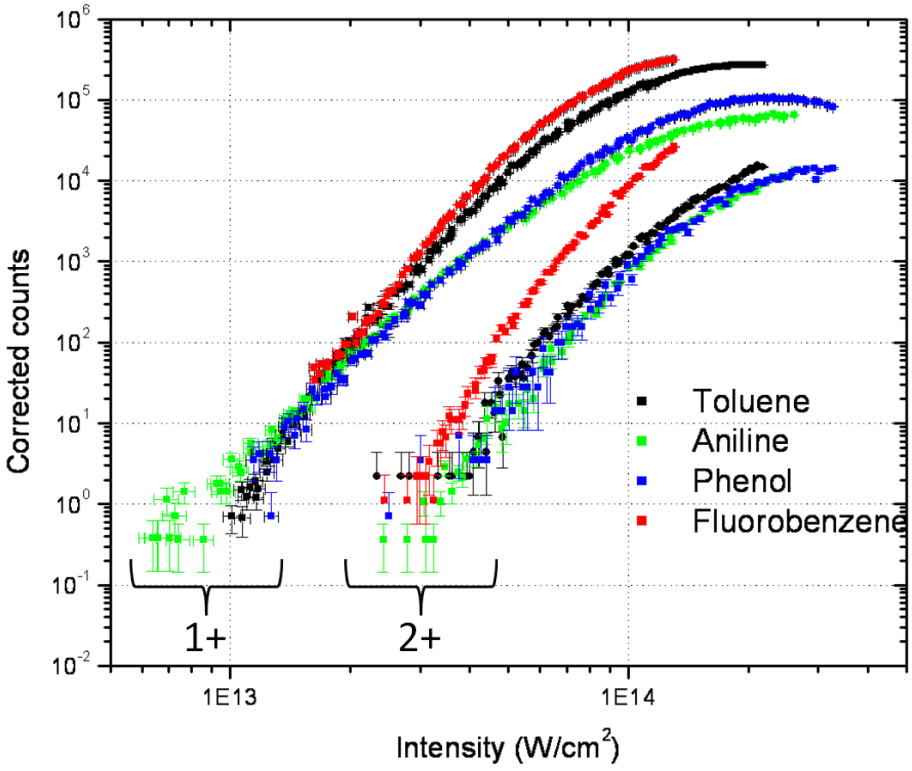

Figure 6 – Multiply-charged CNOF series. Each species is detected as both a singly- and doubly-charged parent ion. While toluene (black), aniline (green), and phenol (blue) have nearly identical yields of doubly-charged ions, the yield of doubly-charged fluorobenzene (red) is significantly enhanced.

Each molecule in this series is also found as a doubly-ionized parent, and their yields are shown in Fig. 6. Unlike the halobenzenes, the yields of the singly- and doubly-charged parents have no overlap at the intensities presented, so they can all be plotted on the same graph for easier comparison. The yields of the singly-charged toluene and fluorobenzene parent are enhanced in comparison to aniline and phenol; whether this is due to fragmentation will be discussed in Chapter 7. The doubly-charged yields show a striking enhancement of fluorobenzene in comparison to the rest of the series, all of which are nearly identical. In fact, the doubly-charged fluorobenzene rises with approximate linear slopes of nine and five, though this does not necessarily represent (4 + 5) REMPI, since the dynamics also depend on the first ionization.

6.3 – Compound functional groups: methyl, hydroxyl, and methoxyl substitutions

Having studied the substitutions in the CNOF series, it is perhaps interesting to examine combinations of these substitutions; to do so, we studied anisole. Anisole is comprised of a phenyl ring with an $–O–CH_3$ side group, which combines the effects of the hydroxyl group of phenol with the methyl group of toluene. Fig. 7 shows the fitted slopes for anisole.

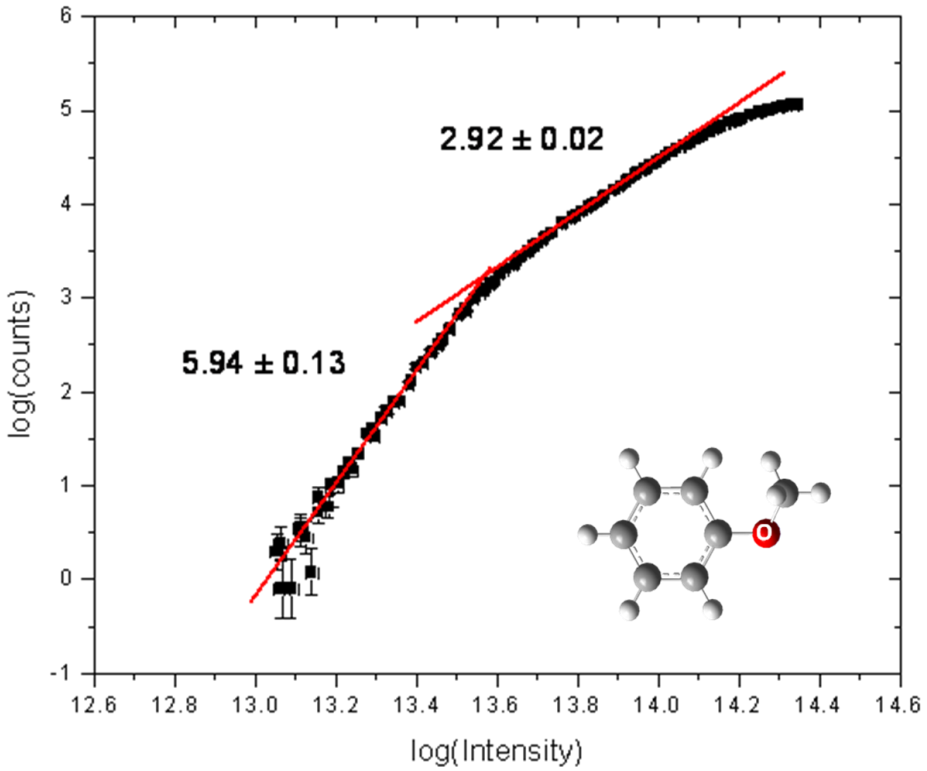

Figure 7 – Parent ion yield of anisole. Anisole shows the signature of (3 + 3) REMPI, with a very sharp kink, suggesting a highly resonant process.

The yield of the singly-charged anisole parent shows a distinct kink with rigid linear slopes of six and three. While some molecules' yields settle on their high-intensity slopes only briefly, the slope three region in anisole is extensive and does not deviate from the fitted line. This suggests a robust resonance in a (3 + 3) REMPI scheme; indeed, the electronic spectrum of anisole [32] shows a strong absorption at 4.62 eV, which is highly resonant with three 800 nm photons. It seems that the presence of the oxygen atom does not affect anisole in the same way it affected phenol. This may be because it is "dressed" with the methyl group such that the perturbation of the oxygen atom is effectively hidden from the phenyl ring.

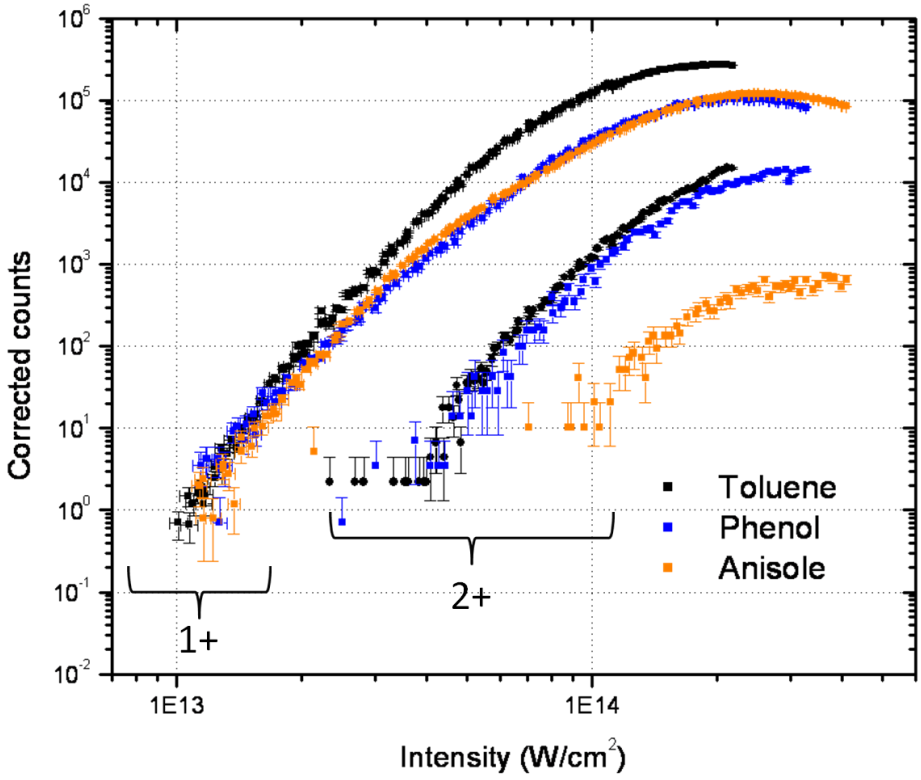

Figure 8 – Singly- and multiply-charged yields of toluene, phenol, and anisole. While the singly-charged ions of all three species have comparable yields, ionization of toluene (black) is enhanced in comparison to phenol (blue) and anisole (orange). The doubly-charged states of toluene and phenol are nearly identical, while doubly-charged anisole is suppressed by nearly two orders of magnitude.

The doubly-charged state of anisole, seen in Fig. 8 along with toluene and phenol for comparison, is considerably suppressed. At present it is not clear why this should be the case, though with a side group which extends physically much farther away from the phenyl ring, the likelihood of fragmentation upon the second ionization may be increased.

6.4 – The azabenzenes

6.4.1 – Through-bond and through-space interactions

The importance of the difference between through-bond and through-space interactions [33] should not be discounted. When two degenerate orbitals interact with significant spatial overlap, they form two combination orbitals: one the symmetric

superposition, and the other the antisymmetric superposition. These orbitals were calculated in Gaussian 03 [34], and are seen in Fig. 9. Of these orbitals, the antisymmetric superposition is usually found at higher energy, as the system is weakened by a node found in the center of the probability distribution, which is a necessary feature to create an antisymmetric state. Through-space interactions tend to dominate molecular electronic structures, as the interaction is direct between two orbitals.

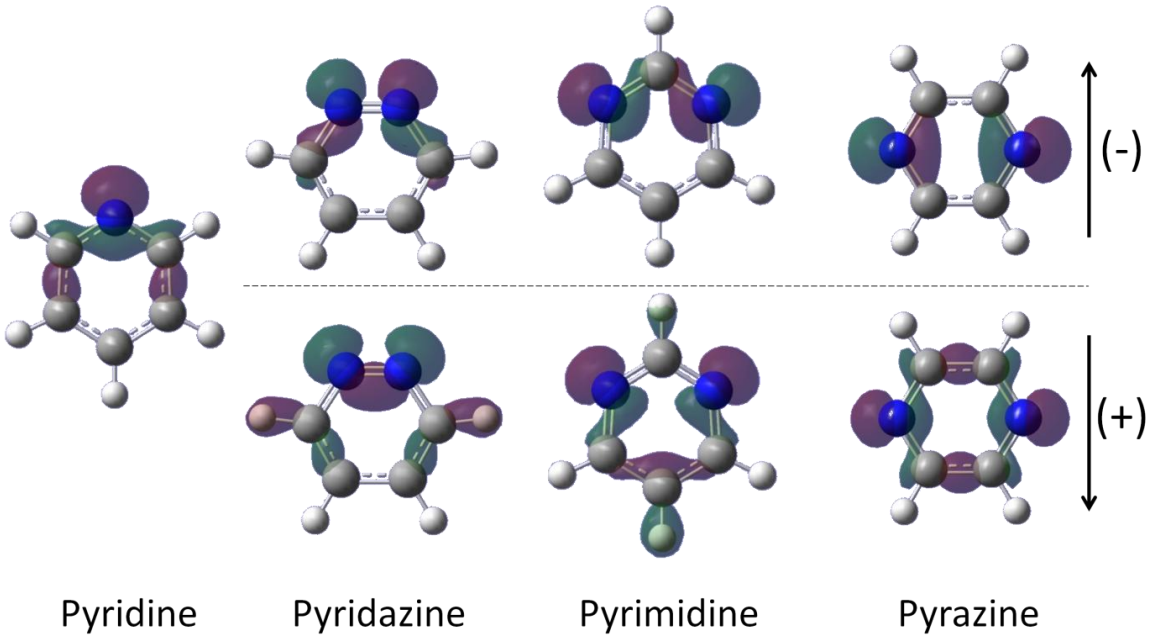

Figure 9 – Lone pair orbitals in the azabenzenes. The lone pairs of the nitrogen atoms play a large role in the dynamics of the azabenzenes. While these orbitals originate from the lone pairs, they contribute electron density throughout the molecule, which increases the availability of through-bond interactions. While pyridine has only one lone pair, pyridazine, pyrimidine, and pyrazine have two lone pair orbitals: one superposition with positive symmetry upon reflection, and one with negative symmetry. The positive-symmetry superpositions spread their electron probability density more generously throughout the ring.

When the degenerate orbitals do not have significant spatial overlap, they can interact only indirectly. This is accomplished through a neighboring bond; the presence of a lone pair in pyrazine, for example, perturbs a σ orbital, which in turn affects the other lone pair. Such an indirect coupling is called a through-bond interaction, since an

intermediate bond is necessary to couple the degenerate orbitals. Again looking to pyrazine, the nature of the interaction depends on the symmetries of the orbitals involved. Only orbitals of like symmetry will interact with each other; the interaction integral of a symmetric and an antisymmetric orbital vanishes due to orthogonality. As such, the symmetric superposition of lone pairs ($n_1 + n_2$) interacts with the on-axis (C2-C3) σ orbital, and the antisymmetric superposition ($n_1 - n_2$) interacts with the nonbonding σ* orbital. In pyrazine the symmetric n-σ-n interaction moves to higher energy, while the antisymmetric n-σ*-n interaction moves to lower energy. A diagram of these energies, taken from Ref. [35], is seen in Fig. 10.

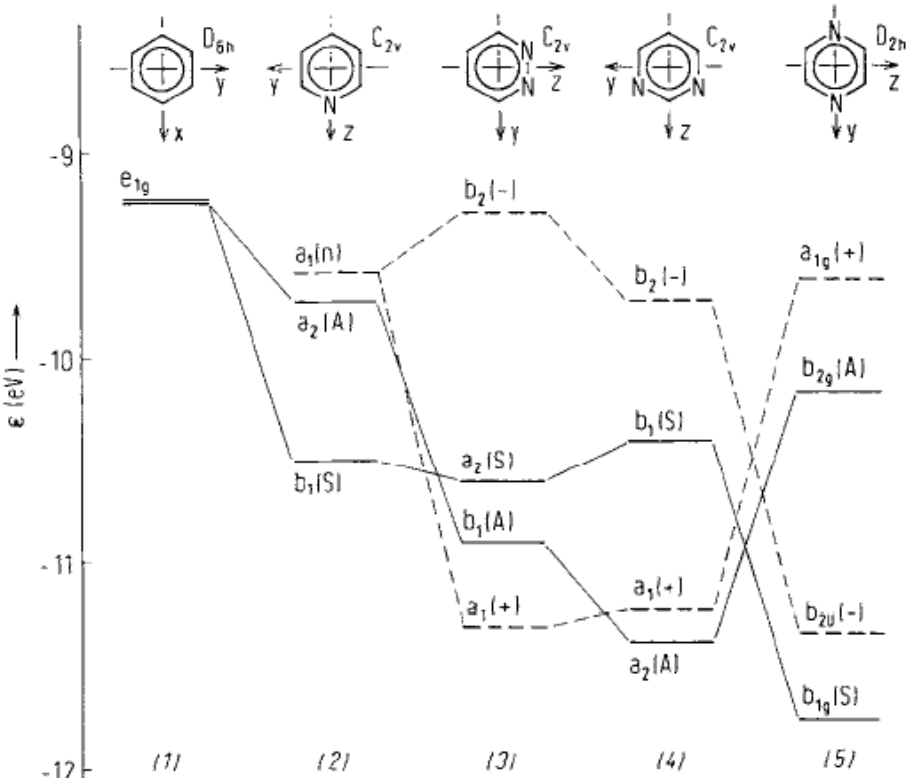

Figure 10 – The HOMO band of benzene and the azabenzenes. The lone pair orbitals of the azabenzenes complicate the highest occupied orbitals considerably. Benzene, on the far left, had two energetically degenerate orbitals; in pyridine three nondegenerate orbitals are present, and in the diazines four must be taken into account. Solid lines represent π orbitals, and dotted lines represent lone pair superpositions. Note that for pyrazine (far right) the symmetric and antisymmetric orbitals cross; this sets pyrazine apart from the rest of the series in a fundamental way.

This runs counter to the conventional through-space interaction, which results in the antisymmetric state having a higher energy than the symmetric superposition. This sets pyrazine apart from the other azabenzenes we consider; the electronic structure has symmetric orbitals as the HOMO and HOMO–1, and since the dynamics of ionization and fragmentation typically hinge on the properties of the most weakly-bound orbitals, the presence of the through-bond interaction is significant.

6.4.2 – Parent Ion Yields

Parent ion yields of all four species are seen in Fig. 11, and are summarized in Table 3. The curve for pyridine, when fit to two regions with integer log-log slope, displays a slope of six at low intensity giving way to a slope of three at higher intensity, indicative of a (3 + 3) REMPI process. Six-photon ionization is expected when considering ionization from either the HOMO or HOMO–1, which are nearly-isoenergetic π and n orbitals (the *n* orbital strongly correlating to the lone pair of the substituent nitrogen atom), as only these orbitals are within the range of six 800 nm photons (although only barely) [36]. Of these two orbitals, only the π has a single-photon transition energetically resonant with three 800 nm photons necessary to observe (3 + 3) REMPI. In this case, the excitation mechanism is the $^1\pi\pi^*$ transition analogous to the $E_{1g}^4 E_{2u}^0 \rightarrow E_{1g}^3 E_{2u}^1$ transition in benzene. These benzene-like structures prove to be fairly robust throughout this molecular series; the most relevant in this case is the HOMO to LUMO $^1\pi\pi^*$ transition in benzene (vertical energy 4.9 eV). In the molecules considered here, this transition is only slightly perturbed to vertical values between 4.8-5.1 eV [36-39].

Upon close examination of pyridine in Fig. 11 (**a**), however, it is apparent that at the lowest intensities the data trends slightly, but definitively, beneath a line with slope six. In fact, when fitting only the 29 lowest-intensity data points, a slope of seven is found, followed by a slope six from points 29-55, and again the slope three from points 73-94 before higher-order processes (multiple ionization, fragmentation) bring the parent yield down. Alternatively, if all of the first 55 points are fitted together, one finds a slope of 6.27; however, when this fit is applied, it becomes clear that this slope is too low for the slope-seven region and too high for the slope-six region. This makes it a poor overall compromise, since no range of intensities exists in which a slope 6.27 is a good fit. Due to the experimental uncertainties at low intensity (particularly low count rate and precise calibration of the intensities) we conclude that the slope of six is legitimate[†].

Pyridazine, seen in Fig. 11 (**b**), also exhibits log-log slopes of six and three, again indicative of (3 + 3) REMPI. Although this result is the same as the curve for pyridine in a qualitative sense, the dynamics appears to be different. The introduction of the second nitrogen substituent creates an energetic splitting of the two lone pair states which owes to the symmetric (n_+) and antisymmetric (n_-) superpositions. Because the lone pairs in this case are adjacent, there is substantial spatial overlap which leads to a larger splitting than in the other diazines.

[†] The ionization suppression at low intensity is repeatable through several datasets subjected to a wide array of experimental parameters, yet remains unique to pyridine, though it must be emphasized that the lowest intensities have the largest relative uncertainties in both intensity calibration and counting statistics. If one were to assume the suppression to be physical, one could imagine that the dominant excitation transition is slightly off resonance until the rising edge of the laser pulse is strong enough to reinforce the resonance through a dynamical Stark shift, known as a dynamic resonance. Though our data alone cannot support this, it could serve as a plausible hypothesis.

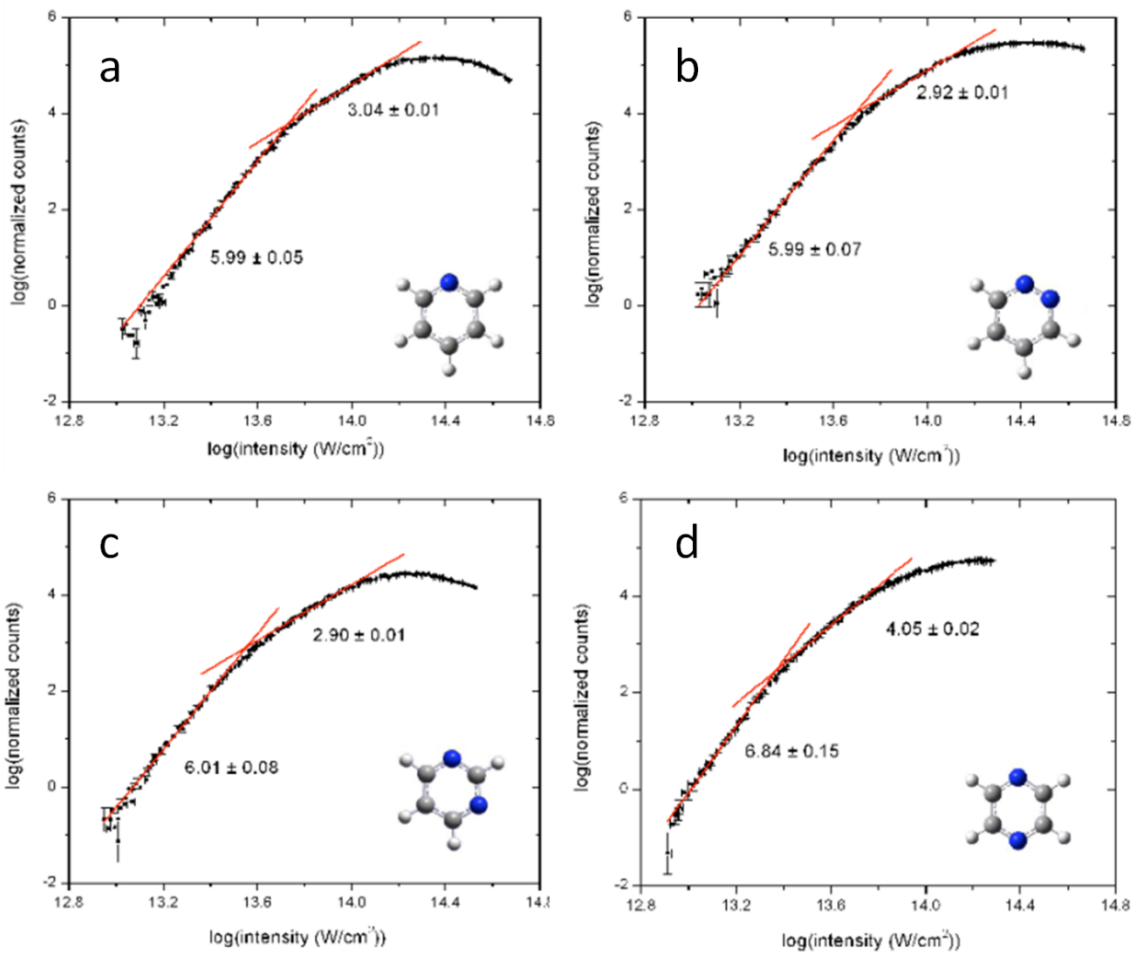

Figure 11 – Mathematically-fitted slopes of the azabenzenes. While the specific transitions which govern the dynamics appear to be different, pyridine (**a**), pyridazine (**b**), and pyrimidine (**c**) all demonstrate (3 + 3) REMPI. Pyrazine (**d**), however, shows signatures of (3 + 4) REMPI which does not occur from the HOMO.

The energy difference between the HOMO and all other bound states leaves the n_ as the only orbital capable of supporting six-photon ionization, so the ionization dynamics must originate there. But although the electronic excitations in pyridazine have been well-documented [37,40] there are no transitions to nπ* or n(Rydberg) excited states that are on (or even near) resonance for excitation by three 800 nm photons. At present this issue remains unresolved unless the vertical and adiabatic binding energies of the HOMO–1 (of π structure) differ by more than ≈1.1 eV (in which case the benzene-like

$^1\pi\pi^*$ structure could again be responsible for (3 + 3) REMPI). However, such a large difference between the vertical and adiabatic energies is unlikely [41]. At present we hypothesize that the AC Stark shift of the $n\pi^*$ state is significant enough to bring the transition into a dynamic resonance [42], since the field is large enough at these intensities to induce ponderomotive shifts [43] of several eV. Unfortunately, we must speculate here; the definitive dynamics in pyridazine remains open to interpretation.

Pyrimidine is also most accurately fit with log-log slopes of six and three, as seen in Fig. 11 (**c**). In this case the dynamics must originate from the HOMO, here the antisymmetric n_-, since it is the only orbital within the energetic range of six photons (although only barely; the first IP of pyrimidine is 9.342 eV [44], where six 800 nm photons are 9.30 with a spread of 0.06 eV due to the pulse bandwidth). Here a $^1n\pi^*$ transition ($^1A_2$ character [45]) is most likely responsible for the dynamics. This transition has been observed in VUV absorption [46] and electron-energy loss spectra [38] at a vertical energy of 4.6-4.7 eV. The multiphoton processes we typically observe seem to be restricted by adiabatic energies (three-photon absorption of 4.65 eV dominates the excitation in benzene [30] in spite of a well-documented vertical energy of 4.9 eV [37]). Nevertheless, we find it reasonable to envision either a Stark shift of the levels involved in this transition or excitation to a vibrationally-excited state such that a three-photon $^1n\pi^*$ excitation could find itself on resonance.

The curve for pyrazine, seen in Fig. 11 (**d**), shows slopes of seven and four, indicative of either (3 + 4) or (4 + 3) REMPI. The low-intensity slope is seven, although the HOMO (n_+) should be within the reach of six photons (its IP is 9.309 eV [47]; six 800 nm photons is 9.30 eV). This would make the likeliest ionization a (3 + 4) REMPI in the

benzene-like π system once again. In fact, even if the n_+ orbital is also in the seven-photon range, electron-energy loss and single-photon experiments indicate that the benzene-like ππ* transitions tend to dominate over the much weaker nπ* transitions [39].

Species	IP (eV)	Low intensity slope	High intensity slope
Pyridine	9.26	5.99 ± 0.05	3.04 ± 0.01
Pyridazine	8.74	5.99 ± 0.07	2.92 ± 0.01
Pyrimidine	9.33	6.01 ± 0.08	2.90 ± 0.01
Pyrazine	9.31	6.84 ± 0.15	4.05 ± 0.02

Table 3 – Fitted slopes and ionization potentials of the azabenzenes.

We note that a part of the benzene structure includes transitions expected to be nearly resonant with four photons which could contribute to a (4 + 3) REMPI process. We consider in principle all energetically-allowed transitions, such as the ππ* ($^1B_{1u}$) and n3s ($^1A_{1g}$), even those which are typically forbidden by symmetry in the single-photon case; calculating the transition matrix elements for multiphoton processes [48] is prohibitively involved, and the complexity of multiphoton interaction can lead to "forbidden" single-photon transitions being allowed in the multiphoton case, as was discussed in Chapter 4. However, a population rate model based on generalized cross sections with I^N optical pumping rates in multiphoton absorption [43] demonstrates that, if both three- and four-photon excitations are resonant, the three-photon channel dominates the excited state population. Even for similar generalized cross-sections [43] the three-photon resonant state acquires the majority of the probability density. In other words, a three-photon transition saturates at lower intensity that a four-photon transition. As a result, we determine that the (3 + 4) REMPI is the leading source of parent ionization.

As seen in Fig. 12, the parent ion yields differ significantly in their total yields near saturation. At each molecule's saturation intensity, it is expected that every target molecule undergoes either ionization or fragmentation; thus, differences in the parent ion yields at saturation must be due to fragmentation. Nevertheless, for the purposes of this chapter it is useful to identify general trends, such as the relative instability of the singly-ionized pyrimidine parent and the relative enhancement of the singly-ionized pyridazine parent. Oddly, these two are the most similar in their electronic orbital configuration, both having their antisymmetric *n* and π orbitals as the HOMO and HOMO–1, respectively.

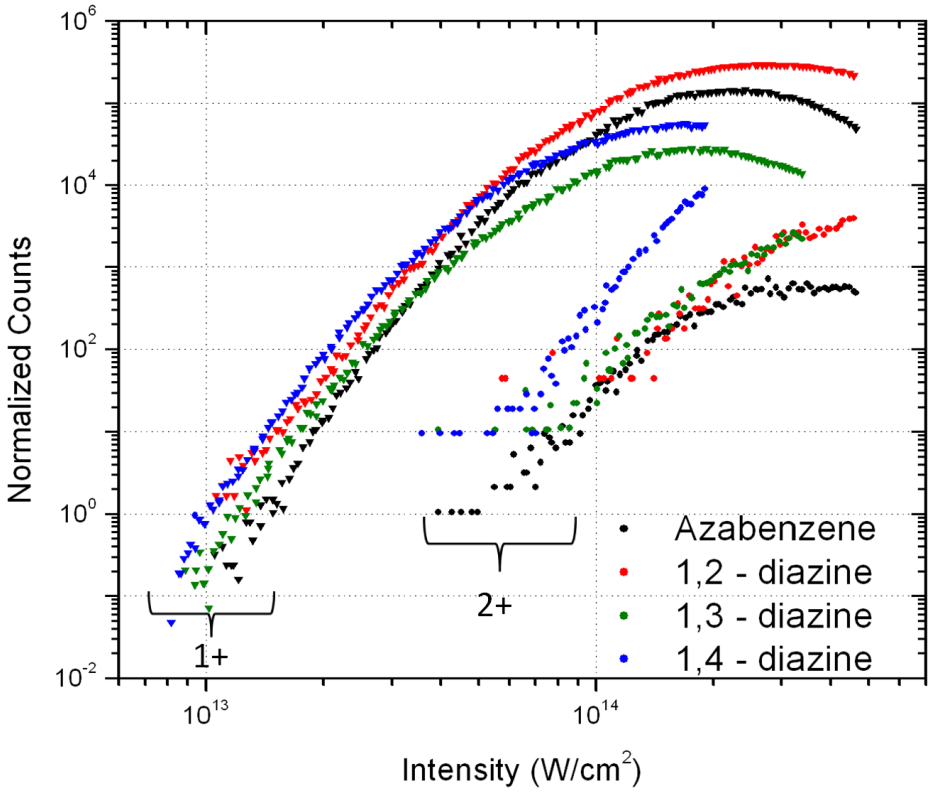

Figure 12 – Multiple ionizations of the azabenzenes. The maximum yields of the singly-charged parent ions differ considerably, with pyridazine (red) largely enhanced and pyrimidine (green) suppressed, details of which will be explored in Chapter 7. In the doubly-charged parent ion yields, pyridine (black) is suppressed, while pyrazine (blue) is comparatively enhanced. This is yet another example of the differences between pyrazine and the rest of the series.

Each of the molecules presented is also found in its dicationic state. While the precise dynamics of the second ionization cannot be inferred through the results of the current experiment, we note that pyrazine has a larger propensity to form a doubly-charged ion than the other species. We attribute this to the fact that pyrazine's symmetry (D_{2h}) differentiates it from the rest of the series (C_{2v}) and gives it a symmetric (A_g) HOMO [49,50], though why this leads to a more stable dication needs further investigation. The doubly-charged parent ions of each species have approximately the same appearance intensity (≈6-8×10^{13} W/cm^2), but the yield for pyrazine rises more prominently than the rest. In fact, the pyrazine dication yield rises with a log-log slope of six, although due to the more complicated dynamics of multiple ionizations, this is not likely indicative of a six-photon absorption.

We also observe that the pyridine dication yield is suppressed in comparison to the rest of the series, even saturating between 3-4×10^{14} W/cm^2. This suggests an inherent instability in the multiply-charged parent ion of pyridine in comparison to the other species; this is further upheld by the appearance of broader features in the mass spectra suggestive of long-lived metastable states which fragment during their flight to the detector [51]. The details of this process are presented in Chapter 8. Pyridine shows a large (multiple orders of magnitude) enhancement in the yield of such broad features in the mass spectra, which adds credence to the sort of instability seen in the dication.

While the π system inherited from benzene is only mildly perturbed, and thus capable of playing a strong role in the intense-field dynamics of the mono- and di-substituted azabenzenes, the presence of lone pair states allows for much richer dynamics. In particular, the number of possible transitions in competition is increased

compared to benzene and, in some cases, it is these transitions that dominate the intense-field ionization dynamics.

In particular, it seems that the introduction of the *n* state in pyridine does little to perturb the dynamics compared to benzene other then to destabilize the dication. It is only in the diazines, where multiple lone pairs interact with each other, that the dynamics becomes significantly perturbed. In pyrazine, where the symmetric superposition of lone pair orbitals becomes the HOMO, the perturbation affects the system differently. This sets pyrazine apart from the other species in terms of different ionization dynamics and increased yield of the doubly-charged parent.

References

[1] Corkum, P. 1993, "Plasma Perspective on Strong-Field Multiphoton Ionization," *Physical Review Letters,* vol. 71, no. 13, pp. 1994-1997.

[2] Becker, A. & Faisal, F.H.M. 2005, "Intense-field many-body S-matrix theory," *Journal of Physics B-Atomic Molecular and Optical Physics,* vol. 38, no. 3, pp. R1-R56.

[3] Hertel, I.V. & Radloff, W. 2006, "Ultrafast dynamics in isolated molecules and molecular clusters," *Reports on Progress in Physics,* vol. 69, no. 6, pp. 1897-2003.

[4] Sansone, G., Poletto, L. & Nisoli, M. 2011, "High-energy attosecond light sources," *Nature Photonics,* vol. 5, no. 11, pp. 655-663.

[5] Chang, Z., *Fundamentals of Attosecond Optics,* CRC Press, 2011.

[6] Boutu, W., Haessler, S., Merdji, H., Breger, P., Waters, G., Stankiewicz, M., Frasinski, L.J., Taieb, R., Caillat, J., Maquet, A., Monchicourt, P., Carre, B. & Salieres, P. 2008, "Coherent control of attosecond emission from aligned molecules," *Nature Physics,* vol. 4, no. 7, pp. 545-549.

[7] Rabitz, H. 2006, "Strong-arming molecular dynamics," *Science,* vol. 314, no. 5797, pp. 264-265.

[8] Sansone, G., Kelkensberg, F., Morales, F., Pérez-Torres, J.F., Martín, F. & Vrakking, M.J.J. 2012, "Attosecond Time-Resolved Electron Dynamics in the Hydrogen Molecule," *IEEE Journal of Selected Topics in Quantum Electronics,* vol. 18, no. 1, pp. 520-530.

[9] Methods are beyond reach (see http://www.physorg.com/news194276894.html). Though impressive, this research required immense and costly resources on a record supercomputer, with software developed and specifically optimized for its architecture. No resources exist to simulate the intense-field photodynamics of larger molecules.

[10] Zhang, X.P., Wei, Z.R., Lee, W.B., Chao, T.J. & Lin, K.C. 2008, "Photodissociation of dibromobenzenes at 266 nm by the velocity imaging technique," *Chemphyschem : a European journal of chemical physics and physical chemistry,* vol. 9, no. 12, pp. 1721-1728.

[11] Philis, J., Bolovinos, A., Andritsopoulos, G., Pantos, E. & Tsekeris, P. 1981, "A comparison of the absorption spectra of the fluorobenzenes and benzene in the region 4.5-9.5 eV," *Journal of Physics B: Atomic and Molecular Physics,* vol. 14, no. 19, pp. 3621-3635.

[12] Yoon O.K., Hwang W.G., Choe J.C. & Kim M.S. 1999, "Internal energy content of n-butylbenzene, bromobenzene, iodobenzene and aniline molecular ions generated

by two-photon ionization at 266 nm. A photodissociation study," *Rapid Communications in Mass Spectrometry*, vol. 13, no. 14, pp. 1515-1521.

[13] Talebpour, A., Bandrauk, A., Vijayalakshmi, K. & Chin, S. 2000, "Dissociative ionization of benzene in intense ultra-fast laser pulses," *Journal of Physics B-Atomic Molecular and Optical Physics,* vol. 33, no. 21, pp. 4615-4626.

[14] Kjeldsen, T. & Madsen, L. 2005, "Strong-field ionization of diatomic molecules and companion atoms: Strong-field approximation and tunneling theory including nuclear motion," *Physical Review A,* vol. 71, no. 2.

[15] Kimura K., *Handbook of HeI photoelectron spectra of fundamental organic molecules: ionization energies, ab initio assignments, and valence electronic structure for 200 molecules*, Japan Scientific Societies Press, 1981.

[16] Ruscic, B., Klasinc, L., Wolf, A. & Knop, J.V. 1981, "Photoelectron spectra of and *ab initio* calculations on chlorobenzenes. 1. Chlorobenzene and dichlorobenzenes," *The Journal of Physical Phemistry,* vol. 85, no. 11, pp. 1486-1489.

[17] Unny, S., Du, Y., Zhu, L., Truhins, K., Gordon, R.J., Sugita, A., Kawasaki, M., Matsumi, Y., Delmdahl, R., Parker, D.H. & Berces, A. 2001, "Above-Threshold Effects in the Photodissociation and Photoionization of Iodobenzene," *The Journal of Physical Chemistry A,* vol. 105, no. 11, pp. 2270-2280.

[18] Kadi, M., Davidsson, J., Tarnovsky, A., Rasmusson, M. & Akesson, E. 2001, "Photodissociation of aryl halides in the gas phase studied with femtosecond pump-probe spectroscopy," *Chemical Physics Letters*, vol. 350, no. 1-2, pp. 93-98.

[19] Lee, S., Tang, K., Chen, I., Schmitt, M., Shaffer, J.P., Schultz, T., Underwood, J.G., Zgierski, M.Z. & Stolow, A. 2002, "Substituent Effects in Molecular Electronic Relaxation Dynamics via Time-Resolved Photoelectron Spectroscopy: ππ* States in Benzenes," *The Journal of Physical Chemistry A,* vol. 106, no. 39, pp. 8979-8991.

[20] Rasmusson, M., Lindh, R., Lascoux, N., Tarnovsky, A., Kadi, M., Kuhn, O., Sundstrom, V. & Akesson, E. 2003, "Photodissociation of bromobenzene in solution," *Chemical Physics Letters,* vol. 367, no. 5-6, pp. 759-766.

[21] Anders Borg, O., Karlsson, D., Isomäki-Krondahl, M., Davidsson, J. & Lunell, S. 2008, "Predissociation of chlorobenzene, beyond the pseudo-diatomic model," *Chemical Physics Letters*, vol. 456, no. 4-6, pp. 123-126.

[22] Sage, A.G., Oliver, T.A.A., Murdock, D., Crow, M.B., Ritchie, G.A.D., Harvey, J.N. & Ashfold, M.N.R. 2011, "nσ* and πσ* excited states in aryl halide photochemistry: a comprehensive study of the UV photodissociation dynamics of iodobenzene," *Physical Chemistry Chemical Physics*, vol. 13, no. 18, pp. 8075-8093.

[23] Dietz, T.G., Duncan, M.A., Liverman, M.G. & Smalley, R.E. 1980, "Resonance enhanced two-photon ionization studies in a supersonic molecular beam:

Bromobenzene and iodobenzene," *Journal of Chemical Physics,* vol. 73, no. 10, pp. 4816.

[24] Wilkerson, C.W. & Reilly, J.P. 1990, "Variations in detection efficiency of halobenzenes studied by using gas chromatography/laser ionization mass spectrometry: correlation with excited-state lifetimes," *Analytical Chemistry,* vol. 62, no. 17, pp. 1804-1808.

[25] Cheng, P., Zhong, D. & Zewail, A. 1995, "Kinetic-Energy, Femtosecond Resolved Reaction Dynamics - Modes of Dissociation (In Iodobenzene) from Time-Velocity Correlations," *Chemical Physics Letters,* vol. 237, no. 5-6, pp. 399-405.

[26] Matsumoto, J., Lin, C. & Imasaka, T. 1997, "Enhancement of the molecular ion peak from halogenated benzenes and phenols using femtosecond laser pulses in conjunction with supersonic beam multiphoton ionization mass spectrometry," *Analytical Chemistry,* vol. 69, no. 22, pp. 4524-4529.

[27] Stapelfeldt, H. 2003, "Colloquium: Aligning molecules with strong laser pulses," *Reviews of Modern Physics,* vol. 75, no. 2, pp. 543-557.

[28] Honda, Y., Hada, M., Ehara, M. & Nakatsuji, H. 2002, "Excited and ionized states of aniline: Symmetry adapted cluster configuration interaction theoretical study," *Journal of Chemical Physics,* vol. 117, no. 5, pp. 2045.

[29] King, G.A., Oliver, T.A. & Ashfold M.N.R. 2010, "Dynamical insights into 1πσ* state mediated photodissociation of aniline," *Journal of Chemical Physics,* vol. 132, no. 21, pp. 214307.

[30] Scarborough, T.D., Strohaber, J., Foote, D.B., McAcy, C.J. & Uiterwaal, C.J.G.J. 2011, "Ultrafast REMPI in benzene and the monohalobenzenes without the focal volume effect," *Physical Chemistry Chemical Physics,* vol. 13, no. 30, pp. 13783-13790.

[31] Schick, C.P. & Weber, P.M. 2001, "Ultrafast Dynamics in the Three-Photon, Double-Resonance Ionization of Phenol via the S2 Electronic State," *The Journal of Physical Chemistry A,* vol. 105, no. 15, pp. 3735-3740.

[32] Ribblett, J.W., Sinclair, W.E., Borst, D.R., Yi, J.T. & Pratt, D.W. 2006, "High resolution electronic spectra of anisole and anisole-water in the gas phase: hydrogen bond switching in the S1 state," *The Journal of Physical Chemistry.A,* vol. 110, no. 4, pp. 1478-1483.

[33] Hoffmann, R. 1971, "Interaction of orbitals through space and through bonds," *Accounts of Chemical Research,* vol. 4, no. 1, pp. 1-9.

[34] Frisch, M. J. *et al*, Gaussian 03, Gaussian Inc., Wallingford CT, 2004.

[35] Gleiter, R., Heilbronner, E., and Hornung, V. 1970, "Lone Pair Interaction in Pyridazine, Pyrimidine, and Pyrazine," *Angewandte Chemie International,* vol. 9, no. 11, pp. 901-902.

[36] Walker, I., Palmer, M. & Hopkirk, A. 1990, "The Electronic States of the Azines .2. Pyridine, Studied by Vuv Absorption, Near-Threshold Electron-Energy Loss Spectroscopy and *ab initio* Multireference Configuration-Interaction Calculations," *Chemical Physics,* vol. 141, no. 2-3, pp. 365-378.

[37] Palmer, M. & Walker, I. 1991, "The Electronic States of the Azines .5. Pyridazine, Studied by Vuv Absorption, Near Threshold Electron Energy-Loss Spectroscopy and *ab initio* Multireference Configuration-Interaction Calculations," *Chemical Physics,* vol. 157, no. 1-2, pp. 187-200.

[38] Palmer, M., Walker, I., Guest, M. & Hopkirk, A. 1990, "The Electronic States of the Azines .3. Pyrimidine, Studied by Vuv Absorption, Near-Threshold Electron Energy-Loss Spectroscopy and *ab initio* Multireference Configuration Calculations," *Chemical Physics,* vol. 147, no. 1, pp. 19-33.

[39] Walker, I. & Palmer, M. 1991, "The Electronic States of the Azines .4. Pyrazine, Studied by Vuv Absorption, Near-Threshold Electron Energy-Loss Spectroscopy and *ab initio* Multireference Configuration-Interaction Calculations," *Chemical Physics,* vol. 153, no. 1-2, pp. 169-187.

[40] Hannay, C., Duflot, D., Flament, J. & Hubin-Franskin, M. 1999, "The core excitation of pyridine and pyridazine: An electron spectroscopy and *ab initio* study," *Journal of Chemical Physics,* vol. 110, no. 12, pp. 5600-5610.

[41] *NIST Chemistry WebBook,* National Institute of Standards and Technology, http://webbook.nist.gov/chemistry.

[42] Bordyug, N.V. & Krainov, V.P. 2007, "Dynamic resonances in ultra-short laser pulses," *Laser Physics Letters,* vol. 4, no. 6, pp. 418-420.

[43] Yamanouchi, K. (ed), *Lectures on Ultrafast Intense Laser Science 1*, Springer, 2010.

[44] Sato, S., Omiya, K. & Kimura, K. 1998, "Cation vibrational spectra of pyrimidine and its van der Waals complexes with Ar and N-2 by ZEKE photoelectron spectroscopy," *Journal of Electron Spectroscopy and Related Phenomena,* vol. 97, no. 1-2, pp. 121-129.

[45] Stener, M., Decleva, P., Holland, D.M.P. & Shaw, D.A. 2011, "A study of the valence shell electronic states of pyrimidine and pyrazine by photoabsorption spectroscopy and time-dependent density functional theory calculations," *Journal of Physics B-Atomic Molecular and Optical Physics,* vol. 44, no. 7, pp. 075203.

[46] Vall-llosera, G., Coreno, M., Erman, P., Huels, M.A., Jakubowska, K., Kivimaki, A., Rachlew, E. & Stankiewicz, M. 2008, "VUV photoionisation of free azabenzenes: Pyridine, pyrazine, pyrimidine, pyridazine and s-triazine," *International Journal of Mass Spectrometry,* vol. 275, no. 1-3, pp. 55-63.

[47] de Groot, M. & Buma, W.J. 2007, "Photoelectron studies on vibronic coupling in pyrazine.," *The Journal of chemical physics,* vol. 127, no. 10, pp. 104301.

[48] Boyd, R.W., *Nonlinear optics* Academic Press, 2003.

[49] Cotton, F.A., *Chemical Applications of Group Theory, 3rd Edition*, Wiley, 1990.

[50] Harris, D.C. & Bertolucci, M.D., *Symmetry and spectroscopy: an introduction to vibrational and electronic transitions*, Dover, 1989.

[51] Foote, D.B., Scarborough, T.D. & Uiterwaal, C.J. 2012, "Observation and Identification of Metastable Excited States in Ultrafast Laser-Ionized Pyridine," *Journal of the American Society for Mass Spectrometry*, DOI: 10.1007/s13361-012-0346-6.

Chapter 7

Molecular fragmentation of systematic series

Intense-field molecular photodynamics is certainly not restricted to ionization. In many cases, things can be learned by studying the ways in which the molecules break apart. Our experiments measure the mass-to-charge ratio of all ions created in the focus (there are some exceptions, though this will be discussed in Chapter 8), so the ionic yields can be evaluated for many relevant molecular fragments. Because these yields are the results of more complex dynamics than just the removal of an electron, the log-log slopes of the yields do not necessarily denote any particular physical processes. As such, the results in this chapter will be discussed in an empirical sense.

Since our goal is to study the effects of perturbations to the benzene system, we first look at how benzene fragments in intense fields. The prominent ionic fragments are shown in Fig. 1. It should be noted that $C_3H_3^+$ and $C_6H_6^{2+}$ have the same charge-to-mass ratio; this is not a problem, as the doubly-charged parent is also found as a "heavy" parent (with a single mass-13 carbon atom). As such, the doubly-charged parent is measured and scaled up to compensate for its lower isotopic abundance (about 6.5% of all benzene molecules have a heavy carbon isotope). This calibrated amount is then

subtracted from the yield of the $C_3H_3^+$ to eliminate contributions from the doubly-charged parent.

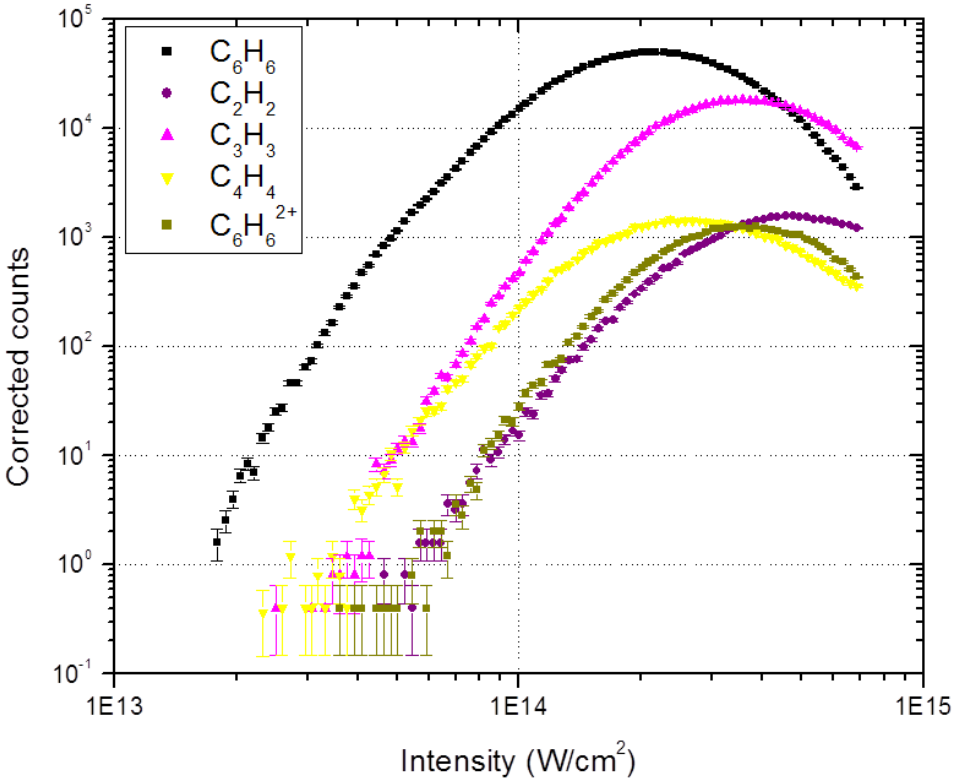

Figure 1 – Fragmentation of benzene. Ionic yields of prominent fragments of benzene are shown as a function of intensity. Benzene primarily avoids fragmentation, remaining a parent ion. When it does break apart, it prefers to create ionic fragments with three carbon atoms (pink) over four-carbon (yellow) or two-carbon (purple) fragments. Comparatively little of the doubly-charged parent ion (dark yellow) is observed.

Benzene shows a predisposition to fragment to molecular ions which contain the same number of carbons and hydrogens. The most common fragment is the $C_3H_3^+$, though this could be somewhat skewed since any dissociation to C_3H_3 inherently gives another C_3H_3, which can also be ionized either immediately during the dissociation or later in the laser pulse. The yield of C_4H_4 is considerably larger than that of C_2H_2, which suggests a preference toward the dissociation channel $C_6H_6^+ \rightarrow C_4H_4^+ + C_2H_2$ with the lighter group remaining neutral. Benzene is found as a stable doubly-charged ion, though

the yield is nearly 100 times smaller than the singly-charged parent at their respective saturation intensities. It seems that, as a second electron is removed (both almost certainly from the π orbitals, which are the most weakly-bound [1]), the deviation from Hückel's (4*n*+2) rule (see Chapter 4) for aromatic stabilization becomes greater, and the molecule's probability to fragment increases considerably.

As we look to substitutions to the benzene system, any differences between the yields above and those of the substituted fragments will be a direct result of the substitution.

7.1 – The halobenzenes

Let us first examine the substitution of a hydrogen atom with an atomic halogen. We see little change in the mass spectra with respect to C_nH_n fragments. The lone exception is the suppression of the C_3H_3 yields, which will be addressed in Section 7.2 with the CNOF series. Here, we will instead focus the discussion on what turns out to be the dominant fragmentation process: dissociation of the halobenzene parent into the phenyl ring and the atomic halogen.

In the time-of-flight (TOF) spectra we observe increasing amounts of ionized halogens in the order F < Cl < Br < I. This can be seen in Figure 2, with each curve representing the sum over all charge states of the halogen. This is evidence of the *heavy atom effect*, in which spin-orbit coupling (SOC) increases in the excited state, leading to a transition to a dissociative triplet state; this intersystem crossing (ISC) has been well-documented in the halobenzenes [2-5] and is described in Chapter 4. However, at high intensities we see bromine overtake iodine and fluorine overtake chlorine when the yields become saturated. This is counter to the heavy atom effect, which should result in larger

yields with increasing halogen mass due to higher dissociation rates; this is likely due to a dependence on yield of the molecular parent ions, which follow similar patterns. Ref. [6] shows the saturation intensities I_{sat} of the parent yields; when the presence of the parent molecule starts to diminish, so will the yields of the ionization processes which depend on the parent. Since I_{sat}(PhI) < I_{sat}(PhBr) and I_{sat}(PhCl) < I_{sat}(PhF) ("Ph" denoting a phenyl group, C_6H_5), this may be why the post-saturation yields do not increase stepwise with higher halogen mass.

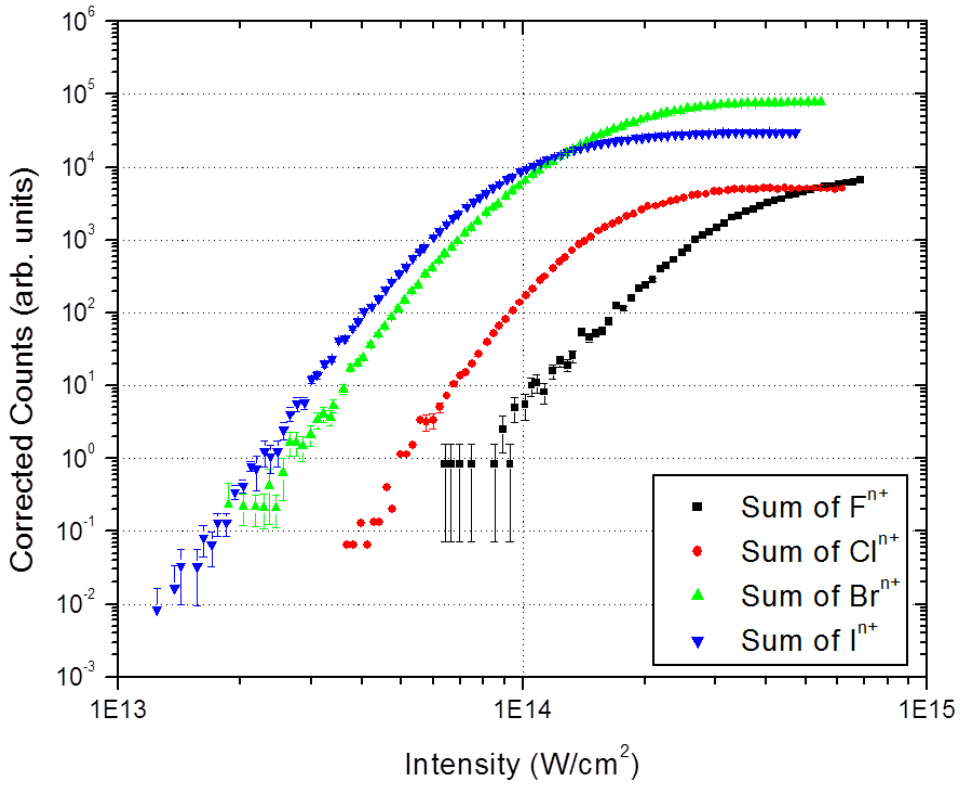

Figure 2 – Ionized halogen atoms from halobenzene parents. Following dissociation from the parent halobenzene molecule, atomic halogen ions are formed. We observe increasing amounts of ions with increasing atomic mass, from fluorine (black) to chlorine (red) to bromine (green) to iodine (blue), indicative of the heavy atom effect. In this representation, all charge states of the halogen are counted.

Though this result lends evidence toward the strength of the heavy atom effect, it is not conclusive by itself. The dynamics involves multiple steps (excitation,

fragmentation, and ionization, though not necessarily in that order); further, the ionization potentials (IP) of the atomic halogens also could account for the observed patterns, as they increase in the order of decreasing yields ($IP_F > IP_{Cl} > IP_{Br} > IP_I$) [7]. As such, we must attempt to disentangle the nature of these events. Seen in Fig. 3 are the ionic yields of the phenyl groups which result from the same dissociation, PhX + photons → Ph^{m+} + X^{n+} (X denotes a halogen).

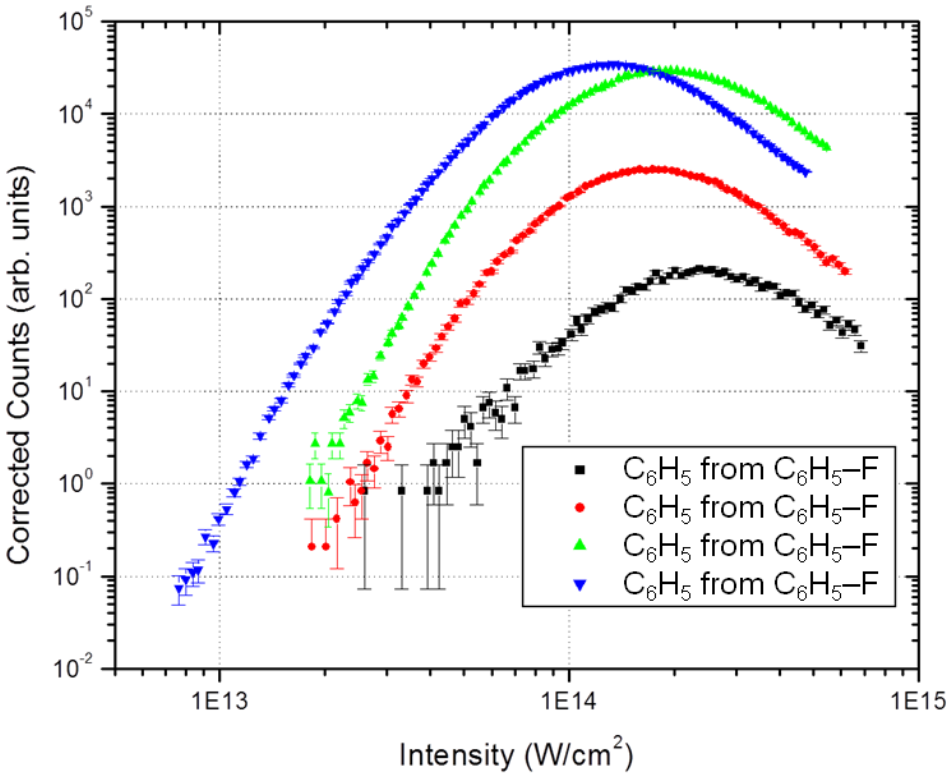

Figure 3 – Phenyl ions from halobenzene parents. Because their final states are identical, any differences in the yields of the phenyl (C_6H_5) ions must be the result of the dynamics of the parent halobenzene. Shown are the phenyl yields following dissociation from parent fluorobenzene (black), chlorobenzene (red), bromobenzene (green), and iodobenzene (blue).

The phenyl yields are instructive, as the differences between them are unlikely to result from differences in the dynamics of the phenyl groups (though they could in principle begin in different excited or ionic states coming from different parents). The

differences of these yields, shown in Figure 3, are instead attributed to the dynamics of either parent ionization or fragmentation.

Also of interest are the individual charge states of the halogen ions. Two primary factors contribute to creation of higher charge states: lower IPs and increased time as a neutral atom in the laser field. The IPs, as mentioned above, decrease with increasing halogen mass; the time spent as a neutral atom in the laser field after dissociation increases with increasing halogen mass due to increased rates of ISC. These factors both contribute to more highly-charged states for larger halogens; indeed, that is what we see in the data.

The fluorobenzene spectra show three charge states of fluorine, seen in Figure 4. The first begins to rise at ~10^{14} W/cm^2, and the second and third charge states remain weak in comparison until the highest intensities explored. However, we see here the first evidence that suggests a property of the ionization mechanism: just as the first ion begins to sag beneath its linear slope around 2.5×10^{14} W/cm^2, the second ion begins to rise. Then the second ionic yield begins to drop below its initial slope (this time with a sharp kink) around 4.5×10^{14} W/cm^2, and this is coincident with the appearance of the third ionic state. That these events coincide suggests that the ionizations are sequential, and that the n^{th} ionization relies on the saturation of some process in the $(n\text{-}1)^{th}$ ion.

As mentioned above, the yields reveal linear slopes on a log-log scale ($N \approx 6$ for the first ion, and $N \approx 7$ for the second; the third is inconclusive). Though this is typically indicative of multiphoton ionization (MPI), there is no guarantee that it is the case given the added dissociation dynamics. In fact, these slopes seem to be unrelated to the IPs of the respective charge states, so the simplistic version of MPI in which N photons are

absorbed from the ground state to create an ion yield which increases as I^N must be incorrect.

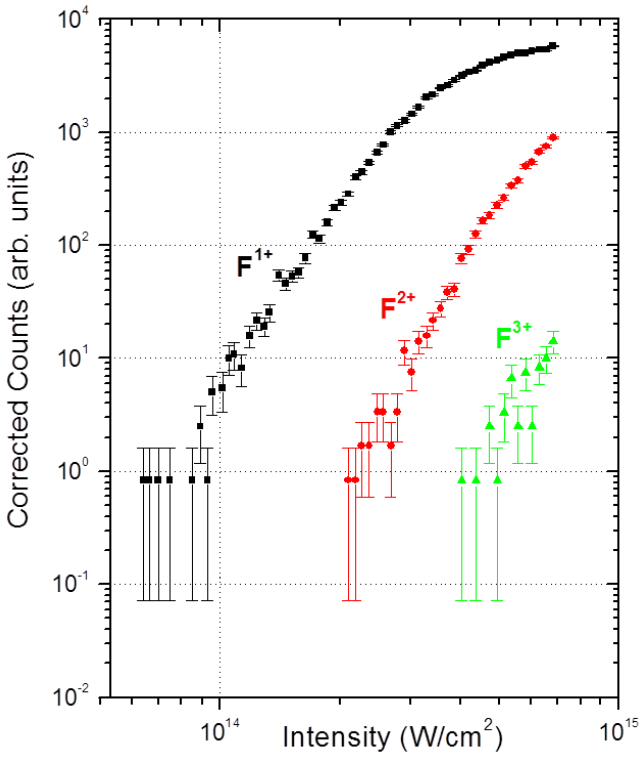

Figure 4 – Fluorine ions. Fluorine is observed through its third ionic state following dissociation from fluorobenzene.

Atomic chlorine ions are seen at lower intensities than fluorine, with the first charge state rising around 4×10^{13} W/cm^2, as seen in Figure 5. We observe up to the fourth ionic state of chlorine. Again each charge state seems to rise with an approximately linear slope: they rise with slopes of 8 (1+), 9 (2+), 9 (3+), and 7 (4+). Based on the unperturbed IP [7], the first ionization should require nine 800 nm photons in a multiphoton process, so the simplistic MPI is again an unsatisfying description of the dynamics. However, we again see evidence of sequential ionization as in fluorine. The linear slopes go away as the next ionic state appears around 9×10^{13} W/cm^2 ($1^+ \rightarrow 2^+$), 1.6×10^{14} W/cm^2 ($2^+ \rightarrow 3^+$), and 2.5×10^{14} W/cm^2 ($3^+ \rightarrow 4^+$).

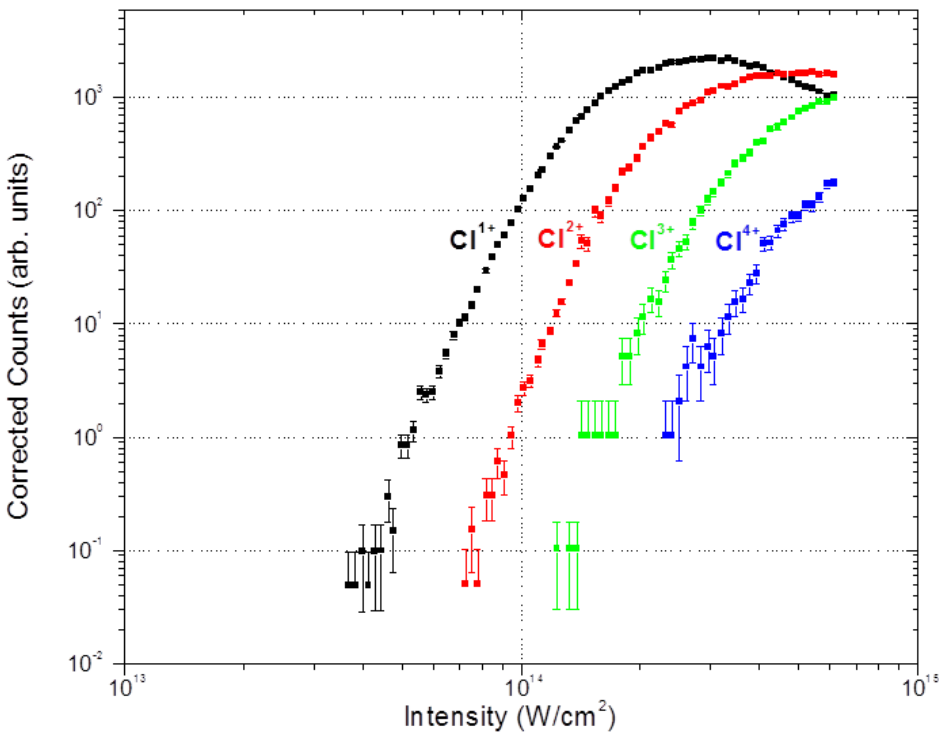

Figure 5 – Chlorine ions. Chlorine is observed through its fourth ionic state following dissociation from chlorobenzene.

The ionic yields of bromine continue the trends seen in fluorine and chlorine. Appearance intensities of each charge state are lower, with the first ionic state appearing at 2×10^{13} W/cm^2, as seen in Figure 6. We observe up to the fifth charge state of bromine in significant amounts, likely emptying the 4p orbital. Once again each charge state rises with an approximately linear slope: in bromine we find slopes of approximately 8 (1+), 9 (2+), 10 (3+), 8 (4+), and 7 (5+). In this case, the eight-photon result for the single ion does match the IP of neutral bromine; the simplistic MPI in this case may be a reasonable description of the dynamics. This could indicate that the SOC is strong enough that dissociation occurs quickly. If a majority of the neutral bromine is produced early in the laser pulse, the molecular interaction would be minimal and the yields would indicate only the dynamics in atomic bromine. Finally, we again see the signatures of sequential

ionization: linear slopes recede as the next ionic states appear at 6×10^{13} W/cm^2 ($1^+ \rightarrow 2^+$), 1.2×10^{14} W/cm^2 ($2^+ \rightarrow 3^+$), 1.8×10^{14} W/cm^2 ($3^+ \rightarrow 4^+$), and 3.2×10^{14} W/cm^2 ($4^+ \rightarrow 5^+$).

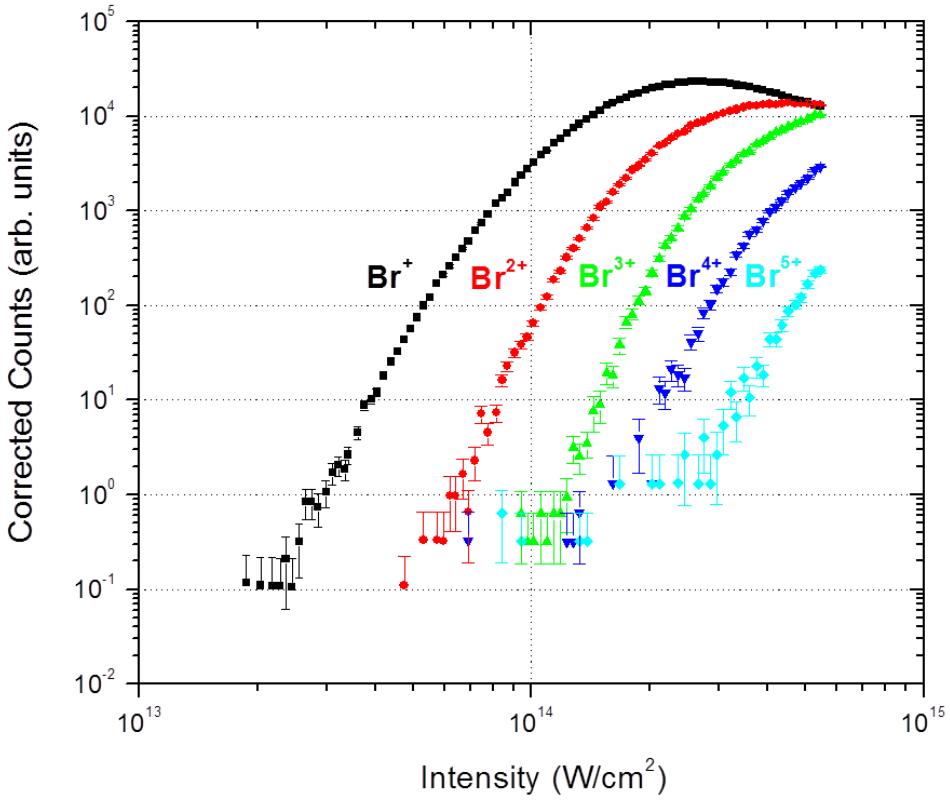

Figure 6 – Bromine ions. Bromine is observed through its fifth ionic state following dissociation from bromobenzene.

Finally, we observe the ionic yields of iodine, as seen in Figure 7. Due to the known lifetime of the SOC in the first excited state of iodobenzene [5,8,9] and its ability to affect the intense-field dynamics [6], we expect to find an abundance of atomic iodine ions in the spectra, and this is indeed what we observe. We find the singly-charged ion appearing as low as 1.25×10^{13} W/cm^2, and we observe charge states as high as I^{8+} (with the exception of I^{7+}, which lands within the water vapor peak in the mass spectra, making it impossible to distinguish accurately).

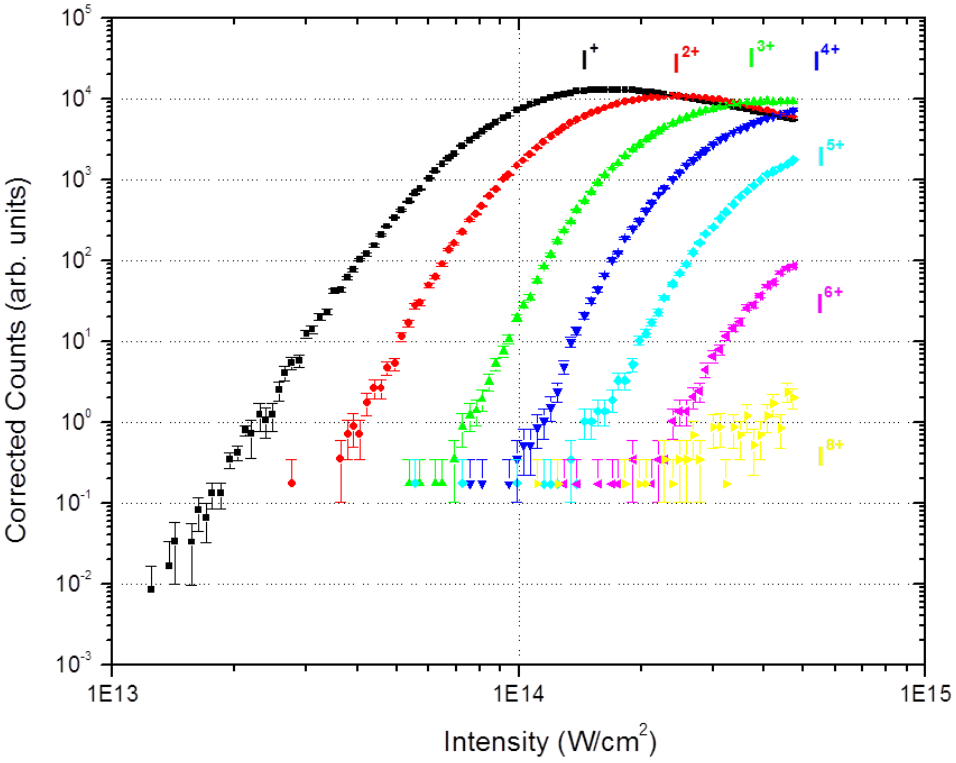

Figure 7 – Iodine ions. Iodine is observed through its eighth ionic state following dissociation from iodobenzene. The seventh ionic state is not present, as it landed at the same time of flight as another peak.

Once again each charge state rises with an approximately linear slope, though at higher charges these become less convincing: in iodine we find slopes of approximately 8 (1+), 10 (2+), 10 (3+), 11 (4+), 9 (5+), and 8 (6+). In this case, the eight-photon result for the single ion does not match the IP of neutral bromine unless the ponderomotive energy is also considered (U_p = 0.6 eV at 10^{13} W/cm^2) which could lead to channel closing [10] (see Chapter 2). Here we see the signatures of sequential ionization in the $1^+ \rightarrow 2^+ \rightarrow 3^+$, but in higher charge states this pattern becomes less clear, as the appearance intensities become more compact. At present it remains unclear what sort of dynamics are occurring in iodine.

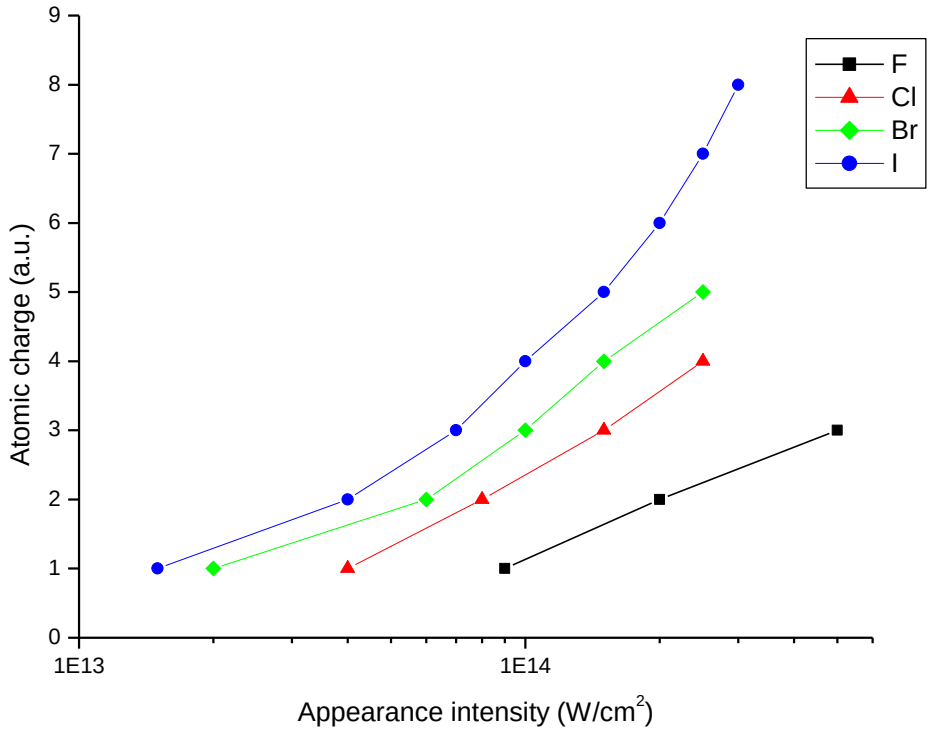

Figure 8 – Appearance intensities of halogen charge states. Heavier halogens are prone to ionize at lower intensities, and to reach higher charge states than lighter halogens. Shown are the appearance intensities for all observed charge states of atomic fluorine (black), chlorine (red), bromine (green), and iodine (blue). The appearance intensity of the seventh charge state of iodine is inferred, as it could not be measured experimentally.

A summary of the trends in the halobenzenes is shown in Figure 8. As the halogen size increases, we observe more halogen ions in higher charge states at lower intensities. Although the heavy atom effect cannot be predicted quantitatively for such a large molecular system (the Z^4 dependence in Chapter 4 is for the hydrogen-like atomic case), we nevertheless see patterns indicative of progressively increasing SOC for progressively larger substituents.

7.2 – The CNOF isoelectronic series

We can also examine perturbations from methyl, amine, and hydroxyl groups along with the fluorine atom. As was the case in Chapter 6, the yields of fluorobenzene

are different in the CNOF series and the halobenzenes; data on the two series was taken months apart, so fluorobenzene was measured separately with each series to ensure experimental consistency within each series. No significant differences arise between the two fluorobenzene datasets other than differing ranges of measured intensity.

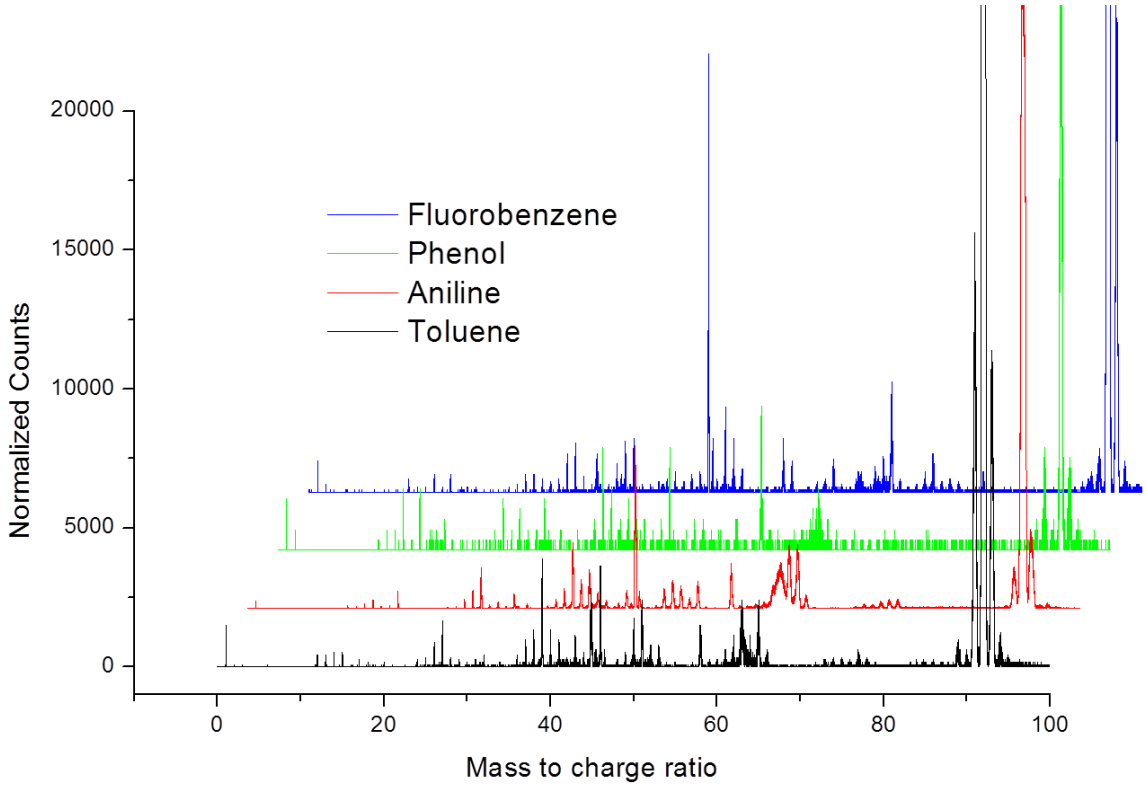

Figure 9 – Mass spectra of the CNOF series. Mass spectra were collected at 1.0×10^{14} W/cm^2 for toluene (black), aniline (red), phenol (green), and fluorobenzene (blue). Fragmentation patterns appear to be generally similar with the exception of a large peak in fluorobenzene (mass 43) which represents the doubly-charged parent ion. Parent ion peaks exceed the displayed region. The cause of the wider-than-normal peak at mass 63 in aniline will be discussed in Chapter 8.

The mass spectra of these molecules are seen in Figure 9. In a qualitative sense, differences between these species are not substantially clear. Aniline displays a wider-than-normal peak in the displayed spectrum at mass 63; the presence and cause of such peaks will be discussed in Chapter 8. When the most prominent peaks are studied as a

function of intensity, the subtle differences between species becomes evident. These yields are presented in Figure 10. In this series, C_2H_n peaks could not be characterized distinctly since the mass of the primary atoms of the side groups is close to the mass of carbon. Multiple fragments contribute to each of these peaks without anything to distinguish them, and so these peaks are not examined in this section.

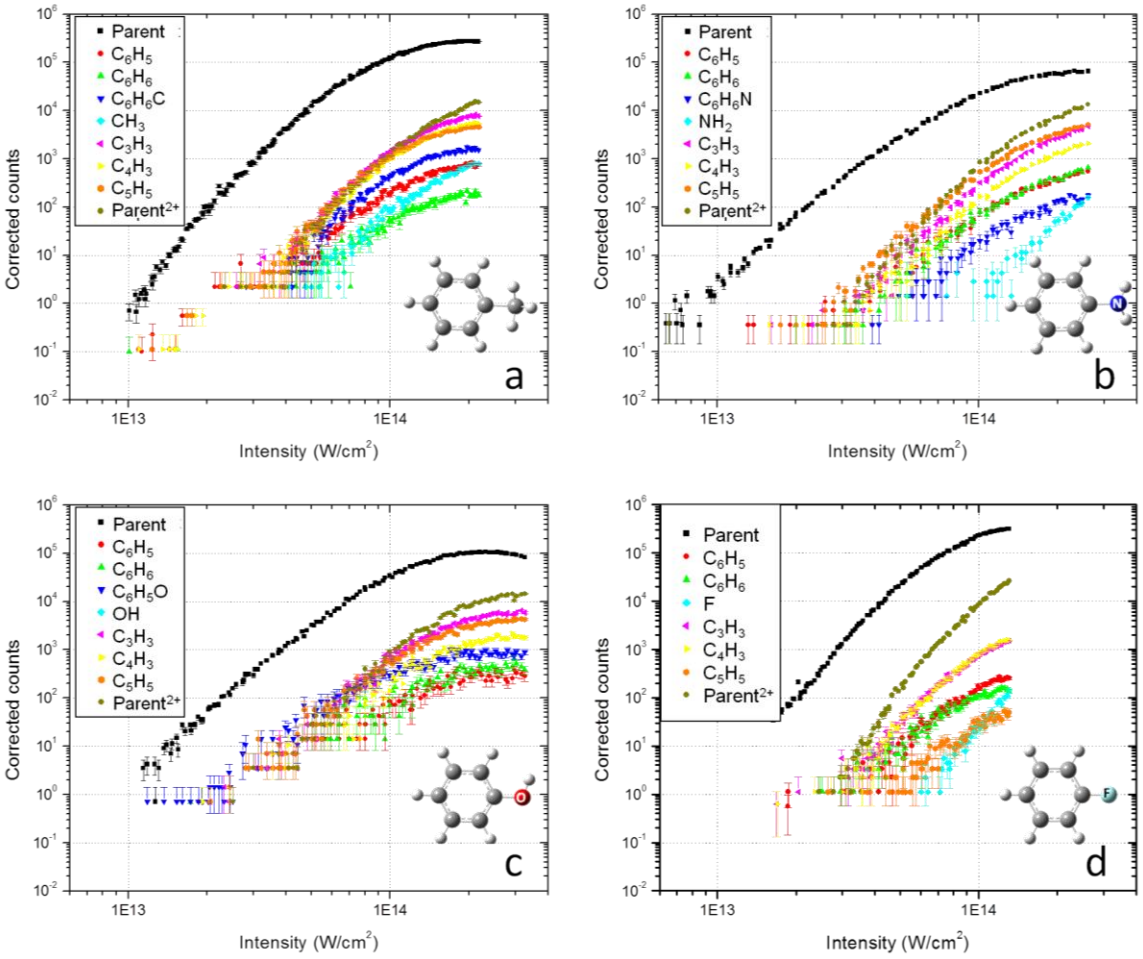

Figure 10 – All fragment yields of the CNOF series. Ionic yields of all prominent fragments are displayed for toluene (**a**), aniline (**b**), phenol (**c**), and fluorobenzene (**d**) as a function of intensity.

While it is useful in terms of cross-comparison to see all of the relevant fragments in this representation, the number of relevant fragments with similar behaviors clutters the data. For the sake of clarity, these data are broken down into groups; the largest peak

of each C_nH_m fragment group is shown in Figure 11, and the fragments relevant to the dissociation of the substituent group are shown in Figure 12.

The addition of the side groups seems to have an overall stabilizing effect on the molecule. Not only are the molecular parent ions (black) the most prominent yields, but the doubly-charged parents (dark yellow) are the second-leading process; in benzene the doubly-ionized parent was scarce in comparison to the C_3 and C_4 fragments (pink and yellow, respectively). This is most prominent in fluorobenzene, for which the charge states of the parent molecule dominate all fragmentation processes.

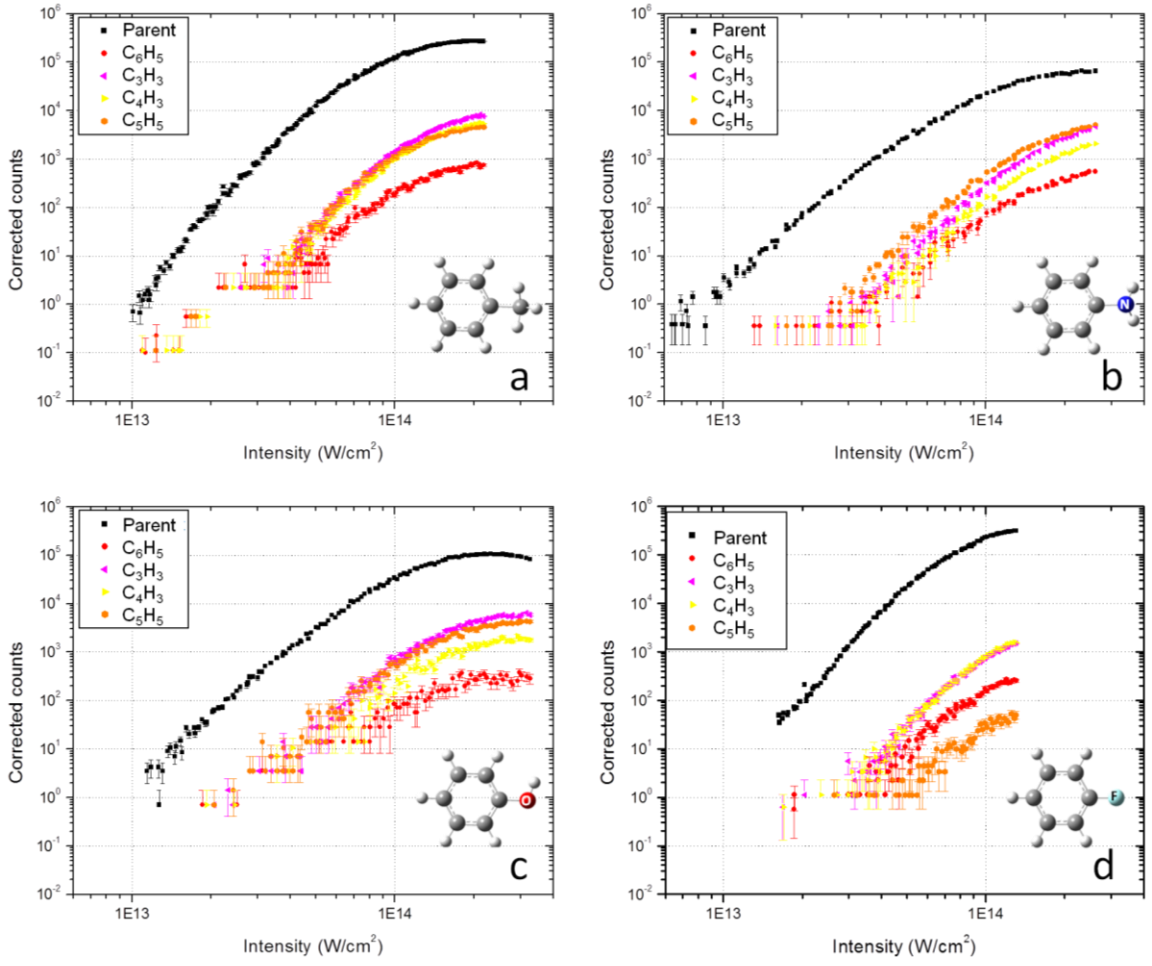

Figure 11 – Fragments with differing numbers of carbons in the CNOF series. Ionic yields of fragments containing three (pink), four (yellow), five (orange), and six (red) carbon atoms are displayed for toluene (**a**), aniline (**b**), phenol (**c**), and fluorobenzene (**d**) as a function of intensity. The parent yields (black) are shown for comparison.

In each species, there is little fragmentation into an ionic phenyl group (red); this is perhaps unsurprising given that the mechanism for this dissociation in the halobenzenes involves the heavy atom effect (described in Chapter 4), and each substituent in this series has approximately the same mass as fluorine. While fragments of the C_5 group (orange) were practically nonexistent in benzene and the halobenzenes, here they are among the leading fragments in all species but fluorobenzene. Other than this, fragmentation in this series is consistent, with C_3 fragments being most prominent and C_4 fragments somewhat lower.

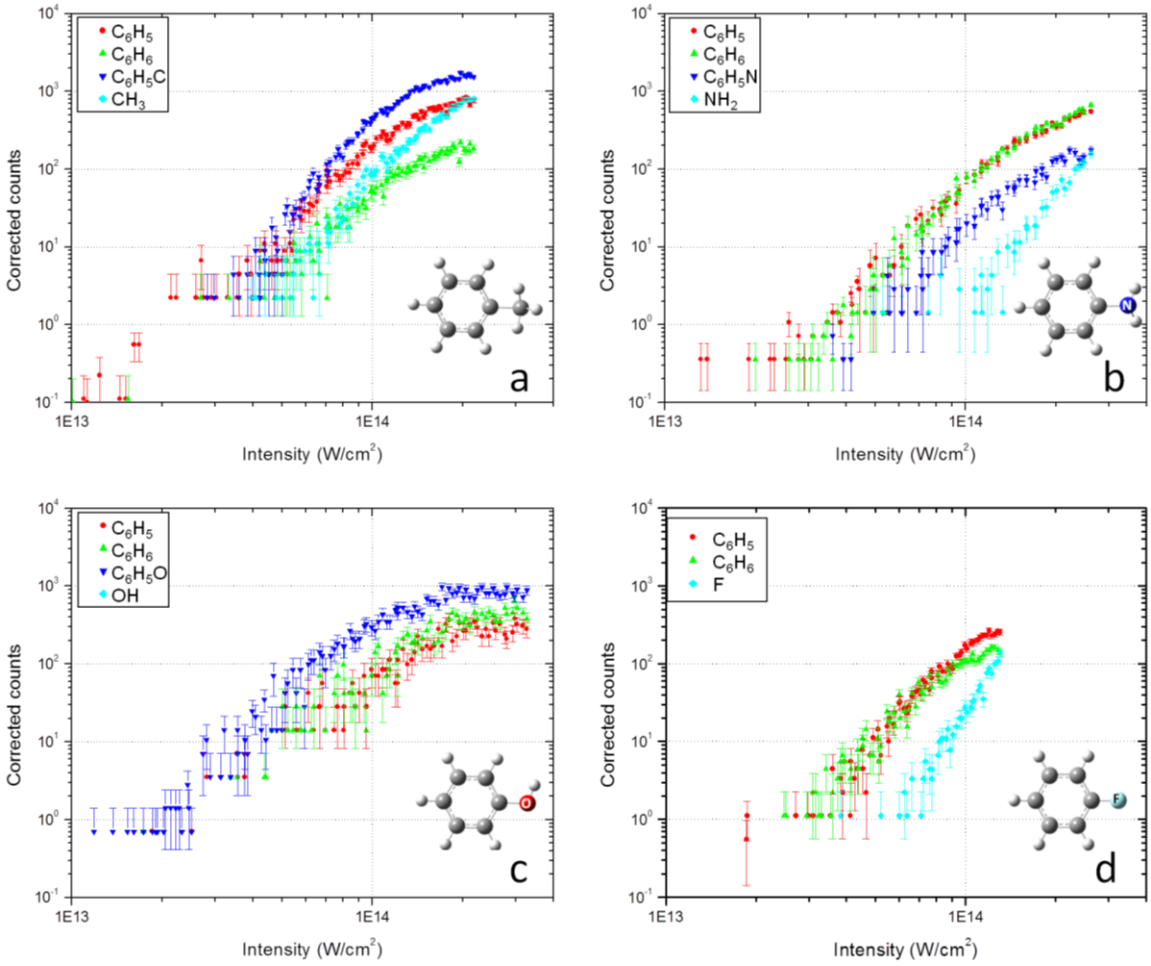

Figure 12 – Fragments relevant to substituent dissociation in the CNOF series. Ionic yields of fragments relevant to dissociation of the parent molecule into the phenyl ring (red) are displayed for toluene (**a**), aniline (**b**), phenol (**c**), and fluorobenzene (**d**) as a function of intensity.

In all species, the ion yield of the side group (light blue) is smaller than that of the phenyl ring (C_6H_5, red), suggesting that when the side group breaks off, it does so as a neutral leaving the phenyl ring as the ion. Phenol seems to prefer hydrogen detachment to dissociation of the hydroxyl group, and toluene similarly shows a large yield of what could be the bare methyl group; because toluene has only carbon and hydrogen atoms, however, the structure of its final state is not distinguishable.

An interesting effect is noticed when comparing the yields of the mass-77 phenyl ring with the mass-78 peak. As a first assumption one may assume that, with no traces of benzene in the system at the time of the measurements, any peaks with mass of 78 amu must be the heavy phenyl ring[†]. The yield from toluene suggests that this makes sense, where the phenyl ions (red) outnumber the mass-78 ions (green) by nearly a decade. However, based on the isotopic abundances of heavy carbons, the phenyl should be more abundant by a factor of approximately 15. Further, the yields in aniline are nearly identical, while the yields in phenol are reversed.

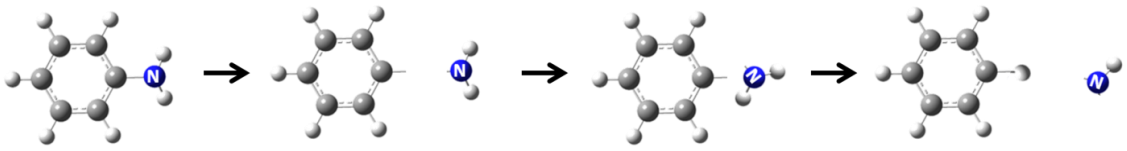

Figure 13 – Hydrogen rearrangement. In our ionic yields, we see evidence of the rearrangement of a hydrogen atom to form benzene. Shown is aniline, for which a C–N bond breaks, and the amine group leaves a hydrogen atom behind as it dissociates.

What appears to be happening here is the recombination of a hydrogen atom from the side group back into the phenyl ring, forming benzene while leaving the side group without one of its hydrogen atoms. This process is pictured in Figure 13.

[†] All chemicals in this series are purchased from Sigma-Aldrich with ≥ 99.5% purity. It is unknown if the impurities are benzene molecules.

7.3 – Compound functional groups: methyl, hydroxyl, and methoxyl substitutions

Examining the compound methoxyl (–O–CH_3) perturbation displays many of the same properties seen in the yields for the CNOF series, such as a prominent C_5H_5 peak with comparatively suppressed C_4H_3 and C_3H_3 peaks, and an equal abundance of phenyl and benzene yields. Yields are seen in Figure 14. However, because the side group has multiple non-hydrogen bonds by which it can dissociate, the dynamics here are somewhat richer. The oxygen atom is bonded to a carbon on either side, and so it can break up into a methoxyl group and the phenyl ring:

$$Ph–O–CH_3 \rightarrow Ph + O–CH_3$$

or the phenyl ring can hold on to the oxygen and leave the methyl group:

$$Ph–O–CH_3 \rightarrow Ph–O + CH_3.$$

These four final states have yields which increase as $Ph^+ > Ph–O^+ \approx CH_3^+ > O–CH_3^+$. The disparity between the phenyl and methoxyl yields suggests a dissociation which prefers to leave the phenyl ionized:

$$(Ph–O–CH_3)^+ \rightarrow Ph^+ + O–CH_3.$$

While their yields depend on the ionization of the fragments, the abundance of the phenyl ions combined with the C_6H_6 yield (from hydrogen loss of the O–CH_3 fragment) suggests that the methoxyl group is more likely to stay together as it breaks from the ring.

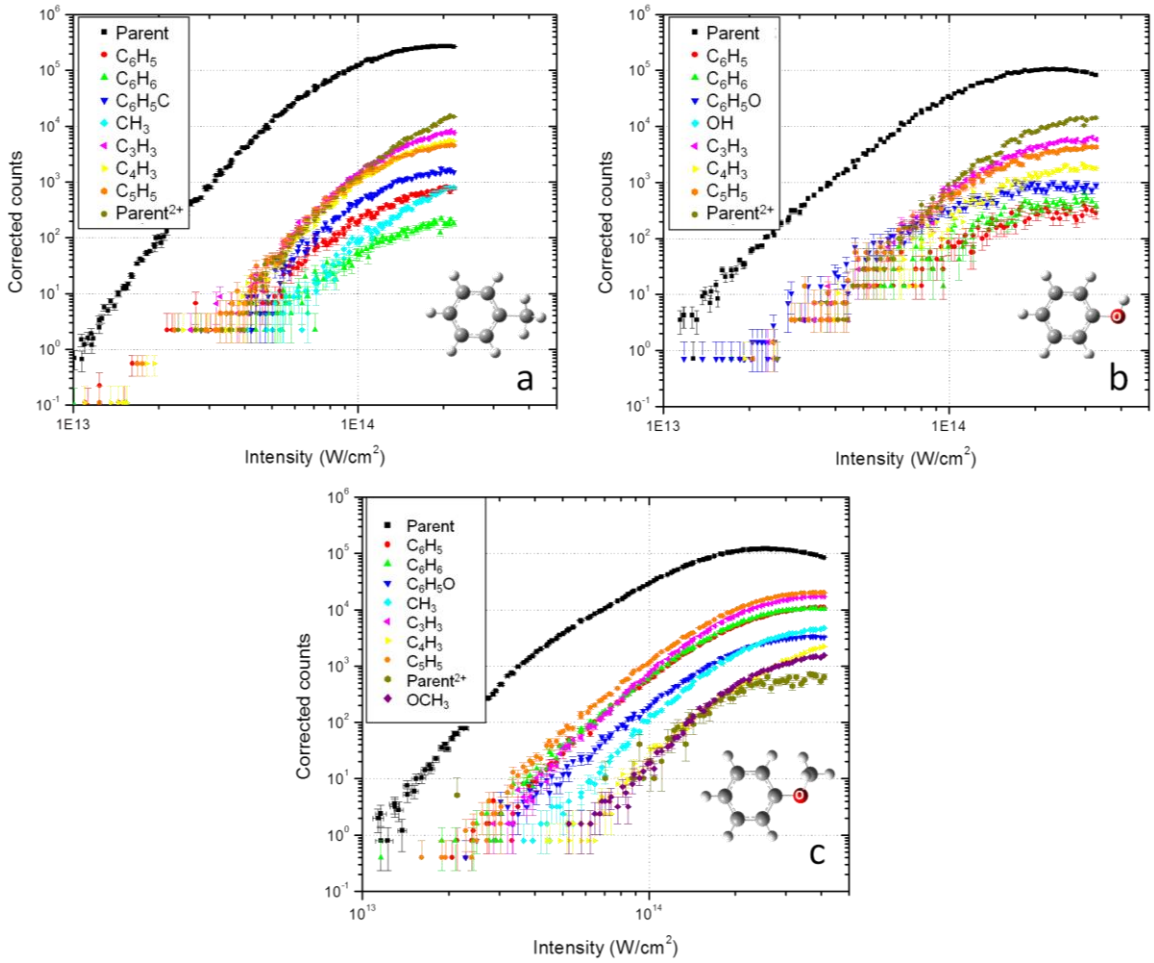

Figure 14 – All fragment yields of the toluene, phenol, and anisole. Ionic yields of all prominent fragments are displayed for toluene (**a**), phenol (**b**), and anisole (**c**) as a function of intensity. Anisole represents a compound perturbation (a methoxyl group) which is a combination of the methyl group of toluene and the hydroxyl group of phenol.

The additional loss channels due to the compound functional group may also contribute to the suppressed yield of the doubly-charged parent yield, as it is nearly two decades lower than the yields of the doubly-charged parents of both toluene and phenol at comparable intensities. Little else changes in the fragmentation patterns, with the exception of a slight suppression of the C_4 fragments. The sharp kink in the parent yield of anisole makes it evident that the appearance intensity of the fragments is approximately the same as the intensity of the kink; saturation of the resonant process in

the parent makes fragmentation more likely. For the most part, the methoxyl group seems not to perturb the stability of the molecule differently than the methyl or hydroxyl groups except to suppress the doubly-charged parent.

7.4 – Amine vs. nitro substitution

One aspect of molecular substituents that is particularly relevant to substituents which are external to the ring is whether they donate or withdraw electron density from the ring. To study the difference this property has on molecular fragmentation, aniline was compared to nitrobenzene; electron densities for these molecules are shown in Figure 15. The amine (NH_2) group of aniline is known to be highly-donating [11]; with additional electron density pushed into the ring, it is easier to remove electrons from the π states, which is why aniline has a considerably lower IP (7.85 eV) than most other benzene-like systems [7]. In contrast, the nitro (NO_2) group of nitrobenzene is highly-withdrawing [11]. This removes electron density from the ring, making it more difficult to remove further density through ionization; this is why the IP of nitrobenzene is larger (9.94 eV) [7].

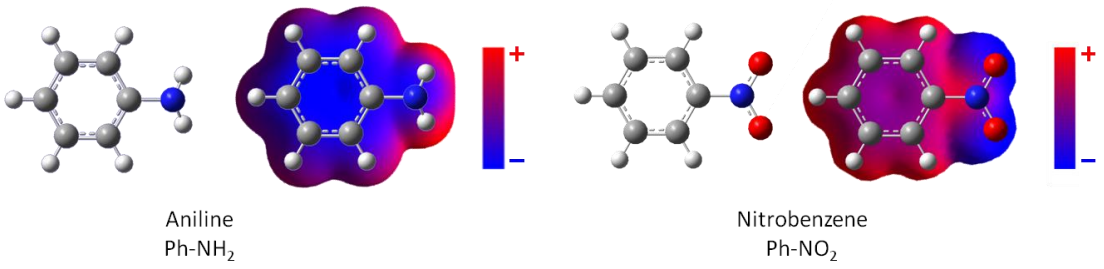

Figure 15 – Donating and withdrawing groups. When substituted onto a phenyl ring, an amine group (left, in aniline) donates electron density into the ring. A nitro group (right, in nitrobenzene), on the other hand, withdraws electron density from the ring. Electron-rich regions are shown in blue, and electron-poor regions are shown in red.

Comparing the mass spectra of these two molecules gives starkly different results in fragmentation. Seen in Figure 16 are the mass spectra at various intensities for nitrobenzene. While fragmentation in aniline is suppressed (its two most abundant peaks are the singly- and doubly-ionized parent), nitrobenzene is barely detectable as a parent molecule.

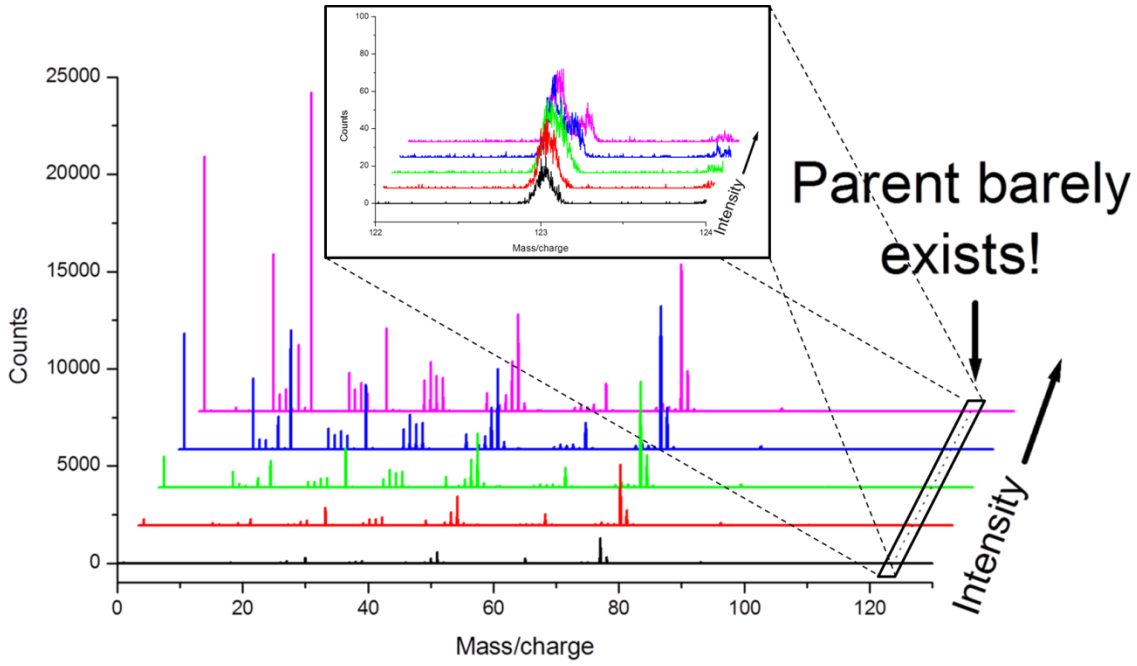

Figure 16 – Mass spectra of nitrobenzene. At any intensity which is capable of producing ions, the yield of the nitrobenzene parent ion is barely distinguishable in the mass spectra in comparison to its fragments.

The nitro group destabilizes the ring to such an extent that parent ionization is effectively eliminated in favor of fragmentation; in fact, all fragments with mass greater than the phenyl ring are heavily suppressed. Figure 17 shows the corrected counts as a function of intensity for several relevant peaks, along with those for aniline.

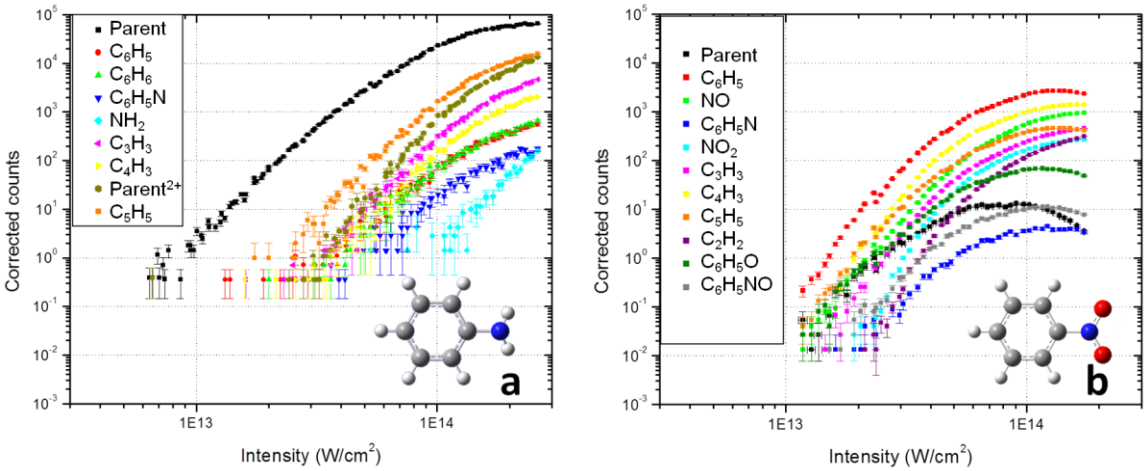

Figure 17 – All fragment yields of aniline and nitrobenzene. Ionic yields of all prominent fragments are displayed for aniline (**a**) and nitrobenzene (**b**) as a function of intensity. Note the difference of several orders of magnitude in molecular parent ions (black curves).

We find that the parent ion is extraordinarily scarce; the comparison between aniline and nitrobenzene would have been made in the previous chapter to discuss the ionization dynamics, but there was so little data that no comparison of dynamics could be made with any accuracy. To delve further into the fragmentation of nitrobenzene, it is again helpful to sort the fragments into groups for analysis due to the clutter that results from plotting all fragments on a single graph.

The first group, shown in Figure 18, contains the fragments with differing numbers of carbon atoms from the phenyl ring. Dissociation into the phenyl group is the most likely, followed by C_4, C_5, C_3, and C_2 groups. This is a stark contrast to the fragmentation of both benzene and aniline; aniline fragments in preference of $C_5 > C_3 > C_4$. At present, explanations of this behavior are only speculative.

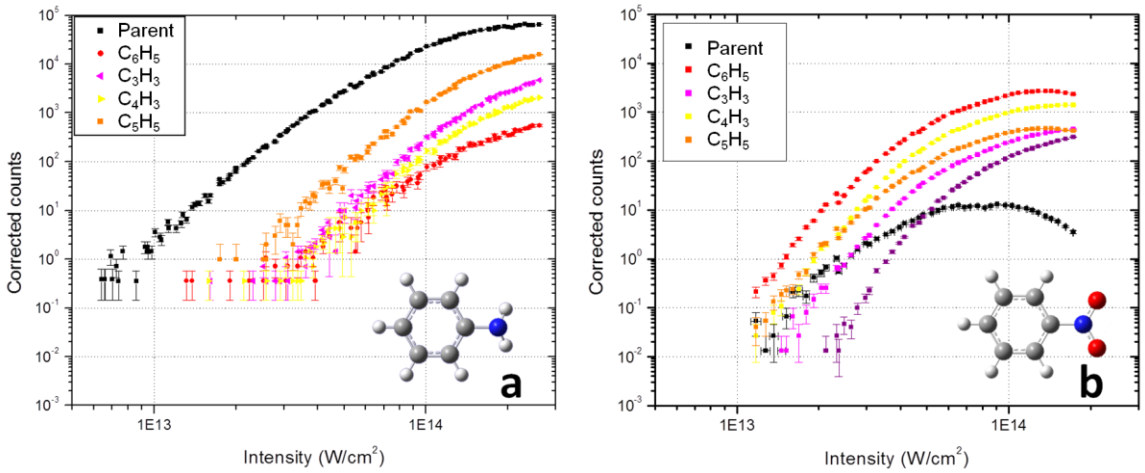

Figure 18 – Fragments with differing numbers of carbons in aniline and nitrobenzene. Ionic yields of fragments containing three (pink), four (yellow), five (orange), and six (red) carbon atoms are displayed for aniline (**a**) and nitrobenzene (**b**) as a function of intensity. The parent yields (black) are shown for comparison.

The second and third groups of fragments concern the loss of pieces of the nitro group from the parent. The pieces of the side group are shown in Figure 19 (**a**), while what remains with the phenyl ring is shown in Figure 19 (**b**). When the nitro group dissociates from the ring, it is more likely to be found as a nitric oxide (NO) ion than as the whole nitro group. Since the phenyl group remains the largest ionic fragment (thus we know the nitro group prefers to dissociate from the ring as a whole), this may be due to an inherent instability of the nitro group in its ionic state; its IP [7] is comparable to that of the phenyl ring.

The Ph–N and Ph–NO yields are the rarest final states. Both of these make sense given that the Ph–N leaves the nitrogen with two unpaired valence electrons, and the Ph–NO fragments means that a lone oxygen atom exists in the final state. Neither of these final states represents a minimum-energy final state, and so the rates of dissociation to these states are suppressed. However, it appears that a rearrangement takes place with much greater likelihood: $Ph–NO_2 \rightarrow Ph–O + NO$. This mirrors the behavior of aniline,

which leaves a hydrogen atom with the phenyl ring to form benzene and NH. This rearrangement in nitrobenzene has previously been observed by Tasker [12] and He [13].

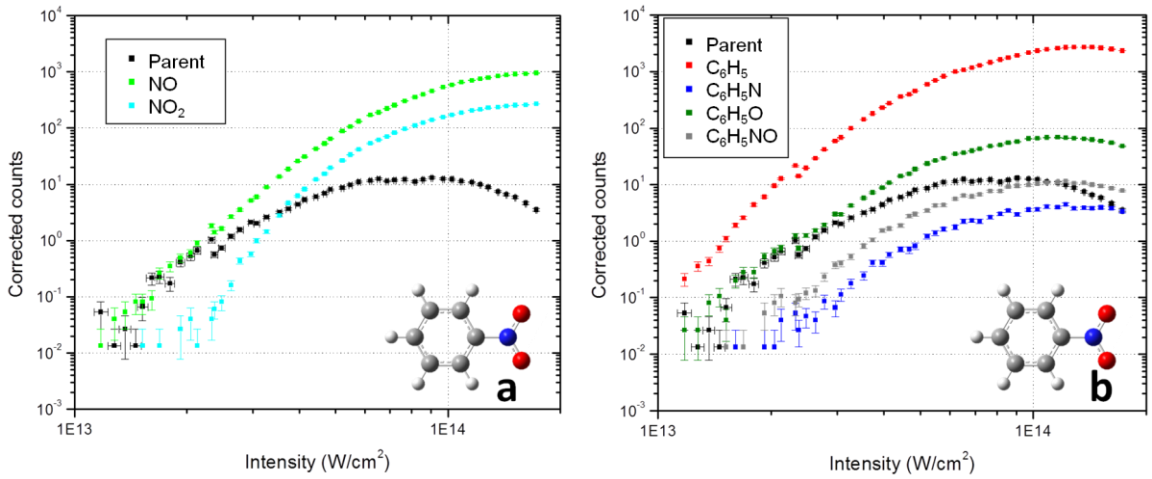

Figure 19 – Fragments relevant to dissociation of the nitro group in nitrobenzene. Ionic yields of fragments relevant to dissociation of the nitro group are displayed for nitrobenzene as a function of intensity. Remnants of the nitro group (**a**) and what is left on the ring (**b**) are shown with the parent yield (black) for comparison.

Based on these results, it is abundantly clear that a highly-withdrawing substituent group such as NO_2 can have devastating effects on the stability of the benzene structure in the ionic state.

7.5 – The azabenzenes

7.5.1 – Understanding the perturbation to the ring

The azine series, unlike the halobenzenes or isoelectronic CNOF series previously examined, involves a direct perturbation inside the ring. This is a fundamentally different perturbation than adding a functional group to the outside of the ring; in the azabenzenes the π structures are altered directly. In this section we will try to approximate these perturbations using first-order perturbation theory. The aromatic π system will be approximated by the simple "particle in a ring" model [14], which is analogous to the

quantum-mechanical “particle in a box” generalized into polar coordinates. Qualitative potentials are illustrated in Fig. 20. In this model, the Hamiltonian is represented as

$$H = -\frac{\hbar^2}{2mr^2}\frac{\partial^2}{\partial\theta^2}. \tag{7.1}$$

This assumes the radius to be fixed; while this assumption is not necessarily valid for a real case, the purpose of this section is to investigate the effects of the perturbations of replacing a C-H in the ring with a nitrogen atom. Due to its higher nuclear charge, the nitrogen will deepen the potential well seen by an electron, perturbing the constant potential of the particle in the ring. In the case of zero perturbation, the solutions are plane waves around the ring

$$\left|\varphi_n^{(0)}\right\rangle = \frac{1}{\sqrt{2\pi}}e^{\pm in\theta} \tag{7.2}$$

with energies

$$E_n = \frac{n^2\hbar^2}{2mr^2}, \text{ where } n = 0, \pm1, \pm2, \ldots \tag{7.3}$$

If this uniform potential is perturbed, plane waves of different frequencies may take part in the solution; if this is the case, these different mode contributions could affect the stability of the molecule against fragmentation. By considering the first-order perturbation theory, one can find the corrections to the perturbed wavefunctions

$$\left|\varphi_n^{(1)}\right\rangle = \sum_j c_{nj}\left|\varphi_j^{(0)}\right\rangle = \sum_j \frac{\left\langle\varphi_j^{(0)}\left|H^{(1)}\right|\varphi_n^{(0)}\right\rangle}{E_n^{(0)} - E_j^{(0)}}\left|\varphi_j^{(0)}\right\rangle \tag{7.4}$$

where the coefficients c_{nj} represent the amount of contribution a mode makes to the superposition. By calculating these coefficients, one can then compare the contributions

of higher-frequency states as the perturbations change positions and infer properties of the azabenzenes.

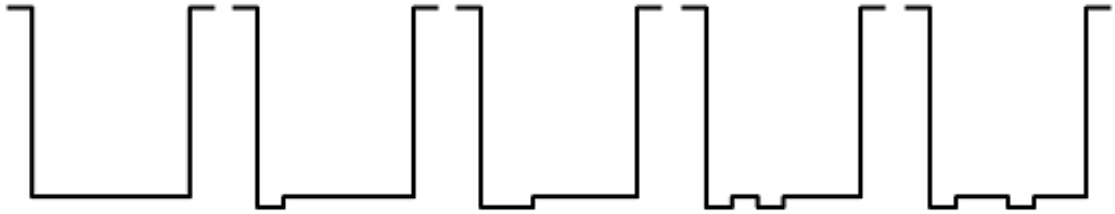

Figure 20 – Perturbed potentials. The relevant potentials under perturbations in the azine series. From left to right: unperturbed (benzene), azabenzene (pyridine), (1,2)-diazine (pyridazine), (1,3)-diazine (pyrimidine), (1,4)-diazine (pyrazine). Vertical lines are shown at the boundaries θ = 0 and θ = 2π only to emphasize that the electron is bound; in reality, the barrier is, of course, continuous at 0 and 2π.

Calculating the first-order corrections yields the following. For pyridine (1-azine):

$$\begin{aligned}\left|\varphi_n^{(1)}\right\rangle_{pyridine} &= \frac{2mr^2}{\hbar^2}\sum_j \frac{1}{n^2-j^2}\left(\frac{1}{2\pi}\int_0^{\pi/3}(-V)e^{i\theta(n-j)}d\theta\right)\left|\varphi_j^{(0)}\right\rangle \\ &= i\frac{Vmr^2}{\pi\hbar^2}\sum_j \frac{1}{n^2-j^2}\frac{1}{n-j}\left(e^{i\frac{\pi}{3}(n-j)}-1\right)\left|\varphi_j^{(0)}\right\rangle\end{aligned} \quad \textbf{(7.5)}$$

For pyridazine ((1,2)-diazine):

$$\begin{aligned}\left|\varphi_n^{(1)}\right\rangle_{pyridazine} &= \frac{2mr^2}{\hbar^2}\sum_j \frac{1}{n^2-j^2}\left(\frac{1}{2\pi}\int_0^{2\pi/3}(-V)e^{i\theta(n-j)}d\theta\right)\left|\varphi_j^{(0)}\right\rangle \\ &= i\frac{Vmr^2}{\pi\hbar^2}\sum_j \frac{1}{n^2-j^2}\frac{1}{n-j}\left(e^{i\frac{2\pi}{3}(n-j)}-1\right)\left|\varphi_j^{(0)}\right\rangle\end{aligned} \quad \textbf{(7.6)}$$

For pyrimidine ((1,3)-diazine):

$$\begin{aligned}\left|\varphi_n^{(1)}\right\rangle_{pyrimidine} &= \frac{2mr^2}{\hbar^2}\sum_j \frac{1}{n^2-j^2}\left(\frac{1}{2\pi}\int_0^{\pi/3}(-V)e^{i\theta(n-j)}d\theta+\frac{1}{2\pi}\int_{2\pi/3}^{\pi}(-V)e^{i\theta(n-j)}d\theta\right)\left|\varphi_j^{(0)}\right\rangle \\ &= i\frac{Vmr^2}{\pi\hbar^2}\sum_j \frac{1}{n^2-j^2}\frac{1}{n-j}\left(e^{i\frac{\pi}{3}(n-j)}-1+(-1)^{(n-j)}-e^{i\frac{2\pi}{3}(n-j)}\right)\left|\varphi_j^{(0)}\right\rangle\end{aligned} \quad \textbf{(7.7)}$$

For pyrazine ((1,4)-diazine):

$$\left|\varphi_n^{(1)}\right\rangle_{pyrazine} = \frac{2mr^2}{\hbar^2}\sum_j \frac{1}{n^2-j^2}\left(\frac{1}{2\pi}\int_0^{\pi/3}(-V)e^{i\theta(n-j)}d\theta + \frac{1}{2\pi}\int_{\pi}^{4\pi/3}(-V)e^{i\theta(n-j)}d\theta\right)\left|\varphi_j^{(0)}\right\rangle$$
$$= i\frac{Vmr^2}{\pi\hbar^2}\sum_j \frac{1}{n^2-j^2}\frac{1}{n-j}\left(e^{i\frac{\pi}{3}(n-j)} - 1 + e^{i\frac{4\pi}{3}(n-j)} - (-1)^{(n-j)}\right)\left|\varphi_j^{(0)}\right\rangle \quad \textbf{(7.8)}$$

In order to examine how these perturbations affect the wavefunction, a MATLAB [15] program was written to calculate $\left|c_{nj}\right|^2$; this simulation can be found in Appendix A.5. By doing so, one can see which modes contribute to the perturbed wavefunction and which modes remain unperturbed.

Figure 21 shows a cross section of $\left|c_{nj}\right|^2$ coefficients where n = 1 for a variety of values of j; this represents the contributions of each mode necessary to correct the n^{th} perturbed mode. Among the observations from this result is that the 1-substitution (pyridine) results in a perturbed wavefunction where the contributions of every sixth correcting wavefunction are suppressed; this is fitting given the six-fold symmetry of the benzene molecule and the fact that the perturbation only adds contributions without the same symmetry to represent the correction. Similarly, every third mode is suppressed in the contributions to the corrected wavefunction for the 1,2-substitution. Every sixth mode is suppressed for the 1,3-substitution, while every third mode between the suppressed modes is enhanced compared to the rest. Finally, the 1,4-substitution gives a smooth curve, with no single mode significantly suppressed or enhanced compared to its neighbors. This suggests something fundamentally different in the symmetry of this perturbation.

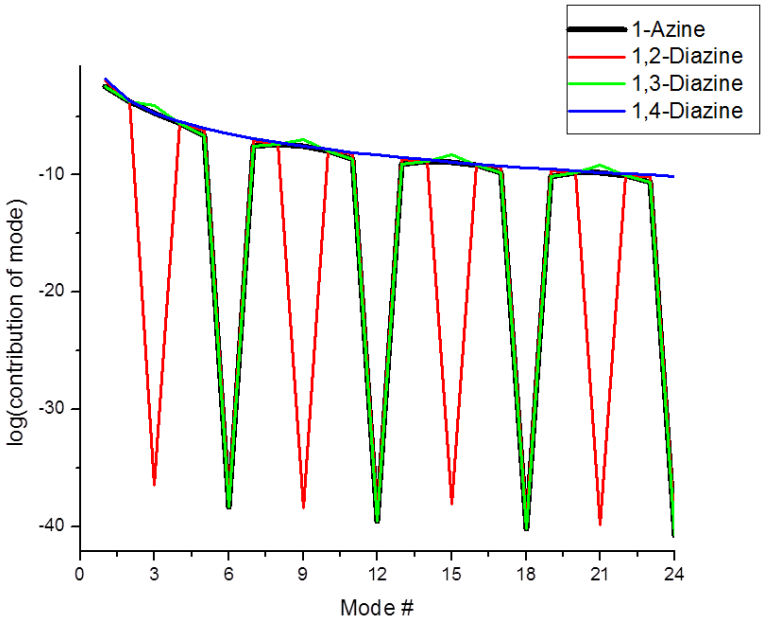

Figure 21 – Correction coefficients to the lowest-order mode. The analysis of a perturbed particle in a ring shows a suppression of certain modes in the correction coefficients for different species. Note that the corrected wavefunction for pyrazine (1,4-diazine, blue curve) has correction terms from all modes.

Fig. 21 represents only the corrections to the first mode in the superposition of the total wavefunctions, $\left|\varphi_n^{(0)}\right\rangle = \frac{1}{\sqrt{2\pi}} e^{\pm i\theta}$. Figure 22, however, shows the values of $\left|c_{nj}\right|^2$ for a wide array of initial (n) and correcting (j) wavefunctions, with each ranging from one to 50. The contributions to the perturbed wavefunctions are the same the case discussed above, with the caveat that the suppressed and enhanced modes occur when $(n - j)$ is six or three. Once again, the 1,4-substitution requires contributions from all modes to create the perturbed wavefunction.

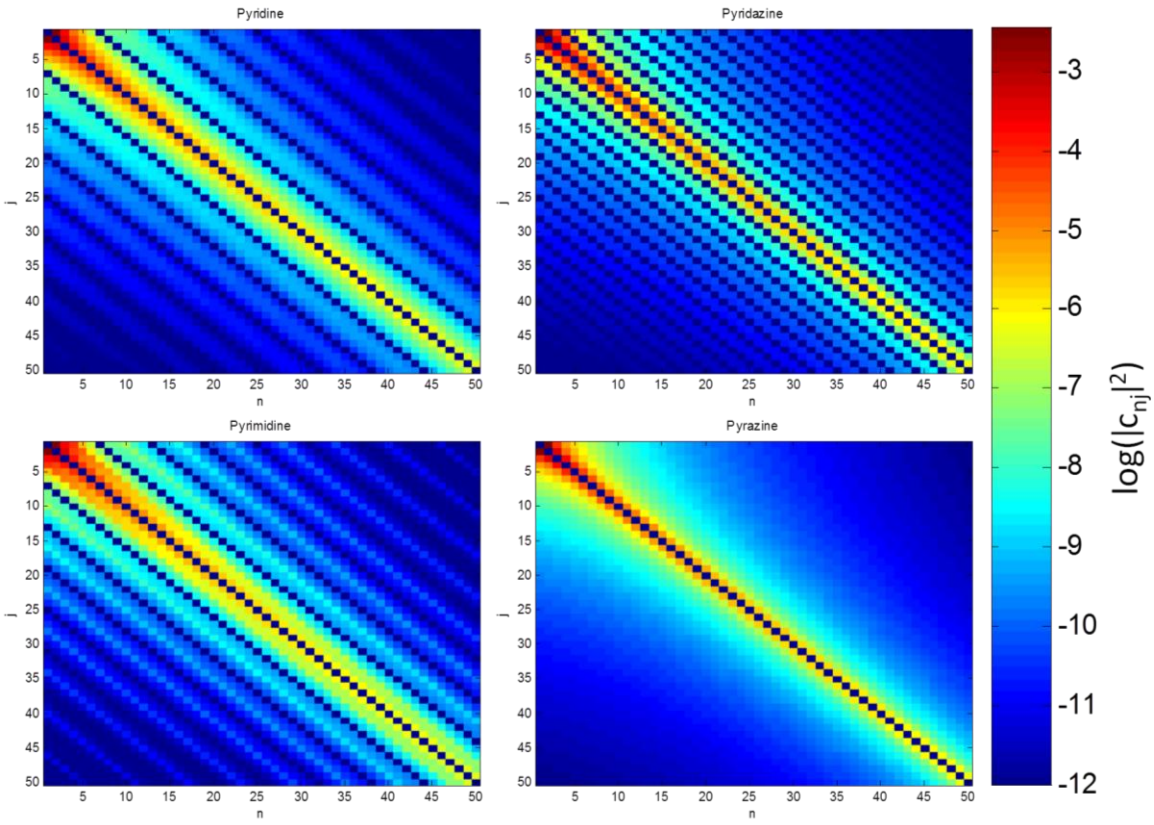

Figure 22 – Correction coefficients for all modes. The analysis of a perturbed particle in a ring shows a suppression of certain modes in the correction coefficients for different species. Contributing terms from coefficients $|c_{nj}|^2$ depend on the difference between the corrected mode and the contributed mode $|n-j|$. Note again that corrected wavefunctions for pyrazine have correction terms from all modes.

The reason this analysis is relevant to the present work is that the mono- and di-substituted azabenzenes pyridine (azabenzene), pyridazine (1,2-diazine), pyrimidine (1,3-diazine), and pyrazine (1,4-diazine) are all formed around the same sort of uniform potential of the benzene structure with perturbations to the ring caused by the implanted nitrogen atoms. As in the case of the perturbative analysis, the 1,4-substituted molecule, pyrazine, belongs to a different symmetry group (D_{2h}, while the others are C_{2v}) [16]. As was discussed in Section 6.4.1, its electronic structure is also somewhat different than the

other azabenzenes, and this will be a key element in determining the intense-field dynamics and stability against fragmentation.

While this analysis describes the perturbations to the π structures, the lone pair orbitals affect the σ structures as well. The lone pair orbitals of the nitrogen atoms contribute electron density throughout various σ bonds in the molecule, which distorts the uniformity of the bonds around the ring. Benzene has enhanced stability because every carbon-carbon bond around the ring has a bond order of 1.5; the added density of the lone pairs, as seen in Figure 23 for the case of pyrimidine, leads to effective double bonds in the ring.

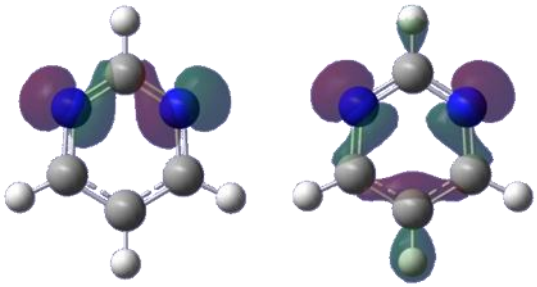

Figure 23 – Lone pair orbitals in pyrimidine. While the origin of the *n* orbitals in the azabenzenes is the lone pairs of the nitrogen atoms, they contribute electron density throughout the molecule. Shown are the antisymmetric n_- (left) and symmetric n_+ (right) orbitals in pyrimidine.

The azabenzenes studied here are default molecular structures when building molecules for simulation in the Gaussian 03 [17] quantum chemistry simulation program. In this program, they are represented as seen in Figure 24, with double bonds in several places throughout the ring. This lack of uniformity in the ring forms natural breaking points for fragmentation to occur, since some bonds are inherently weaker than others.

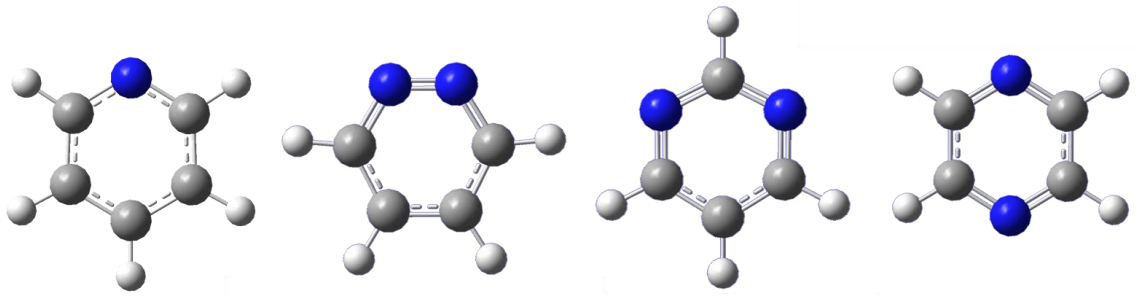

Figure 24 – Increased bond orders in the azabenzenes. Because of the contributions of electron density throughout the molecule from *n* orbitals, the computational quantum chemistry program Gaussian 03 draws the azabenzenes by default with double bonds in the ring. In the unperturbed benzene system (as is also the case for pyridine, far left) each carbon-carbon bond in the ring is uniform, with bond order 1.5. Nonuniform bond strengths give natural breaking points for fragmentation.

7.5.2 – Fragmentation

As seen in the perturbative analysis of the differently symmetric substitutions of a six-member ring, pyridine and the diazines represent unique perturbations to the electronic structure of benzene. As will be seen in this section, the differences in the perturbations do significantly affect the fragmentation of the molecules in intense fields.

As was seen in Section 7.1, the halobenzenes remained fairly stable against fragmentation, and Section 7.2 showed that the CNOF series also remained stable, with singly- and doubly-charged parents being the leading yields. As a series, the azabenzenes fragment significantly more than the other series relative to the parent yields. Further, the amount of fragmentation varies much more within the series. This makes sense given the nature of the perturbation to the benzene system; the previous series discussed were comprised of a single external perturbation to a phenyl ring, whereas the azabenzenes involve fundamentally different perturbations to the ring itself. These perturbations affect the wavefunctions in very different ways (as was discussed in Section 7.5.1).

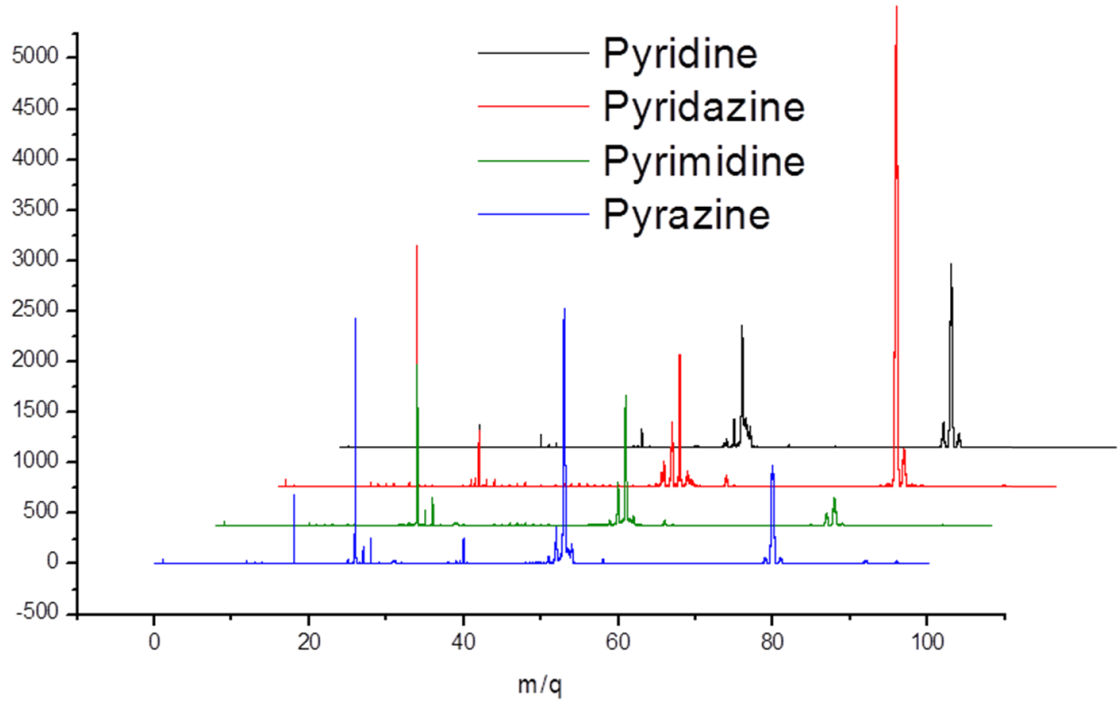

Figure 25 – Mass spectra of the azabenzenes. Mass spectra were collected at 1.55×10^{14} W/cm^2 for pyridine (black), pyridazine (1,2-diazine, red), pyrimidine (1,3-diazine, green), and pyrazine (1,4-diazine, blue). Fragmentation patterns are more varied in the azabenzenes than in the halobenzenes or CNOF series; this is most easily seen in the yields of the ionic parents.

Figure 25 shows a mass spectrum for each molecule. Each spectrum was taken at 1.55×10^{14} W/cm^2 and normalized for pressure and integration time. Abundance of the molecular parent ions varies significantly, with the pyridazine parent ion significantly enhanced, and the pyrimidine parent significantly reduced in comparison to the others. The photodynamics of the parent ionizations are significantly influenced by the lone pair orbitals of the nitrogen atoms and the way they interact; as the nitrogens are moved farther apart, the spatial overlap of the lone pairs is reduced and the through-space interactions (discussed in Section 6.4.1) are weakened.

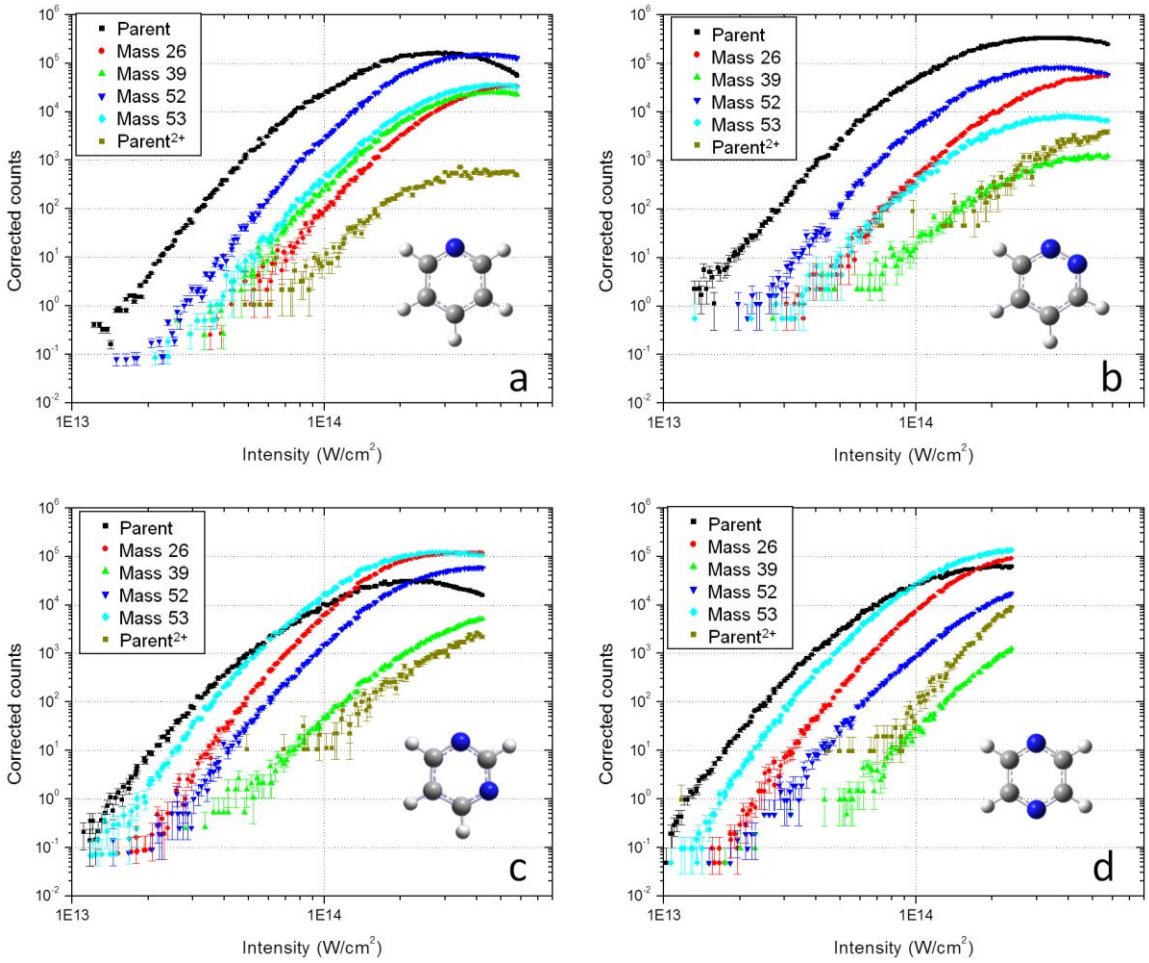

Figure 26 – All fragment yields of the azabenzenes. Ionic yields of all prominent fragments are displayed for pyridine (**a**), pyridazine (**b**), pyrimidine (**c**), and pyrazine (**d**) as a function of intensity. The variance in fragmentation between species is larger than in the other series we have studied.

The ionic yields of the prominent fragments are presented in Figure 26 as a function of intensity. Here one can see the influence of substituting atoms into the ring: the azabenzenes show considerably more variation in the nature of their fragmentation than the halobenzenes or the CNOF series. It is useful to compare the yields of ions with mass 52 and 53 amu. While the fragments resulting in these peaks are not precisely distinguishable (since C–H and N differ by only one mass unit), we can still gain some information from their yields. We have seen from the benzene yields that C_4H_5 is a very

unlikely fragment, so the 53 amu peak is more likely to contain nitrogen atoms from the ring (and for the diazines, there are not five hydrogens to make this fragment). In pyridine and pyridazine (Fig. 26 (**a**) and 26 (**b**)), the 52 amu fragments dominate the 53 amu fragment. Pyridine, with only one nitrogen atom, has two dissociation pathways to form a four-carbon chain, so the C_4H_4 yield is comparatively enhanced. Pyridazine can fragment into C_4H_4 and N_2; pyrimidine and pyrazine, on the other hand (Fig. 26 (**c**) and 26 (**d**)), do not have four consecutive carbons in the chain, and are thus less likely to form a 52 amu fragment. As such, the 53 amu fragments dominate the 52 amu fragments in pyrimidine and pyrazine, while the reverse is true for pyridine and pyridazine.

The 39 amu peaks, which represent C_3H_3 or C_2HN, are fairly consistent throughout the series, though they are enhanced in pyridine and suppressed in pyridazine (although both effects are fairly small). It is difficult to make any substantial claims about the fragmentation which leads to these peaks, since multiple dissociation channels contribute. Further, we cannot merely assume them to be C_3H_3, since this fragment cannot form from pyrazine, yet we still see a substantial yield from the C_2HN in Fig. 26 (**d**). Finally, we see the yield of the 26 amu fragment (C_2H_2 or CN) increase from Fig 26 (**a**) to (**b**) to (**c**) to (**d**). As the number of ways to form large carbon chains decreases progressively along this same pattern, the final states may be forced into smaller fragments such as these.

With the exception of nitrobenzene, the azabenzenes are the four likeliest to fragment in comparison to their parent ion yields that we have studied. This emphasizes the significance of the effects of a substitution inside the ring as opposed to adding a functional group to the outside.

References

[1] Kimura K., *Handbook of HeI photoelectron spectra of fundamental organic molecules: ionization energies, ab initio assignments, and valence electronic structure for 200 molecules*, Japan Scientific Societies Press, 1981.

[2] Rasmusson, M., Lindh, R., Lascoux, N., Tarnovsky, A., Kadi, M., Kuhn, O., Sundstrom, V. & Akesson, E. 2003, "Photodissociation of bromobenzene in solution," *Chemical Physics Letters*, vol. 367, no. 5-6, pp. 759-766.

[3] Anders Borg, O., Karlsson, D., Isomäki-Krondahl, M., Davidsson, J. & Lunell, S. 2008, "Predissociation of chlorobenzene, beyond the pseudo-diatomic model," *Chemical Physics Letters*, vol. 456, no. 4-6, pp. 123-126.

[4] Zhang, X.P., Wei, Z.R., Lee, W.B., Chao, T.J. & Lin, K.C. 2008, "Photodissociation of dibromobenzenes at 266 nm by the velocity imaging technique," *Chemphyschem : a European journal of chemical physics and physical chemistry*, vol. 9, no. 12, pp. 1721-1728.

[5] Zhang, X., Wei, Z., Tang, Y., Chao, T., Zhang, B. & Lin, K. 2008, "Halogen effect on the photodissociation mechanism for gas-phase bromobenzene and iodobenzene," *Chemphyschem*, vol. 9, no. 8, pp. 1130-1136.,

[6] Scarborough, T.D., Strohaber, J., Foote, D.B., McAcy, C.J. & Uiterwaal, C.J.G.J. 2011, "Ultrafast REMPI in benzene and the monohalobenzenes without the focal volume effect," *Physical Chemistry Chemical Physics*, vol. 13, no. 30, pp. 13783-13790.

[7] *NIST Chemistry WebBook*, National Institute of Standards and Technology, http://webbook.nist.gov/chemistry.

[8] Cheng, P., Zhong, D. & Zewail, A. 1995, "Kinetic-Energy, Femtosecond Resolved Reaction Dynamics - Modes of Dissociation (In Iodobenzene) from Time-Velocity Correlations," *Chemical Physics Letters*, vol. 237, no. 5-6, pp. 399-405.

[9] Sage, A.G., Oliver, T.A.A., Murdock, D., Crow, M.B., Ritchie, G.A.D., Harvey, J.N. & Ashfold, M.N.R. 2011, "nσ* and πσ* excited states in aryl halide photochemistry: a comprehensive study of the UV photodissociation dynamics of iodobenzene," *Physical Chemistry Chemical Physics*, vol. 13, no. 18, pp. 8075-8093.

[10] Kruit, P., Kimman, J., Muller, H. & Vanderwiel, M. 1983, "Electron-Spectra from Multiphoton Ionization of Xenon at 1064, 532, and 355 nm," *Physical Review A*, vol. 28, no. 1, pp. 248-255.

[11] Johnson, A.W., *Invitation to organic chemistry*, Jones and Bartlett Publishers, 1999.

[12] Tasker, A.D., Robson, L., Ledingham, K.W.D., McCanny, T., Hankin, S.M., McKenna, P., Kosmidis, C., Jaroszynski, D.A. & Jones, D.R. 2002, "A High Mass Resolution Study of the Interaction of Aromatic and Nitro-Aromatic Molecules with Intense Laser Fields," *The Journal of Physical Chemistry A*, vol. 106, no. 16, pp. 4005-4013.

[13] He, Y., Gahlmann, A., Feenstra, J.S., Park, S.T. & Zewail, A.H. 2006, "Ultrafast electron diffraction: structural dynamics of molecular rearrangement in the NO release from nitrobenzene," *Chemistry, an Asian journal*, vol. 1, no. 1-2, pp. 56-63.

[14] Lowe, J.W. & Peterson, K., *Quantum chemistry*, Elsevier Academic Press, 2006.

[15] MATLAB 6.1, The MathWorks Inc., Natick, MA, 2000.

[16] Harris, D.C. & Bertolucci, M.D., *Symmetry and spectroscopy: an introduction to vibrational and electronic transitions*, Dover, 1989.

[17] Frisch, M. J. *et al*, Gaussian 03, Gaussian Inc., Wallingford CT, 2004.

Chapter 8

Metastable molecular fragmentation

The work represented in this chapter originated from what first appeared to be an error in the time of flight (TOF) spectra of several molecules under investigation. Peaks in the spectra were observed which were not consistent with integer values of mass and charge; further, these peaks were broad, typically landing over a time range an order of magnitude (or more) greater than the surrounding peaks. These broad features were observed in many different molecules under investigation. They showed up at the same TOF over multiple data runs of a particular molecule, but were at different TOFs for different molecular targets, suggesting a substance-dependent process. The anomalous peaks are identified as metastable excited-state ions [1-15] which exist as a stable ion long enough to survive into the drift region (see Chapter 5 for details of the spectrometer) before fragmenting, which puts their decay lifetime greater than ~100 ns.

8.1 – Kinematics of a metastable molecular ion

Section 5.3 detailed the kinematics of molecular ions in the mass spectrometer. This section will carry out the same analysis for the case of metastable fragmentation. For identification of the various distances and potentials, refer to Fig. 4 in Chapter 5.

The velocity of an ion, initially at rest at a distance x_0 from the slit, with mass m_i (denoting initial mass) and initial charge q_i at the end of the acceleration region of the TOF apparatus is

$$v_a = \sqrt{\frac{V_r q_i}{m_i d_r} \cdot 2d_0} \tag{8.1}$$

as was shown in Chapter 5. The time the ion spends in the acceleration region is the quotient of this velocity and the acceleration due to the potential V_r :

$$t_a = \sqrt{\frac{2d_0 m_i d_r}{V_r q_i}}. \tag{8.2}$$

An ion that passes through the slit enters a drift region of length d_1. In this region there is no electric field, so the ion travels with velocity v_a. For the non-metastable case as previously discussed, the ion would travel with this velocity for the entire length of the drift chamber. However, here the assumption is made that after some distance $d_e < d_1$ beyond the acceptance slit, the ion breaks apart into another, smaller fragment ion (mass m_f and charge $q_f = q_i$) and one or more neutral fragments. We assume the charge to remain unchanged, we will drop the subscripts and simply call the charge q; this condition may not always be valid, but without it there are too many degrees of freedom to resolve the dissociation dynamics. The subscript in d_e refers to the position of the "explosion" of the ion in the drift region. The new velocity of the second ion is equal to the original center-of-mass velocity v_a in addition to a velocity component determined by some kinetic energy T_e released during the dissociation of the ion. Let us therefore define an altered, post-decay drift velocity $\tilde{v}_a$ such that

$$\tilde{v}_a = v_a + \sqrt{\frac{2T_e}{m_f}} \cos\theta. \tag{8.3}$$

A typical kinetic energy release (~1 eV) [10] will be much smaller than $\frac{1}{2}m_f v_a^2$ (~1 keV), so $\tilde{v}_a \cong v_a$. The total TOF in the drift region is the sum of the pre-decay and post-decay times, so

$$t_1 = \frac{d_e}{v_a} + \frac{d_1 - d_e}{\tilde{v}_a}. \quad \textbf{(8.4)}$$

At the end of the drift region, the ion enters the first deceleration region, in between a grounded mesh grid ($V_1 = 0$) and a similar grid held at a potential V_2. While stable ions created in the laser's focus are not turned around in this first deceleration region, that is not necessarily true for the metastable case. We thus will consider two cases.

In the first case, the ionic fragment is not halted in this region. By the time the ion reaches the second grid, it will have a reduced but nonzero speed given by

$$v_2 = \sqrt{\tilde{v}_a^2 - \frac{2qV_2}{m_f}} \quad \textbf{(8.5)}$$

Note that the difference from the standard, non-metastable case is manifested in the altered velocity at the first grid and the presence of m_f instead of m_i. The total time spent in this region is given by

$$t_2 = \frac{(\tilde{v}_a - v_2)}{a_2} = \frac{m_f d_2}{qV_2}\left(\tilde{v}_a - \sqrt{\tilde{v}_a^2 - \frac{2qV_2}{m_f}}\right). \quad \textbf{(8.6)}$$

At the end of the first deceleration region, the ion enters a second deceleration region of length d_3, between grid 2 and grid 3. In this region, the ion does turn around, so its final velocity is taken to be 0. This allows us to easily compute the time t_3:

$$t_3 = \frac{v_2}{a_3} = \frac{m_f d_3}{q(V_3 - V_2)}\sqrt{\tilde{v}_a^2 - \frac{2qV_2}{m_f}}. \quad \textbf{(8.7)}$$

There is the second drift region of length d_{MCP} in which the ion travels to the MCP and is measured. Due to the symmetry of the TOF chamber setup, the ion should have velocity $\tilde{v}_a$ after it leaves the acceleration region traveling the opposite direction, so the time that it spends in this second drift region is

$$t_4 = \frac{d_{MCP}}{\tilde{v}_a}. \tag{8.8}$$

The total expression for the TOF, combined and simplified, can therefore be expressed in terms of known values and some specifiable parameters: the initial and final masses, the distance at which the dissociation occurs d_e, the kinetic energy released T_e, and the angle of the added velocity component θ (the final three parameters are contained inside $\tilde{v}_a$). The final expression is

$$TOF = \frac{v_a}{a_r} + \frac{d_e}{v_a} + \frac{d_1 - d_e + d_{MCP}}{\tilde{v}_a} + \left(\frac{2m_f}{q}\right)\left(\frac{d_2}{V_2}\right)\left(\tilde{v}_a - \sqrt{\tilde{v}_a^2 - \frac{2qV_2}{m_f}}\right)$$

$$+ \left(\frac{2m_f}{q}\right)\left(\frac{d_3}{V_3 - V_2}\right)\sqrt{\tilde{v}_a^2 - \frac{2qV_2}{m_f}}. \tag{8.9}$$

A MATLAB [16] program which simulates the TOF under conditions of metastable fragmentation can be found in Appendix A.3. With the substitution that $\tilde{v}_a \cong v_a$, Eq. 8.9 reduces nearly to the original, non-metastable case (Eq. 5.9), with the only difference being that the trajectory between grids 1 and 3 is now influenced by the reduced mass of the fragment. This implies that the TOF of the fragments is largely determined by the change in mass. Furthermore, the decay distance d_e drops out of the equation in the limit $\tilde{v}_a = v_a$, making the breakup distance on the TOF of the metastable peak unimportant.

For the second case, the ionic fragment is halted in the first deceleration region, and so its final velocity before reaching the second grid is zero. In this case, the time for the ion to come to a halt is

$$t_2 = \frac{\tilde{v}_a}{a_2} = \frac{m_f d_2}{qV_2}\tilde{v}_a \qquad \textbf{(8.10)}$$

Again, this time is doubled when computing the total TOF, and the second drift region time t_4 is included again, leading to a new expression for the total TOF:

$$TOF = \frac{v_a}{a_r} + \frac{d_e}{v_a} + \frac{d_1 + d_{MCP} - d_e}{\tilde{v}_a} + \frac{2m_f d_2}{qV_2}\tilde{v}_a. \qquad \textbf{(8.11)}$$

The particular tuning of the potentials, which is responsible for a tight focusing of the ions that exist in both deceleration zones, is incorrect to focus ions which only reach the first deceleration zone.

The condition for the ions to turn around in the first deceleration region is that

$$\tilde{v}_a^2 - \frac{2qV_2}{m_f} \leq 0 \qquad \textbf{(8.12)}$$

Again using the approximation that $\tilde{v}_a \cong v_a$, and using the values $V_2 = 800$ V, $V_r = 1530$ V, $d_r = 3$ mm, and $x_0 = 2$ mm, one concludes that the condition on m_f for the daughter ion to turn around before the second grid is $m_f \leq 0.78\, m_i$. For pyridine, this corresponds to a final mass of 62 atomic mass units (amu), so we conclude that for most metastable decays with the given potentials, the daughter ion is turned around before the second grid.

8.2 – Observation of metastable ions

We have observed peaks indicating metastable dissociation in a number of aromatic molecules, including pyridine (C_6H_5N), pyridazine, pyrimidine, and pyrazine (all $C_4H_4N_2$), phenol (C_6H_5OH), aniline ($C_6H_5NH_2$), fluorobenzene (C_6H_5F),

bromobenzene (C_6H_5Br), iodobenzene (C_6H_5I), anisole ($C_6H_5OCH_3$), and nitrobenzene ($C_6H_5NO_2$). These features are typically small (~ a few hundred counts) even at high intensities. Pyridine, however, has a feature containing over an order of magnitude more counts than any other metastable feature we observe. For this reason pyridine was chosen for further experimental analysis.

8.2.1 – Metastable fragments of pyridine

Fig. 1 shows an example of the largest broad feature in the TOF spectrum of pyridine. It lands at a similar TOF to its counterparts in the azabenzene series. What makes pyridine a prime candidate to investigate, more so than all the other molecules previously discussed, is its relative propensity to undergo metastable fragmentation. The broad peak contains a comparable number of counts to the parent ion peak, which remains the dominant feature. As Fig. 2 shows, the total ion yield as a function of intensity for the broad peak closely follows that of the molecular parent at high intensities, suggesting that the metastable fragmentation originates from the parent ion. The two curves do deviate at low intensities; this could be indicative of an intensity-dependent population of a metastable excited ionic state. However, at present no solid conclusions can be drawn in this regard. Pyridine was ionized with focused, high-intensity, 50 fs laser pulses at 800 nm, with (3 + 3) resonance-enhanced multiphoton ionization (REMPI) being the dominant ionization mechanism [17].

The data presented in Fig. 2 differ from those of the REMPI experiment from Ref. [17] in that Fig. 2 represents only two-dimensional spatial resolution; the REMPI signatures are not visible here, but this more accurately describes the comparative yields

of the parent and metastable ions, since the metastable ion cannot be three-dimensionally resolved as described in Chapter 5.

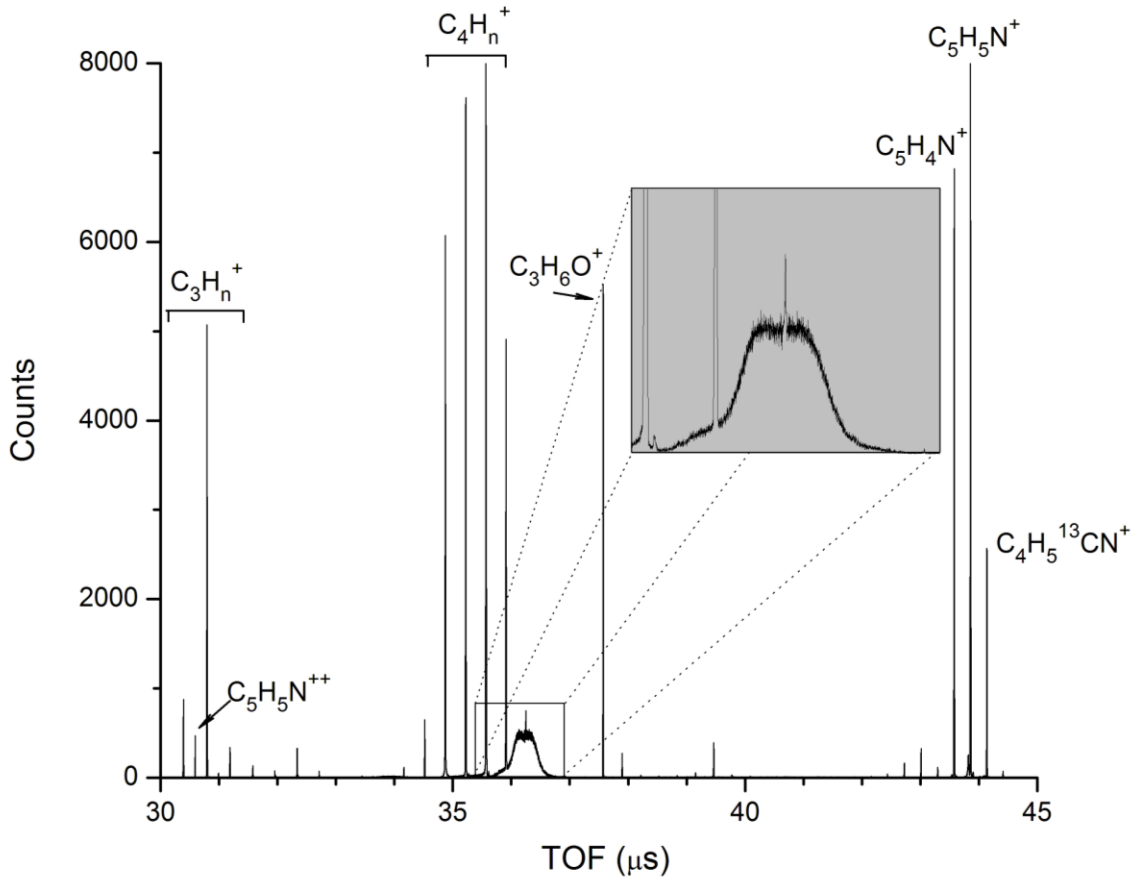

Figure 1 – Diffuse peak in pyridine. The locations of several surrounding prompt ion peaks are included for reference. Notice the scale on the y-axis: The broad feature in pyridine contains orders of magnitude more counts than any of its counterparts in the diazines (or any of the other molecules we have studied). While the prompt ion peaks, measured on a tuned TOF setting, are confined to 10 ns regions on the TOF spectrum, the broad feature is nearly 500 ns in full width at half maximum. The coincident sharp peak which appears on top of the diffuse peak in the inset is unrelated to the metastable feature and is there only by chance.

We assume that these broad peaks arise from the metastable dissociation of an ion (not necessarily the singly-ionized molecular parent) in the drift region of the TOF. Part and parcel with this assumption are four unknowns: the parent ion mass and charge, the daughter ion mass and charge, the dissociation lifetime, and the kinetic energy release

(KER) distribution. A method for obtaining information on such metastable dissociations in TOF mass spectrometers was presented in Ref. [3]. In the present work, this method of tuning reflectron voltages to energy-select ions in the TOF is employed to identify dissociative products and propose metastable pathways for pyridine. Simulating the proposed dissociation is shown to produce similar results to those obtained experimentally.

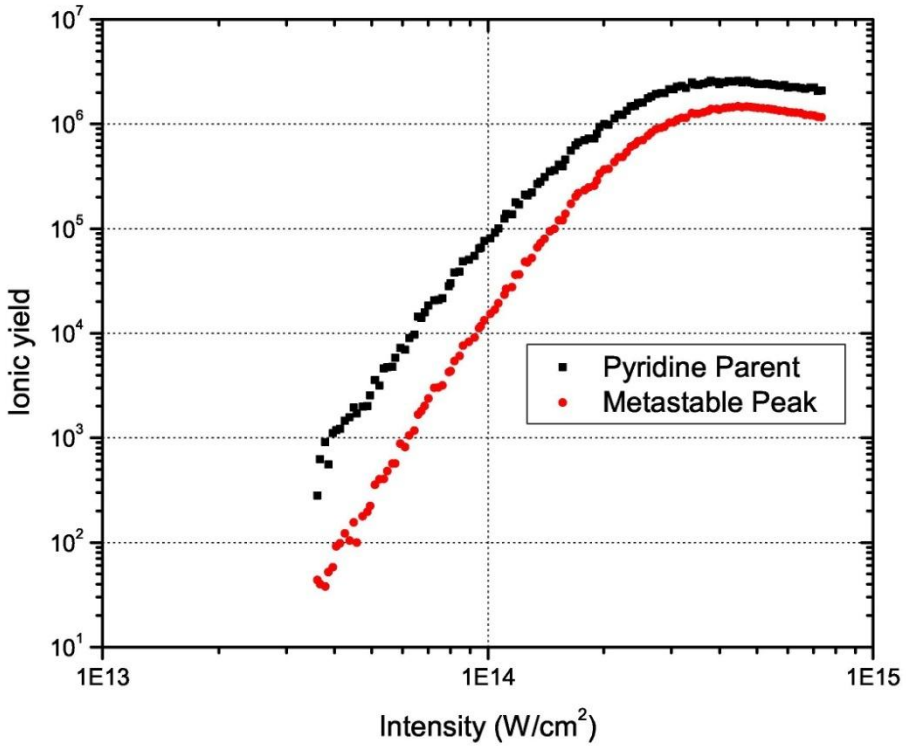

Figure 2 – Ionic yield as a function of intensity. The two curves represent the integrated total ion yield for singly-ionized pyridine (black squares) and the metastable state (red circles). The correspondence of total yield at high intensity suggests that this metastable feature arises from the ionized parent. At low intensities, poor statistics inhibit rigorous analysis of the data, but the metastable state clearly falls further under the parent ion. It is a hypothesis that the excited ionic state responsible for the metastable dissociations is only substantially populated at high intensities.

The broad features were first observed in all molecules while the TOF spectrometer was configured to spatially resolve the incoming ions. A retuning of this

voltage allows this effect to be negated, creating the tuned TOF dispersion curve throughout the interaction region. It is important to rule out the spatial resolution for the monotonically increasing case as being some unaccounted source of the spreading of the observed features. As such, data were taken on both time-focused and spatially-resolved tunings of the spectrometer to observe the effect of changing the voltage on the structure of each peak. As expected, the form of the wide feature did not change for different tunings. Fig. 3 shows the consistency of the broad feature in pyridine, with and without spatial resolution.

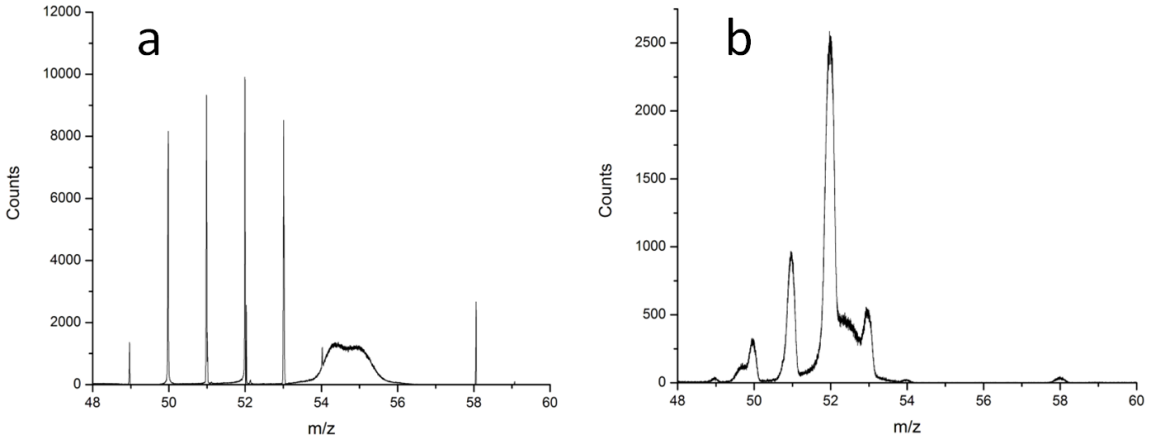

Figure 3 – Consistency of the metastable feature. Data were taken both on focused-in-time (left) and spatially-resolved (right) settings of the TOF mass spectrometer. The position of the metastable feature relative to the surrounding ions changed when this setting was switched as a result of the different potentials on the spectrometer grids. However, the peak remained, eliminating the possibility that this feature was some artifact of the tuning of the grid potentials.

8.2.2 – Recovering mass information

Let us state the assumptions taken in order to reach this point. First, it is assumed that the ion breaks apart in the first drift region ($d_e < d_1$). Second, the angle at which the additional velocity is added to the trajectory must be sufficiently small that the ion still reaches the multichannel plate (3 cm diameter). This acceptance angle will depend on the

total TOF of the fragment. Third, it is assumed that the ion has sufficiently small kinetic energy to be turned around in one of the deceleration regions. In other words, the fragment ion does not pass by both grids without being halted. At the moment, this assumption says nothing about which deceleration region the ion is actually halted in, only that it does in fact get halted.

The first assumption is taken as a hypothesis for the experiment. The first and second assumptions are accounted for in the code used for modeling (see [18] for details). For the third assumption, to avoid being transmitted through grid 3 (and thus disappearing from the mass spectrum), the kinetic energy must be less than some cutoff voltage, which is determined by the potential of grid 3. Mathematically, we have ions with kinetic energy

$$T = \frac{1}{2} m_f v_a^2 = \frac{d_0 m_f}{d_r m_i} q V_r \tag{8.13}$$

For ions to be detected, qV_3 must be greater than this kinetic energy. In fact, this condition can be used to identify the final masses of the daughter ions, as described by Ref. [3]. By decreasing V_3 until the daughter ions disappear from the TOF spectrum and using the relation

$$V_3 = \left(\frac{d_0}{d_r}\right)\left(\frac{m_f}{m_i}\right) V_r \tag{8.14}$$

from equating the two expressions for energy, one can solve for the ratio m_f/m_i. This result is the crucial point of Boesl et al. [3], and is what allows us to make any conclusions about the metastable states in pyridine. While this is a compelling result, it should be stressed here that making any definitive claims beyond this ratio is not supported by the kinematics. For instance, while m_i could be the mass of the molecular parent ion, but there is nothing in the derivation prohibiting the metastable dissociation

from some other fragment ion. Even the mass ratio itself may be incorrect if the dissociation happened from a doubly-charged parent ion. Despite these limitations, this method used in conjunction with other methods of investigation of the process at hand should often be able to isolate the particular dissociation observed.

8.2.3 – Recovering lifetime and kinetic energy release information

As was mentioned in section 8.1, for the likely case that $\tilde{v}_a \cong v_a$, the actual position in the drift tube that the parent ion dissociates does not significantly influence the total TOF of the parent-daughter combination. Since this distance would be the only way from the data to measure how long it took for the dissociation to occur, there is little that can be said about the scale of the dissociation lifetime. However, we can place limitations of the dissociation lifetime. For the metastable process to occur in the field-free drift region (one of the hypotheses of our analysis), it must survive longer than the time that it spends in the acceleration region. This time is $t_a \cong 80$ ns for pyridine. Furthermore, it must dissociate before it exits the first deceleration region, and the total time since ionization that an ion would spend to reach this point would be $t = t_a + t_1 \cong 20$ μs. From this, we conclude that the lifetime must be $10^{-7} - 10^{-5}$ s, a range that is well-documented as a typical metastable lifetime [19,20].

In order to make a statement about the KER distribution, consider first the kinetic energy distribution of ions that are created in the laser focus and do not decay. The kinetic energy of these ions is determined entirely (up to thermal effects) by where the ion was created in the focus. Ions at different positions in the focus experience the electric field of the acceleration region of the TOF for differing distances, creating some spread of kinetic energies. By measuring the extinction curve for the molecular parent ion

peak, one can obtain the kinetic energy distribution of the ions, since the extinction curve statistically represents the continuous distribution function (CDF) for kinetic energy in the laser's focus. This kinetic energy distribution was found to have a $1/e^2$ width of about 10.1 eV; the parent extinction curve is found in Fig. 4. This information could also be used to determine the size of the pulse focus (at least the size of the region able to create pyridine ions), but this information is not directly relevant to this study.

The extinction curves were fit using a Logistic function. Although this is not not purely the CDF of a Gaussian distribution, it is a close approximation. This function has the form

$$B(x) = \frac{a}{1+e^{k(x-x_c)}} \quad \textbf{(8.15)}$$

$a, x_c,$ and k are freely-specifiable parameters. When this function was determined, its derivative is taken to generate a synthesized probability density function (PDF). The PDF is plotted and fit to a Gaussian to finally determine the $1/e^2$ width.

The fragments produced by metastable decay will retain the kinetic energy distribution from their parent ion in the focus, but will have some additional kinetic energy component due to the exothermic bond breaking during decay. Therefore, if the fragments came from the parent ion, any extra KER width will be due to metastable decay. Furthermore, if the extinction curve $1/e^2$ width is less than 10.1 eV, one can conclusively determine that the metastable feature did not arise from the molecular parent ion, but rather some other precursor ion. The widths for these precursor ions could be smaller than that of the molecular parent because the region of the laser focus in which light is intense enough to produce these ions (the interaction volume) can be smaller for fragments and multiply-ionized states than it is for singly-ionized pyridine. As fragments

and multiply-ionized states will likely require a higher laser intensity to be produced (and thus be limited to a smaller interaction volume), such a conclusion fails to isolate a single new candidate for the metastable parent.

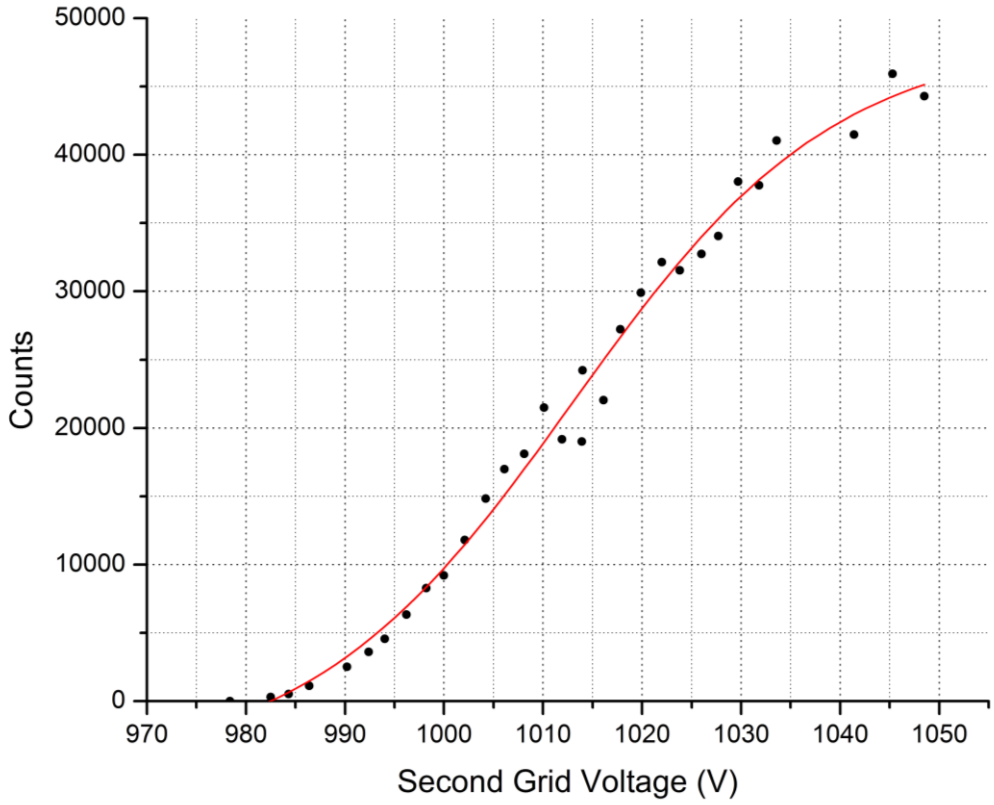

Figure 4 – Extinction curve for the molecular parent ion. Measuring the central value of this extinction curve allows measurement of the average initial position in the focus d_0, from Eq. 8.2 (the mass does not change, so the quotient in that equation is 1). Measuring the width provides a benchmark distribution to compare with the metastable extinction curves, for the purposes of calculating kinetic energy release distribution. This will be done in Section 8.2.5.

8.2.4 – Tuning diffuse peaks

By proportionally lowing the grid voltages V_2 and V_3, the shape of the TOF curve is maintained; meanwhile, the range of fragment energies which are focused in time is reduced by the same proportion. Seen in Fig. 5, this essentially walks the interaction

region along the TOF curve until, at low enough voltages, the metastable peaks are focused.

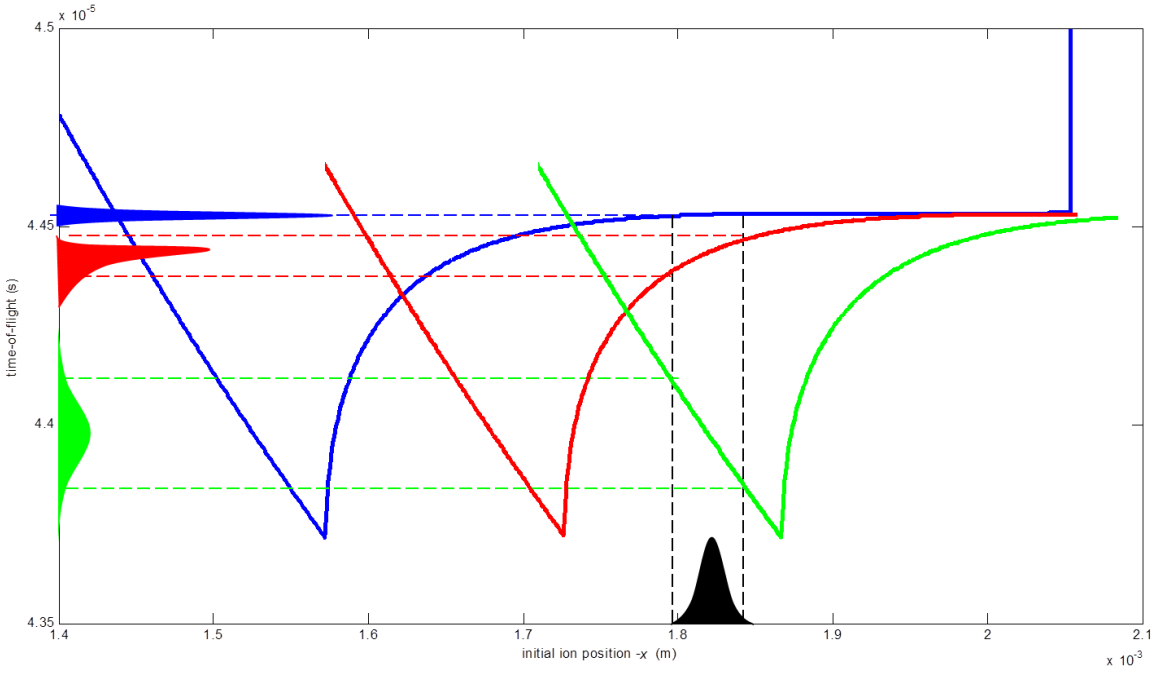

Figure 5 – Tuning the metastable peaks. As the voltages of the mesh grids are lowered, the TOF curve for different positions of the focus maintains its shape, but is tuned for a different range of kinetic energies. High grid voltages turn peaks around in the first deceleration region, resulting in broad ion peaks (green). Lower voltages allow ions into the second deceleration region, but not into the region where the TOF is focused in time (red). Still lower voltages allow for proper focusing in time (blue).

The cutoff voltage V_3 was lowered until all of the stable ions produced in the laser focus could no longer be reflected and thus escaped detection. Measuring the extinction of the stable peaks as a function of V_3 allowed the measurement of the initial position of the ions in the TOF chamber (the position of the focus). By modifying Eq. 8.2, with $m_f = m_i$ for non-metastable ions, it is found that $d_0 = 1.993 \pm 0.005$ mm. As the cutoff potential was continually lowered, it became apparent that the main metastable

peak observed in the original mass spectrum actually consists of three separate features, closely spaced, as shown in Fig. 6.

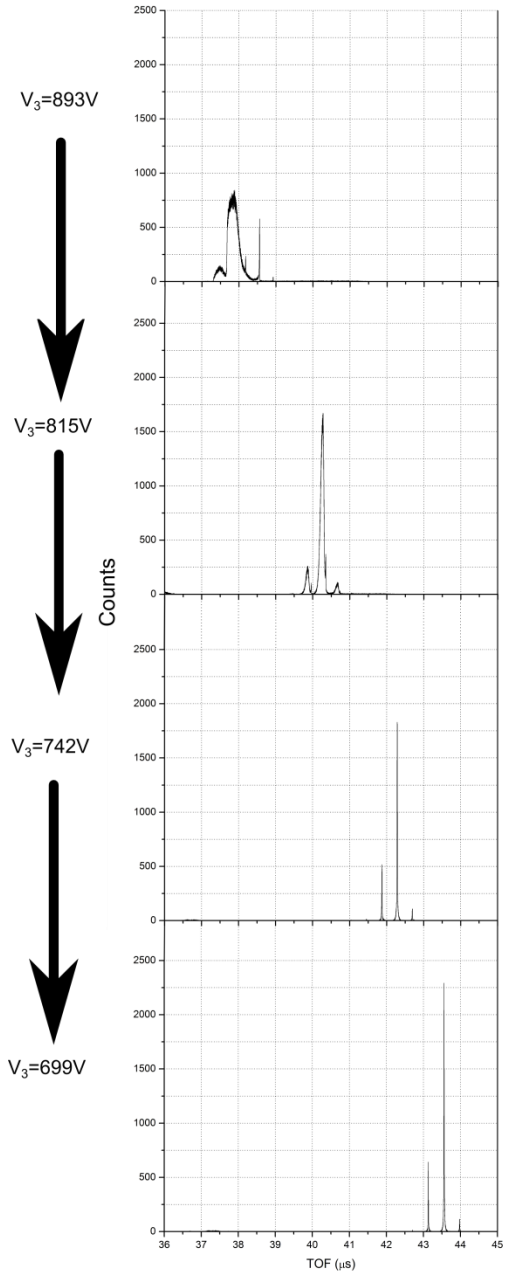

Figure 6 – Broad feature evolution. As the back grid potential was continually lowered, the three metastable peaks became focused in time and migrated towards higher TOF values. Prior to the highest (top) potential, the single broad feature split into three distinguishable peaks; the trio becomes more distinct as the potential is lowered.

By keeping the middle potential V_2 proportional to V_3 as it was when the normal ions were tuned, the metastable peaks were brought into sharp focus. The three peaks will be henceforth referred to by their numbering in Fig. 7. This numbering system uses boldfaced numbers, in parentheses, from left (highest TOF) to right (lowest TOF). Therefore, these three peaks are **(1)**, **(2)**, and **(3)**, and we will refer to these as a triplet of peaks. It should also be noted that the peaks move to the right as they are brought into focus; it appears to be a pattern that the peaks move to the right with increasing V_3 until they reach approximately 45 μs TOF. After this they begin to decay as V_3 is no longer large enough to reflect the ions. This terminal TOF of 45 μs is independent of the actual final cutoff potential.

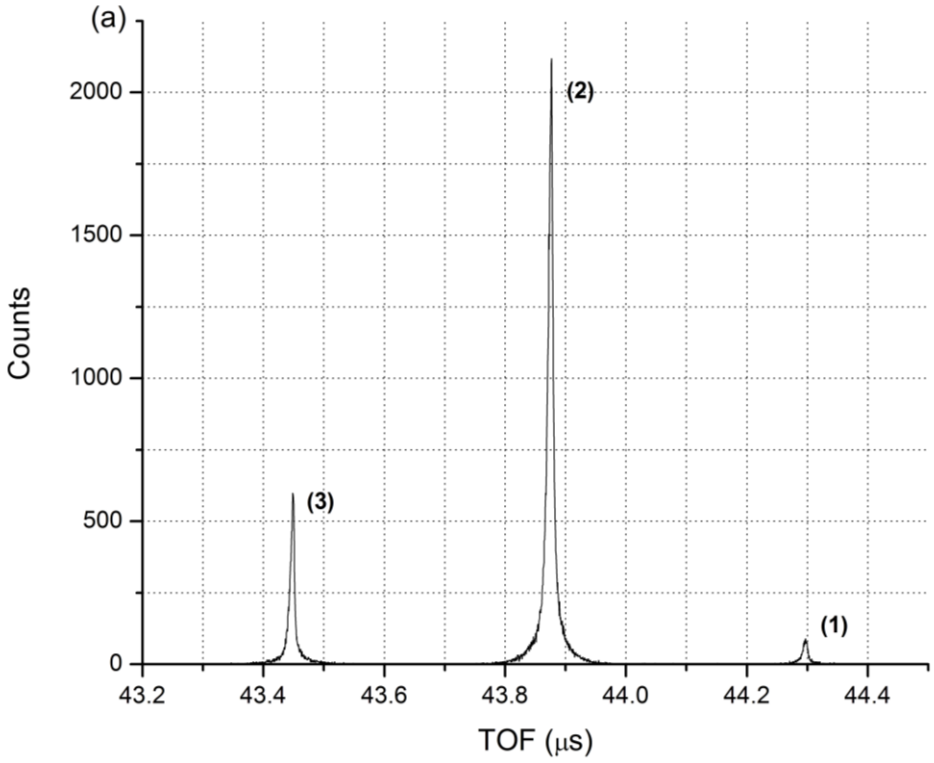

Figure 7 – The labeling scheme for the peaks (1), (2), and (3). For this spectrum, V_3=689 V, which is a potential just above the point at which these peaks start to disappear. All three exhibit a broadening at the base, likely indicative of a kinetic energy release during dissociation.

As these three features disappear (V_3 drops below ~670 V), three more diffuse peaks begin to become recognizable on the mass spectrum. As one continues to lower the cutoff potential, these peaks become similarly focused and migrate to the higher TOF. We similarly label these peaks **(4)**, **(5)**, and **(6)**, as seen in Fig. 8. These three peaks are spaced farther apart in time at all potentials, and **(5)** has a different shape than **(4)** and **(6)** always. This suggests that treating **(4)**, **(5)**, and **(6)** as a triplet, as was done for **(1)**, **(2)**, and **(3)**, is not appropriate. Once V_3 is sufficiently low (below 500 V), these three peaks also begin to disappear, but do so over a much longer range of potentials than the first triplet did.

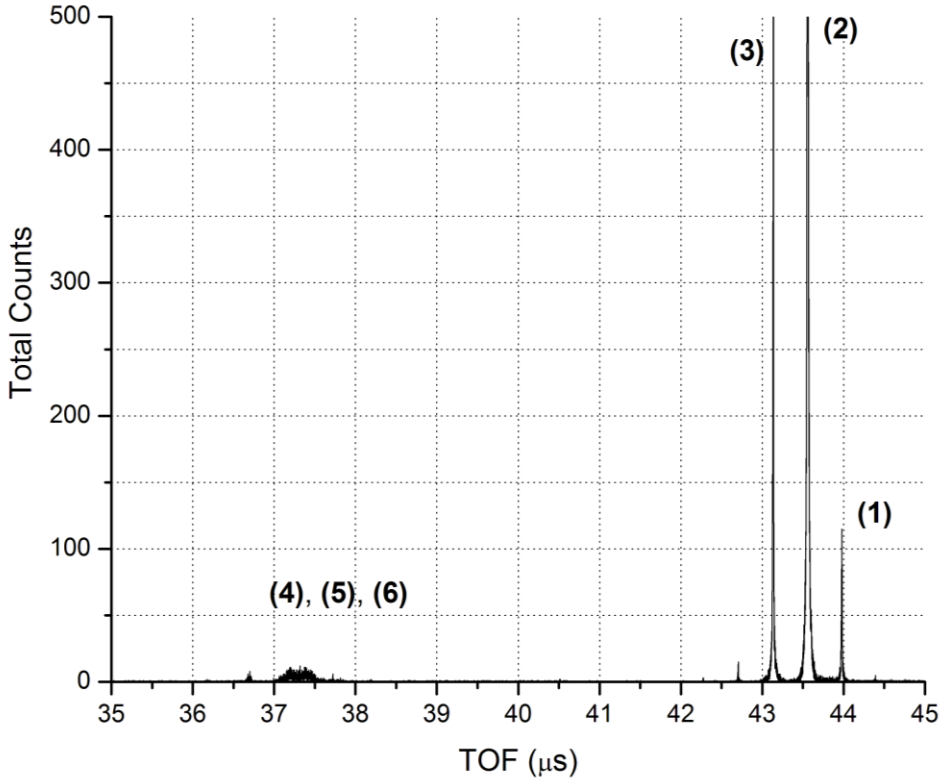

Figure 8 – All six metastable peaks. As **(1)**, **(2)**, and **(3)** are focused, **(4)**, **(5)**, and **(6)** are still diffuse. V_3=699 V for this plot.

However, as the voltages are lowered further, it is revealed that peak **(5)** is itself a triplet, as seen in Fig. 9. Although it appears in the TOF spectrum between peaks **(4)** and **(6)**, this indicates that it is the result of a fundamentally different dissociation process. This will be discussed in further detail in the next section.

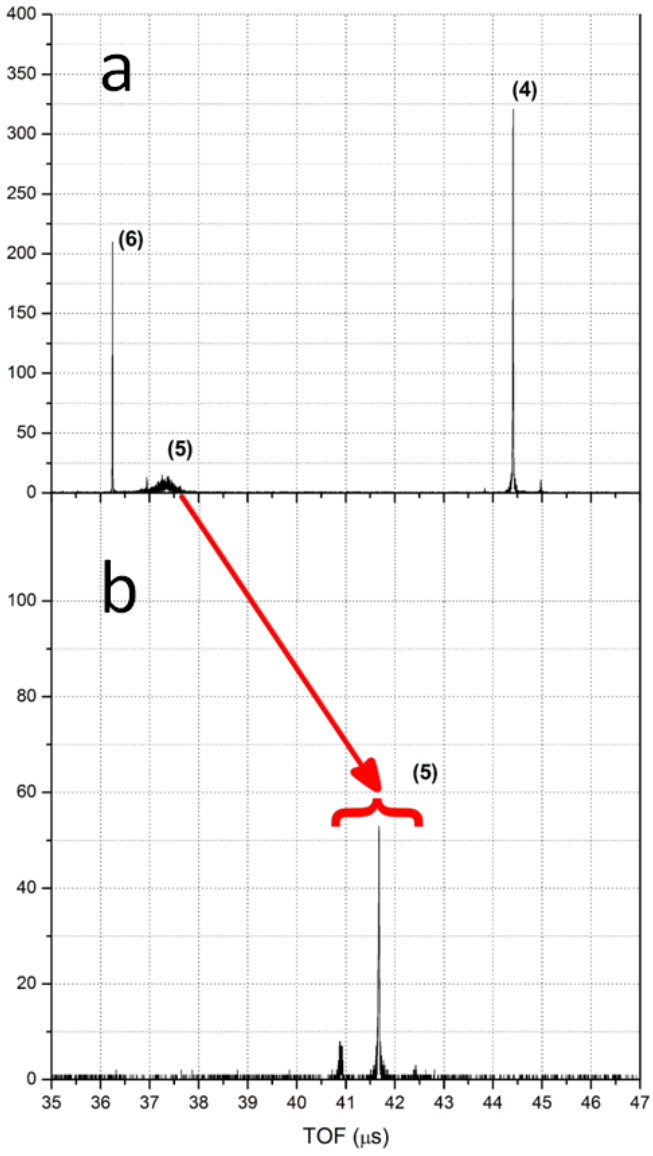

Figure 9 – Labeling scheme and decreasing voltage progression of (4), (5), and (6). Between (**a**): V_3=504 and (**b**): V_3=410 V, **(4)** and **(6)** disappear, while **(5)** is brought into focus and moves substantially to the right. The significantly different behavior of **(5)** suggests a different precursor, possibly the doubly-ionized parent.

8.2.5 – Determining mass values

We define the cutoff potential for each peak as the potential at which the ion yield per unit time for that peak is exactly 50% of the full ion yield (at a potential far above the cutoff potential). These extinction voltages, and the corresponding m_f/m_i ratio as determined from Eq. 8.2, are shown in Table 1. With the assumption that the parent ion lies somewhere in the parent or parent-minus-hydrogen group ($^m/_Z = 78, 79, 80$), the daughter ion falls somewhere in the C_4H_n group. Specifically, if for **(2)**, the dominant metastable feature, $m_i = 79$ amu, then $m_f \cong 52$ amu, suggesting the decay $C_5H_5N^+ \rightarrow C_4H_4^+ + HCN$. This particular decay channel has been previously documented in pyridine and pyrazine [21,22].

Peak	V_E(V)	m_f/m_i	Proposed $m_f \rightarrow m_i$ (amu)	Hypothesized dissociation scheme	KE dist. width (eV)
(1)	679.9 ± 0.719	0.669	80 → 53	$C_4H_5{}^{13}CN^+ \rightarrow C_3H_4{}^{13}C^+ + HCN$	10.2
(2)	673.1 ± 0.793	0.662	79 → 52	$C_5H_5N^+ \rightarrow C_4H_4^+ + HCN$	11.4
(3)	670.4 ± 0.311	0.660	78 → 51	$C_5H_4^+ \rightarrow C_4H_3^+ + HCN$	14.2
(4)	492.9 ± 0.585	0.490	79 → 39	not identified	6
(5)	358.9 ± 0.773	0.357	79 → 52	$C_5H_5N^{++} \rightarrow C_4H_n^{+(+)} + H_{(5-n)}CN$	7.5
(6)	488.7 ± 0.374	0.486	79 → 38	not identified	7.1
Parent	1013 ± 1.11	N/A	N/A	N/A	10.1

Table 1 – Extinction voltages for the six observed metastable peaks. From the extinction curves and Eq. 8.2, the mass ratio can be calculated. This mass ratio is used to claim dissociative pathways for each of the metastable peaks. These pathways are only taken as a hypothesis, and **(4)** and **(6)** are shown to not be the result of 79 → 39, 38 when one considers the KER distribution. **(5)** is speculative, and merely states that the peak could likely result from the doubly-charged molecular parent decaying into some C_4H_n fragment (possibly multiply-charged as well). The kinetic energy distribution width for the metastable peaks is assumed to have a component due to kinetic energy release, so the width should be at least as wide as the parent.

While it seems reasonable to assume that **(2)** comes from the parent ion given its abundance, identification of **(1)** and **(3)** is more ambiguous. Either could come from a heavy parent molecular ion, $C_4H_5N(^{13}C)^+$, or potentially $C_5H_4N^+$, which is photochemically similar to the ionic parent. Conclusive results from the experimentally-determined mass ratios are not attainable, but simulations can help to determine the parent and final ion states, as is documented in [18]. **(1)** and **(3)** were shown by modeling to have likely come from $m_f \rightarrow m_i : 80 \rightarrow 53$ amu and $m_f \rightarrow m_i : 78 \rightarrow 51$ amu, respectively. This conclusion is shown in [18]. The conclusion for **(1)** can be further reinforced by looking at the ratio of total counts in **(1)** and **(2)**. By considering the natural abundances of isotopes of carbon and nitrogen, one can determine about 5.92% of pyridine molecules should be one amu heavier. Direct measurement of the counts in **(1)** and **(2)** at $V_3 = 776$ yields the ratio **(1)** / [**(2)** + **(1)**] = 0.060. We therefore conclude that **(1)** comes from the heavy molecular ion.

We assume that **(3)** comes from a molecular parent-minus-hydrogen ion, although we cannot use yield ratios to confirm this. This assumption is mostly speculative, but we assume that the dynamics of the parent are similar to those of the dehydrogenated parent. If this is the case, there would likely be a corresponding metastable excited state in $C_5H_4N^+$, and it would presumably behave similarly to the molecular parent metastable state (i.e. have a similar cutoff potential). Moreover, a metastable state in any other fragment ion would be unlikely to closely follow the parent ion's metastable state, so we conclude that **(3)** comes from the dehydrogenated parent ion.

The extinction data for **(4)**, **(5)**, and **(6)** are also included in Table 1. The m_f/m_i ratios suggest that **(4)** and **(6)** represent a C_3H_n fragment after decaying from the

molecular parent. **(5)** would have to represent the molecular parent decaying to a fragment of $m_f = 28$ under this assumption. While this could correspond to a C_2H_4 fragment, this daughter ion is unlikely as no carbon atom binds to multiple hydrogen atoms in the precursor. Furthermore, if the same process occurred for **(5)** as for **(4)** and **(6)**, one would expect this peak to lie at a lower TOF than the other two, as it has a substantially smaller final mass and is therefore turned around much more quickly by the same grid potentials in the reflecting portion of the mass spectrometer. However, it is observed between **(4)** and **(6)** (see Fig. 9), which also suggests some entirely different metastable process involved in the creation of this fragment. This ion is perhaps a product of some other ionic fragment, or perhaps it decays from a multiply-ionized parent. The latter is plausible as it appears to resolve into a triplet peak shortly before extinction, similar to the **(1)**, **(2)**, **(3)** triplet. Our experiment is capable of producing multiply-charged ions as was seen in Chapter 6.

8.2.5 – Kinetic energy release values

Extinction curves for all six metastable fragments of pyridine are seen in Fig. 10. In order to make a statement about the KER distribution, recall from Section 8.2.3 the kinetic energy distribution of ions that are created in the laser focus and do not decay. The kinetic energy distribution had a $1/e^2$ width of 10.1 eV. The six metastable peaks' total kinetic energy distributions are determined by a similar process to that described earlier, and the process and results are summarized in Fig. 11 and Table 1. Fig. 11 converts the extinction curves, into a corresponding PDF of a Gaussian shape. The Gaussian profile, as mentioned before, was created using a fitted equation for the CDF, and does not contain actual experimental data. This was done to more accurately measure

the width, as the option of fitting to an error function was not available in Origin 8.0 [23]. Notice the deviation of the data from the fit line on many of the plots in Fig. 10. This data manipulation was done to work around this problem.

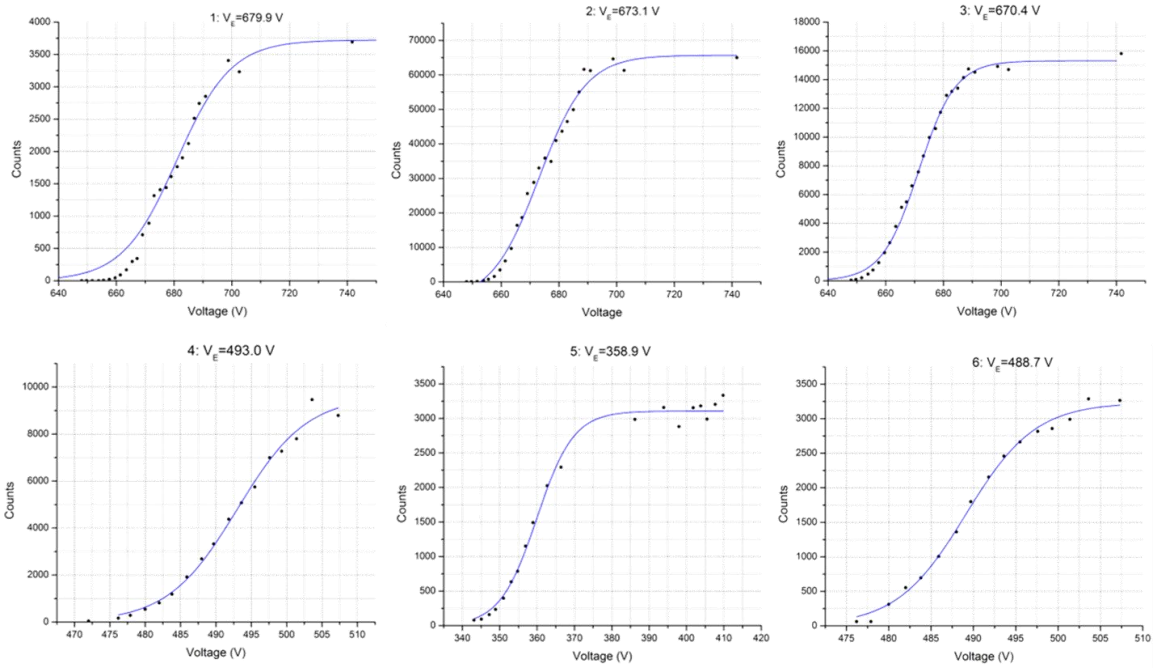

Figure 10 – Extinction curves for all six metastable peaks. These curves were used to calculate the mass ratio and estimate the KER distribution. The KER distribution estimate is done in the following section.

As Table 1 shows, **(1)**, **(2)**, and **(3)** do indeed have somewhat wider kinetic energy peaks than the molecular parent. However, **(4)**, **(5)**, and **(6)** have noticeably smaller widths than the parent ion. This suggests that all three peaks and not just **(5)**, as proposed earlier, decay from some ion besides the singly-ionized parent. This conclusion is reinforced by simulation, details of which can be found in [18].

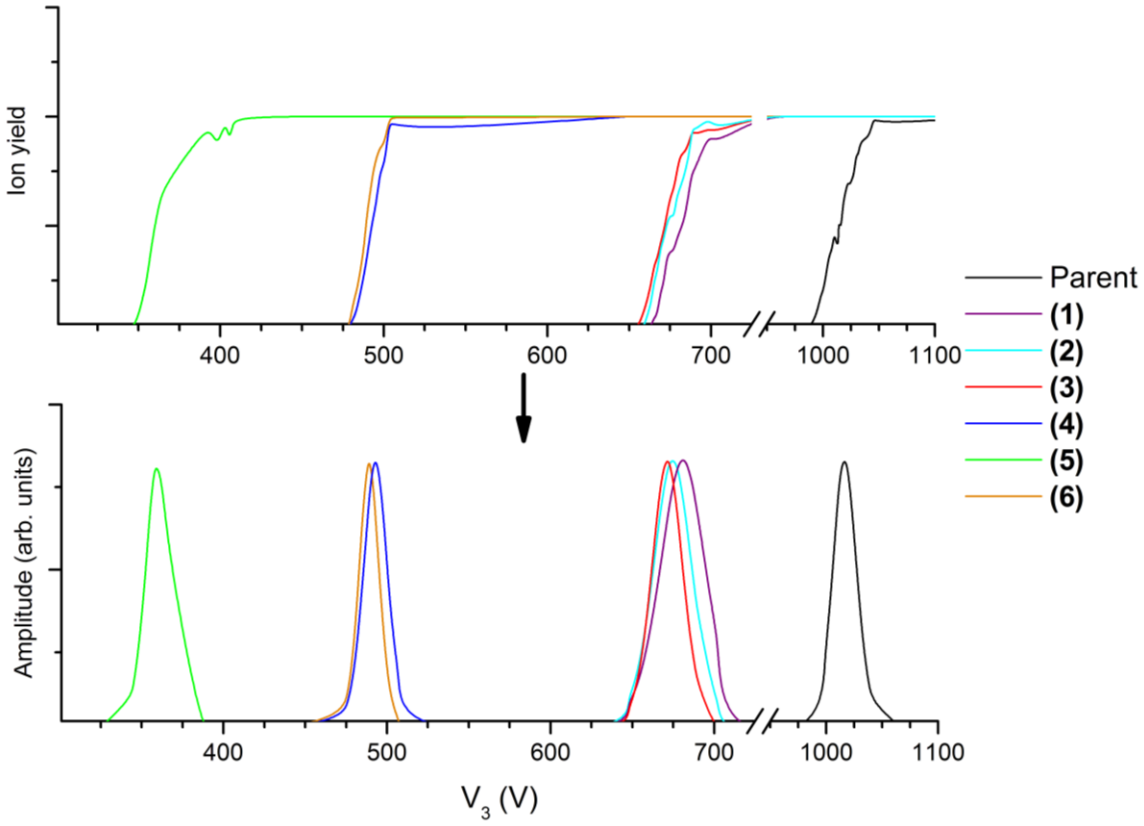

Figure 11 – Extinction curves to energy distributions. Taking the derivative of the experimentally-measured extinction curves (top) produces energy profiles (bottom) for each of the peaks. All of the extinction curves and kinetic energy distributions have been normalized.

8.3 – Conclusions

Metastable ions are known not to be unique to pyridine; as discussed at the beginning of section 8.2, the appearance of metastables in TOF mass spectra seems to be the norm rather than the exception in aromatic systems. As our data on the six observed metastable states have shown, pyridine specifically presents a wealth of informative results on metastable processes, some of which may be uniquely accessible through femtosecond ionization. By deliberately detuning the potentials applied to the reflecting grids of a reflectron TOF mass spectrometer, the specific fragmentation pathways of three metastable states of pyridine can be determined explicitly. One of these metastable

states dominates in pyridine. The amount of information available by studying metastable dissociations in pyridine, coupled with the observed abundance of metastable states in similar molecules, suggests that many benzene-like systems may be good targets for further investigation of metastable states. Of particular interest relevant to this work are the metastable states in the diazines, as they appear to display systematic behavior similar to pyridine. Performing the same experiments on these three molecules would shed light on some of the as yet to be explained results in pyridine, and would contribute to a greater understanding of how similarities in chemical structure of aromatic molecules affect photochemical and photophysical processes.

References

[1] Shannon, T.W. & McLafferty, F.W. 1966, "Identification of Gaseous Organic Ions by use of Metastable Peaks," *Journal of the American Chemical Society*, vol. 88, pp. 5021-5022.

[2] Kaufmann, R., Kirsch, D. & Spengler, B. 1994, "Sequenching of Peptides in a Time-of-Flight Mass Spectrometer: Evaluation of Postsource Decay Following Matrix-Assisted Laser Desorption Ionisation (MALDI)," *International Journal of Mass Spectrometry and Ion Processes*, vol. 131, pp. 355-385.

[3] Boesl, U., Neusser, H.J., Weinkauf, R. & Schlag, E.W. 1982, "Multi-Photon Mass-Spectrometry of Metastables - Direct Observation of Decay in a High-Resolution Time-of-Flight Instrument," *Journal of Physical Chemistry*, vol. 86, pp. 4857-4863.

[4] Kuhlewind, H., Neusser, H.J. & Schlag, E.W. 1983, "Metastable Fragment Ions in Multi-Photon Time-of-Flight Mass-Spectrometry - Decay Channels of the Benzene Cation," *International Journal of Mass Spectrometry and Ion Processes*, vol. 51, pp.255-265.

[5] Kuhlewind, H., Neusser, H.J. & Schlag, E.W. 1985, "Multiphoton Metastable Ion Spectra and Ion Dissociation Kinetics - Analysis of the Decay Channels of the Aniline Cation with a Reflectron Time-of-Flight Instrument," *Journal of Chemical Physics*, vol. 82, pp. 5452-5456.

[6] Neusser, H.J. 1987, "Multiphoton Mass-Spectrometry and Unimolecular Ion Decay," *International Journal of Mass Spectrometry and Ion Processes*, vol. 79, pp. 141-181.

[7] Della-Negra, S. & Le Beyec, Y. 1985, "New Method for Metastable Ion Studies with a Time of Flight Mass Spectrometer. Future Applications to Structure Determinations," *Analytical Chemistry*, vol. 57, pp. 2035-2040.

[8] Ioanoviciu, D., Yefchak, G.E. & Enke, C.G. 1991, "Metastable Peak Shapes Induced by Internal Energy-Release in Electrostatic Mirror Time-of-Flight Mass Spectrometers," *International Journal of Mass Spectrometry and Ion Processes*, vol. 104, pp. 83-94.

[9] Hagan, D.A., Eland, J.H.D. & Lablanquie, P. 1993, "Slow Dissociation Reactions of Singly Charged Ions in Reflectron Mass Spectrometers," *International Journal of Mass Spectrometry and Ion Processes*, vol. 127, pp. 67-74.

[10] Barofsky, D.F., Brinkmalm, G., Håkansson, P. & Sundqvist, B.U.R. 1994, "Quantitative Determination of Kinetic Energy Releases from Metastable Decompositions of Sputtered Organic Ions using a Time-of-Flight Mass Spectrometer with a Single-Stage Ion Mirror," *International Journal of Mass Spectrometry and Ion Processes*, vol. 131, pp. 283-294.

[11] Cornish, T. & Cotter, R. 1994, "A Curved Field Reflectron Time-of-Flight Mass-Spectrometer for the Simultaneous Focusing of Metastable Product Ions," *Rapid Communications in Mass Spectrometry*, vol. 8, pp. 781-785.

[12] Ponciano, C.R., Ávalos, F.E.; Rentería, A. & da Silveira, E.F. 2001, "Analysis of Metastable Decay by Time-of-Flight Coincidence and Kinetics Energy Measurements," *International Journal of Mass Spectrometry*, vol. 209, pp. 197-208.

[13] Ponciano, C.R., Martinez, R. & da Silveira, E.F. 2007, "Fragmentation of $(LiF)_nLi^+$ Clusters in the Acceleration Region of TOF Spectrometers," *Journal of Mass Spectrometry*, vol. 42, pp. 1300-1309.

[14] Cooks, R.G. & Beynon, J.H. 1974, "Metastable Ions and Ion Kinetic-Energy Spectrometry - Development of a New Research Area," *Journal of Chemistry Education*, vol. 51, pp. 437-443.

[15] Cooks, R.G. *Metastable Ions.* Elsevier, 1973.

[16] MATLAB 6.1, The MathWorks Inc., Natick, MA, 2000.

[17] Scarborough T.D., Foote D.B. & Uiterwaal C.J.G.J. 2012, "Ultrafast Resonance-enhanced Multiphoton Ionization in the Azabenzenes: Pyridine, Pyridazine, Pyrimidine, and Pyrazine," *Journal of Chemical Physics*, vol. 136, pp. 054309.

[18] Foote, D.B., *Metastable excited states in ultrafast laser-ionized pyridine and other aromatic molecules*, Undergraduate thesis for graduation with distinction, Department of Physics and Astronomy, University of Nebraska – Lincoln, 2012.

[19] Barker J., *Mass Spectrometry: Second Edition*, Wiley, 1999.

[20] Andersen T., Andersen L.H., Balling P., Haugen H.K., Hvelplund P., Smith W.W. & Taulbjerg K. 1993, "Metastable-ion Lifetime Studies Utilizing a Heavy-ion Storage Ring: Measurements on He^-," *Physical Review A*, vol. 47, pp. 890-896.

[21] Lin, M., Dyakov, Y.A., Tseng, C., Mebel, A.M., Lin, S.H., Lee, Y.T. & Ni, C. 2005, "Photodissociation Dynamics of Pyridine," *Journal of Chemical Physics*, vol. 123, pp. 054309.

[22] Jung, S.H., Yim, M.K. & Choe, J.C. 2011, "Loss of HCN from the Pyrazine Molecular Ion: A Theoretical Study," *Bulletin of the Korean Chemical Society*, vol. 32, pp. 2301-2305.

[23] Origin 8.0, OriginLab, Northampton, MA, 2007.

Chapter 9

Predicting the dynamics of astatine-containing molecules

In our previous studies on the intense-field behaviors of the halobenzenes, atomic substitutions were made using fluorine, chlorine, bromine, and iodine. There is one other halogen which is known to exist: astatine. However, of all the isotopes of astatine, none lasts longer than a few hours before undergoing radioactive decay. The goal of this chapter is to predict the intense-field dynamics of molecules substituted with an astatine, namely astatobenzene, and to discuss the feasibility of an experiment.

But why undertake an experiment with the added complications of radioactivity? Astatine (At) occurs in nature only through radioactive decay chains, as it has no stable isotopes, but can be created in cyclotron colliders [1]. It is the heaviest observed halogen, which makes it suitable as a substituent in molecular systems, as the halogens readily form a single bond with a variety of organic functional groups. In fact, it has been shown to bond to a variety of molecules with pharmacokinetic properties that make them suitable carriers toward specific places in the body. This makes it possible for At to bond to these molecules and be sent off toward a tumor; once there, its decay damages cells in the tumor and treatment has begun. As such, there is significant medical interest in

molecules containing the radioisotope 211-astatine. This nucleus undergoes high-energy alpha (α) decay [2,3]; α particles (bare helium nuclei) are highly interacting and upon decay are typically very energetic (several MeV). This makes them ideal for treating cancers [4-6], since their energy is enough to destroy harmful cells with only a few decays and they can only travel the distance of a few cells before being stopped. This maximizes the damage to the targeted cells while minimizing the interaction with healthy material. A list of molecules which have been synthesized and their relevancies to medicine, taken from Ref. [3], is summarized in Table 1.

Agent	**Medical application**
[^{211}At]astatine-tellurium colloid diphosphate	Compartmental tumors
6-[^{211}At]astato-2-methyl-1,4-naphthoquinol	Adenocarcinomas
^{211}At-labeled methylene blue	Melanoma
Meta-[^{211}At]astatobenzyl guanidine	Neuroendocrine tumors
5-[^{211}At]astato-2-deoxyuridine	Various
^{211}At-labeled biotin conjugates	Various pretargeting
^{211}At-labeled octreotide	Somatostatin receptor
^{211}At-labeled mAbs and fragments	Various
^{211}At-labeled bisphosphonates	Bone metastases

Table 1 – Astatine-containing molecules and their relevance to medicine.

Because of its size (nuclear charge 85, mass ~200), At substitution in molecules makes these molecules susceptible to very fast dynamics, namely *internal conversion* and *intersystem crossing* (ISC) (these processes are detailed in Chapter 3). These processes

can occur on timescales as short as a few femtoseconds; investigation of At-containing molecules on ultrafast timescales may result in new understanding on the stability and dynamics of these molecules. Further, since several of the molecules in Table 1 have an astatine atom attached to a phenyl group, astatobenzene is a good source of comparison given our previous work with the halobenzenes.

9.1 – Comparison to the halobenzenes

Because At is difficult to produce, experiments involving At-containing molecules are scarce. Much of the experimental work relies on inferring the behavior of At-containing molecules [4] by analyzing similar halogen-containing molecules and identifying trends, the exceptions being medical radioisotope experiments which only require trace amounts of At. Otherwise studies remain computational in nature, but this poses a problem: no computational systems presently exist which can carry out fully *ab initio* calculations involving molecular dynamics in intense radiation fields. For the purposes of the present manuscript, we are left with the method of inferring the intense-field behaviors of the desired molecules through series of halogenated systems.

We have previously published work on the intense-field behaviors of the monosubstituted halobenzenes (C_6H_5-X, with X the halogen substituent) [7], which serves well for the present purposes since astatobenzene (C_6H_5-At) is a relatively common At-containing molecule. Further, as mentioned above, several of the relevant At compounds used for targeted radiotherapy contain an At atom attached to a phenyl (C_6H_5) ring [3]. But before we begin making assumptions about astatobenzene, we must determine if it is realistic to expect it to have similarities to the other halobenzenes. To this end, calculations were performed in Gaussian 03 [8] to compare the electronic

structure of the halobenzenes including astatobenzene. Resulting energy levels are seen in Fig. 1.

Unfortunately, comparisons in the present calculations can only be qualitative. For the sake of consistency between calculations, the same computational method and basis set was used for each of the five molecules; however, in Gaussian 03 few basis sets are available with the capability to perform calculations for atoms larger than Krypton. To optimize the amount information that could be extracted about the excited states, a CIS method was chosen in the CEP-121g basis. This combination of basis and method is not ideally suited for these calculations, but in this case consistency was chosen over quantitative accuracy.

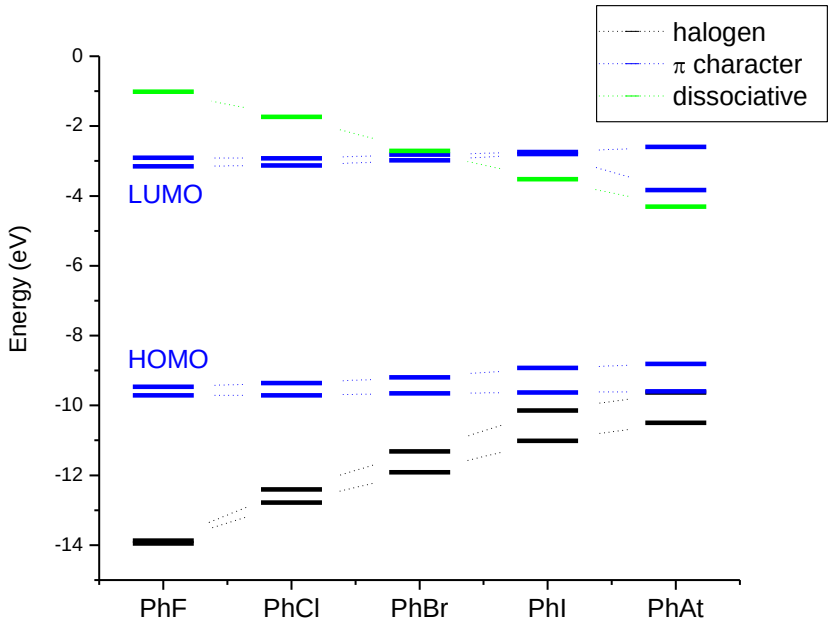

Figure 1 – Calculated energies of the phenyl halides. Energy levels were calculated in Gaussian 03, and intended only to give qualitative information on the relation of astatobenzene to the other halobenzenes. Black levels indicate molecular orbitals of largely atomic nature in the halogen, blue levels indicate orbitals of π character, and green levels indicate a predissociative triplet orbital of ^{3}nσ* character.

9.3 – Intense-field dynamics

9.3.1 – Predicting the dynamics

The resulting energy levels do qualitatively match experimental observations [9] regarding the orbitals near the highest occupied (HOMO) and lowest unoccupied (LUMO) molecular orbitals. The electronic structure of astatobenzene does not appear to differ substantially from the rest of the series other than to continue existing trends (such as the approach of the HOMO-2 and HOMO-3 (seen in black) toward the HOMO, or the lowering in energy of the predissociative triplet ^{3}nσ* state (seen in green). Accordingly, it seems likely that the intense-field dynamics of astatobenzene will continue to follow recognized trends seen in the rest of the series.

The previous work on the halobenzenes [7] done in our group dealt primarily with the ionization of the parent molecules (C_6H_5-X^+) with 50 fs, 800 nm (1.55 eV per photon) laser pulses. Based on the electronic orbital structure, astatobenzene appears to offer little change to the dynamics of the parent ionizations; the singlet π structures remain very similar throughout the series, as they are a particularly robust remnant of the benzene structure. The only new transition which could reasonably be expected in astatobenzene would be the excitation to a π state from the HOMO-2 (classified as a ^{1}nπ* transition). This becomes plausible as the HOMO-2 (largely of *p* character from an atomic At orbital) approaches the energy of the HOMO, meaning that it could become nearly resonant with a three-photon excitation.

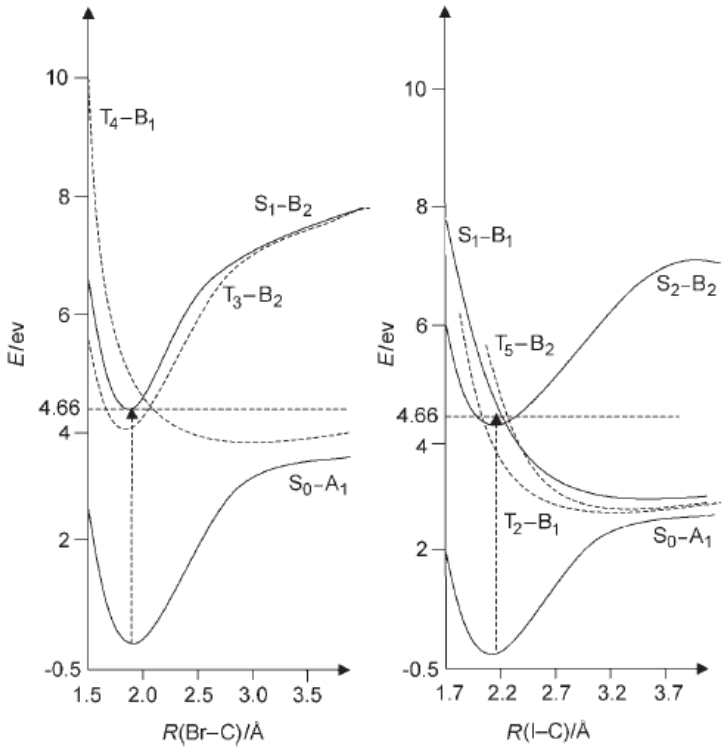

Figure 2 – Intersystem crossing in bromobenzene and iodobenzene. Energies of bromobenzene (left) and iodobenzene (right) calculated along the C-X bond distance (X = Br or I) taken from Ref. [10]. Singlet states are denoted S and represented by solid lines, and triplet states are denoted T with dotted lines. The overlap in energy of the singlet and triplet states at the ground state bond distance plays a large role in determining the strength of intersystem crossing.

Molecular fragmentation is where astatobenzene should offer more interesting dynamics. Specifically, there is a predissociative triplet state that, in bromobenzene and iodobenzene, has substantial overlap in energy with the excited singlet state [10]. Energetic overlap is important in a radiationless transition such as ISC. The so-called *energy-gap law* as described in Ref. [11] states that transition rates for ISC and internal conversion (also a radiationless relaxation like ISC, but without the change in spin states) decrease exponentially as the energy difference between initial and final states increases.

The energetic overlaps between excited singlet and predissociative triplet states in bromobenzene and iodobenzene are seen in Fig. 2.

The relevant predissociative states (T_4 in bromobenzene and T_2 in iodobenzene as labeled in Fig. 2) cross the excited states differently, with the energetic difference at the ground-state bond distance being much smaller for iodobenzene, thus increasing the strength of ISC.

It remains unclear exactly what sort of energetic overlap would be observed in astatobenzene. The Gaussian 03 calculation as described above is not reliable in a quantitative sense, particularly toward the excited states. However, given the observations in the rest of the halobenzenes, it remains likely that the excited ($^1\pi\pi^*$) state and predissociative ($^3n\sigma^*$) triplet state should have substantial overlap. The

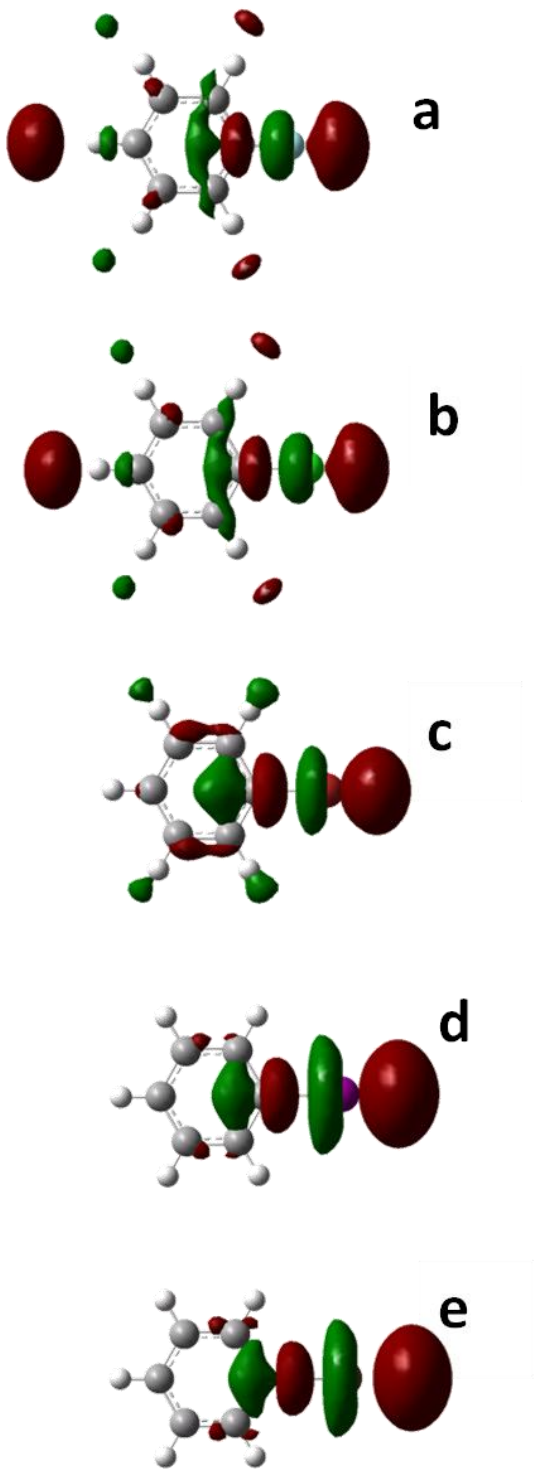

Figure 3 – Triplet states. Dissociative *n*σ* states in the halobenzenes with substituents F (a), Cl (b), Br (c), I (d), and At (e). Note that for increasing halogen size, electron density shifts toward the C-X bond, and the nodes in this bond grow larger. Larger nodes in the electron density increase the likelihood of dissociation into the phenyl ring and a neutral halogen (PhX → Ph + X).

spatial distributions of the triplet states are seen in Fig. 3.

So assuming there is substantial energetic overlap to support ISC, what sort of intense-field behaviors could be expected? Based on the results of Section 7.1, it is clear that ISCs do indeed play a role as progressively larger halogens are involved. As it applies to the halobenzenes previously studied, the ionization potentials and ISC lifetimes both decreased considerably as heavier halogens were introduced. Ionization potentials and ISC lifetimes of the halobenzenes are summarized in Table 2.

	Atomic IP (eV)	**Ph-X IP (eV)**	**Ph-X ISC Lifetime**	Z_X^4/Z_F^4
Fluorine	17.42	9.20	~ 5 ns [12]	1
Chlorine	12.97	9.07	~500 ps [12]	12.7
Bromine	11.81	9.00	~25 ps [10,12,13]	228.7
Iodine	10.45	8.72	20-100 fs [10]	1202.6
Astatine	9.2 ± 0.4	?	?	7956.2

Table 2 – Ionization potentials and spin-orbit properties of the halogens and halobenzenes. All ionization potentials are taken from the NIST Chemistry WebBook [14].

If the observed trends continue, astatobenzene would be even more likely to fragment very quickly. In the iodobenzene mass spectra there was a greater yield of atomic iodine than the parent iodobenzene for intensities greater than 1×10^{14} W/cm^2. In all likelihood, atomic At would be the leading ionic process observed throughout the majority of the intensity range.

9.2.2 – A possible sub-femtosecond process?

Having established that ISC in astatobenzene would most likely lead to increased dissociation compared to the other halobenzenes along the path Ph–At → Ph + At (“Ph”

denotes a phenyl ring, C_6H_5), it is worth investigating the timescale of such an interaction. As summarized in Table 2, the unperturbed ISC timescales of the halobenzenes decrease by at least an order of magnitude between each species. Applying this trend toward astatobenzene would suggest that its transition lifetime could potentially be sub-femtosecond. This would be significant, as current experimental capabilities to produce sub-100 as laser pulses are, to some extent, still thought of as a solution in search of a problem [15].

To get a quantitative estimate of the timescale for ISC in astatobenzene, the spin-orbit coupling (SOC) matrix elements can be applied to Fermi's golden rule for radiationless transitions:

$$k_{i\to f} = \frac{2\pi}{\hbar}\left|\left\langle \Psi_f \left| H_{SOC} \right| \Psi_i \right\rangle\right|^2 \rho_E \qquad \textbf{(9.1)}$$

where $k_{i\to f}$ is the rate constant of a transition from the initial to final state and ρ_E the density of final states at the energy of the initial state. Direct calculations of this type are very complicated. It is difficult to say anything quantitative about the density of final states other than to compare energetic overlap between species. As was mentioned in Chapter 4, the Z^4 dependence of the SOC matrix element was derived from the hydrogen-like atomic case, and likely has little bearing on the dependence of this matrix element for a large molecular system.

As is often the case for complex systems, when calculations become difficult and full of assumptions, one must turn to experimental results as a more reliable indicator. Seen in Fig. 4 is a log-scale plot of the experimentally-measured ISC lifetimes for the halobenzenes.

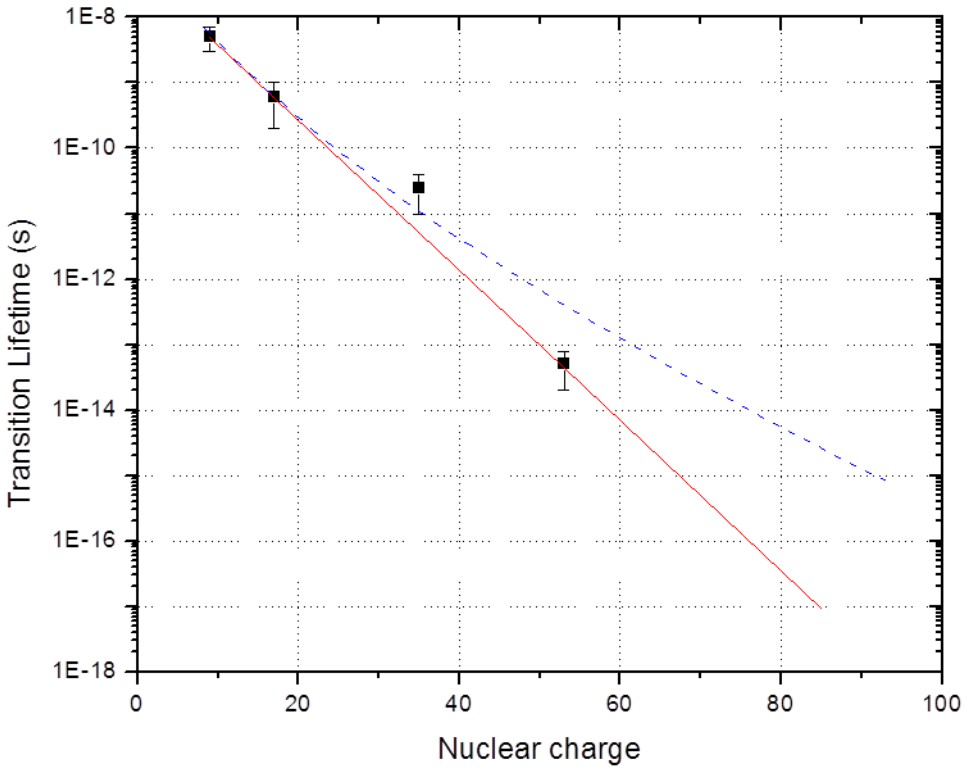

Figure 4 – Predicting the intersystem crossing lifetime of astatobenzene. Plotted are the experimentally measured intersystem crossing lifetimes of the halobenzenes against the nuclear charge of the substituent halogen. The red curve represents a mathematical fit to exponential decay, and the blue curve is a hand-drawn estimate of an approximate upper limit. Projecting the trend to nuclear charge 85, the intersystem crossing lifetime to astatobenzene is unlikely to be larger than a few femtoseconds.

The data points and their error bars represent the range of experimental measurements for the ISC lifetimes [10,12,13,16,17]. The red curve represents a mathematical fit to exponential decay, and the blue curve represents a hand-drawn estimate of what may represent a somewhat more realistic trend toward high-*Z* substituents. This was included because of the importance of energetic overlap between the singlet and triplet states; each species in this series decreases the energy gap, culminating with iodobenzene, which has virtually no energy gap as was seen in Fig. 2. While this contributed to the shorter lifetimes throughout the halobenzenes, it is unlikely that the energy gap in astatobenzene

would be smaller than in iodobenzene, though they may be similar. As such the blue curve indicates a high-end estimate of the ISC lifetime in astatobenzene. This analysis suggests that the ISC lifetime in astatobenzene would be at most a few femtoseconds (the blue curve crosses $Z = 85$ at approximately 3 fs).

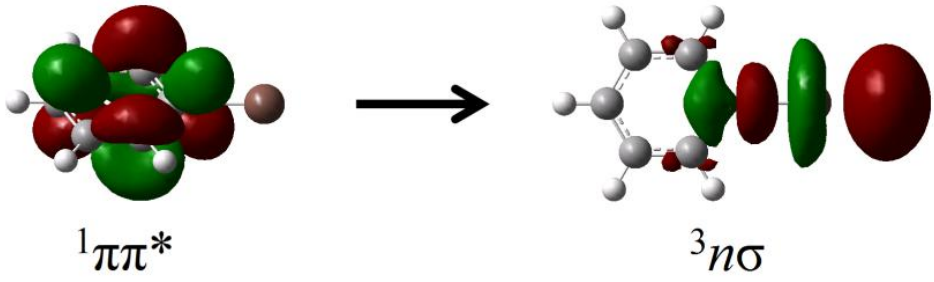

Figure 5 – Intersystem crossing in astatobenzene. Shown are the orbitals relevant to an intersystem crossing from a singlet $^1\pi\pi^*$ orbital to a triplet $^3n\sigma^*$ in astatobenzene. The spatial redistribution of the electronic distribution could make this transition a good candidate for research in sub-femtosecond scale dynamics.

While this process may or may not be strictly sub-femtosecond, accurate measurement would likely require sub-femtosecond probing, so ISC in astatobenzene could be an interesting candidate for ultrafast molecular dynamics research. This transition, once excited, requires no external influence to undergo ISC through a $^1\pi\pi^* \rightarrow {}^3n\sigma^*$ transition and molecular dissociation. Further, this transition (orbitals can be seen in Fig. 5) involves considerable spatial redistribution of the electron density, so it should be observable through electron diffraction experiments. This would be a very difficult experiment, requiring both attosecond-scale optical and electron pulses as the pump and probe, respectively, but methods for both have been proposed [15,18] if not experimentally realized.

9.3 – Plausibility of an experiment

For any of these predictions to be verified, they must be tested in an experiment. For our group to attempt an experiment with an At-containing molecule (most likely astatobenzene due to our previous experience with the halobenzenes) a number of experimental concerns must first be addressed. In particular, none of our past experiments have involved radioactive isotopes, and this causes several issues falling into three subgroups: safety of the people, interactions of radiation with the equipment, and availability of the necessary resources.

As in all experimental work, the safety of the people involved is paramount when dealing with potentially harmful radiation, and we must begin our choice of experimental conditions with safety in mind. Although ^{211}At has become the most commonly used At isotope in medical studies [3], in our experiment we are free to choose whichever isotope suits our needs best. The only five At isotopes (out of 37 known) with a half-life greater than one hour all have nuclear spin ranging from 9/2 to 6. While the choice of isotope would indeed have an effect on the strength of SOC, these concerns are outweighed by the very different safety considerations between isotopes.

Four of the five long-lived isotopes (with masses 207-210) decay almost entirely through positron emission (β^+ decay). This causes a considerable safety concern, as the positron quickly annihilates with a nearby electron to create two gamma (γ) particles (high-energy photons). γ radiation has a large penetration depth, which allows it to penetrate into the body before interacting, and shielding is difficult, requiring several inches of lead for thorough protection.

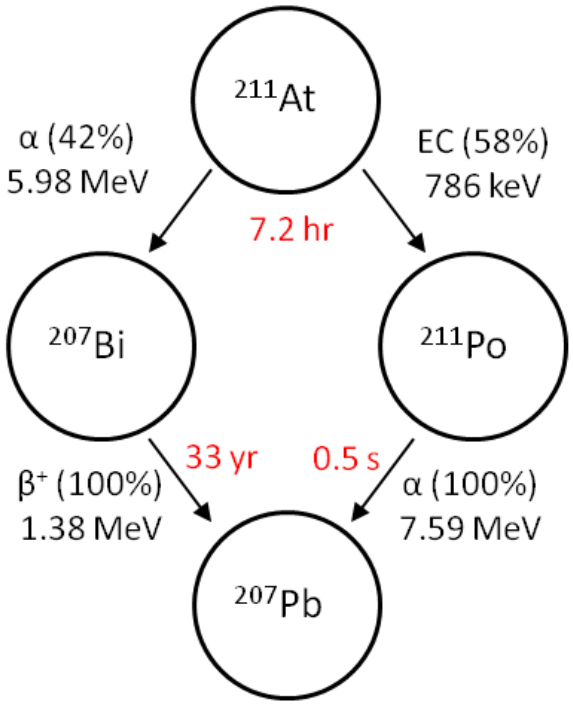

Figure 6 – The decay chain of 211-astatine. Astatine has two decay processes: it undergoes either alpha decay (α) or electron capture (EC) followed by alpha decay, but through either process ends in the stable 207-lead isotope.

Alpha radiation (a helium nucleus, denoted α), on the other hand, is quite easily shielded, and can be stopped by a mere piece of paper[†]. As it happens, in the decay chain of the heaviest long-lived isotope (mass 211) α decay is the primary process. This decay chain is seen in Fig. 6. In this chain the only β^+ decay has a half-life of 33 years, so it is not much concern to safety. The only troublesome step in the decay chain is the electron capture changing ^{211}At into ^{211}Po, as this decay leaves the electrons in a highly excited

[†] Alpha radiation is typically harmless; however, if ingested it can be extremely lethal. The reason for the medical community's interest in alpha-decaying isotopes is the targeted destruction of harmful cells; without the targeting the radiation destroys cells indiscriminately. In a famous case, Russian former KGB agent Alexander Litvinenko was poisoned with a dose of approximately 10 μg (lethal dose for ingestion is listed as 50 ng) of ^{210}Po, an alpha emitter with a lifetime of 138 days and similar decay energy to ^{211}At and ^{211}Po. Litvinenko died three weeks after ingestion. Due to the much shorter lifetimes of ^{211}At and ^{211}Po, the body's reaction would likely be much more violent in comparable doses. However, because ingestion is easily avoided, because inhalation can be prevented with a facemask, and because the Russian secret service has relatively little presence in our laboratory, alpha radiation remains a low risk.

state, which then decays by emitting x-rays and/or Auger electrons. Additional shielding around the sample and possibly around the ion chamber (made of 1-inch thick stainless steel) would likely be necessary for protection from the x-rays.

^{211}At is a good choice of isotope for our experiment; its decay chain is the least dangerous of the long-lived isotopes and it has the second longest lifetime of the group at 7.2 hours. Further, because of the medical community's interest in this isotope, more work has gone into improving methods of production of ^{211}At than other isotopes [1,4], so its availability may be less of a problem.

In considering an experiment with radiation, one must also examine potential danger to equipment. Our present experimental setup sends ions toward a double multichannel plate (MCP) such that singly-charged ions have 1 kV of kinetic energy. To date, the highest charge state witnessed in our system was the eighth ionic state of atomic iodine, meaning the detector was bombarded by an 8 kV ion. The α radiation in the proposed experiment would be 5.98 or 7.59 MeV coming from ^{211}At and ^{211}Po, respectively, so they present a risk on two levels to a MCP: physical damage to the plates and excessive current flow in electron multiplication.

Due to its small penetration depth in metals (~10 μm) and small collision cross section (on a detector-sized scale), it is unlikely for α radiation to cause significant structural damage [19]. It is, however, certainly within the realm of possibility for such energetic particles. It remains unfortunate that it is not only possible but necessary for α particles to strike the detector, since the parent molecule must reach the detector before decay, and will likely be deposited on or near the detector until decay.

The ultimate purpose of a MCP is to detect single ions by turning a single energetic particle into an observable electrical signal. This is accomplished by taking the release of a few electrons by the initial particle striking the MCP and multiplying the electron signal in multiple stages until a measurable current is produced. For such high energy α decays the first stage is likely to have a significant electrical signal even before multiplication; this could overload the electrical capabilities of the detector. Potential damage in this case could be calibrated ahead of time with an α source by starting the MCP gain voltage low and increasing until ions become detectable. If the radiation causes damage at a lower gain voltage than is capable of measuring molecular ions, other types of detectors could be explored or modifications could be made to the circuitry of a MCP for further attempts.

Another possibly problematic interaction is the collision of α radiation with a pressure gauge. Our system uses an ion gauge filament to read the pressure; similar to the case of the MCP, physical damage to the thin filament is unlikely, but α collisions could send a large burst of current through the filament. This current could distort the pressure readout which is used to normalize the data; the pressure readouts would need to be analyzed to filter out anomalous spikes in the measurements.

Considerations would also have to be made regarding the pumping of radioactive species under vacuum. Our system presently uses turbomolecular vacuum pumps backed with rotary vane pumps. While At should not pose any serious problems to the pumping process, one must ask where it is going as it is pumped out of the chamber. The tubes connecting the pumps to the output would need additional shielding to keep the laboratory safe, but the output itself would likely need to be altered to meet state and

federal regulations for disposal of radioactive materials. Again, this is likely manageable as the amount of gas pumped out is negligible at atmospheric pressure (100 L/s at 10^{-7} mbar is ≈10 nL/s at atmosphere).

Ultimately, these experimental issues will likely prove irrelevant, as the resources to create and control ^{211}At in amounts large enough for the experiment are far too scarce [4]. Current methods of production are limited to high-energy reactions in cyclotrons, and can only reach a maximum amount on the order of a μg. To maintain experimental conditions which are optimized for maximum count rate without creating distortion in the MCP, we operate at pressures ~10^{-7} mbar. Approximately 400 ng of ^{211}At would be needed to create enough astatobenzene to fill our chamber with this partial pressure. The problem is that our ~500 L chamber is kept at low pressures by turbomolecular vacuum pumps which operate at pumping speeds greater than 100 L/s, so the supply to the chamber must be refreshed every few seconds. At this rate the largest attainable supply of ^{211}At is exhausted in just a few minutes.

One could suppose that this problem will be solved as new methods increase the amount of ^{211}At that can be synthesized. This in itself becomes a problem due to the short lifetime of the radioactive decay. A single mg of ^{211}At produces approximately 100 Watts generated in heat due to the rate and high energy of decay. As a result, increasing the experimental availability of targets by using a larger sample becomes problematic, as the sample is contaminated by its own ionizing radiation. Even in a very dilute sample, working with more than a few μg of ^{211}At would be a cause for concern.

Instead of increasing the sample size, a better solution would be to use a gas jet. Doing so would pressurize only a small interaction region instead of filling the entire

chamber; this would reduce the effective volume kept at pressure from ~500 L to less than 1 mm^3, so the pumping rate of the sample is reduced by greater than 10^8.

The primary hurdle then is the decay of the sample prior to and during the experiment. The sample would have to go from production and isolation of ^{211}At in a cyclotron to synthesis of the astatobenzene molecule in solution to the experiment without undergoing substantial loss. Synthesis of the molecule can be done quickly and efficiently [20], but results in samples of ~10^{-10} M solution; production, isolation, and transportation would be more complicated. Such an experimental undertaking may be possible, but in practice may prove very difficult.

9.5 – Conclusions

Due to its behavioral similarity to the rest of the halogen series, At-containing molecules would be expected to follow the trends set by molecules containing the lighter halogens. In the case of ISC due to the heavy atom effect, At substitution can play a very large role in determining the dynamics of excited states. When comparing astatobenzene to the other halogenated benzenes, the series produces increased yields of halogen dissociation in intense laser fields in the order F < Cl < Br < I, with At likely being larger than all of these.

The key result of this analysis is the presence of an extremely fast process in the ISC, likely shorter than a few femtoseconds, and possibly even sub-femtosecond. Radiationless transition dynamics on the timescales of electron motion would be an excellent target for attosecond pulse experiments, and the exploitation of the heavy-atom effect could be used to search for similar targets.

References

[1] Maiti, M. & Lahiri, S. 2009, "Theoretical approach to explore the production routes of astatine radionuclides," *Physical Review C,* vol. 79, no. 2, pp. 024611.

[2] Zalutsky, M. R., Zhao, X. G., Alston, K. L. & Bigner, D. 2001 "High-level production of alpha-particle-emitting (211)At and preparation of (211)At-labeled antibodies for clinical use," *Journal of Nuclear Medicine*, vol. 42, no. 10, pp. 1508-15.

[3] Zalutsky, M. R., "Radionuclide Therapy," Handbook of Nuclear Chemistry, by Vértes, A. *et al*, Springer 2011, pp. 2179-2209.

[4] Vaidyanathan, G. & Zalutsky, M. R. 2008 "Astatine Radiopharmaceuticals: Prospects and Problems," *Current Radiopharmaceuticals,* vol. 1, no. 3, pp. 177-207.

[5] Zalutsky, M. R. *et al* 2008, "Clinical Experience with α-Particle–Emitting 211At: Treatment of Recurrent Brain Tumor Patients with 211At-Labeled Chimeric Antitenascin Monoclonal Antibody 81C6J," *Nuclear Medicine,* vol. 49, pp. 30–38.

[6] Zalutsky, M., Pozzi, O., Zhao, X. & Alston, K. 2003, "Evaluation of astatine-211 labeled targeted radiotherapeutics," *Abstracts of Papers of the American Chemical Society,* vol. 225, pp. U264-U264.

[7] Scarborough, T.D., Strohaber, J., Foote, D.B., McAcy, C.J. & Uiterwaal, C.J.G.J. 2011, "Ultrafast REMPI in benzene and the monohalobenzenes without the focal volume effect," *Physical Chemistry Chemical Physics,* vol. 13, no. 30, pp. 13783-13790.

[8] Frisch, M. J. *et al*, Gaussian 03, Gaussian Inc., Wallingford CT, 2004.

[9] Porter, G. & Ward, B. 1965, "Electronic Spectra of Phenyl Radicals," *Proceedings of the Royal Society of London Series A-Mathematical and Physical Sciences,* vol. 287, no. 1411, pp. 457-470.

[10] Zhang, X., Wei, Z., Tang, Y., Chao, T., Zhang, B. & Lin, K. 2008, "Halogen effect on the photodissociation mechanism for gas-phase bromobenzene and iodobenzene," *Chemphyschem,* vol. 9, no. 8, pp. 1130-1136.

[11] Klán, P. & Mirz, J., *Photochemistry of Organic Compounds*, Wiley, 2009.

[12] Matsumoto, J., Lin, C. & Imasaka, T. 1997, "Enhancement of the molecular ion peak from halogenated benzenes and phenols using femtosecond laser pulses in conjunction with supersonic beam multiphoton ionization mass spectrometry," *Analytical Chemistry,* vol. 69, no. 22, pp. 4524-4529.

[13] Rasmusson, M. *et al* 2003, "Photodissociation of bromobenzene in solution," *Chemical Physics Letters,* vol. 367, no. 5-6, pp. 759-766.

[14] *NIST Chemistry WebBook*, National Institute of Standards and Technology, http://webbook.nist.gov/chemistry.

[15] Chang, Z., *Fundamentals of Attosecond Optics*, CRC Press 2011.

[16] Cheng, P., Zhong, D. & Zewail, A. 1995, "Kinetic-Energy, Femtosecond Resolved Reaction Dynamics - Modes of Dissociation (In Iodobenzene) from Time-Velocity Correlations," *Chemical Physics Letters,* vol. 237, no. 5-6, pp. 399-405.

[17] Kadi, M., Davidsson, J., Tarnovsky, A., Rasmusson, M. & Akesson, E. 2001, "Photodissociation of aryl halides in the gas phase studied with femtosecond pump-probe spectroscopy," *Chemical Physics Letters,* vol. 350, no. 1-2, pp. 93-98.

[18] Hilbert, S.A., Uiterwaal, C., Barwick, B., Batelaan, H. & Zewail, A.H. 2009, "Temporal lenses for attosecond and femtosecond electron pulses," *Proceedings of the National Academy of Sciences of the United States of America,* vol. 106, no. 26, pp. 10558-10563.

[19] Shipp, J. D., Hart, R. R., Saglam, M., Unlu, K. & Wehring, B. W. 1999, "The effects of Alpha Particle Irradiation on Stainless Steel," *Amarillo National Resource Center for Plutonium*, Report to U.S. Department of Energy.

[20] Berei, K. & Vasáros, L., *Recent Advances in the Organic Chemistry of Astatine*, Wiley, 2009.

Chapter 10

Conclusions and future outlook

10.1 – Conclusions

Throughout the molecular series we have studied, the robust nature of the π system, a remnant of the benzene structure, has proved itself to have thorough consistency. Even when multiple carbon atoms are replaced from the ring (as in the azabenzenes), the energies of the π orbitals are perturbed by no more than a few hundred meV, but remain intact. As a result of the resilience of these structures, we have observed signatures of resonance-enhanced multiphoton ionization (REMPI) throughout 12 of the 13 molecules studied. The only outlier is nitrobenzene, whose ionization dynamics remain undetermined due to the extremely low count rates.

The controlling substituent interaction in the halobenzene series is the heavy atom effect, which progressively increases the coupling between singlet and triplet states for increasing halogen mass. This coupling leads to a bond cleavage between the halogen and its neighboring carbon atom, which causes the primary dissociation route to be the removal of the halogen [1]. The CNOF series showed less consistent behavior as the substituent moves across the periodic table; the effects of these side groups act more like distinctly different perturbations than a progressive series. Combining the hydroxyl and methyl substitutions to form anisole provided results more similar to toluene than aniline, as it appears that the outer methyl group effectively shields the molecule from the withdrawing effects of the oxygen atom. When comparing aniline to nitrobenzene, the

effects of donating and withdrawing side groups could clearly be seen in the fragmentation, as nitrobenzene nearly failed to exist as an ionized parent molecule. Finally, the azabenzenes revealed ionization from the lone pair orbitals of the substituent nitrogen atoms, while the fragmentation within the series differed wildly as a result of the fundamentally different symmetries within the series.

10.2 – Future outlook

10.2.1 – Biomolecules

A large part of our motivation for studying the variety of perturbations to the benzene structure is that we hope to build upon what we have studied and use it to understand the more complicated dynamics of chemically and biologically relevant systems. Having studied pyrimidine as well as external substitutions involving oxygen atoms, amine and methyl groups, we have built a level of experience that will be applicable to the DNA and RNA nucleotides, which are pictured in Fig. 1.

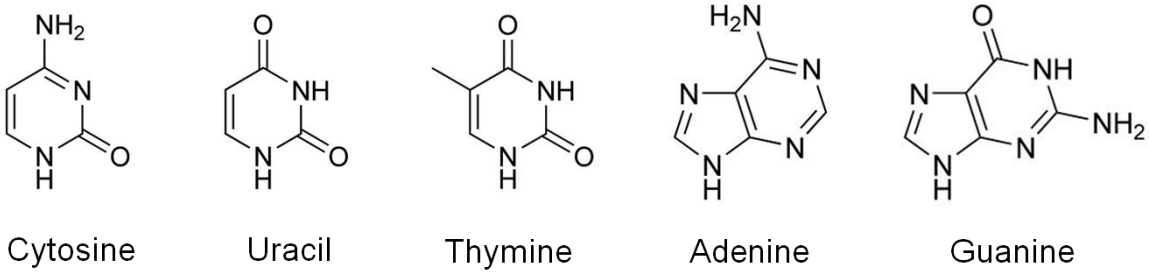

Figure 1 – DNA and RNA nucleotides. The pyrimidine molecule, which we have studied, consists of a six-member carbon ring in which two carbons are replaced by nitrogen atoms. This is also the base structure of the DNA and RNA nucleotides: cytosine, uracil, thymine, adenine, and guanine.

As the building blocks of DNA and RNA, cytosine, uracil, thymine, adenine, and guanine form a series of aromatic molecules whose relevance to biology cannot be overstated. Preliminary measurements have been undertaken for cytosine, and while the ionization

dynamics have yet to be determined precisely, the fragmentation appears to be heavily influenced by the pyrimidine system.

It is often stated [2-4] that the ultimate goal of intense-field molecular dynamics research is the ability to influence molecular reactions to the point where the dynamics are controlled by the experimenter. Surely then, control over interactions involving the DNA/RNA nucleotides would offer fascinating and important implications.

10.2.2 – Tunable laser source

The experiments presented within this dissertation were all bound by one common experimental condition: the laser outputs radiation centered at 800 nm. This means that some molecular transitions are not available to our experiment unless a dynamic resonance (discussed in Chapter 2) is forced. However, our group has recently added a wavelength-tunable optical parametric amplifier system (Spectra-Physics TOPAS). This system takes the output of our primary (Spitfire) beam and engages in frequency mixing which produces femtosecond light pulses which are tunable from 475-1600 nm. This is enough range to venture from tunneling to multiphoton ionization to (3 + 3) REMPI to (2 + 2) REMPI.

The transition between orders of multiphoton absorption from the ground state could have very interesting implications. The nature of dynamic resonances is not well understood in a quantitative sense; the highest bound states are thought to undergo AC Stark shifts comparable to the continuum [5], which sees a shift equal to the ponderomotive energy as described in Chapter 2. By progressively tuning the intense laser pulses onto (and then away from) resonant transitions, we could measure the true capabilities of excited state dynamics in aromatic molecules.

Consider, for example, the case in which both the ground and excited states couple weakly to the external field in comparison to the ponderomotive energy. The resonance will be stationary and the ionic yield for a given intensity will be suppressed throughout the majority of laser frequencies. In this case we would observe a sharp increase in the yield when a resonance was met. This case is diagrammed in Fig. 2.

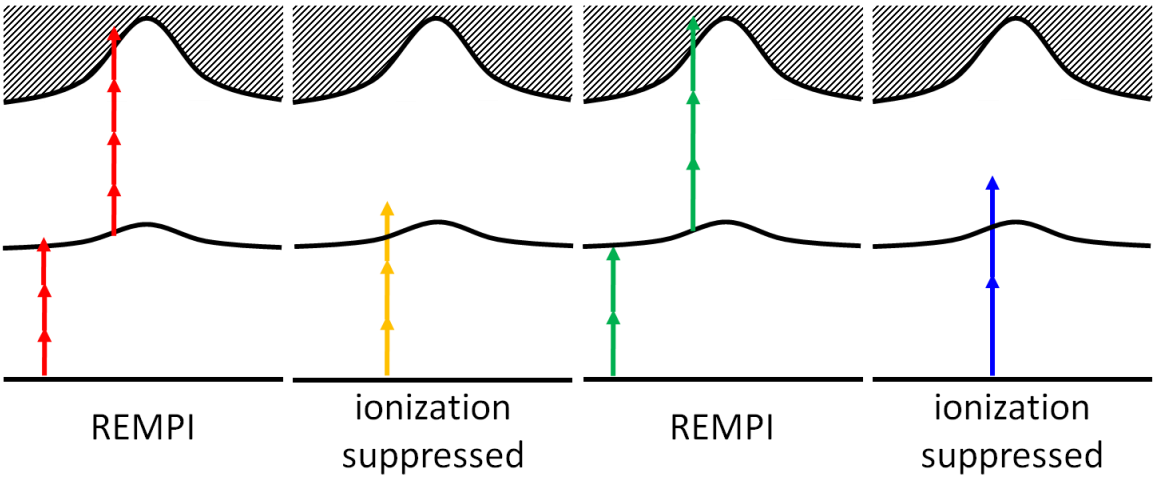

Figure 2 – Rigid dynamic resonance in a tunable laser source. If the nature of a dynamic resonance was rigid compared to the energy shift of the continuum, there would be resonance enhancement of the ionization yield for laser wavelengths which were strongly resonant with the rigid transition energy.

Alternately, if both the excited state and the continuum experience greater energetic shifts, the resonance condition could become very flexible. Because the ponderomotive energy can be large on a molecular scale (6 eV at 10^{14} W/cm^2 at 800 nm), if the excited state undergoes the same shift, there will be some point in the laser pulse where virtually any color of light will find itself resonant with an integer number of photons. Fig. 3 shows a qualitative example where, for considerably different photon energies, a resonance can be found in each case. As the laser pulses are tuned across a variety of wavelengths, the ionic yield in this case would see gradual changes with changing laser wavelength instead of sharp resonance enhancements.

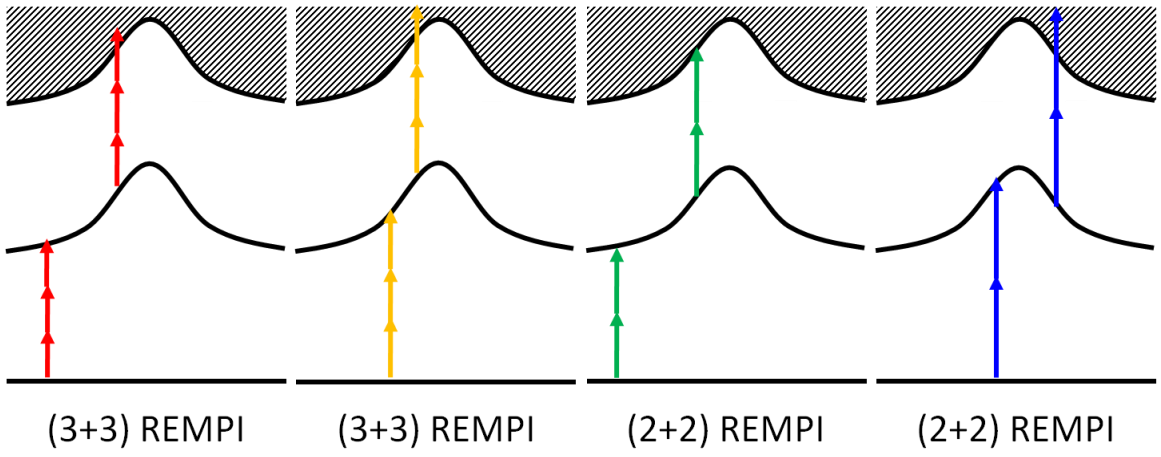

Figure 3 – Flexible dynamic resonance in a tunable laser source. If a dynamic resonance was flexible such that its energetic shift was comparable to the energy shift of the continuum, there would be resonance enhancement of the ionization yield for a broad range of laser wavelengths.

The ability to measure the true dynamics of excited states in aromatic molecules would have broad-reaching impact in our ability to influence molecular dynamics. This would be a fundamentally important step toward understanding how the control of molecular dynamics can be enforced.

Additionally, the tunable source will enable us to conduct two-color pump-probe experiments. By separating the beam prior to the TOPAS, we can create two separate beamlines of femtosecond pulses with different wavelengths. The ability to induce excitation and ionization with different wavelengths would allow finer precision in determining the dynamics and exploring molecular processes on the ultrafast scale.

References

[1] Kadi, M., Davidsson, J., Tarnovsky, A., Rasmusson, M. & Akesson, E. 2001, "Photodissociation of aryl halides in the gas phase studied with femtosecond pump-probe spectroscopy," *Chemical Physics Letters*, vol. 350, no. 1-2, pp. 93-98.

[2] Rabitz, H. 2006, "Strong-arming molecular dynamics," *Science*, vol. 314, no. 5797, pp. 264-265.

[3] Hertel, I.V. & Claus-Peter Schulz, *Atome, Moleküle und optische Physik 1: Atomphysik und Grundlagen der Spektroskopie*, Springer, 2008.

[4] Sansone, G., Kelkensberg, F., Morales, F., Pérez-Torres, J.F., Martín, F. & Vrakking, M.J.J. 2012, "Attosecond Time-Resolved Electron Dynamics in the Hydrogen Molecule," *IEEE Journal of Selected Topics in Quantum Electronics*, vol. 18, no. 1, pp. 520-530.

[5] de Boer, M. & Muller, H. 1992, "Observation of large populations in excited states after short-pulse multiphoton ionization", *Physical Review Letters*, vol. 68, no. 18, pp. 2747-2750.

Appendix A – Programs and simulations

A.1 – REMPI rate model

```
%This program calculates the rate models presented in Chapter 3. It can
%be generalized to include various transitions and cross sections.*****

clear, clc;

%Initializing parameters*********************************************
%Generalized cross sections
s3 = 1e4;               %Ground to 3-photon excited state
s3ion = 0*1e4;          %3-photon ionization
s4 = 0*5e3;             %Ground to 4-photon excited state
s4ion = 5e3;            %4-photon ionization
s1 = 0.0;               %3-photon excited state to 4-photon excited
state
s7 = 1e7;               %Nonresonant seven-photon ionization

%Initializing matrices***********************************************
length=200;
n1 = zeros(length,2);  n1(:,1)=1; %Ground state of REMPI process
n2 = zeros(length,2;              %Three-photon excitation
n3 = zeros(length,2);             %Four-photon ionization from excited
n4 = zeros(length,2);             %REMPI ionized parent
ng = zeros(length,2);  ng(:,1)=1; %Ground state of nonresonant process
ni = zeros(length,2);             %Nonresonant ionized parent

for i=1:length;
    LogIPeak(i) = -3.5+0.0125*i;  %logarithm of the peak intensity
        for j=1:2401;
            Pulse = exp(-(4*log(2)/(50^2))*(-60.05+0.05*j)^2);
%Shape of laser pulse: 50 fs fwhm where -60.05+0.05*j is the time
%within the pulse
            tpp = ((10)^(LogIPeak(i))^3)*Pulse^3;    %3 - photon
                                                     %process
            fpp = ((10)^(LogIPeak(i))^4)*Pulse^4;    %4 - photon
                                                     %process
            opp = ((10)^LogIPeak(i))*Pulse^1;        %one-photon
                                                     %process

            spp = ((10)^(LogIPeak(i))^4)*Pulse^7;    %one-photon
                                                     %process

%Equations dictating the transitions of the rate model***************
            n1(i,2)=n1(i,1) - s3*tpp*n1(i,1) + s3*tpp*n2(i,1) -
s4*fpp*n1(i,1) + s4*fpp*n3(i,1);
            n2(i,2)=n2(i,1) + s3*tpp*n1(i,1) - s3*tpp*n2(i,1) -
s1*opp*n2(i,1) + s1*opp*n3(i,1) - s4ion*fpp*n2(i,1);
            n3(i,2)=n3(i,1) + s4*fpp*n1(i,1) - s4*fpp*n3(i,1) +
s1*opp*n2(i,1) - s1*opp*n3(i,1) - s3ion*tpp*n3(i,1);
            n4(i,2)=n4(i,1) + s3ion*tpp*n3(i,1) + s4ion*fpp*n2(i,1);
            ng(i,2)=ng(i,1) - s7*spp*ng(i,1);
            ni(i,2)=ni(i,1) + s7*spp*ng(i,1);
```

```
n1(i,1)=n1(i,2);n2(i,1)=n2(i,2);n3(i,1)=n3(i,2);n4(i,1)=n4(i,2);ng(i,1)
=ng(i,2);ni(i,1)=ni(i,2);                %reinitializing parameters
            if  (n1(i,1)>1); n1(i,1)=1; %renormalizing parameters
                (n2(i,1)>1); n2(i,1)=1;
                (n3(i,1)>1); n3(i,1)=1;
                (n4(i,1)>1); n4(i,1)=1;
                (ng(i,1)>1); ng(i,1)=1;
                (ni(i,1)>1); ni(i,1)=1;
            end
        end
end

%Taking the logarithm of the parent ion yield************************
for i=1:length;
    LogParentYield(i)=log10(n4(i,1)); %REMPI
    LogNonResonant(i)=log10(ni(i,1)); %Nonresonant MPI
end

%Calculating the log-log slopes**************************************
for i=1:length-1;
    slope(i)=(LogParentYield(i+1)-LogParentYield(i))/(Intensity(i+1)-
Intensity(i));
    slopeNR(i)=(LogNonResonant(i+1)-LogNonResonant(i))/(Intensity(i+1)-
Intensity(i));
    Intensity2(i)=Intensity(i+1);
end

figure, plot(Intensity,LogParentYield,Intensity,LogNonResonant)
        xlabel('log(Peak Intensity) (arb. units)');
        ylabel('log(Counts) (arb. units)');
        title('Ionization rate');
figure, plot(Intensity2,slope,Intensity2,slopeNR)
        xlabel('log(Peak Intensity) (arb. units)');
        ylabel('Slope (# of photons)');
        title('Log-log Slope Value');
figure,
plot(Intensity,n1,Intensity,n2,Intensity,n4,Intensity,ng,Intensity,ni)
        xlabel('log(Peak Intensity) (arb. units)');
        ylabel('Population');
        title('Population of states');

%********************************************************************
```

A.2 – Time of flight program

```
%TOF Mass Specrometer Breakup Calculator*****************************
%This program calculates the time of flight for molecules which break
%up in the drift region within the TOF chamber, with a distribution
%chosen by the user.

clear, clc

% Declare initial values*********************************************
x0=0.001993;          %Distance from repeller voltage to slit
dr=0.003;             %Distance from slit to mesh 1
d1=1.000;             %Drift region length
d2=0.1464;            %First deceleration region length
d3=0.0616;            %Second deceleration, turnaround region length
dMCP=0.346;           %Drift region to MCP
Vr=1530;              %Repeller voltage
V1=0;                 %Voltage in mesh 1
V2=389;               %Voltage in mesh 2
V3=504;               %Voltage in mesh 3
y=0.015;              %Radius of the MCP plate (meters)

%User-specified parameters******************************************
Mi=79;                          %Initial mass of ion (in amu)
Mf=52;                          %Altered mass after explosion (in amu)
CenterTe=0.1;                   %Energy released in explosion (in eV)
StDev=1;                        %Standard deviation, in CenterTe's, of
                                %energy release (i.e. 0.5 means standard
                                %deviation is 0.5*CenterTe)

lft=5E-7;                       %lifetime (1/e) of the dissociation, (s)

centerTe=1.602*10^-19*(CenterTe);  %Energy released in explosion (J)

mi=1.6605*10^-27*(Mi);             %Intial mass of ion (in kg)
mf=1.6605*10^-27*(Mf);             %Final mass after explosion (kg)
q=1.602*10^-19*(1);                %Initial charge of ion (Coulombs)

size=100000;                       %number of data points to take

%Compute spatial rate parameter (1/spatial "lifetime") of the
dissociation*******************************************************
slft=lft*sqrt((2*Vr*x0*q)/(mi*dr)); %computes the spatial lifetime,
                                    %i.e. the 1/e distance the particle
                                    %travels past the slit, from
                                    %velocity in the drift region

lambda=1/slft;                      %The spatial rate parameter, if it
                                    %is negative, the molecule does not
                                    %break up in the drift region

%This section calculates the TOF for the ith data point, using a
%distribution of breakup distances and orientation of velocity after
explosion***********************************************************

TOFs = zeros(size,1);      %initializes the array of TOF's; values
```

```
                            %will be added in the for loop
TOFes = zeros(size,1);      %array of post-explosion TOF's
des = zeros(size,1);        %array of breakup distances
thetas = zeros(size,1);     %array of explosion angles
Tes = zeros(size,1);        %array of kinetic energies
thetamaxs = zeros(size,1); %array of thetamaxs

for (i=1:size)
    de=-1*slft*log(1-rand(1));                %specifies the position
                                              %where the molecule
                                              %breaks apart in the TOF
                                              %drift region
    theta=acos(1-2*rand(1));                  %Angle of exploding ions
    Te=abs(centerTe+StDev*centerTe*randn(1)); %random KER
    va=0;                                %The initial velocity
    TOFa = sqrt((2*mi*dr*x0)/(q*Vr)); %TOF in acceleration region

    v1a = sqrt((2*Vr*x0*q)/(mi*dr));  %Velocity of particle at the slit
    TOF1a = de/v1a;                   %TOF in drift region prior to
                                      %breakup
    v1b = sqrt((2*Vr*x0*q)/(mi*dr))+  %Velocity of the particle at the
    sqrt((2*Te)/(mf))*cos(theta);     %first mesh (after the drift
                                      %region)
    TOF1b = (d1-de)/v1b;              %TOF in drift region after
                                      %breakup
    v2=sqrt(v1b^2-(2*q*V2)/(mf));     %Velocity of the particle at the
                                      %second mesh (after the first
                                      %deceleration region)
    TOF2 = ((mf*d2)/(q*V2))*(v1b-v2); %TOF in first deceleration region
    v3 = 0;                           %Velocity at the third
                                      %mesh/stopping point: it turns
                                      %around here so the velocity is
                                      %zero.
    TOF3 = v2*((mf*d3)/(q*(V3-V2)));  %TOF in second deceleration
                                      %region
    v4 = v1b;                         %Velocity at the start of the MCP
                                      %drift region: same as when it
                                      %left the first drift region.
    TOF4 = dMCP/v1b;                  %TOF in MCP drift region
    TOF = TOFa + TOF1a + TOF1b +      %Total time of flight; TOF2 &
                                      %TOF3
    2*TOF2 + 2*TOF3 + TOF4;           %doubled because of turnaround
                                      %time.
    TOFe = TOF1b + 2*TOF2 +           %Total time of flight after
                                      %breakup
    2*TOF3 + TOF4;

    TOFs(i) = TOF;                    %concatenate TOF onto array
    TOFes(i) = TOFe;                  %concatenate TOFe onto array
    des(i) = de;                      %concatenate distance onto array
    thetas(i) = theta;                %concatenate angle onto array
    Tes(i) = Te;                      %concatenate Te onto array
end

TOFs = real(TOFs);                    %takes the real part of each TOF
TOFes = real(TOFes);
```

```
%*********************************************************************
%The next section calculates the maximum explosion angle for the ith
%data point (it depends on TOFe). If the ith value of theta is greater
%than this, it sets the time of flight to zero in that spot. Otherwise,
%the time of flight remains unchanged. It also set the total TOF to
%zero if the breakup happens outside the field-free drift region.

outside=0; %The number of times the angle is outside the acceptance
range.

for (i=1:size)
    if sqrt((2*Tes(i))/mf)*sin(thetas(i))*TOFes(i) > y
        TOFs(i)=0;
        outside=outside + 1;
    else
        TOFs(i)=TOFs(i);
    end
    if des(i) > d1
        TOFs(i)=0;
        outside=outside+1;
    else
        TOFs(i)=TOFs(i);
    end
end
%*********************************************************************

TOFs = 1E6.*TOFs;      %Change the x-axis from seconds to microseconds

%Save the distributions of breakup distances, angles, energy releases,
%and total time of flights to text files*******************************

csvwrite(['D:\TOFBreakup\ExplosionOutput\distances_mi',int2str(Mi),'_mf
_',
 int2str(Mf),'_T_',int2str(CenterTe),'_lft_',int2str(lft),'.dat'],
des);
csvwrite(['D:\TOFBreakup\ExplosionOutput\angles_mi',int2str(Mi),'_mf_',
 int2str(Mf),'_T_',int2str(CenterTe),'_lft_',int2str(lft),'.dat'],
thetas);
csvwrite(['D:\TOFBreakup\ExplosionOutput\energies_mi',int2str(Mi),'_mf_
',
 int2str(Mf),'_T_',int2str(CenterTe),'_lft_',int2str(lft),'.dat'],
Tes);
csvwrite(['D:\TOFBreakup\ExplosionOutput\timeofflights_mi',int2str(Mi),
'_mf_'
 ,int2str(Mf),'_T_',int2str(CenterTe),'_lft_',int2str(lft),'.dat'],
TOFs);

%*********************************************************************
```

A.3 – Ion yield analysis program

```
%This program analyzes the yields of ions from a specified peak in a
%mass spectrum. Ion yields are counted from a selected detection volume
%and normalized to a pressure of 1e-7 mbar and an integration time of
%one minute.***********************************************************

clear, clc;

%Load the data from ASCII files***************************************
load -ascii 'SPECTRUM.DAT';
load -ascii 'POWER.DAT';
load -ascii 'PRESSURE.DAT';

P=POWER;
DATA=SPECTRUM;
Pressure=PRESSURE;
L=length(P)-1;

%Define intensity with power, pulse duration, focal size and position
in focus**************************************************************
I=(1/1.25)*1.6*((P)/1000)/(48E-15)/pi/1.59/(38.7E-4)^2;

%Defining the center of the peak to be analyzed***********************
for i=1:length(P);
    center(i)=88665;
end

%Defining the number of bins which fixes a 15 micron focus************
for i=1:length(P);
    for j=-29:29;
        Resolved(j+30,i)=DATA(center(i)+j,i);
    end
end

%Normalizing to 1 min runtime and 1e-7 mbar pressure for data and error
bars******************************************************************
for i=1:length(P),
      SumResolved(i)=((1e-7)/Pressure(i))*2*sum(Resolved(:,i));
      EB(i)=((1e-7)/Pressure(i))*2*sqrt(sum(Resolved(:,i)));
end

%Calculating the log-log slopes of the yields*************************
w=5; %number of points to average on each size
for j=1:w;
      for i=1:L+1; %i is the number of the datapoint, j is the number
of points from the ith data point
      if i==1;
            for j=1:w, Slope(j+i-1)=(log10(SumResolved(i))-
log10(SumResolved(i+j)))/(log10(I(i))-log10(I(i+j)));
            end
      elseif i<w+2;
            for j=-i+2:-1; Slope(j+i-1)=(log10(SumResolved(i))-
log10(SumResolved(i+j)))/(log10(I(i))-log10(I(i+j)));
            end
```

```
            for j=1:w; Slope(j+i-2)=(log10(SumResolved(i))-
log10(SumResolved(i+j)))/(log10(I(i))-log10(I(i+j)));
            end
      elseif i>L-w;
            for j=-w:-1; Slope(j+w+1)=(log10(SumResolved(i))-
log10(SumResolved(i+j)))/(log10(I(i))-log10(I(i+j)));
            end
            for j=1:L+1-i; Slope(j+w)=(log10(SumResolved(i))-
log10(SumResolved(i+j)))/(log10(I(i))-log10(I(i+j)));
            end
      else
            for j=-w:-1; Slope(j+w+1)=(log10(SumResolved(i))-
log10(SumResolved(i+j)))/(log10(I(i))-log10(I(i+j)));
            end
            for j=1:w; Slope(j+w)=(log10(SumResolved(i))-
log10(SumResolved(i+j)))/(log10(I(i))-log10(I(i+j)));
            end
      end
      SlopeAvg(i)=sum(Slope(:))/(2*w); %taking the weighted average
end

%Plotting the results of the yields and the slopes*********************
figure, semilogx(I,SlopeAvg,'bo')
figure, loglog(I,SumResolved,'bo')

%Fitting the spatial distribution of the peak to a Gaussian
%distribution and plotting the Gaussian width as a function of
%intensity*************************************************************
x=transpose([103000:1:103750]);
for i=1:length(P);
    y=DATA(103000:103750,i);
    FIT(i,:)=coeffvalues(fit(x, y, 'gauss1'));
end
figure,plot(FIT(:,3))

%*********************************************************************
```

A.4 – Simulating a Gaussian focus

```
%This program calculates the range of intensities found in a given
%focus. The focus is assumed to be an ideal Gaussian in shape, and the
%detection volume is rectangular and sampled on a cubic grid. Each
%sample represents a discreet cubic volume with uniform intensity.*****

clear, clc;

D=000;                                  %Distance from minimum waist of
                                        %Focus in microns
w0=35;                                  %Beam waist in microns
z0=3.1415927*(w0^2)/0.8;                %Rayleigh range
sizeX=15;                               %Test tube dimensions in microns
sizeY=100;
sizeZ=500;
dx=sizeX/15;                            %Step size in each direction
dy=sizeY/100;
dz=sizeZ/500;
dV=dx^3;
I=zeros(round(sizeX/dx), round(sizeY/dy), round(sizeZ/dz));

%Calculating the intensity on a cubic grid. Random numbers can be
included to eliminate pixelation************************************
for i=1:sizeX/dx+1;
    x=-sizeX/2 + dx*(i-1)*(1+0*randn(1));
    for j=1:sizeY/dy+1;
        y=-sizeY/2 + dy*(j-1)*(1+0*randn(1));
        for k=1:sizeZ/dz+1;
            z=D-sizeZ/2 + dz*(k-1)*(1+0*randn(1));
            I(i,j,k)=1/((1+((z)^2)/(z0^2)))*exp((-
2*((x^2)+(y^2)))/((w0^2)*(1+((z)^2)/(z0^2))));
        end
    end
end
Iround=roundn(I,-6);

%Reducing from a three-dimensional array to a two-dimensional array****
for i=1:sizeX/dx+1;
    for j=1:sizeY/dy+1;
        for k=1:sizeZ/dz+1;
            listnumbers2d(i+size(I,1)*(k-1),j)=I(i,j,k);
        end
    end
end

%Reducing from a two-dimensional array to a one-dimensional array******
for i=1:size(listnumbers2d,1);
    for j=1:size(listnumbers2d,2);
        listnumbers1d(i+size(listnumbers2d,1)*(j-
1))=listnumbers2d(i,j);
    end
end

%Creating and plotting a histogram of intensities********************
for i=1:100; range(i)=10^(log10(100)*(i/100))/100; end
```

```
figure, hist (listnumbers1d, 50); figure(gcf)
        xlabel('Intensity (% Imax)');
        ylabel('Volume (um^3)');
        title('Volume per unit intensity');
Histogram=dV*(hist (listnumbers1d, range));
Histogram=transpose(Histogram);
[n,xout] = hist (listnumbers1d, 1000);
for i=1:length(n); nSum(i)=(sum(n(1:i)))/(sum(n(:))); end
figure, plot(xout,nSum)

%*********************************************************************
```

A.5 – The perturbed "particle in a ring"

```
clear, clc

%This program describes the "particle in a ring", the analogy of the
%"particle in a square well" generalized into polar coordinates. As
%presented, the ring is perturbed by slightly deeper spots in the well,
%meant to simulate the more deeply-bound potentials of the nitrogen
%atoms in pyridine and the diazines. Coefficients are calculated to
%find the superposition of unperturbed states in the corrected
%wavefunction.*********************************************************

V=1;                                %depth of the perturbation in volts
m=9.11e-31;                         %electron mass
e=1.602e-19;                        %electron charge
r=1.2e-10;                          %radius of unperturbed benzene
hbar=1.05e-34;
A=e*V*m*(r^2)/pi/(hbar^2);          %coefficient in front of all terms
N=50; J=50;
CnjPyridine=zeros(N,J);             %first-order perturbation coefficients
CnjPyridazine=zeros(N,J);
CnjPyrimidine=zeros(N,J);
CnjPyrazine=zeros(N,J);
ProbPyridine=zeros(N,J);            %Absolute square of Cnj
ProbPyridazine=zeros(N,J);
ProbPyrimidine=zeros(N,J);
ProbPyrazine=zeros(N,J);
min=1e-12;                          %any value less than "min" is set to
                                    "min" to enhance plotting

%Calculating the values of Cnj coefficients**************************
for n=0:N-1;
    for j=0:J-1;
        CnjPyridine(n+1,j+1)=A*i/(((n^2)-(j^2))*(n-
j))*(exp((i*pi/3)*(n-j))-1);
        CnjPyridazine(n+1,j+1)=A*i/(((n^2)-(j^2))*(n-
j))*(exp((i*2*pi/3)*(n-j))-1);
        CnjPyrimidine(n+1,j+1)=A*i/(((n^2)-(j^2))*(n-
j))*(exp((i*pi/3)*(n-j))-exp((i*2*pi/3)*(n-j))+((-1)^(n-j))-1);
        CnjPyrazine(n+1,j+1)=A*i/(((n^2)-(j^2))*(n-
j))*(exp((i*pi/3)*(n-j))-exp((i*4*pi/3)*(n-j))-((-1)^(n-j))-1);
        ProbPyridine(n+1,j+1)=(abs(CnjPyridine(n+1,j+1)))^2;
        ProbPyridazine(n+1,j+1)=(abs(CnjPyridazine(n+1,j+1)))^2;
        ProbPyrimidine(n+1,j+1)=(abs(CnjPyrimidine(n+1,j+1)))^2;
        ProbPyrazine(n+1,j+1)=(abs(CnjPyrazine(n+1,j+1)))^2;

        if ProbPyridine(n+1,j+1)<min,ProbPyridine(n+1,j+1)=min;
      elseif j==n,ProbPyridine(n+1,j+1)=min;
  else end

        if ProbPyridazine(n+1,j+1)<min,ProbPyridazine(n+1,j+1)=min;
      elseif j==n,ProbPyridazine(n+1,j+1)=min;
        else end

        if ProbPyrimidine(n+1,j+1)<min,ProbPyrimidine(n+1,j+1)=min;
      elseif j==n,ProbPyrimidine(n+1,j+1)=min;
```

```
  else end

        if ProbPyrazine(n+1,j+1)<min,ProbPyrazine(n+1,j+1)=min;
      elseif j==n,ProbPyrazine(n+1,j+1)=min;
  else end
    end
end

%Plotting the absolute squares of Cnj coefficients for all four
species*************************************************************
figure, imagesc(log10(ProbPyridine)), xlabel('n'), ylabel('j'),
title('Pyridine')
figure, imagesc(log10(ProbPyridazine)), xlabel('n'), ylabel('j'),
title('Pyridazine')
figure, imagesc(log10(ProbPyrimidine)), xlabel('n'), ylabel('j'),
title('Pyrimidine')
figure, imagesc(log10(ProbPyrazine)), xlabel('n'), ylabel('j'),
title('Pyrazine')

%*************************************************************************
```

Appendix B – Symmetry point groups and operations

Prismatic point groups

D_{6h}: benzene

$\boldsymbol{D_{6h}}$	E	$2C_6$	$2C_3$	C_2	$3C_2'$	$3C_2''$	i	$2S_3$	$2S_6$	σ_h	$3\sigma_d$	3_σ		
A_{1g}	1	1	1	1	1	1	1	1	1	1	1	1		x^2+y^2,z^2
A_{2g}	1	1	1	1	-1	-1	1	1	1	1	-1	-1	R_z	
B_{1g}	1	-1	1	-1	1	-1	1	-1	1	-1	1	-1		
B_{2g}	1	-1	1	-1	-1	1	1	-1	1	-1	-1	1		
E_{1g}	2	1	-1	-2	0	0	2	1	-1	-2	0	0	(R_z, R_z)	(xz,yz)
E_{2g}	2	-1	-1	2	0	0	2	-1	-1	2	0	0		x^2-y^2,xy
A_{1g}	1	1	1	1	1	1	-1	-1	-1	-1	-1	-1		
A_{2u}	1	1	1	1	-1	-1	-1	-1	-1	-1	1	1	z	
B_{1u}	1	-1	1	-1	1	-1	-1	1	-1	1	-1	1		
B_{2u}	1	-1	1	-1	-1	1	-1	1	-1	1	1	-1		
E_{1u}	2	1	-1	-2	0	0	-2	-1	1	2	0	0	(x,y)	
E_{2u}	2	-1	-1	2	0	0	-2	1	1	-2	0	0		

D_{2h}: pyrazine

$\boldsymbol{D_{2h}}$	E	$C_2(z)$	$C_2(y)$	$C_2(x)$	i	$\sigma(xy)$	$\sigma(xy)$	$\sigma(xy)$		
A_g	1	1	1	1	1	1	1	1		x^2,y^2,z^2
B_{1g}	1	1	-1	-1	1	1	-1	-1	R_z	xy
B_{2g}	1	-1	1	-1	1	-1	1	-1	R_y	xz
B_{3g}	1	-1	-1	1	1	-1	-1	1	R_x	yz
A_u	1	1	1	1	-1	-1	-1	-1		
B_{1u}	1	1	-1	-1	-1	-1	1	1	z	
B_{2u}	1	-1	1	-1	-1	1	-1	1	y	
B_{3u}	1	-1	-1	1	-1	1	1	-1	x	

Cyclic point groups

C_{2v}: fluorobenzene, chlorobenzene, bromobenzene, iodobenzene, nitrobenzene, pyridine, pyridazine, and pyrimidine

$\boldsymbol{C_{2v}}$	E	C_2	$\sigma_v(xz)$	$\sigma'_v(yz$		
A_1	1	1	1	1	z	x^2,y^2,z^2
A_1	1	1	-1	-1	R_z	xy
B_1	1	-1	1	-1	x,R_y	xz
B_2	1	-1	-1	1	y,R_x	yz

C_s: toluene, aniline, phenol, and anisole

$\boldsymbol{C_s}$	E	σ_h		
A'	1	1	x,y,R_z	x^2,y^2,z^2,xy
A''	1	-1	R_x, R_y,z	xz,yz

Appendix C – Further evidence of REMPI

We observe evidence of REMPI beyond the log-log slopes as presented in Chapter 6, though for the yields of many molecules this further evidence is unconvincing. The focus of the laser has some spatial distribution of intensities in the unresolved direction (between the slit and the repeller as seen in Chapter 5, Fig. 4). Fitting these spatial distributions, which neglects our full three-dimensional spatial resolution, tells us the spatial width in the focus of a given process; if we know from the ion yields that the process involves seven photons, this tells us that the spatial width is proportional to the distribution of intensity to the seventh power. As the resonance begins to saturate at higher intensity, the center of the focus (which is the most intense) saturates first. This results in a spatial ion distribution for which the yield at the center is the result of a different process, and thus has a different Gaussian fit. If the resonance is then consistent over a large range of intensities, at higher intensity the yield throughout the entire focus may result from the saturated process, and its width would then be defined by the fourth power of intensity (in the example of (3 + 4) REMPI with the three-photon transition saturating first). This is illustrated in Fig. C1.

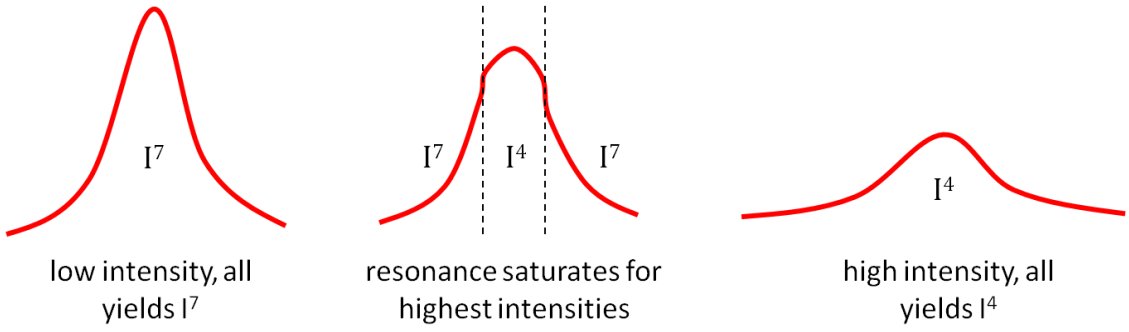

Figure C1 – Spatial ion widths as a function of the order of the process. Because the laser focus has a distribution of intensities, the ionization rates in different regions of the focus may depend on a different power of intensity.

As the order of the process decreases, the width of the spatial ion distribution becomes wider, and we observe this in our data. Fig. C2 shows the spatial width of the ion yields as a function of intensity for iodobenzene. Because of inaccuracies in the fitting process, the blue curves represent the upper and lower bounds at 95% confidence for a Gaussian fit. Unfortunately, iodobenzene is the only molecule for which the higher-intensity slope lasts long enough to make a confident determination of its spatial width; all other molecules we have studied never pass the center frame of Fig. C1, where a Gaussian spatial distribution is a poor fit due to mixed processes throughout the focus. A few molecules, such as pyridine and anisole, have yields which approach an accurate width, but they never settle on a width long enough to remove subjectivity from the fit.

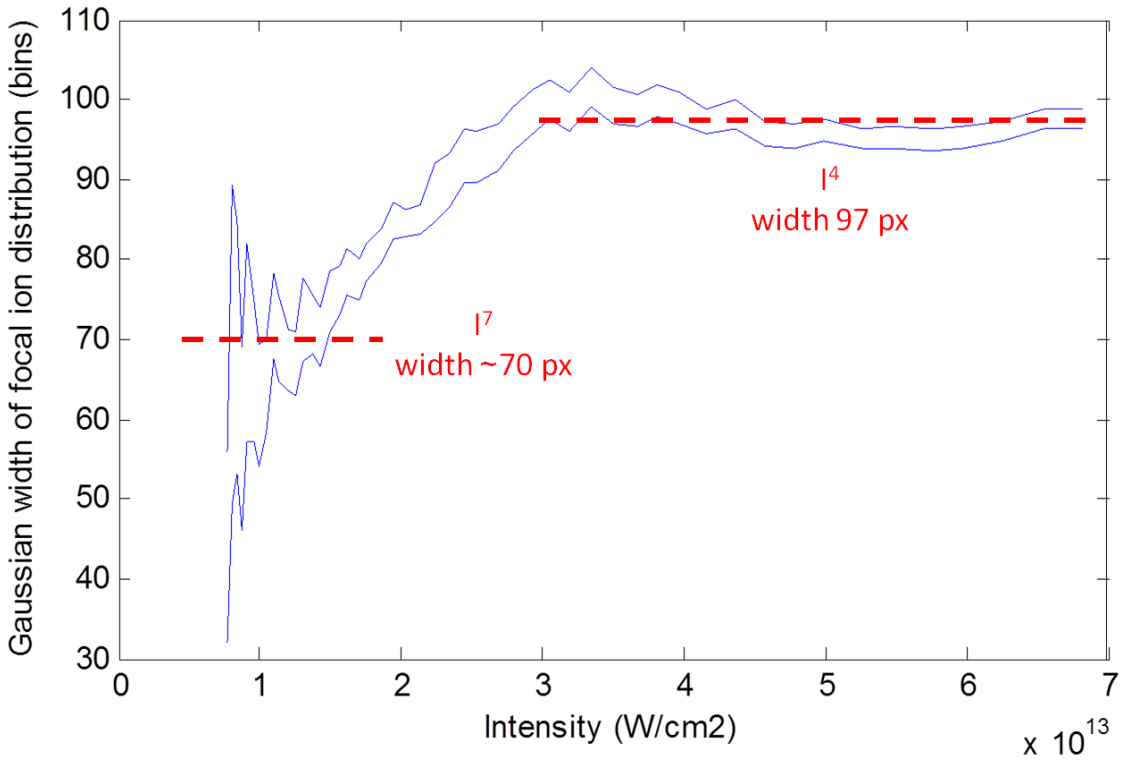

Figure C2 – Changing spatial width. As a resonance saturates, the spatial ion yield depends on a lower power of intensity, and thus the width becomes larger. Shown is the width as a function of intensity for iodobenzene, which saturates from a seven- to a four-photon process.

Comparing the widths before and after saturation of the resonant process serves as confirmation of the orders of each process. For iodobenzene we expect a spatial distribution proportional to I^7 at low intensity, and one proportional to I^4 at high intensity. The relation between the two widths is

$$I^7 = \left(I^4\right)^{7/4} = \left(A_4 e^{-x^2/\omega_4^2}\right)^{7/4} = A_7 e^{-x^2/\omega_7^2}. \quad \textbf{(C.1)}$$

Neglecting the magnitude to consider only the width of the distribution gives

$$e^{-7x^2/4\omega_4^2} = e^{-x^2/\omega_7^2} \quad \textbf{(C.2)}$$

which leads to

$$\omega_7 = \sqrt{\frac{4}{7}}\omega_4. \quad \textbf{(C.3)}$$

The data for iodobenzene shows the I^4 width to be approximately 97 pixels; if the relation between the seventh and fourth powers of intensity is valid, the I^7 width should be $\omega_7 = \sqrt{\frac{4}{7}}(97\text{ px}) = 73\text{ px}$. This fits within the 95% confidence bands shown in Fig. A2, and serves as confirmation of the orders of the processes in addition to the double-logarithmic slopes of the yields.